Controlled Hydrothermal Growth of ZnO Nanorod Arrays: Selective Growth and Cation Doping

Amir Hassanpour

A Thesis

In the Department

of

Physics

Presented in Partial Fulfillment of the Requirements

For the Degree of

Doctor of Philosophy (Physics) at

Concordia University

Montréal, Québec, Canada

April 2017

CONCORDIA UNIVERSITY

School of Graduate Studies

This is to certify that the thesis prepared

By: **Mr. Amir Hassanpour**

Entitled: **Controlled Hydrothermal Growth of ZnO Nanorod Arrays: Selective Growth and Cation Doping**

and submitted in partial fulfillment of the requirements for the degree of

Doctor of Philosophy in Physics

complies with the regulations of the University and meets the accepted standards with respect to originality and quality.

Signed by the final Examining Committee:

Chair's name	______________________	Chair
Dr. Lionel Vayssieres	______________________	External Examiner
Dr. Rafik Naccache	______________________	Examiner
Dr. Valter Zazubovits	______________________	Examiner
Dr. Alexandre Champagne	______________________	Examiner
Dr. Pablo Bianucci	______________________	Supervisor

Approved by ______________________________________

Chair of Department or Graduate Program Director

__________ 2017 ______________________________________

Dean of Faculty

Abstract

Controlled Hydrothermal Growth of ZnO Nanorod Arrays: Selective Growth and Cation Doping

Amir Hassanpour, Ph.D.
Concordia University, 2017

Zinc oxide (ZnO) is a well-studied wide band gap (~3.37 eV) n-type semiconductor material with significant properties such as large exciton binding energy (60 meV). Recently, 1-dimensional ZnO nanostructures have attracted a lot of attention owing to their dimensionality-dependent chemical, physical, electrical, and magnetic properties. In this project, we have grown patterned low-aspect-ratio, well-separated single ZnO nanorods using a hydrothermal method on two different substrates with dissimilar crystal orientations. ZnO nuclei have been used as a seed layer to compensate the crystal mismatch between the substrates and nanorods. Based on XRD results, in order to have highly oriented nanorods, the seed layer must be annealed over 300˚ C. Micro-Raman spectra show that our patterned nanorods have a wurtzite crystal structure, with most nanorods presenting vertical orientation relative to the substrate. Room-temperature micro-photoluminescence spectra from the nanorods show sharp band edge emission at 385 nm and a common broadband defect emission in the visible range. This method is a significant step towards an economical controlled synthesis of 1-dimensional ZnO for application in mass-production advanced devices. In the second part, undoped and C-doped (C: Mg, Ni, Mn, Co, Cu, Cr, Na) ZnO nanorods were synthesized by a hydrothermal method at temperatures as low as 60 ℃. The effect of doping on morphology of the ZnO nanorods was visualized by taking their cross section and top SEM images. The crystallinity change of the ZnO nanorods due to each cationic dopant was thoroughly investigated according to their XRD patterns. The optical Raman active modes of undoped and cation-doped nanorods were measured with a micro-Raman set up at room temperature. The surface chemistry of undoped and doped ZnO nanorods were investigated by X-ray photoelectron spectroscopy and Energy-dispersive X-ray spectroscopy. Finally, the band gap shift and defect emission of undoped and doped nanorods were measured by a photoluminescence set up at room temperature. Our results can be used as a comprehensive reference regarding the engineering of the morphological, structural and optical properties of ZnO nanorods by using a low temperature doping synthesis as an economical mass production approach.

Acknowledgment

I would like to thank Dr. Nicoleta Bogdan who assisted me to sharpen my chemistry skills at the beginning of this project. In following, I want to thank Dr. John Capobianco and his research group members in the department of chemistry and biochemistry of Concordia University for the early collaboration that eventually leaded to our first journal paper.

Special thanks to Dr. Alexandre Champagne and his research group members at the time for generous support and friend ship during my Ph.D. program.

This thesis would not have been possible without the support of technicians at École Polytechnique de Montréal: Laurent, Paul, Marie-Helen, Alireza, Christophe, Arslane, Jean-philippe who soothed the fabrication and characterization of my samples in different stages.

My deepest appreciation goes to Dr. Lionel Vayssieres for accepting me at the prestigious International Research Center for Renewable Energy (IRCRE) in the spring 2016. The cation doping of nanorods could not be done without his insightful guidance, constructive comments and warm encouragement. I am also indebted to Dr. Liejin Guo and Dr. Shaohua Shen and their research group members at the State Key Laboratory of Multiphase Flow in Power Engineering at Xi'an Jiaotong University. My experience in the lab was greatly enhanced by working with the talented graduate students at the School of Energy and Power Engineering during my visit in 2016.

Most of all, I would like to thank my thesis advisor, Dr. Pablo Bianucci, a talented teacher and passionate scientist. For a young researcher who had never before taken on a Ph.D. student, Pablo seemed to be wise beyond his experience. Good supervisors are those who are easy to approach and difficult to blame. Thanks for being one.

Last but not least, I would like to thank my mother who offered me unconditional love and support throughout my whole graduate study. I could always feel her precious love by my side, although we were staying thousands of miles away from each other.

Table of Contents

List of Figures

List of Tables

List of abbreviations

1-D	1- dimensional
Mg	Magnesium
Ni	Nickel
Co	Cobalt
Al	Aluminum
Cu	Copper
Cr	Chrome
In	Indium
Ga	Gallium
P	Phosphorous
N	Nitrogen
As	Arsenic
Li	Lithium
Sb	Antimony
Ag	Silver
Mn	Manganese
PLD	Pulsed laser deposition
Na	Sodium
SEM	Scanning electron microscopy
XRD	X-ray diffraction
PL	Photoluminescence
XPS	X-ray Photoelectron spectroscopy
EDS	Energy-dispersive X-ray spectroscopy
TO	Transversal
LO	Longitudinal
NBE	Near band edge
UV	Ultra violet

Chapter 1 Introduction

Zinc oxide (ZnO) has attracted attention thanks to its remarkable properties such as wide and direct band gap (Eg ~ 3.37eV). The wide band gap affords it to be highly transparent over the whole visible range spectrum, and its large exciton binding energy (~60 meV) leads to excitons that are stable at room temperature. In addition, ZnO is a non-toxic, nature-abundant material, it shows strong piezoelectricity, and it is considered biocompatible. With the advent of straightforward solution-based methods for the synthesis of high-quality ZnO crystalline nanostructures [1], it has become one of the most investigated semiconductor materials [2]. The most similar inorganic semiconductor material to ZnO in terms of crystal structure, optical and electronic properties is GaN. Statistics show that the number of scientific reports published in forms of journal articles, book chapters, and proceeding papers about the ZnO and GaN were almost the same, 10 years ago. The number of works done on GaN remained almost the same during last 10 years, while, as shown in Figure 1.1, the interest in ZnO material grew as the time went by. As shown in Figure 1.2 this difference becomes more distinct by comparing the number of works that are done on the ZnO and GaN in the form of nanorods or nanowires. The strong ongoing interests in ZnO nanorods/nanowires can be due to its vital optical properties as well as its unique flexibility regarding synthesis techniques and growth substrates. Therefore, ZnO has the potential to become a leading contender to replace commonplace semiconductor materials such as GaN in future optoelectronic devices.

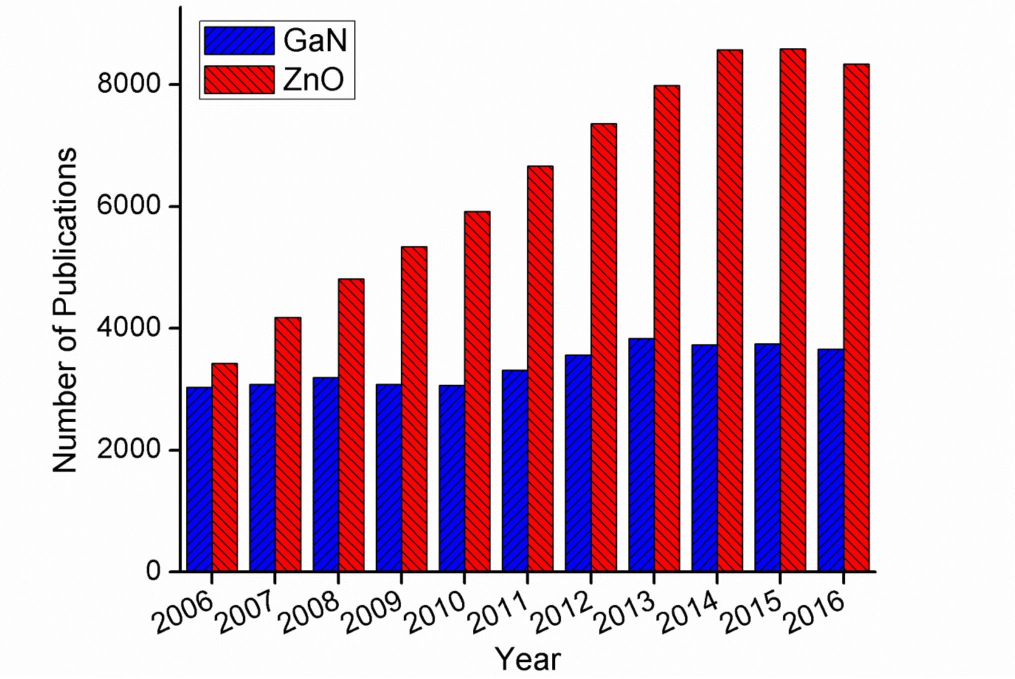

Figure 1.1 Number of publications with the key words "GaN" and "ZnO", based on the data derived from the Web of Science (Feb. 2017) [3].

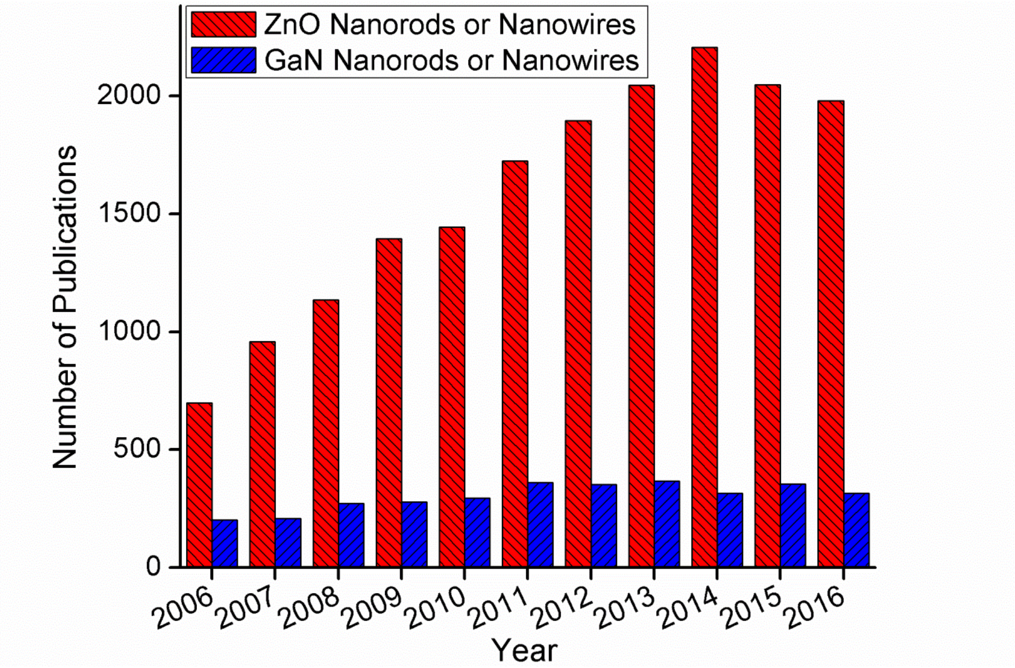

Figure 1.2 Number of publications with the key words "GaN nanorods OR GaN nanowires" and "ZnO nanorods OR ZnO nanowires", based on the data derived from the Web of Science (Feb. 2017) [3].

The optical, electrical, and magnetic properties of ZnO can be improved by synthesizing ZnO in nanoscale form [4]. In fact, the number of structural defects drops in catalyst free grown nano-crystal due to the lower amount of stress in their nanostructure crystal [5]. The mentioned properties can be further enhanced by cation doping of 1-dimensional (1D) ZnO nanostructures. In this direction various cations such as Mg^{2+} [6], Ni^{2+} [7], Co^{2+} [8], Al^{3+} [9], Mn^{2+} [10], Cu^{2+} [11], and etc. have been introduced in ZnO nano-crystals in order to alter their optical, and electrical properties.

The optical band gap of a cation-doped ZnO crystal differs from its pristine form. Upon doping a semiconductor, impurity states are created within its gap. This will cause band gap reduction and most probably a shift of the Fermi energy into the impurity bands [12]. ZnO band gap engineering via cation doping has enabled the fabrication of electron-confining structures where electrons and holes can interact strongly with light [13]. Halm et al.[14] reported strong exciton-photon coupling in a Zn/Zn-Mg-O multilayer deposited via molecular beam epitaxy in a highly controlled manner. One of the most significant signatures of strong light-crystal interaction in semiconductor materials is the emergence of a quasi-particle known as Polariton that is mixture of an electronic excitation and a photon. The prospect of the room temperature polaritonic lasing has brought attention to the large band gap semiconductor materials such as ZnO due to their strongly bound electrons-holes [15]. The common optical devices fabricated for this purpose are multilayer thin films with different band gap energies forming a multiple quantum well (MQW) heterostructure [16]. Alternating intrinsic ZnO band gap with an altered-band gap ZnO via a straightforward metal doping method in order to fabricate MQWs in more compact morphologies such as nanorods could be a fascinating approach. The dimensions of the synthesized nanorods are usually slightly different from each other. Therefore, due to the size dependence of MQWs properties, one needs to fabricate well separated isolated ZnO nanorods to characterize them separately. In this direction we first needed to master a reliable and low cost pathway to grow well separated ZnO nanorods.

1.1 Selective growth of isolated ZnO nanorods

Fabricating highly oriented and ordered arrays of nanomaterials is vital for the development of high-technology nanomaterials-based devices including light-emitting devices [17], random lasers [18], and piezoelectric devices [19]. We chose the most common hydrothermal method to fabricate arrays of isolated ZnO nanorods. The advantages of ZnO hydrothermal growth over other synthesis techniques have been discussed many times in the literature [20]. Hydrothermal methods excel at creating dense "forests" of randomly-located arrays of nanorods, perpendicular to the substrate as shown in Figure 1.3.

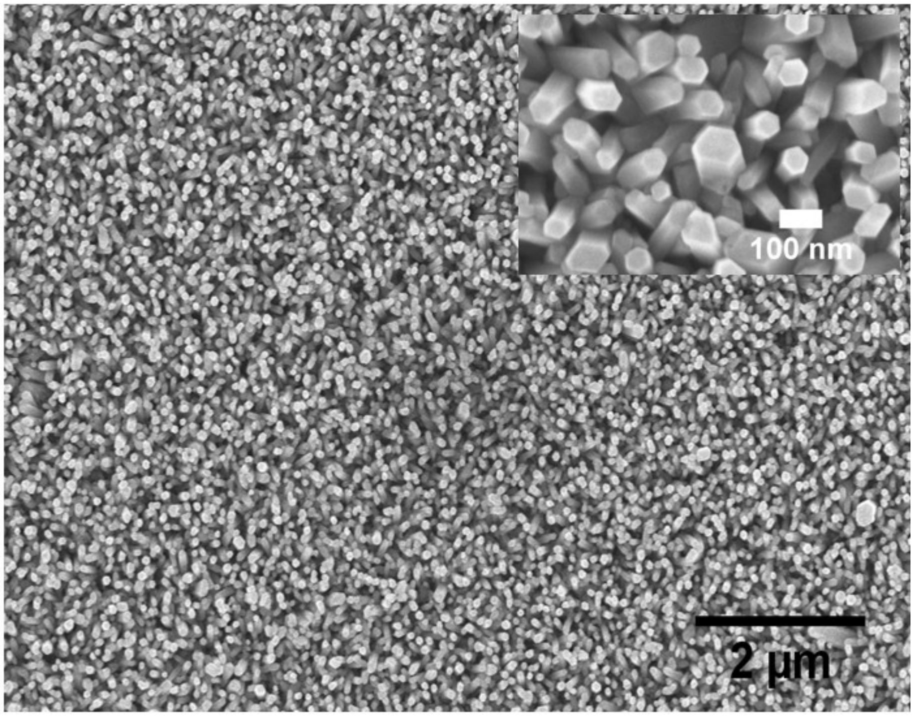

Figure 1.3 SEM image of ZnO nanorods grown by a hydrothermal method at 90℃ on a seeded silicon substrate with a concentration of 5 mM. Inset: high magnification SEM image of the same sample.

Having control over the position and density of ZnO nanorods is of great importance. It has been argued that the performance of ZnO nanorod-based devices could depend strongly on the nanorods spacing, density, and alignment [21-23]. Therefore, an efficient method to create a large-scale position- and dimensionality-controlled nanostructure over different smooth substrates is crucial for future advanced nanodevices. For this purpose, patterned growth of ZnO nanorods and nanowires through various approaches has been reported in the past [24-46]. In many of these reports, which used a mask-based approach, the patterning was limited to micron-sized areas, resulting in the growth of bundles of nanowires in the desired locations rather than single, isolated rods. To be able to easily characterize single nanorod or to fabricate particular nanorod-based nanoscale optical devices, it is necessary to grow single nanorods on arbitrarily designed locations. A particularly interesting possibility would be the fabrication of nanorod-based 2-dimensional photonic crystals. These crystals have been fabricated in other materials via sophisticated physical growth methods for applications such as LEDs [47], microlasers [48], and sensors [49].

Mask-less methods for patterning have been explored in the literature, but without much success in obtaining isolated single nanorods. For instance, inkjet printing of zinc precursors is claimed to be able to produce seeds small enough to grow a single nanowire [50], but in practical implementations that regime has not been reached, yet [51]. Laser-induced hydrothermal growth has also been shown to produce patterns of ZnO nanorods [52-57], but the spot size limited by diffraction results in large seed patterns with multiple nanorod growth. Differential heating at the nanoscale can also result in selective nanowire growth via highly localized thermochemical nano-reactions [58], resulting in patterned hierarchical heterojunctions of ZnO nanowires, but no single nanorod growth. Using electron beam lithography (EBL) to design a pattern brings highly precise control of the size (~50 nm) and position of patterns, allowing for the controlled growth of single nanorods. The hydrothermal method not only provides us with low temperature growth (less than 95℃), but also with control over the size of the grown nanorods [59]. Therefore, the combination of EBL and the hydrothermal growth method provides an excellent approach towards the patterned growth of single ZnO nanorods, which is impossible to obtain using lithography methods with lower resolution.

Homogenous nucleation of solid phases, in particular for metal oxides, occurs at a lower saturation ratio onto any kind of substrate (independent of its crystal structure), than in homogenous solution [1, 60]. Therefore, there is no obligation to use a crystal-matched substrate for the hydrothermal growth of ZnO nanoparticles. However, to improve the heteronucleation and nanorods orientation as well as achieving a lower activation energy barrier the substrates are pre-treated prior to the patterning. Previous reports have used bulk c-plane ZnO single crystals

[61], and substrates with physically deposited ZnO thin films, or materials with similar crystal lattices such as GaN [43, 62]. While these methods resulted in well-patterned growth, the required substrates and substrate preparation are expensive and/or time consuming.

In the second chapter, I will discuss the patterned growth of isolated ZnO nanorods using a hydrothermal growth method with a seeding layer based on spin cast of ZnO precursor followed by a thermal annealing [63]. This method may be applied on any smooth surfaces without any restrictions due to lattice mismatch. Our motivation is to develop a simplified method of substrate pre-treatment for more convenient selective growth of single ZnO nanorods. The seed film used in this thesis is highly bonded to the substrate. It has been reported that the effect of this type of seeding layer on transport properties of ZnO nanorods is minimum [60]. Additionally, low-aspect ratio structures are highly resistant against physical damage, such as that inflicted by the surface tension of evaporating water. In this direction, we have grown low-aspect-ratio nanorods which could be useful in creating photonic confinement (either in a single rod or in a rod-based photonic crystal) with very few transverse modes even at short wavelengths. While our method is inexpensive in terms of substrate materials and preparation, EBL is an expensive technique with low throughput. Other lithography techniques with the capability of making sub-100 nm holes in a mask could be used, such as thermal scanning probe lithography [64], or nano-imprint lithography [45] to further reduce production costs.

1.2 Band gap engineering of ZnO nanorods by cation doping

In order to alter the band gap of ZnO we tried cation doping by using a straight forward hydrothermal method. I had two motivations for this process in my mind. First, find the appropriate doping cations which lead to the largest band gap alteration. Secondly, make sure that the morphology of the ZnO nanorods is not affected by the doping process.

The advantages of cation doping of ZnO nanorods are not limited to band gap alteration. For instance it has been shown that Mn^{2+} doping of ZnO can be an effective solution to overcome its high operating temperature and low performance as gas sensor [65]. In fact, higher concentration of electrons due to dopant atoms in the ZnO host crystal lattice enhances its gas sensitivity. In general, undoped ZnO nanostructures exhibit n-type conductivity behaviour mainly due to the presence of structural defects such as oxygen vacancies and zinc interstitials [66]. It has been shown that the concentration of the electrons in ZnO crystal could be further enhanced by introducing group III cations such as Al^{3+} [67], In^{3+} [68], and Ga^{3+} [69]. While fabricating p-type ZnO is more challenging [70, 71], it can be done through incorporation of phosphorus (P) [72], nitrogen (N) [66], arsenic (As) [73], lithium (Li) [74], antimony (Sb) [75], and silver (Ag) [76] into its host crystal lattice. It is worth to keep in mind that light emitter devices made with ZnO p-n homo junctions are preferable since they have minimum crystal lattice mismatch at the junction [77]. Another crucial application of ZnO, particularly in its 1-D nano-crystal form is based on its photocatalytic properties. Results show that the photocatalytic activity of ZnO can improve by doping with different cations such as Cu^{2+} [78], Ni^{2+} [79], Co^{2+} [80], Mn^{2+} [81], and Mg^{2+} [82] which are isomorphic to ZnO ions. In fact, cation doping of ZnO is an effective way to enhance the charge separation, yielding more crystal electron confinement, and eventually generation of larger number of hydroxyl radicals and active oxygen species in a photocatalytic process [83]. These all result in the reduction of the photo excited electron-hole recombination rate which directly affects the degree of photoactivity of ZnO nano-crystals [84].

The amount of distributed dopant ions in the ZnO host lattice depends on its preparation conditions [85]. High level of dopants can be incorporated into ZnO through physical deposition methods such as pulsed laser deposition (PLD) [86], molecular beam epitaxy [87], and magnetron sputtering [88]. This is due to the higher solubility of transition metal cations in ZnO thin films grown under nonequilibrium conditions such as PLD [89]. However, the intense growth conditions that these methods require often hinder the size and morphology of the final device as well as the possible substitutes that can be used inside the growth chamber. Hydrothermal method, on the other hand, could be an effective substitute for those techniques to insert a variety of cation dopants in 1-D ZnO nanocrystal at a low cost and moderate temperature [90]. The achievable level of doping is generally lower than the ones obtained by physical methods, and the number of the doping candidate materials is limited, however the morphology usually remains unchanged. There are reports of doping of ZnO with Mg^{2+} [91], Ni^{2+} [79], Mn^{2+} [92], Cr^{2+} [93], Cu^{2+} [94], and Co^{2+} [80] via solution growth methods. Most of these reports were mainly focused on the amount of dopant incorporated into the host lattice rather than the morphology of the final device. Besides, those works have been mainly done under different synthesis conditions where the final results are not comparable from one report to the other.

Therefore, there is a need for a comprehensive work to be done, using the most common low temperature synthesis method similar for all the dopant cations, and comparing the results to the recent works reported by the others.

In the third chapter, for the first time I report cation-doped growth of free standing large aspect ratio arrays of ZnO nanorods via a hydrothermal method at temperatures as low as 60℃. An extensive overview on application of each cation-doped ZnO nanorod will be given at each section, as well as the most recent synthesis advancements reported in the literature. Eventually, the effect of the cation dopant material on morphology, crystal structure, surface chemical compositions, and photoluminescence of the ZnO nanorods will be discussed. At the end, I report the synthesis of ZnO nanorods doped with Na^+ ions with different concentrations via a hydrothermal method at 60℃. The effect of the Na^+ doping concentration on morphology, crystal structure, surface chemicals, and photoluminescence of the ZnO nanorods will be discussed.

Chapter 2 Selective growth of low aspect ratio isolated ZnO nanorods

Vayssieres [95] successfully used a hydrothermal method for the controlled fabrication of ZnO nanowires on glass and silicon substrates. Since there is no catalyst being used in this method, the final nanorods can be free of contamination. Besides, a low growth temperature allows one to use different kinds of materials, including polymers, as the substrate. It is also an economical method and has a good potential to scale up [96]. By using a hydrothermal method highly ordered arrays of ZnO with the minimal defects were grown from a single-crystalline substrate that has a small lattice mismatch such as sapphire [97]. Alternatively, pre-treatment of crystal mismatch substrates in order to synthesize dense arrays of ZnO nanorods by using a hydrothermal growth was suggested before [98, 99]. A dilute solution of zinc acetate in ethanol was prepared. The solution was spin-coated on silicon substrate followed by a thermal annealing at 200℃ to create ZnO nanocrystals known as seed layer. We used a similar method to cover our substrate with a thin layer of zinc nanoparticles prior to the growth. In order to find the optimum thermal annealing temperature, an investigation about the effect of the annealing temperature on the crystallinity of the seed layer was done. By performing a pre-treatment of the substrates using ZnO seed crystals which were annealed above 300℃, the crystal quality of the nanorods was significantly improved. Spin coating of the seed layer resulted in higher density of nanorods which were grown afterwards. In this method a thin platelike base forms first and acts as a seed for epitaxial nanowire growth [100]. So, by using a pre-seeding process, vertically aligned ZnO can be grown via a hydrothermal growth independent of substrate crystal structure.

I mainly used silicon wafer as a substrate due to its low cost and high conductivity to facilitate the SEM imaging. In the most common hydrothermal method zinc salt and hexamethylenetetramine (HMTA) are dissolved with the same ratio in a nutrient medium such as distilled water. The role of HMTA in the ZnO hydrothermal process is still under debate. Heating up the solution to 90℃ initially shifts the pH towards the more acidic region [101]. Basic conditions are crucial for the hydrothermal growth, because divalent metal ions do not readily hydrolyze in acidic media [99]. Therefore, an additive such as HMTA must be used to promote 1-D ZnO heteronucleation. In our case HMTA gradually decomposes, increasing the pH locally to above ~9 at the crystal surface [100]. Thus, the zinc hydroxyl species forms at the crystal surface due to the higher local pH. It has been suggested that solid ZnO nuclei are formed by the dehydration of these hydroxyl species. Because dehydration of the zinc hydroxide intermediates controls the growth of ZnO, the slow release of hydroxide may have a significant effect on the kinetics of the reaction [100].

In summary, series of reactions leading to the formation of ZnO in the growth bottle are as follows [102]:

$$(CH_2)_6N_4 + 6H_2O \leftrightarrow 6HCHO + 4NH_3 \qquad (2\text{-}1)$$

$$NH_3 + H_2O \leftrightarrow NH_4^+ + OH^- \qquad (2\text{-}2)$$

$$Zn^{2+} + 2OH^- \leftrightarrow Zn(OH)_2 \qquad (2\text{-}3)$$

$$Zn(OH)_2 \leftrightarrow ZnO + H_2O \qquad (2\text{-}4)$$

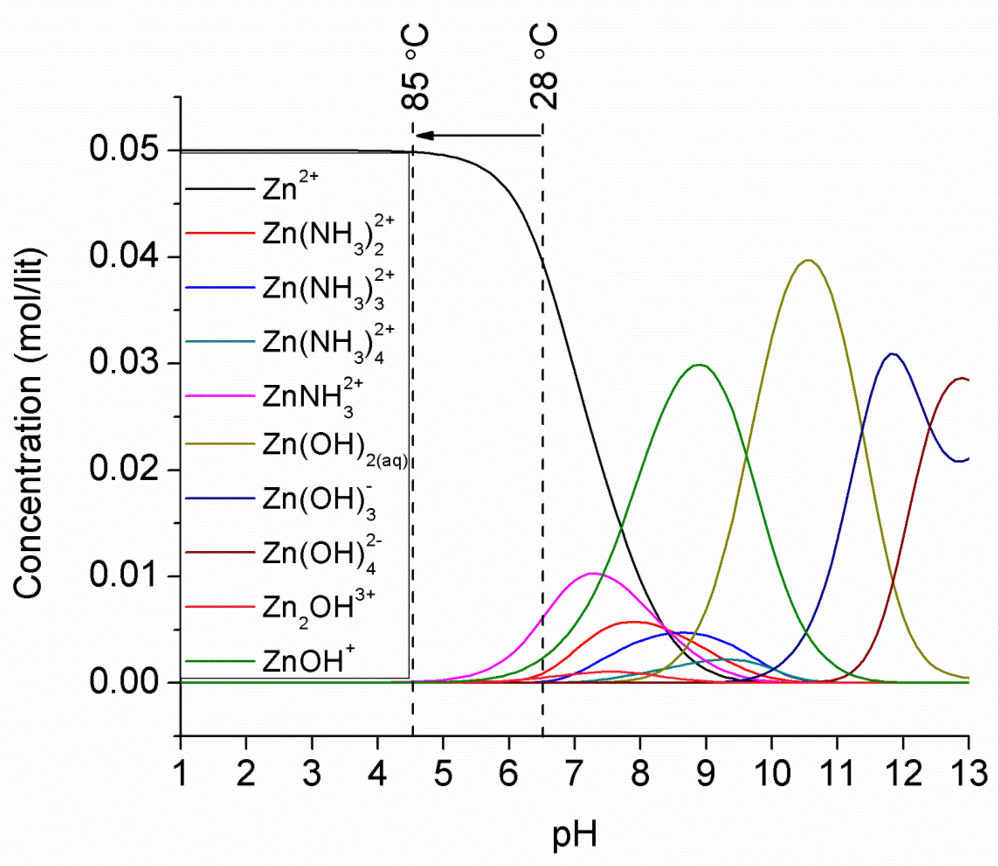

Figure 2.1 Speciation diagrams of Zn(II) species at 85 °C as a function of pH ranging from 0 to 13 as computed with Visual MINTEQ software.

In order to elaborate the chemical route that ions take to form ZnO, the concentrations of different soluble Zn(II) species were simulated by using Visual MINTEQ 3.1 software, and the results are shown in Figure 2.1. The simulations were done by considering Zn^{2+}, HO^- and NH_4^+ as the initial ions interacting in the growth solution at 85℃. The combination of Zn^{2+} ions as metallic cations beside HO^- ions and NH_4^+ as ligands results in the formation of Zn(II) hydroxide and amine complexes as follows: Zn^{2+} ions, $Zn(NH_3)_2^{+2}$, $Zn(NH_3)_3^{+2}$, $Zn(NH_3)_4^{2+}$, $Zn(OH)_{2(aq)}$, $Zn(OH)_3^-$, $Zn(OH)_4^{2-}$, Zn_2OH^{3+}, $ZnNH_3^{2+}$, and $ZnOH^+$. In my simulation the concentration of NH_4^+ was taken as equal to the concentration of HMTA. The pH of the growth solution was measured by an Orion 2 star pH meter and its electrode was optimized for measurements at room temperature. However, the electrode was calibrated for both room temperature and 85℃ to minimize the temperature effect error in our pH measurements. The pH evolution during the growth as a function of time is shown in Figure 2.2. It can be seen that the pH of the growth solution was alternating between 6.5- 4.4 at the early stage of the growth. Thus, Zn atoms may be found in the form of Zn^{2+}, $ZnNH_3^{2+}$ and $ZnOH^+$ in the growth solution at the early stage of the growth. By gradually decomposing of the HMTA, the pH of the solution increases locally. As it can be seen in Figure 2.1, the concentration of zinc hydroxide species increase at the pH ~9. Therefore, the dehydration of these groups at the crystal surface can maintain the nanorods growth.

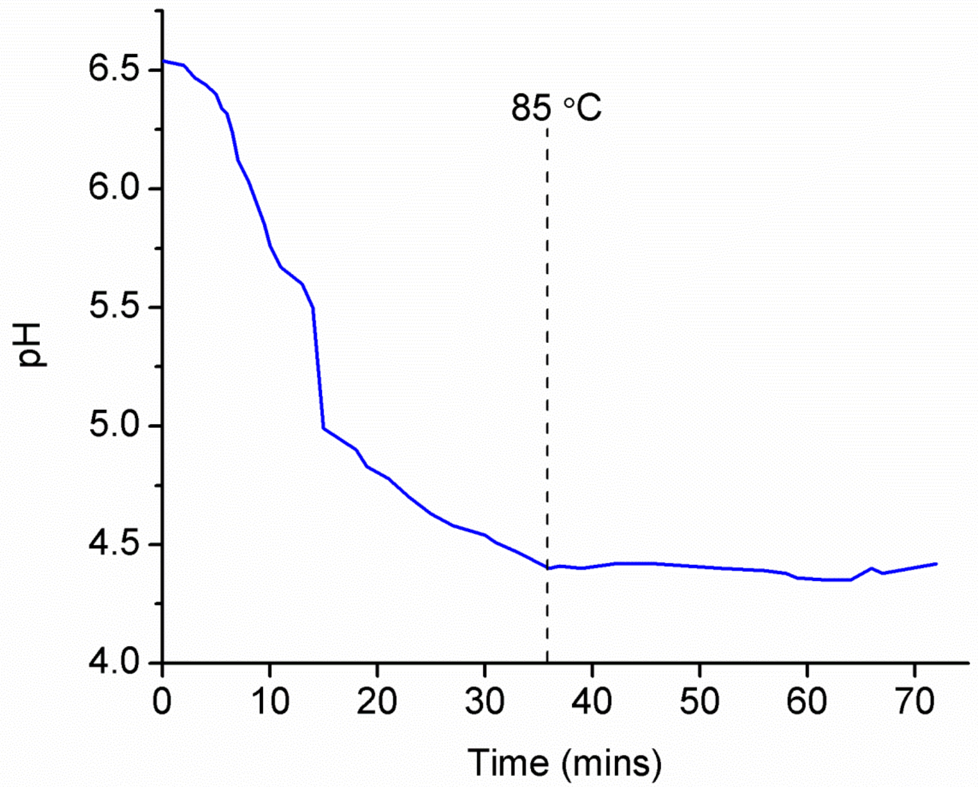

Figure 2.2 Evolution of the pH during the growth as a function of time (temperature up to 86℃)

The most common zinc salt compound which is used in hydrothermal method is zinc nitrate hexahydrate, while other zinc sources such as zinc acetate work in a similar way. Please note that the size of the nanorods in case of using of different compounds of zinc salt might be slightly different [103]. A comprehensive work about the effect of precursor compounds, growth time and temperature on the size of the ZnO nanorods grown by a hydrothermal method has been done by McCune [101]. A couple of years later, Sheng [102] reported various ways of selective growth of ZnO nanorods via a hydrothermal method. These two reports were the main reference for choosing the right growth parameters including time, temperature, and precursor concentrations. Initial results were in a good agreement with the reports; however I had to modify those growth parameters further along the project to reach the final target.

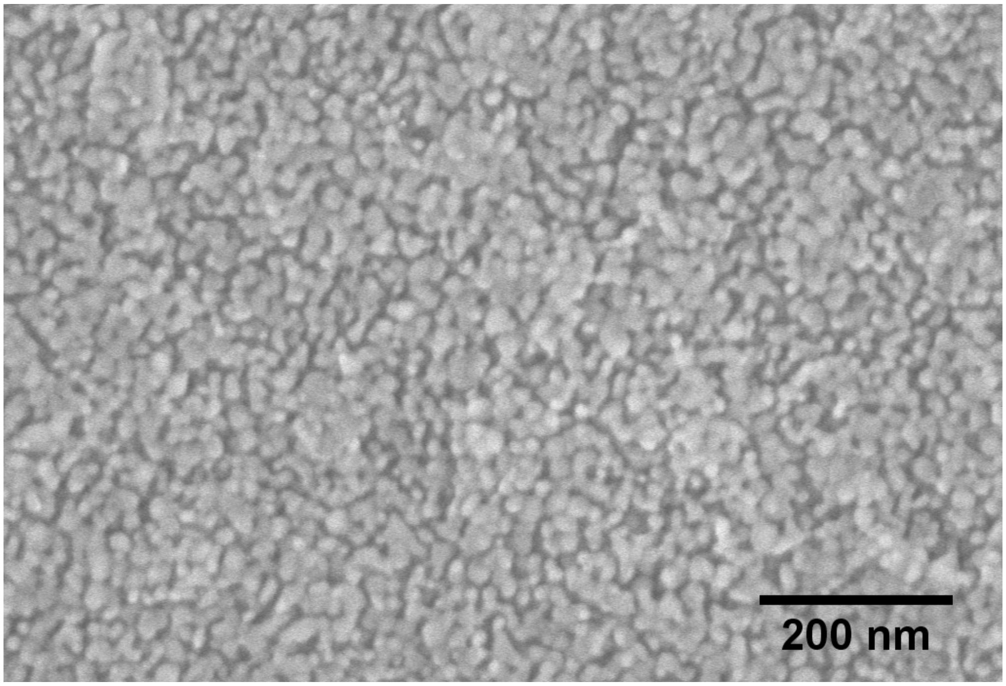

Figure 2.3 SEM image of the ZnO nanoparticles as seed layer annealed at 400℃ for 30 minutes.

For the patterning step I used two different substrates for comparison purposes: glass (a standard pre-cleaned microscope slide) and silicon (<100> crystal orientation). Samples were cleaned by performing three 10 minutes steps in an ultrasonic bath with acetone, isopropyl alcohol, and DI water, respectively. The last step is particularly important since there must be no organic solvent left over on the samples because that could spoil the patterning. A 5 mM solution of 99.98% zinc acetate (Alfa Aesar) in pure anhydrous ethyl alcohol was prepared as a seeding solution. The seeding solution was spin-coated on the pre-heated samples, followed by a low temperature annealing (~120 ˚C) to obtain a better adherence of the seed layer. After this annealing, the samples were washed away with pure ethanol and blow dried with pure nitrogen gas. The spin coating and washing were repeated at least 5 times per sample. It is worth to note that washing the sample with ethanol is critical to ensure a good uniformity of the seed layer for better patterning results. The samples were then annealed in a furnace at different temperatures (200 to 400˚C) for 30 minutes, so that the zinc acetate decomposes and ZnO nanoparticles are formed. The chemical reaction leading to the seed layer starts with transforming zinc acetate to tetrahedral oxy-acetate $Zn_4O(Ac)_6$ as follows [104]:

$$4Zn(Ac)_2.2H_2O \rightarrow Zn_4O(Ac)_6 + 7H_2O + 2HAc \qquad (2\text{-}5)$$

The $Zn_4O(Ac)_6$ can later transform into other primary clusters such as $Zn_{10}O_4(Ac)_{12}$, $Zn_{34}O_{16}(Ac)_{36}$ or $Zn_{130}O_{6}4(Ac)_{132}$. Larger clusters are expected to form with higher solution concentrations. This is in accordance with the experimental results by Guillemin et al. where the diameters of the ZnO nanoparticles were increased with the seeding solution concentration [105]. However, in this work I kept the concentration of the seeding solution constant at 5 mM. The whole seeding process was repeated 3 times for each sample to ensure a full coverage of ZnO nuclei. An SEM image of the common seed layer covering a silicon substrate is shown in Figure 2.3.

PMMA 950-A2 (Micro-chem) was spin-coated on top of the seed layer at 6000 rpm and followed by annealing at 180℃ for 2 minutes in order to create a mask. The thin PMMA mask (~50 nm) was then patterned using a Raith e-line Plus EBL system. A series of dosimetric experiments were done in order to find the appropriate electron beam dose to open a hole with a right diameter.

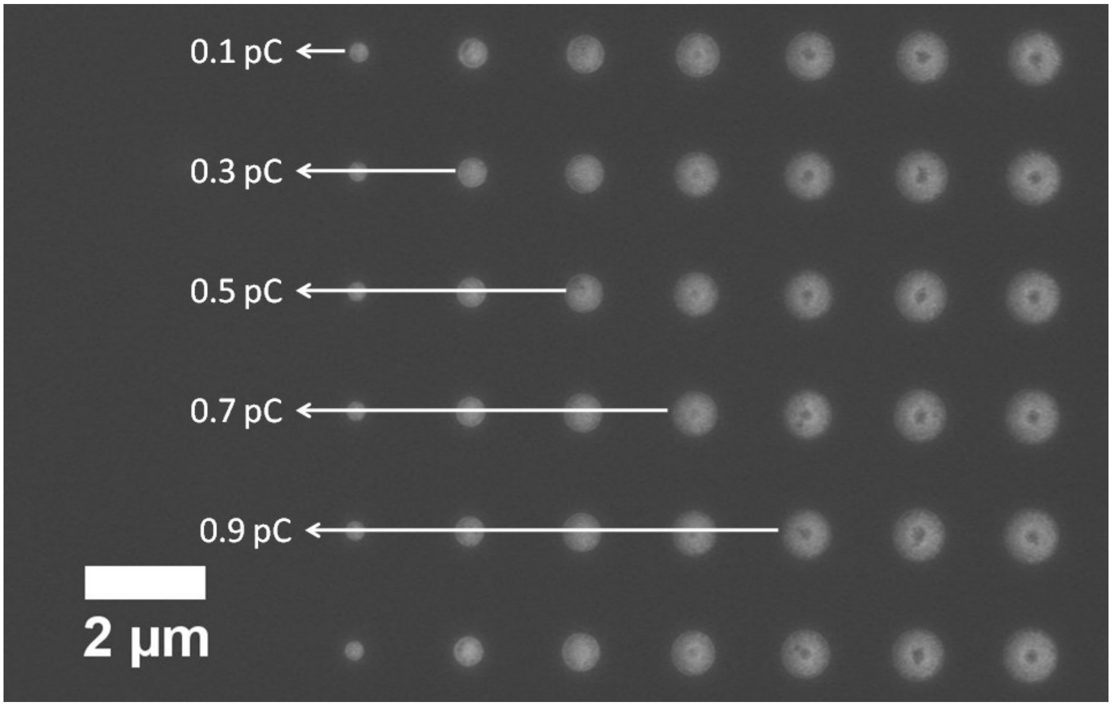

Figure 2.4 PMMA 950-A2 spin coated at 6000 rpm on silicon substrate, post annealed at 180℃ for 2 minutes, and irradiated by electron beam with different doses.

Based on my experiment, with an e-beam accelerating voltage of 10 kV a low dosage of electrons (less than 0.1 picoCoulombs) did not open a hole in the PMMA layer, whereas higher dosage (more than 0.5 picoCoulombs) ended up into crystallization of the PMMA in the center of the hole as shown in Figure 2.4. The crystallized PMMA could not be removed by the developing solution which is following the e-beam radiation. The e-beam dwell time was adjusted based on the e-beam current at the time of the experiment. Based on my dosimetry results in the case of using a dot profile in the patterning design, the dose of electron to open a hole in PMMA 950-A2 with an appropriate diameter is in the range of 0.1 pC to 0.5 pC. The exact dose to achieve a hole with 100 nm diameter depends on the age of the PMMA, its thickness and the working distance at which the patterning process will be done. Thus, each time a series of dosimetry tests are needed starting with approximate dose of electron to get the right hole sizes.

The exposed samples (seed layer + PMMA mask on the top) were then developed using a mixture of methyl isobutyl ketone (MIBK)/isopropyl alcohol (IPA) in a 1 to 3 ratio for 40 seconds. It is critical that the pattern be properly developed to ensure that the holes in the mask are fully open. The patterned samples were then annealed for 10 minutes at 90 ° C to remove water or other organic residues from the holes. In order to grow the nanorods, the patterned substrates were placed upside down in a growth vessel containing a 1:1 ratio of 50 mM solutions of zinc nitrate hexahydrate and hexamethylenetetramine (HMTA) in deionized water (with 18.2 megohm resistivity) . An oil bath was used to maintain the growth temperature at 85℃ for 2 hours. Acetone was used to remove the PMMA layer. The samples were subsequently washed with warm IPA to minimize nanorod breakage due to surface tension.

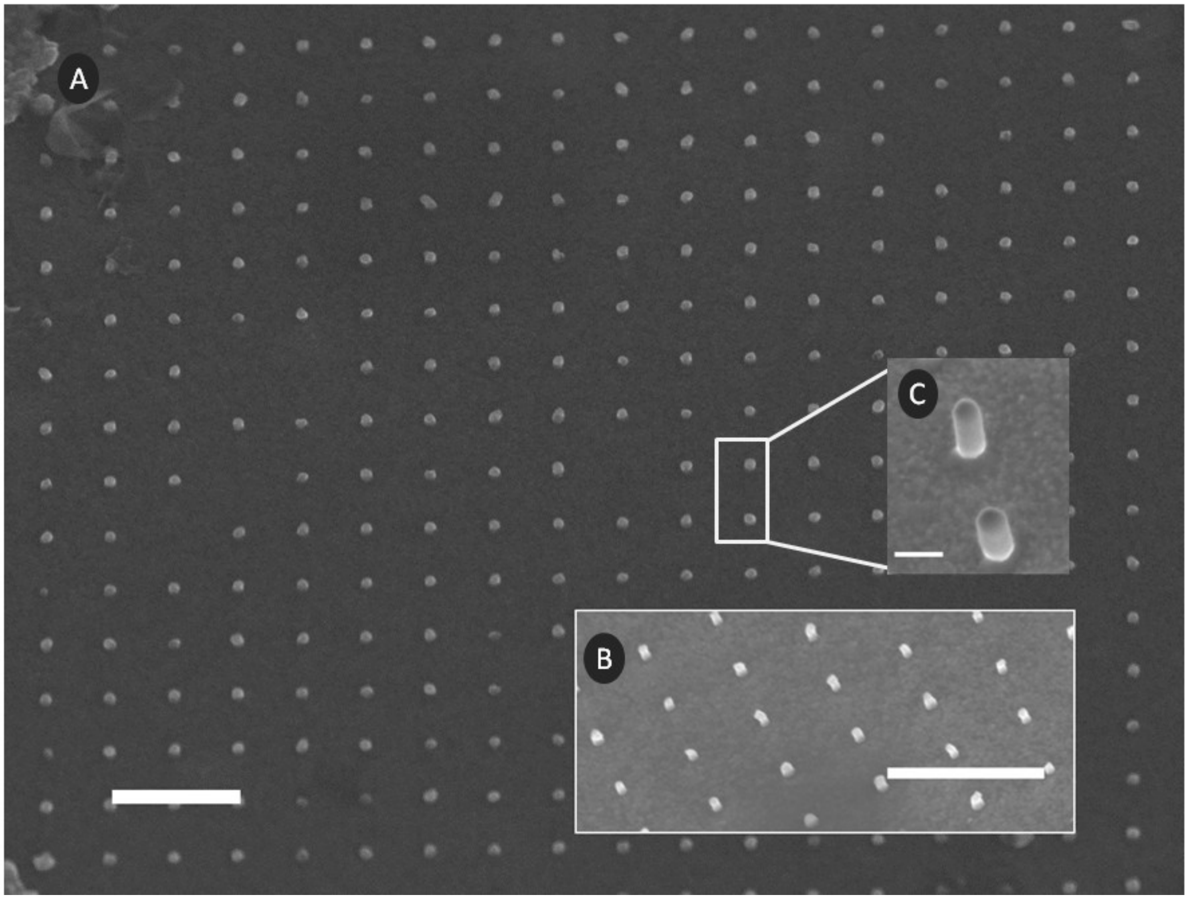

Figure 2.5 SEM images of patterned nanorods on silicon substrates grown at 85℃ for 2 hours with 50 mM zinc nitrate hexahydrate and HMTA. Panel A is a view from the top, while insets B and C are 60°-tilted views. The Scale bars indicate 1 μm for A and B, and 200 nm for inset C.

A Hitachi, S-4700 II field emission SEM was employed to image the nanorods. SEM images of patterned ZnO nanorods on silicon are shown in Figure 2.5, viewed from the top and at a tilt of 60˚. SEM image of the patterned ZnO nanorods on glass is shown in Figure 2.6.

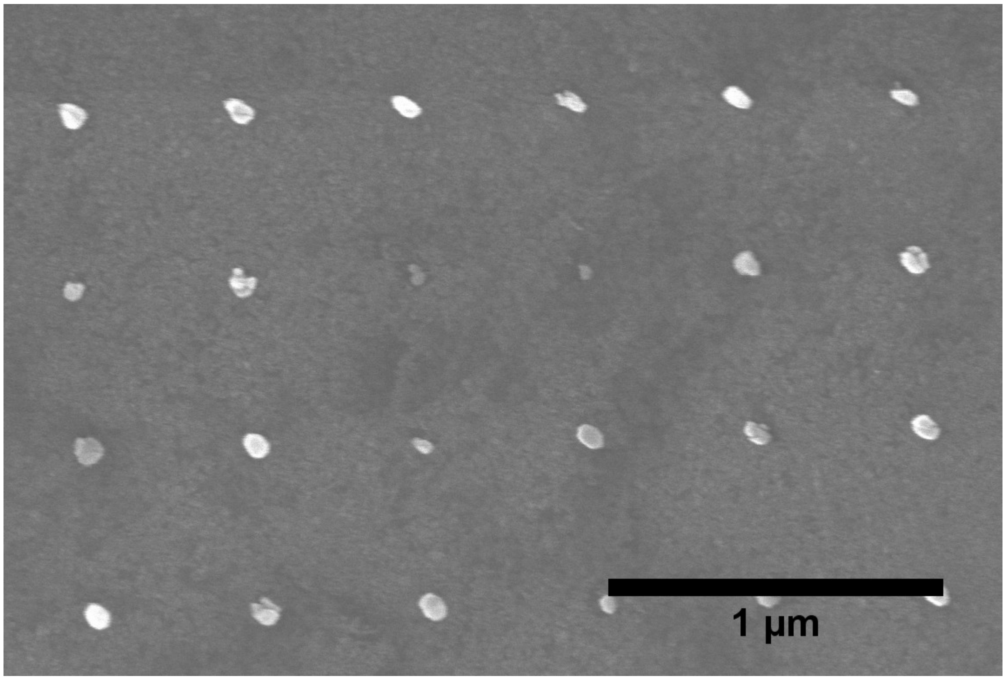

Figure 2.6 SEM image of patterned ZnO nanorods on glass substrate from the top grown at 85 °C for 2 hours.

The patterned mask consisted of a square lattice of 100 nm-diameter holes separated by 500 nm. The images show that the nanorods are predominantly perpendicular to the surface, with an average diameter and height of 103 nm and 175 nm, respectively. It is worth noting that the diameter of the nanorods is comparable to the diameter of the holes on the mask layer. With nanocrystal-seeded substrates, when the hole diameter is large enough to expose more than one ZnO nanoparticle, there will be more than one nanorod grow out of each hole as shown in Figure 2.7 [96].

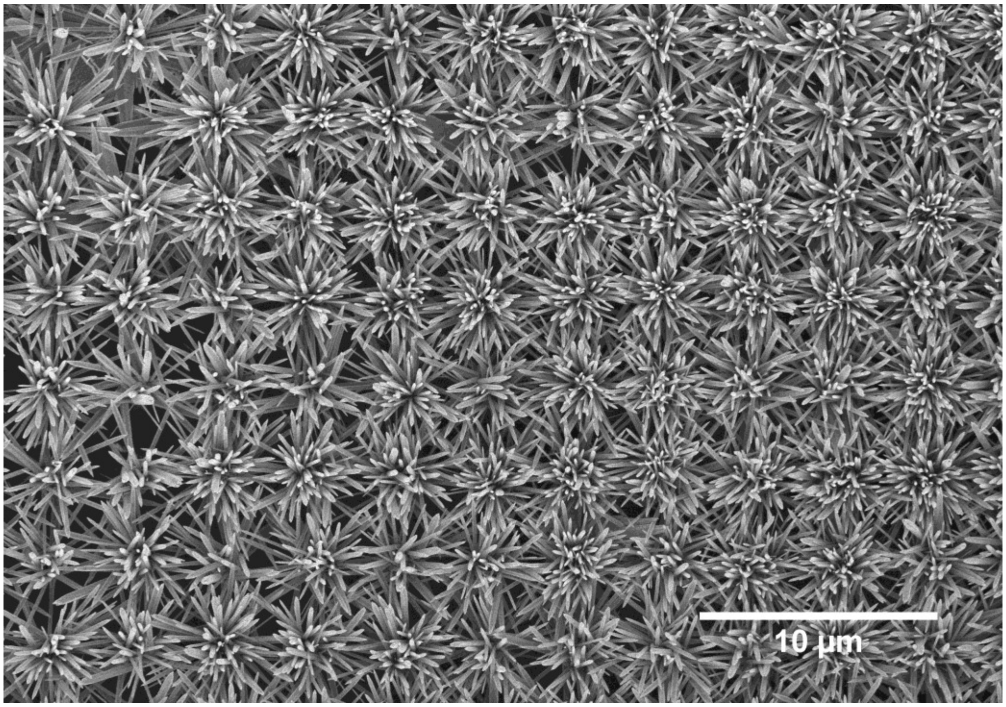

Figure 2.7 Bundles of ZnO nanorods grown out of large diameter patterned holes grown at 90℃.

This behavior is different than when using ZnO or GaN thin films as the substrate, where larger holes resulted in larger nanorods rather than increasing their number [34]. This could be related to in-registry growth of nanorods in the distance of less than 5 Å, where the nanorods coalesces, and they become thicker [106]. We also believe that the nanorods are supported by the mask edge at the early stage of their growth. This support is the main reason we obtain aligned nanorods. Therefore, finding the right patterning parameters to make holes with the proper diameter is critically important for the selective growth of single ZnO nanorods. It can be seen in the SEM image that there are a few missing nanorods in the large area pattern. This is most likely due to non-opened holes on the patterning mask. Due to the small sizes of the rods, we do not see the characteristic hexagonal cross-section (corresponding to the wurtzite crystal structure) typically observed in hydrothermally-grown ZnO nanorods [95]. Therefore, we performed additional analysis to investigate the crystal structure of the nanorods.

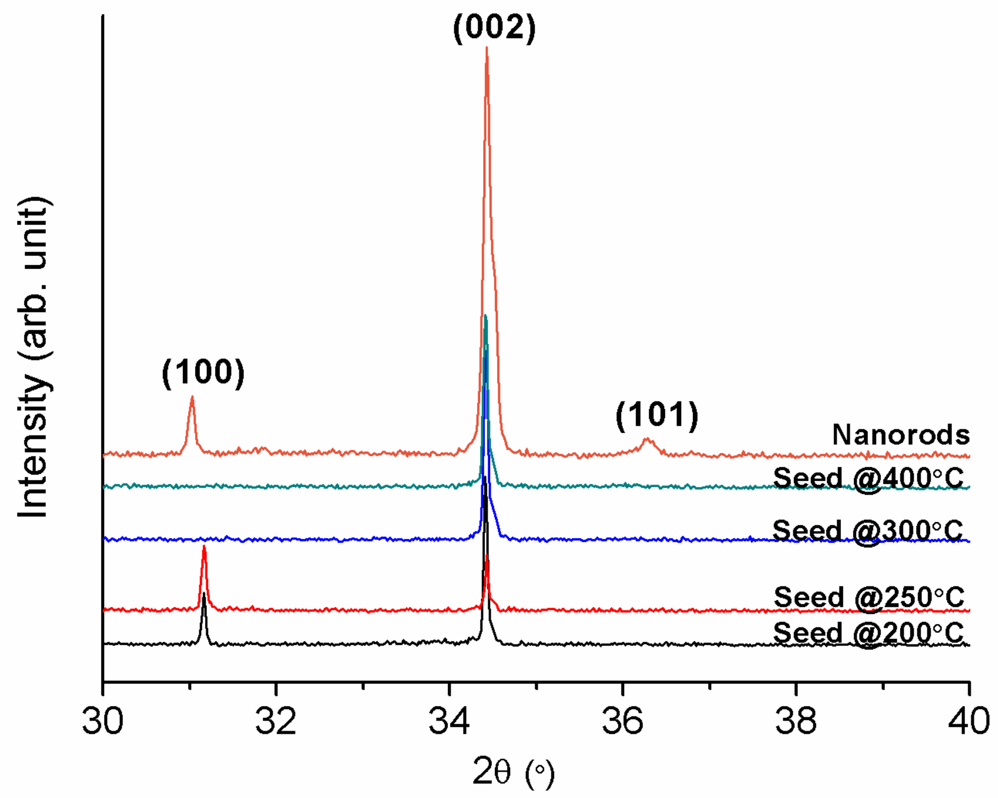

Figure 2.8 XRD spectra of non-patterned ZnO nanorods (top spectrum), and ZnO seed layer (four bottom spectra) annealed at different temperatures on silicon substrate.

Crystal structure of the samples was investigated using a Scintag XRD system with 2Θ angle in the 30 ° to 40 ° range using filtered Cu $K_{\alpha 1}$ radiation. Due to the sparse coverage of nanorods on the patterned sample, the XRD signal was too weak for our system to detect. Thus, we used ZnO nanorods grown using the same procedure, minus the patterning steps for the XRD characterization instead of the patterned samples. We also characterized the seed layer with XRD to ascertain its crystallinity and orientation as the seed-forming annealing temperature was increased. The measured XRD patterns of the seed layer and non-patterned ZnO nanorods are shown in Figure 2.8. The XRD pattern shows peaks corresponding to the hexagonal wurtzite structure typical of ZnO [95] . The peak at 34.42 ° is assigned to the (002) crystal plane and two other peaks at 31 ° and 36.26 ° are assigned to the (100), and (101) crystal planes, respectively. The XRD spectra from seed layers synthesized at different temperatures show two clearly different regimes. For the higher annealing temperatures (above 300 ℃), the formed nanocrystals are highly oriented along the (001) direction. The (001) plane in ZnO typically has a higher surface energy than the non-polar planes. However, It is assumed that the presence of adsorbates on top of the ZnO c-planes could stabilize them during the annealing [105]. Therefore, ZnO nanoparticles are mainly textured along (001) crystal planes. For seed layers annealed at temperatures below 300℃, the appearance of another peak at the (100) direction indicates a less uniform orientation across the film. For ZnO nanorods, the preferred crystallization is along the c-axis, thus the growth will occur preferentially along this axis [1]. Accordingly, the most efficient and uniform growth, leading to higher aspect ratio nanorods, will occur with seed layers annealed at temperatures above 300℃, since they are uniformly oriented along the best growth direction.

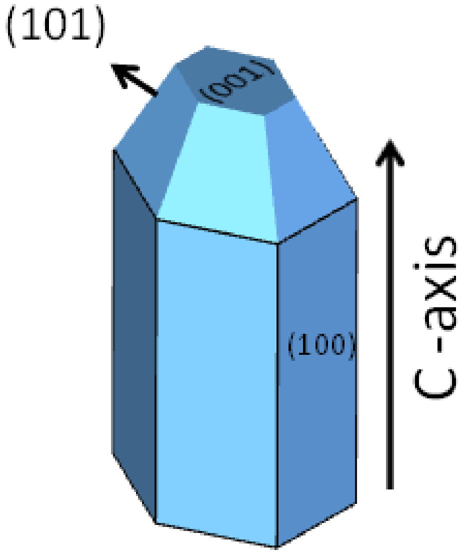

Figure 2.9 Schematic of ZnO hexagonal wurtzite crystal structure.

The XRD pattern of nanorods prepared from a seed layer annealed at high temperature (top trace in Figure 2.8) shows 3 significant peaks, while the seed layer shows only (001) planes. Since the nanorods have a higher aspect ratio the appearance of other planes such as the (100) plane is a must. In fact, although the growth of ZnO is maximum along (001), the crystal also grows along other planes. As can be seen in Figure 2.9, a schematic representation of the ZnO crystal planes, the (100) peak corresponds to the nanorod sidewalls. In practice, the morphology of ZnO nanorods grown by hydrothermal method tends to approach that of a hexagonal pyramid as shown in Figure 2.10. The narrower tip is caused by the drop in concentration of precursors as the growth goes forward. In the case of our patterned growth the width of the nanorods at the bottom is determined by the hole diameter in the mask.

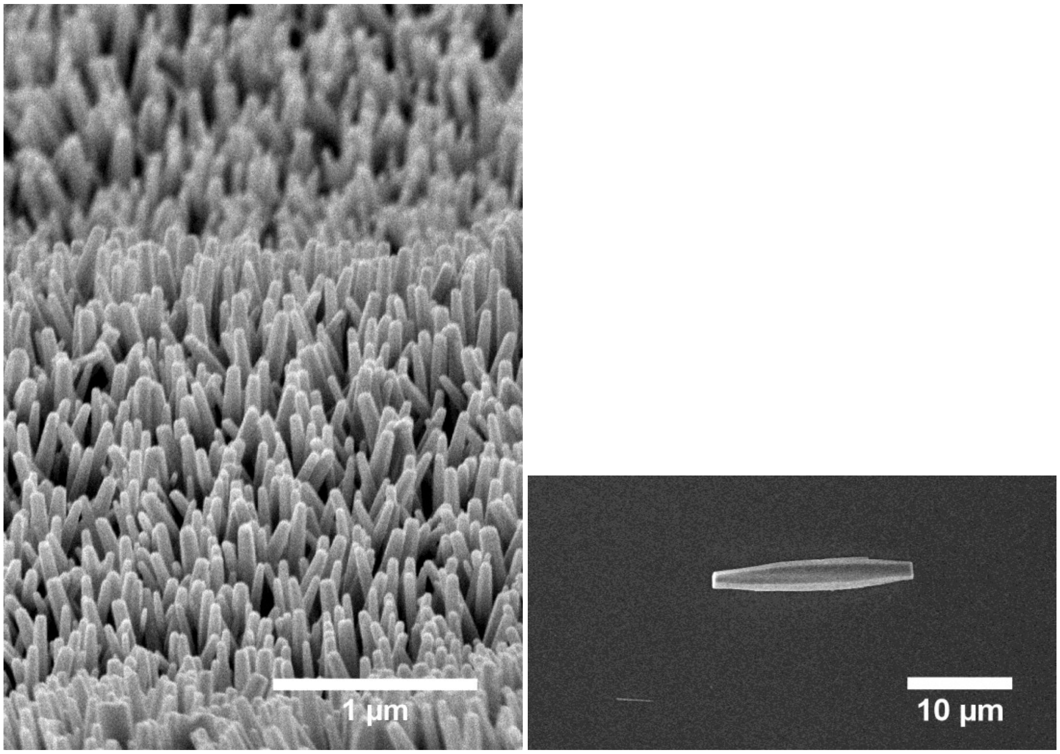

Figure 2.10 Pyramid hexagonal shape of ZnO nanorods grown on zinc nanoparticles (left) and GaN (right) grown at 90℃.

Therefore, in agreement with Shinagawa et al.[107], the presence of the (101) peak in the XRD spectrum may be related to this pyramidal morphology at the top of some of our ZnO nanorods. This fact will be confirmed with micro-Raman analysis in following. In addition, it can be observed that the (100) peak in the nanorods XRD pattern is slightly shifted to lower angles. I assume that the (100) peak of the seed layer in XRD graph comes from a stress-free crystal plane. Therefore, by using the Bragg equation ($2d\sin\theta = k\lambda, k = 1$), and putting λ=1.54 Å, we can calculate the lattice constant of the ZnO crystal. The lattice constants come up to be 2.8677 Å and 2.8795 Å for seed layer and ZnO nanorods, respectively. The strain corresponding to this lattice constant difference can be calculated using the following formula [108]:

$$\varepsilon = \frac{d_{Nanorods} - d_{Seed}}{d_{Seed}} \qquad (2\text{-}6)$$

As a consequence of the existence of strain, the average stress along the (100) plane can be obtained as following [108]:

$$\sigma = \left(\frac{Y}{2\nu} \right) \varepsilon \qquad (2\text{-}7)$$

Where Y=160 GPa is the young modulus of ZnO nanorods with 100 nm diameter, and ν=0.358 is Poisson ratio. The resulting calculated stress is σ =918 MPa. It is clearly a tensile stress, due to its positive value. Such a strain may as well explain the asymmetric hexagonal cross section shown by the ZnO nanorods in Figure 2.11.

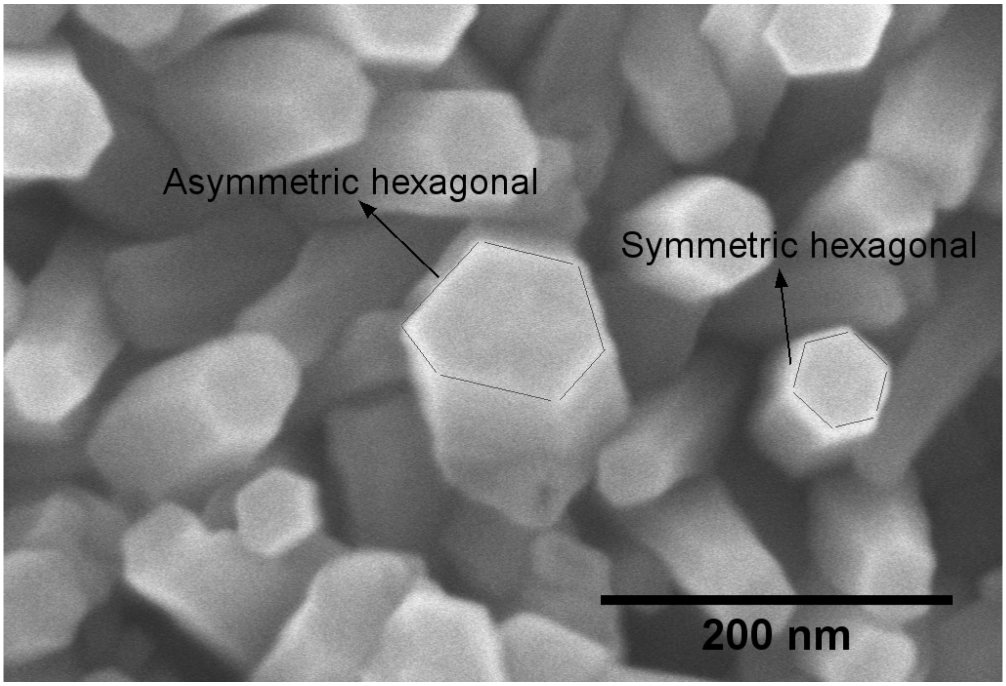

Figure 2.11 Symmetric and asymmetric ZnO nanorod top grown at 90℃ on seeded silicon substrate.

Since the crystal structure of the patterned ZnO nanorods cannot be assessed directly using XRD, we use micro-Raman spectroscopy, a technique of choice to examine the crystal structure of sparsely dispersed nanorods. Local Raman shifts were measured at room temperature using a Renishaw inVia micro-Raman system, with a 532 nm excitation laser and no polarization detection, in the 150 to 475 cm^{-1} range. Micro-Raman spectroscopy allows the probing of a small volume by combining confocal microscopy with the Raman spectroscopy system. The ability to collect Raman data from a small area reduces undesirable background signals and enhances the sensitivity, thus providing detailed structural information.

ZnO nanorods that are grown with low temperature methods often possess a wurtzite crystal structure with C_{6v}^{4} symmetry and two formula units in the primitive cell [109]. The optical phonon modes of ZnO crystals are classified as $A_1+E_1+2E_2+2B_1$, where A_1 and E_1 are polar and split into transverse (TO) and longitudinal (LO) optical phonons. Non-polar phonons with E_2 symmetry show two different frequencies in the Raman spectrum, while B_1 modes are Raman silent. The E_2 phonon modes are related to the oxygen and zinc sub-lattices in the ZnO crystal, also described as E_2(H) and E_2(L), respectively [110]. The possible vibrational modes in ZnO crystal are shown in Figure 2.12.

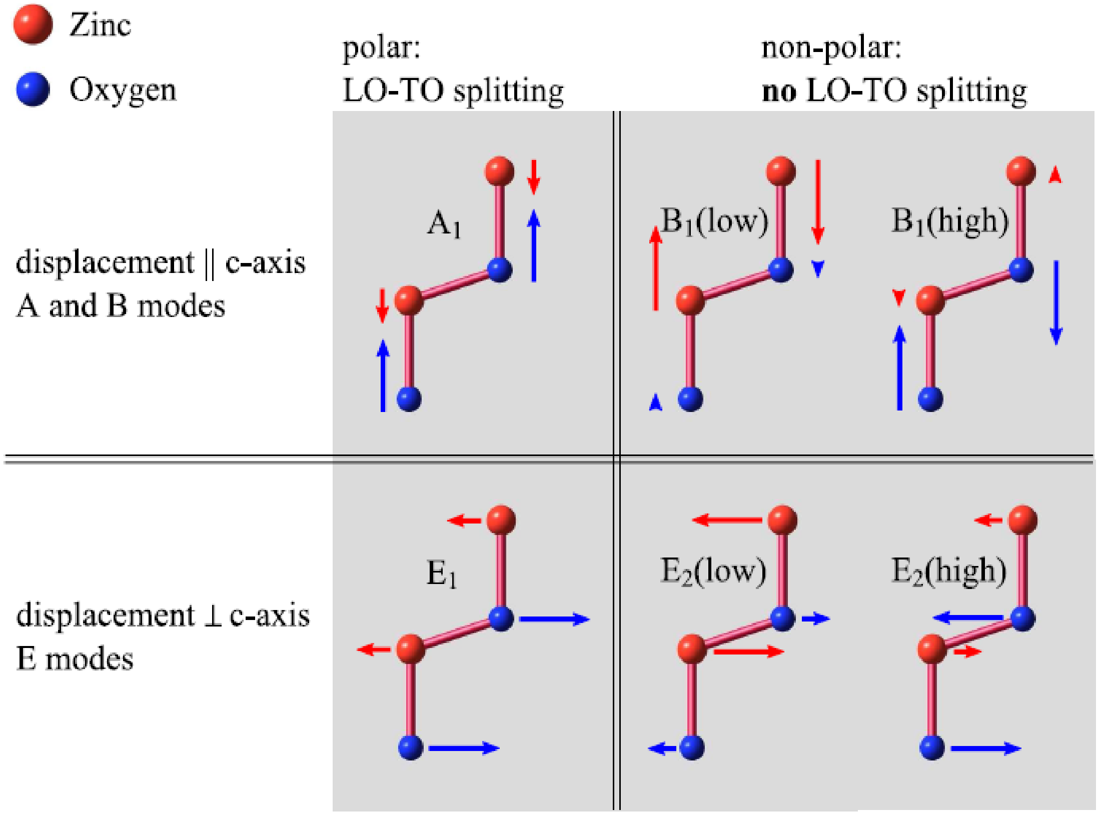

Figure 2.12 Possible vibrational modes in ZnO crystal.

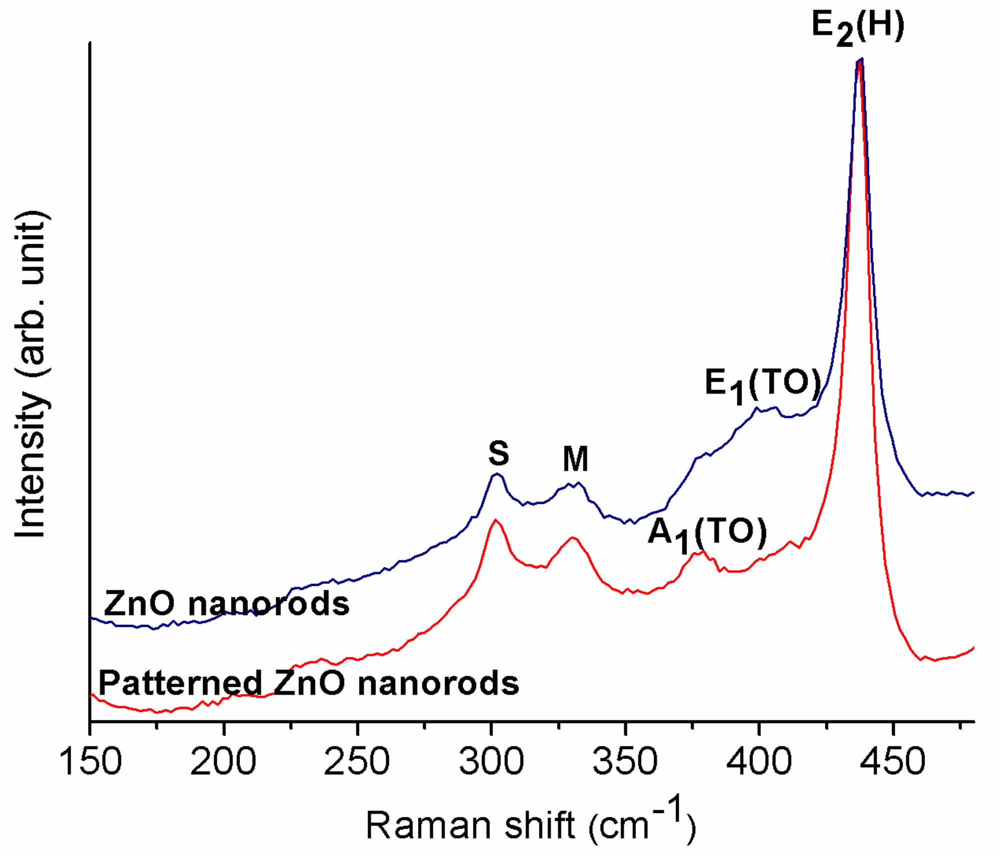

Figure 2.13 Micro-Raman spectra of patterned, and non-patterned ZnO nanorods on silicon substrate.

Figure 2.13 shows the Raman spectra of non-patterned and patterned ZnO nanorods. Our results correspond with the well-known features of wurtzite ZnO, showing Raman active A_1, E_1 and E_2 peaks [111]. The peak at ~438 cm^{-1} is assigned to the E_2(H) mode. This sharp peak is evidence of strong wurtzite crystal orientation in both patterned and non-patterned samples [112] demonstrating that the crystal structure of the ZnO nanorods is not affected by the patterning step. The (S) peaks centered at 300 cm^{-1} are due to the silicon substrate. The M peaks located at ~330 cm^{-1} are known to be Fröhlich-type vibrational modes due to multiple-phonon scattering processes [113]. Multiple-phonon scattering might be due to the quantum confinement effects in the nanorods' sharp tips. The difference in Raman spectra between the patterned and non-patterned ZnO nanorods relates to the peaks observed at ~378 cm^{-1} and ~400 cm^{-1}, assigned as A_1(TO), and E_1(TO), respectively. The intensity of the A_1(TO) peak is much higher for the patterned sample compared to the as-grown nanorods. This may be due to the misalignment of nanorods in the patterned structure. In terms of scattering geometry symmetry, the allowed

Raman modes for E_2 are z(xx)z, z(xy)z, and x(yy)x, whereas for the Raman mode A_1(TO), only x(yy)x is allowed [114]. In this notation the first and the last letter stand for the propagation direction of the laser beam and Raman radiated light, respectively; while the letters within the parenthesis correspond to their polarizations. For perfectly vertically aligned nanorods in our excitation geometry, the laser light is both incident and detected along the crystal z direction, so the A_1(TO) mode would not be allowed. If the nanorods are tilted, then the incident and detected light can have a component along the crystal x direction and the A_1(TO) mode would be allowed. We can see a small shoulder corresponding to this mode in the spectrum for the non-patterned nanorods, indicating that there is a slight tilt in this case, too. For the patterned nanorods, the more significant A_1(TO) peak indicated a more pronounced tilt. This is consistent with known growth mechanisms where the proximity of other nanorods contributes to maintaining the vertical orientation of the growth. It should be noted that in both cases E_2(H) is the dominant mode, which implies that the majority of nanorods are perpendicular to the substrate. The background in the Raman spectra is mainly due to defect emission, which is discussed in the following paragraph.

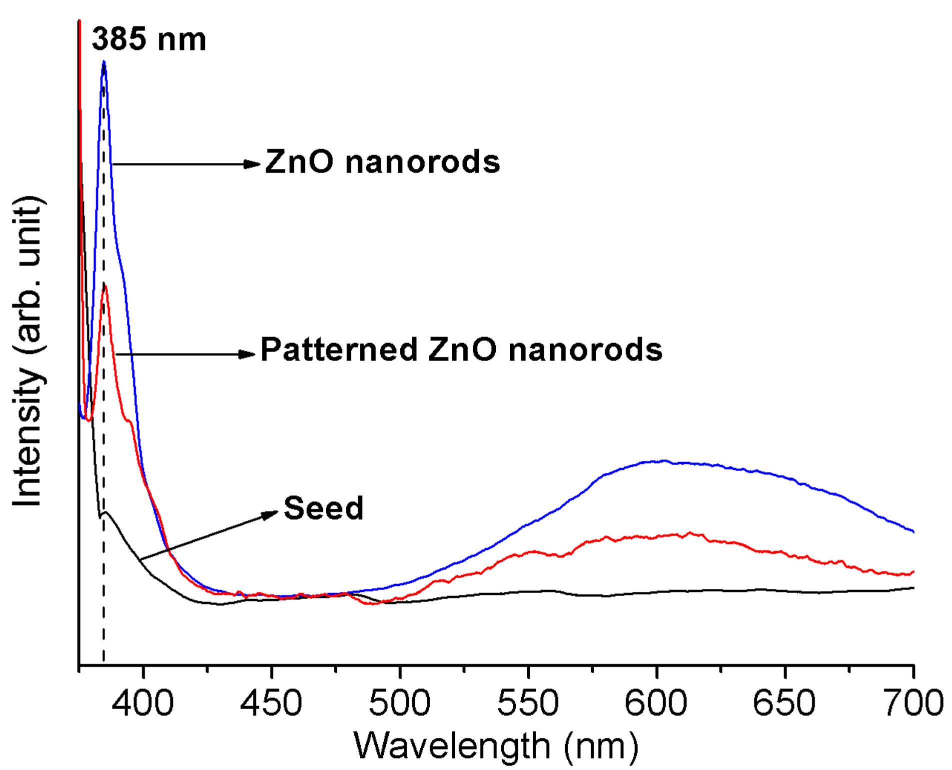

Figure 2.14 Room temperature photoluminescence of the seed layer, patterned and non-patterned ZnO nanorods on silicon substrates.

Finally, room temperature micro-PL spectroscopy was performed with an excitation wavelength of 369 nm in air. We used a home-built micro-PL setup to study the photoluminescence of the samples at room temperature. An excitation wavelength of 369 nm was used, and is incident on the sample at a glancing angle. The emission from the sample is collected with a NUV-optimized microscope objective, spectrally dispersed by a grating spectrometer, and finally imaged by a CCD detector. The photoluminescence spectra of the ZnO seed layer, as-grown nanorods, and patterned nanorods (all taken under the same experimental conditions) are shown in Figure 2.14. The dominant PL peak is a sharp one observed at 385 nm, in both patterned and as-grown nanorods. This peak, known as near band edge emission (NBE), is due to the free-exciton recombination in ZnO [115]. A narrow line width of the NBE peak implies good crystal quality of the nanorods which is consistent with XRD and micro-Raman scattering results. Moreover, the un-shifted NBE emission implies that the crystal lattice constant is the same for ZnO nanoparticles in the seed layer, and the nanorods which were later grown on top of them. This is evidence that the ZnO nanorods which are grown via low temperature methods match the size and crystal properties of seed nanoparticles, such as their lattice constant, at the early stages of the growth. The lower intensity of NBE of pattern nanorods compared to the non-patterned one is due to the lower number of nanorods irradiated by the pump laser (as compared to the non-patterned sample), that results in less photons reaching the detector.

There is a red shift in the NBE peak in comparison to the previous reported value of 375 nm for ZnO wurtzite crystal [116]. It has been established that the NBE emission of ZnO depends on the wavelength of the excitation light (red-shifting for longer excitation wavelengths) [117]. With a wavelength of 369 nm, our exciting laser has a longer wavelength than that generally used in the literature. Therefore, the red-shift of the NBE peak in our sample seems consistent with this effect. While it has been reported that thermal energy due to laser heating might slightly red shift the NBE peak [118], we have not observed this effect when using different excitation powers.

All three samples show a second broad peak starting at ~480 nm which are known as defect emission. Both NBE and defect emissions are typical of the ZnO wurtzite hexagonal crystal structure [119]. ZnO has an open structure that can accommodate native defects such as zinc interstitials and oxygen vacancies [120]. However, the origin of ZnO visible emission is a source of a lot of debate [121]. The defect emission in PL spectra has been mainly attributed to intrinsic host-lattice or surface defects in the literature [122]. The seed nanoparticles possess a higher surface-to-volume ratio than ZnO nanorods. Thus, negligible defect emission in PL spectra of the seed layer weakens the possibility that the defect states are arising from surface states. Based on this, the defect emission in the PL spectrum of our samples is most likely due to zinc and oxygen vacancies, or lattice flaws.

In conclusion, we have grown well-separated single ZnO nanorods in an arbitrary pattern on different substrates including glass and silicon, using a ZnO nanoparticle seed layer to compensate for crystal mismatches. Based on XRD results, in order to achieve the best crystal orientation the seed layer must be annealed at temperatures over 300℃. Raman scattering spectra confirm that as-grown and patterned nanorods have the same wurtzite crystal structure and orientation, although we see a slight tilt of the c-axis in the patterned ZnO nanorods. Micro-PL of both patterned and as-grown ZnO nanorods show a sharp narrow peak at NBE confirming their high quality crystal structure. In addition, we found negligible visible emission in the PL spectrum of the seed layer, implying that the majority of the defect emission is arising from bulk defects such as zinc and oxygen vacancies or lattice imperfections. The proposed method is a practical technique for synthesizing positioned controlled single ZnO nanorods on any type of substrates for applications where low aspect ratios are desirable, such as optoelectronic structures supporting a single transversal optical mode.

Chapter 3 The effect of cation doping on morphology, optical and structural properties of highly oriented wurtzite ZnO nanorod-arrays

Cation-doping of ZnO is a practical way of adjusting its optical, electrical and magnetic properties. In this direction, I chose the most common hydrothermal method with no need of pH surveillance to growth arrays of cation-doped ZnO nanorods on silicon substrates. I used a silicon substrate due to its availability and conductivity, which facilitates SEM imaging. However, this method can be used on various types of substrates independent of their crystal orientations.

The chemicals which were used in my experiment are as follows: zinc nitrate hexahydrate ($Zn(NO_3)_2.6H_2O$), zinc acetate dihydrate ($Zn(CH_3COO)_2{\cdot}2H_2O$), magnesium nitrate hexahydrate ($Mg(NO_3)_2.6H_2O$), nickel nitrate hexahydrate ($Ni(NO_3)_2.6H_2O$) , manganese acetate tetrahydrate ($(CH3COO)_2Mn.4H_2O$), copper nitrate trihydrate ($Cu(NO_3)_2.3H_2O$), anhydrous chromium nitrate ($Cr(NO_3)_3$), cobalt nitrate hexahydrate ($Co(NO_3)_2.6H_2O$), and Hexamethylenetetramine (HMTA) which were all of analytical grade and used without further purification in our experiment.

For all the samples substrate preparation was as follows: silicon -Si(100)- substrates were cleaned by performing three 10 minutes steps in an ultrasonic bath with acetone, isopropyl alcohol, and DI water, respectively. A 5 mM solution of 99.98% zinc acetate in pure ethanol was prepared as a seeding solution. The seeding solution was drop casted on substrates for 7 times, followed by a 400℃ annealing for 30 minutes so that the zinc acetate decomposed, forming ZnO nanoparticles. The whole process was repeated 2 times for each sample to ensure a full coverage of substrate with ZnO nuclei.

In order to grow the nanorods, substrates were placed upside down in a growth vessel containing a 1:1 molar ratio solution of zinc nitrate and HMTA dissolved in deionized water. For growing doped nanorods, 5 mM solution of the dopant was added to the growth vessel as the molarity of zinc precursor and HMTA dissolved in deionized water were kept constant at 50 mM. A conventional furnace was used to maintain the growth temperature at 60℃ for ~20 hours. Samples were thoroughly washed with DI water by the end of the growth and were blown dry by pure nitrogen gas.

The morphological, structural and optical properties of samples were thoroughly investigated by using different techniques. A JEOL JSM-7600 FE SEM was employed to image the nanorods from the top and cross section. Crystal structure of the samples was investigated using a PANalytical X'pert MPD Pro diffractometer operated at 40 kV and 40 mA using Ni-filtered Cu Kα irradiation (wavelength 1.5406 Å). Local Raman shifts were measured at room temperature using a Renishaw inVia micro-Raman system, with a 532 nm excitation laser and no polarization detection, in the 0 to 900 cm^{-1} range. The chemical composition was investigated by X-ray photo-electron spectroscopy (XPS) (Axis UltraDLD, Kratos) with monochromatic aluminum Kα radiation and EDS. An Al X-ray source (1486.6 eV) was used and the spectra were detected in the range from 0 to 1200 eV. The charge calibration was done by setting the C 1s line of adventitious carbon to 284.8 eV to compensate for charge effects. For lower doping concentration Energy-dispersive X-ray spectroscopy (EDS) was used. Finally, room temperature PL spectroscopy was performed with a PTI QM-4 fluorescence spectrophotometer with excitation wavelength of 340 nm.

In following an extensive discussion about the effect of different cation dopants on the structural and optical properties of the ZnO nanorods will be given. A comprehensive review on the most recent works that have been done on the low temperature cation doping of ZnO will be also given in each section.

3.1 Low temperature hydrothermal growth of arrays of Mg-doped ZnO nanorods

Mg^{2+} is one of the most commonly used dopant cations in ZnO crystal. In general Mg-doped ZnO crystals have a wider band gap than undoped ZnO due to the slightly smaller Mg^{2+} ionic radius [91]. The optical band gap of the Mg-doped ZnO can be tuned by adjusting the dopant content, noticing that at low level of dopant concentration the crystal structure of the host lattice remains unchanged [123]. Thus, Mg^{2+} is an ideal dopant for incorporation into ZnO crystal for fabrication of multilayer heterostructures, where two crystals with different band gaps get in direct contact with each other. Halm et al.[14] reported a strong exciton photon coupling in a MQW heterostructure consist of ZnO/Mg-ZnO. Moreover, Mg-doped ZnO solar cells are more efficient than undoped ZnO owing to their more effective light absorption [124]. It has also been shown that Mg-doped ZnO nanowires have better uptake and release hydrogen capabilities [125]. Physical deposition methods are often used to dope ZnO structures with high levels of Mg^{2+} [124], whereas the focus of our current work is on using a low temperature method to grow Mg-doped arrays of ZnO nanorods, perpendicular to the substrate. There have been previous reports on hydrothermal growth of Mg-doped ZnO nanorods. Shimpi et al.[126] synthesized MgO/ZnO composite nanowires in two steps at 150℃ by using a hydrothermal method. This method also used by Liu et al.[91] for synthesizing Mg-doped ZnO nanorods on glass substrate which was pretreated with 80 nm of sputtered Mg-ZnO as a seed layer. In contrast to previous reports, our Mg-doped ZnO nanorods were grown on silicon substrates by using a single-step hydrothermal method at temperatures as low as 60℃.

The pH evolution of the growth solution as a function of time was measured as described before and the results are shown in Figure 3.1. The effect of dopant precursors on pH of the growth solution is very small due to their smaller amount as compared to the Zn^{2+} ions and HMTA. It can be seen that the pH is initially at 6.5 and it is gradually reduced until it becomes almost constant at 5.4 after about an hour at 63℃. The speciation diagram of Zn^{2+} and Mg^{2+} were drawn based on the simulation data which were done by visual MINTEQ software. The

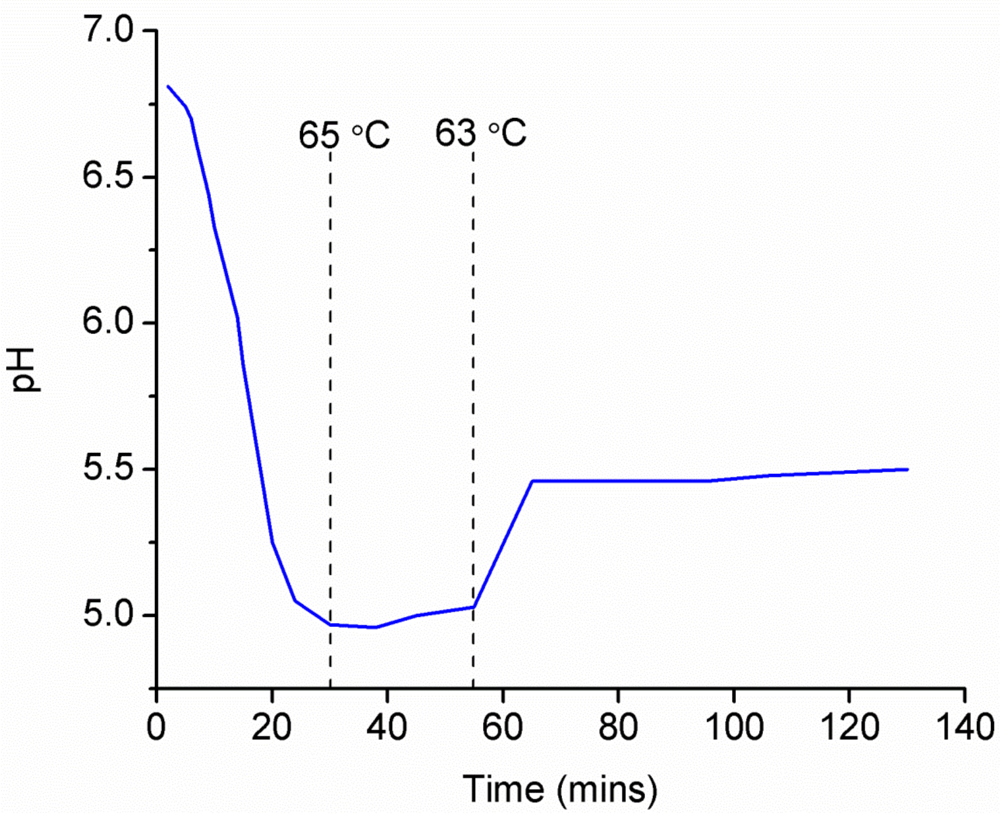

Figure 3.1 Evolution of the pH during the growth as a function of time (temperature up to 63℃).

simulation conditions were similar to the one in chapter 2. The simulation results are shown in Figure 3.2 and Figure 3.3 for Zn^{2+} and Mg^{2+}, respectively. It can be seen that at the initial stage of the growth Zn^{2+} and Mg^{2+} are the only cationic species which exist in the growth solution. As discussed before HMTA gradually release the OH^- groups in the solution, which locally increase the pH at the surface of the crystal. As it comes from the speciation diagrams the cation hydroxide forms at the pH ~9. These compounds will eventually dehydrate and form the nanorods. The broad range of pH in which Mg(II) could exist in the form of Mg^{2+} implies that higher concentration of Mg (>5mM) can be introduced to the growth solution as the dopant. By introducing larger amount of Mg precursors, the Mg^{2+} curve will shift towards the lower pH. But due to the wide range of pH, it would be still possible for the Mg(II) to exist in the form of Mg^{2+} at pH ~5.5 even with higher concentration. I leave the study of effect of different concentration of Mg^{2+} dopant on optical and structural properties of ZnO nanorods for future study.

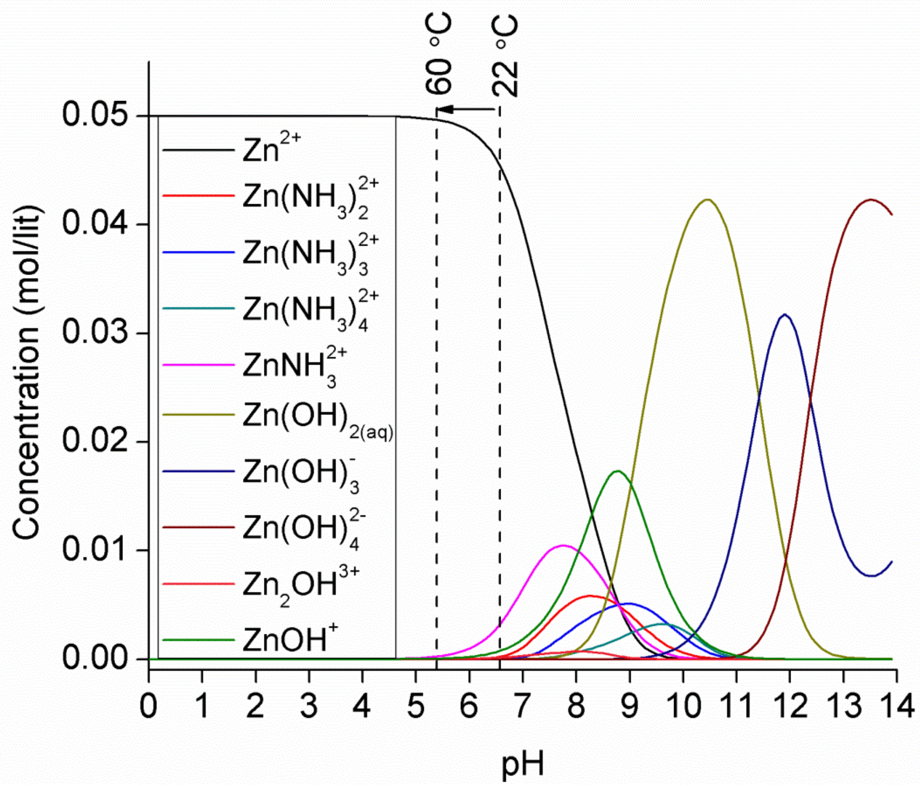

Figure 3.2 Speciation diagrams of Zn(II) species at 60˚C as a function of pH ranging from 0 to 14 as computed with Visual MINTEQ software.

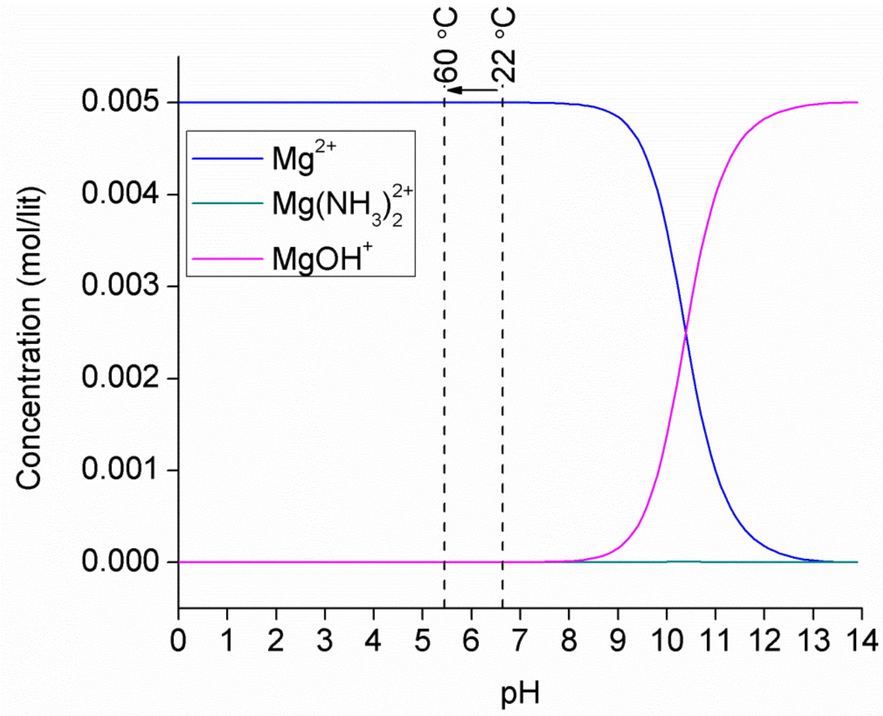

Figure 3.3 Speciation diagrams of Mg(II) species at 60˚C as a function of pH ranging from 0 to 14 as computed with Visual MINTEQ software.

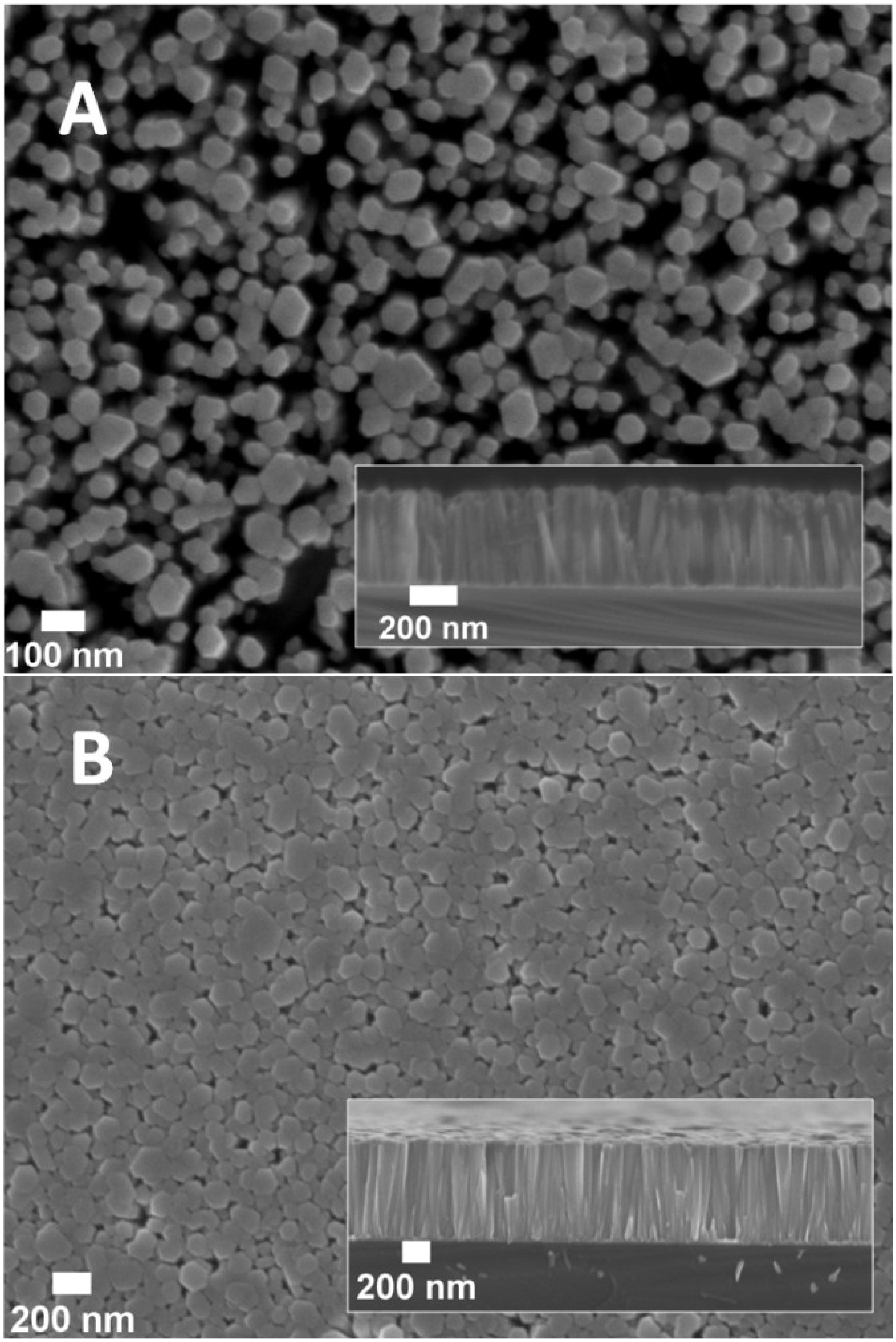

Figure 3.4 SEM images of the top and cross section A) undoped ZnO nanorods and B) Mg-doped ZnO nanorods grown at 60℃ on silicon substrate.

Undoped ZnO nanorods were synthesized and characterized as a reference. The SEM images of undoped and Mg-doped ZnO nanorods are shown in Figure 3.4. It can be seen that low level incorporation of Mg^{2+} into ZnO, has no effect on the hexagonal rod shape; whereas the nanorods became bigger, denser and more uniform in terms of diameter and height. The nanorods average height increased from 352 nm to 677 nm and the average diameter almost doubled from 54 nm to 104 nm by Mg^{2+} addition. The size information of undoped and Mg-doped nanorods is summarized in Table 3-2.

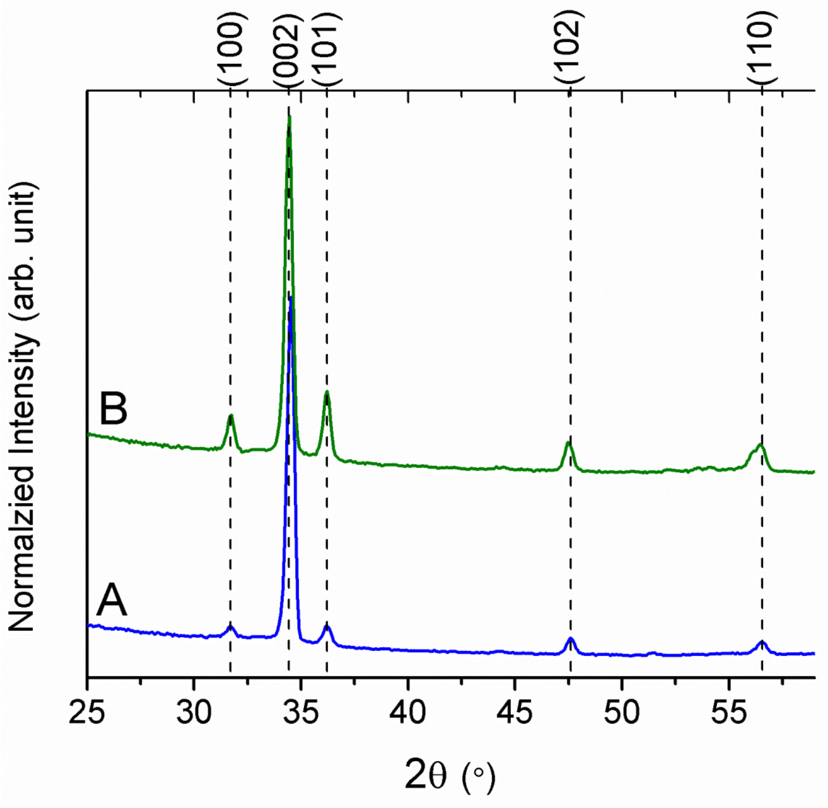

Figure 3.5 XRD patterns of A) undoped and B) Mg-doped ZnO nanorods grown at 60℃ on silicon substrate.

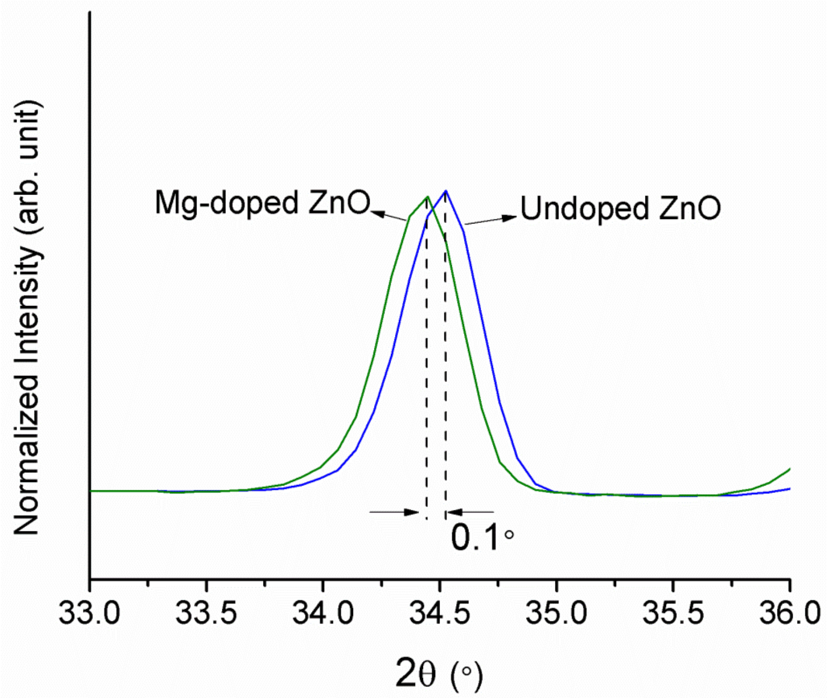

Figure 3.6 High resolution (002) peak position of undoped and Mg-doped ZnO grown at 60℃ on silicon substrate.

The effect of Mg^{2+} doping on crystal phase of ZnO nanorods were investigated by XRD and the results are shown in Figure 3.5. The peaks for both undoped and Mg-doped samples are assigned to the hexagonal wurtzite ZnO crystal structure. Based on the patterns of Figure 3.5 the crystal phase of the ZnO host lattice has not changed by addition of Mg^{2+}. Moreover, no extra peaks regarding the Mg^{2+} compounds in form of metal or oxide were detected in our XRD patterns. However, comparing the intensity of XRD patterns shows that the crystallinity changed along different crystal planes as Mg^{2+} incorporated into ZnO crystal lattice. This change could be due to different atomic environment in ZnO crystal as a result of the presence of an impurity [127]. The XRD results suggest that nanorods grow more effectively along their A and B axis`s by Mg^{2+} addition consistent with our SEM images where thicker nanorods were obtained by Mg^{2+} addition. High resolution peak positions of (002) plane of both undoped and Mg-doped ZnO are shown in Figure 3.6. The (002) plane of Mg-doped sample has slightly shifted towards the lower 2Θ angle due to lattice deformation. This small shift implies slightly higher lattice constant along the c-axis as well as larger crystal plane spacing for the Mg-doped samples in comparison to undoped ZnO. The crystal lattice alteration can be due to the small differences between ionic radius of Zn^{2+} (0.6) A° and Mg^{2+} (0.57) A° [128]. In fact, similar ionic sizes allow

Mg^{2+} to substitute Zn^{2+} atoms in nanorods without any large effects in its lattice constant.

The degree of texture of ZnO nanorod with its c-axis perpendicular to the substrate has been suggested before [129, 130]. Degree of texture is a measure to analyze the crystallographic orientation of a material along its different crystal planes. The degree of texture -crystallographic orientation- can be defined as following [129]:

$$i_{(002)} = \frac{I_{(002)}}{I_{(100)} + I_{(002)} + I_{(101)}} \qquad (3\text{-}1)$$

Where $I_{(100)}$, $I_{(002)}$, and $I_{(101)}$ are the intensity of the corresponding crystal plane peaks in XRD patterns. Based on the calculation the degree of alignment of nanorods has reduced from 82% for undoped ZnO to 69% for Mg-doped nanorods. A summary of crystallographic data of undoped and Mg-doped nanorods are given in Table 3-3.

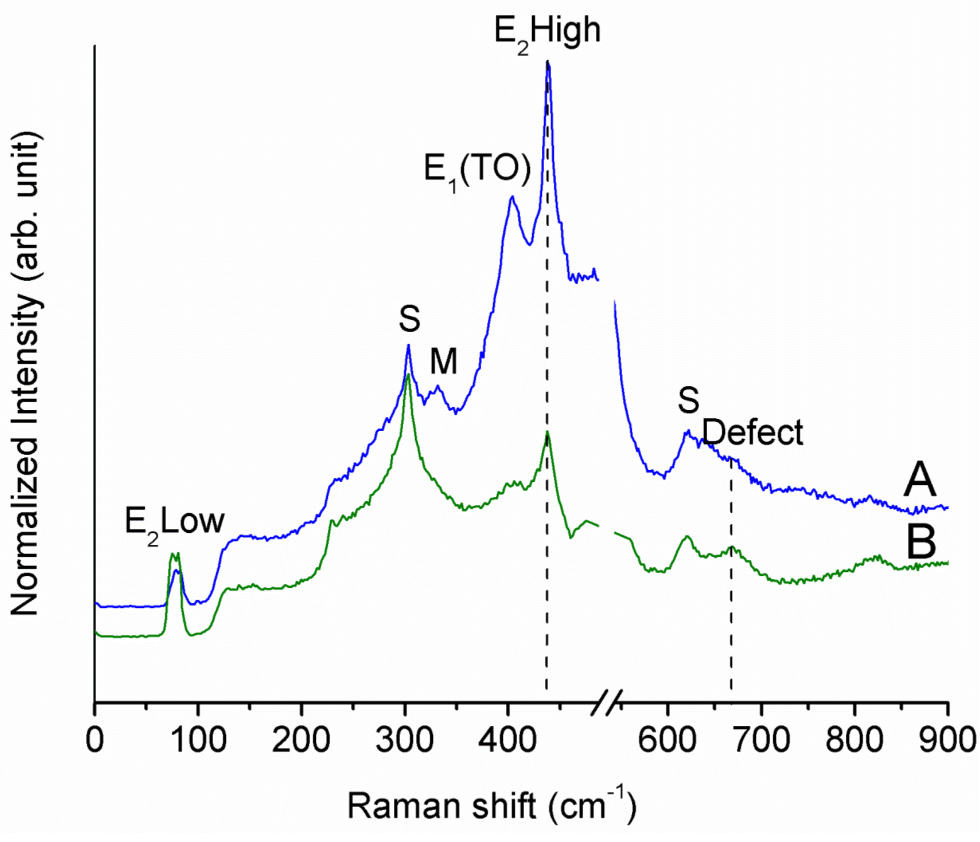

Figure 3.7 Room temperature micro-Raman scattering spectra of A) undoped and B) Mg-doped ZnO nanorods grown at 60℃ on silicon substrate. (Traces were shifted vertically for visibility)

In order to investigate the local crystallinity and structural defects in undoped and doped ZnO nanorods, their micro-Raman spectra were measured at room temperature. Raman scattering can be an effective technique to detect impurities in crystalline ZnO nanocrystals. The propagation of A_1(TO) and E_1(LO) is perpendicular to the c-axis, whereas A_1(LO) and E_1(TO) propagate parallel to the c-axis [131]. A_1(TO) and E_1(TO) reflect the polar lattice bond. And A_1(LO) is attributed to oxygen vacancies and zinc interstitials [132], and it cannot be detected for excitation wavelengths longer than 407 nm [133]. Non-polar phonons with E_2 symmetry show two different frequencies in the Raman spectrum. The E_2(H) modes dominated by the vibration of the Zn sub-lattice and the E_2(L) one is attributed to the vibrations of oxygen atoms [110]. Figure 3.7 shows the Raman spectra of undoped and Mg-doped ZnO nanorods. Our results correspond with the well-known features of wurtzite ZnO, showing Raman active E_1 and E_2 peaks [111].

The S peaks approximately centered at 300 cm^{-1}, 621 cm^{-1} and 817 cm^{-1} are due to the silicon substrate as has been reported before [134]. The M mode at ~332 cm^{-1} is attributed to difference modes E_2(H)-E_2(L) as multiple-phonon scattering processes [113, 135]. From Figure 3.4, the difference between the intensity of the E_2(H) and E_2(L) decreased by incorporation of Mg^{2+} into ZnO in comparison to the undoped ZnO. Multiple-phonon scattering might be due to the quantum confinement effects in the nanorods' sharp tips. We believe that the M peak disappearance is related to the flat top shape of Mg-doped nanorods that can be seen in Figure 3.4. The peaks at 78.8 cm^{-1}, 403 cm^{-1} and ~437.7 cm^{-1} are assigned to the E_2(L), E_1(TO) and E_2(H) modes, respectively. A summary of Raman active modes of undoped and Mg-doped nanorods are given in Table 3-4 for comparison. The sharp E_2(H) peak is evidence of strong wurtzite crystal orientation in both Mg-doped and undoped samples [112] demonstrating that the overall crystal structure of the ZnO nanorods is not affected by the doping process in accordance with our XRD results. The dominant E_2(H) peak also implies that the majority of nanorods are perpendicular to the substrate. Although the intensity of E_2(L) has increased with Mg doping, its peak has slightly shifted to the left. In contrast, the intensity of E_1(TO) is suppressed in the doped sample, and it is shifted to the right. The broadening of E_2 (L and H) peaks could be due to the wurtzite lattice distortion for Mg^{2+} introduced sample. The asymmetric peak shape of E_2(H) for doped sample could be explained in terms of resonant anharmonic interaction of this mode with the band of combined transverse and longitudinal acoustic modes [135]. There is also a small peak at 669 cm^{-1} that has been assigned to the oxygen vacancies or zinc interstitials defect centers in crystal lattice [136]. This peak became more distinct for the Mg-doped sample, which shows larger number of those defects. This fact will be further confirmed with PL measurement.

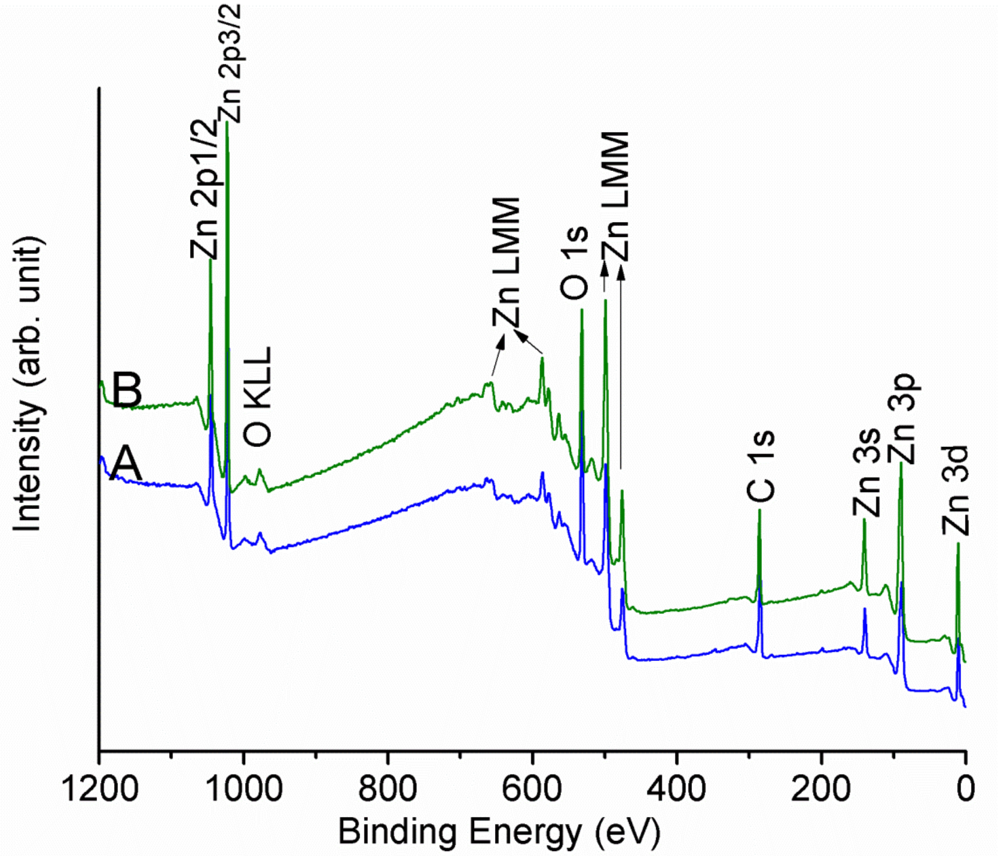

Figure 3.8 XPS spectra of A) undoped and B) Mg-doped ZnO nanorods grown at 60℃ on silicon substrate. (Traces were shifted vertically for visibility)

In order to investigate the surface chemical composition of undoped and Mg-doped ZnO nanorods we used XPS. Analyzing the ejected electrons in this technique could yield information about the atomic composition of the nanorods since the orbital energies are unique to an atom of a specific element. The peaks in the XPS spectrum arise due to two distinct mechanism called photoelectric and Auger effect [137]. Figure 3.8 shows the XPS spectrum of undoped and Mg-doped ZnO nanorods. The Zn_{LMM} and O_{KLL} peaks are the evidence of Auger mechanism in our spectra. The C 1s peak is always detected due to contamination, and it may be used as the reference for data calibration. The asymmetric peak at 530 eV is due to Zn-O bond in wurtzite hexagonal crystal structure which is attributed to O^{2-} ions [138]. Peaks detected at 1021.7 eV and 1044.8 eV are corresponded to Zn 2p3/2 and Zn 2p1/2 core levels, respectively. The former peak is the evidence of Zn^{2+} in the ZnO crystals [139]. The Zn 2p peak is split into two peaks due to spin orbit interactions [140]. Analyzing these two peaks as well as O-1s for undoped and Mg-doped nanorods yield useful information about the effect of dopant on nanorods surface chemistry [141].

As can be seen in Figure 3.8 there is a good agreement in XPS spectra of Mg-doped and undoped ZnO nanorods. An attempt to detect Mg^{2+} in our doped nanorods by using XPS was not successful probably due to the low concentration of incorporated Mg^{2+} in ZnO lattice. On the other hand, XPS has a shallow detection depth (Couple of atomic layers). Therefore, by scanning the nanorods from the top, the possibility of detecting dopants at the bottom of the nanorods is negligible. There might be some Mg^{2+} ions incorporated into the base of our nanorods at the early stage of the growth which may not be detected by XPS. This idea can be supported by the EDS spectrum which is shown in Figure 3.9. The EDS results show that Mg^{2+} content of our sample is 0.5 atomic% on average. The cross section EDS spectrum (not shown here) also confirmed higher Mg atomic% at the bottom of the nanorods than the top.

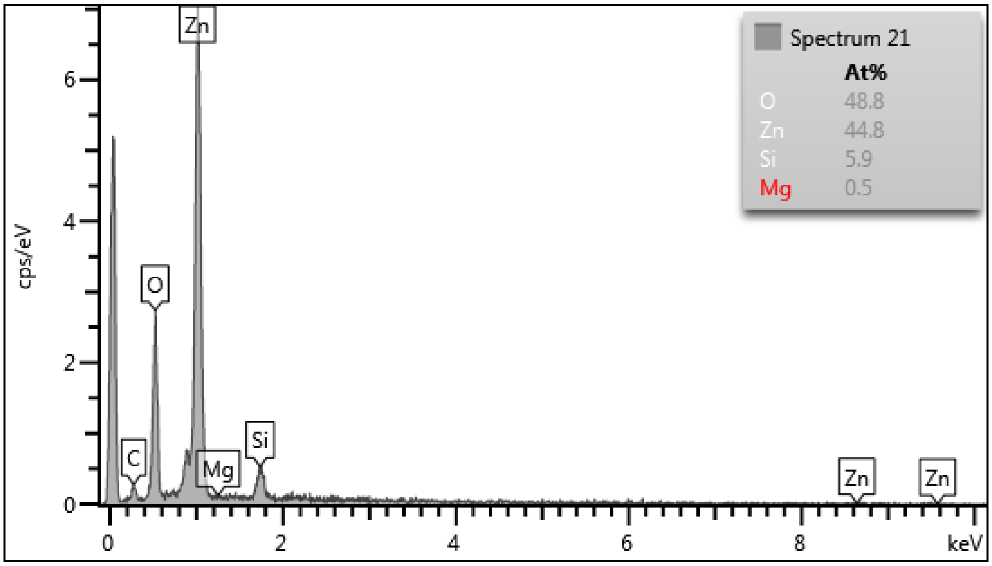

Figure 3.9 EDS elemental microanalysis of Mg-doped ZnO grown at 60℃ on silicon substrate.

No significant changes in the chemical shift and signal were found for Zn 3d, Zn 3p, and Zn 3s peaks with Mg^{2+} addition. While more precise measurements show that the Zn 2p peaks are shifted to lower energies (-0.2 eV) due to Mg^{2+} addition. The reduction of Zn 2p state binding energy by Tungsten addition has been reported before and the peak change was attributed to lower surface energy of the doped nanorods [142]. Similarly, the binding energy shift in our case can be related to the lower surface energy of Mg-doped nanorods as compared to undoped ZnO nanorods. The FWHM of the Zn 2p peaks were also found to be smaller for the Mg-doped sample (1.75 eV) as compared to the undoped nanorods (1.85 eV). This narrowing suggests the presence of less Zn states defects within Mg-doped ZnO structure.

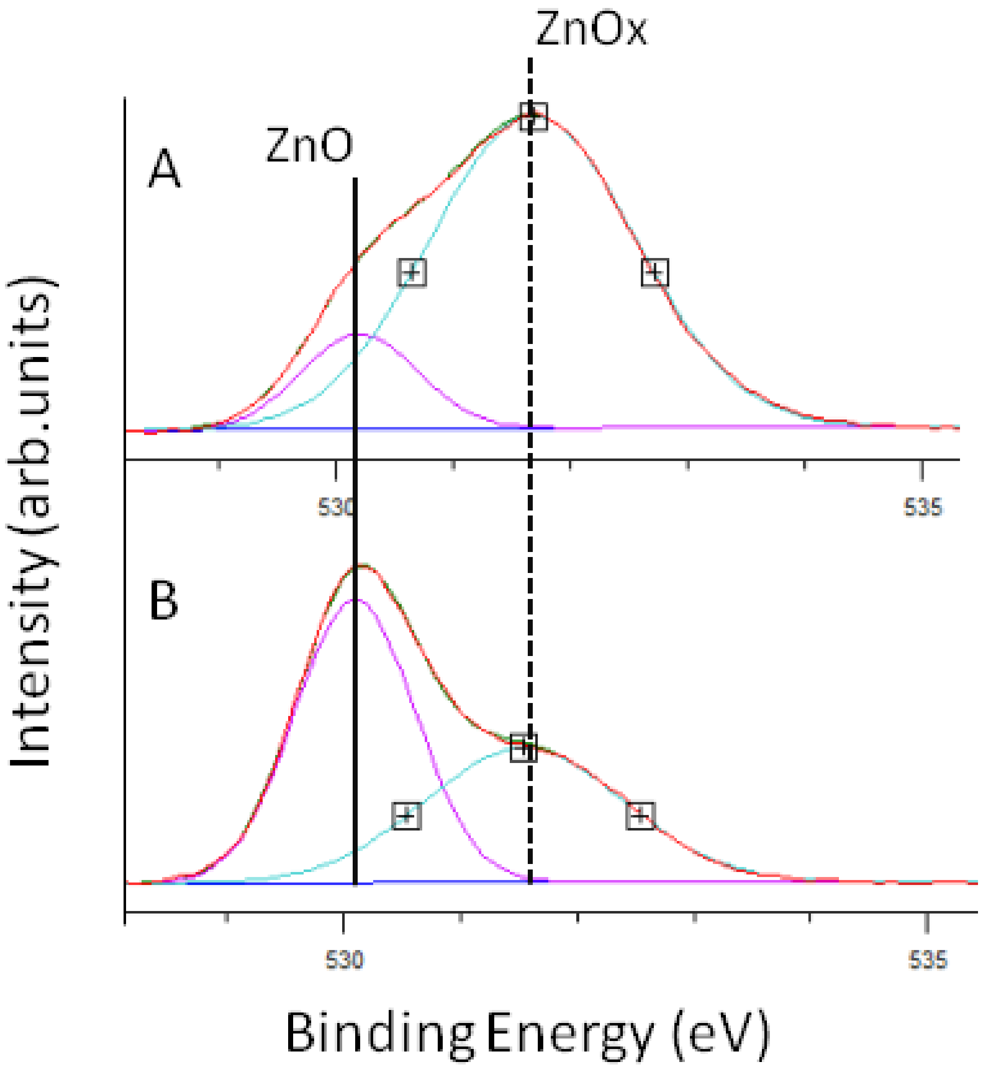

Figure 3.10 High resolution XPS spectra of O 1s core level of A) undoped and B) Mg-doped ZnO nanorods grown at 60℃ on silicon substrate.

The asymmetric O 1s peaks of undoped and Mg-doped ZnO are shown in Figure 3.10. These peaks are deconvolved by two subspecteral components at 530.2 eV and 531.6 eV. The lower energy peak is assigned to O^{-2} ions (O_L) in stoichiometric Zn-O-Zn regions. Whereas the higher binding energy peak is attributed to O^{-2} ions (O_H) in an oxygen deficient ZnOx region or to hydroxyl groups resulting from chemisorbed water [141, 143]. Based on the curve fitting results shown in Figure 3.10, surface O_H percentage decreases to 44% after Mg^{2+} addition which can be an evidence of better stoichiometry of Mg-doped nanorods and/or less hydroxyl groups attached to their surface in comparison to undoped ZnO. Similar components in O 1s have been observed before [143-145], and based on O 1s/Zn 2p XPS intensity, the stoichiometry of ZnOx(OH)y was suggested [143, 146]. In our case this ratio reduced from 3.8 for undoped ZnO to 2.6 for Mg-doped nanorods implying that the overall number of oxygen atoms versus zincs reduced by Mg^{2+} addition. Oxygen vacancies are assigned as defect centers across the ZnO crystal. Therefore, lower number of O/Zn ratio might be related to a larger number of oxygen related defects in our Mg-doped nanorods. The accuracy of this speculation can be investigated by PL measurement. However, the smaller O_H peak in case of the Mg-doped sample indicates that the number of OH groups on the surface is reduced in comparison to the undoped ZnO. The surface chemistry information of undoped and Mg-doped ZnO nanorods is summarized in Table 3-5.

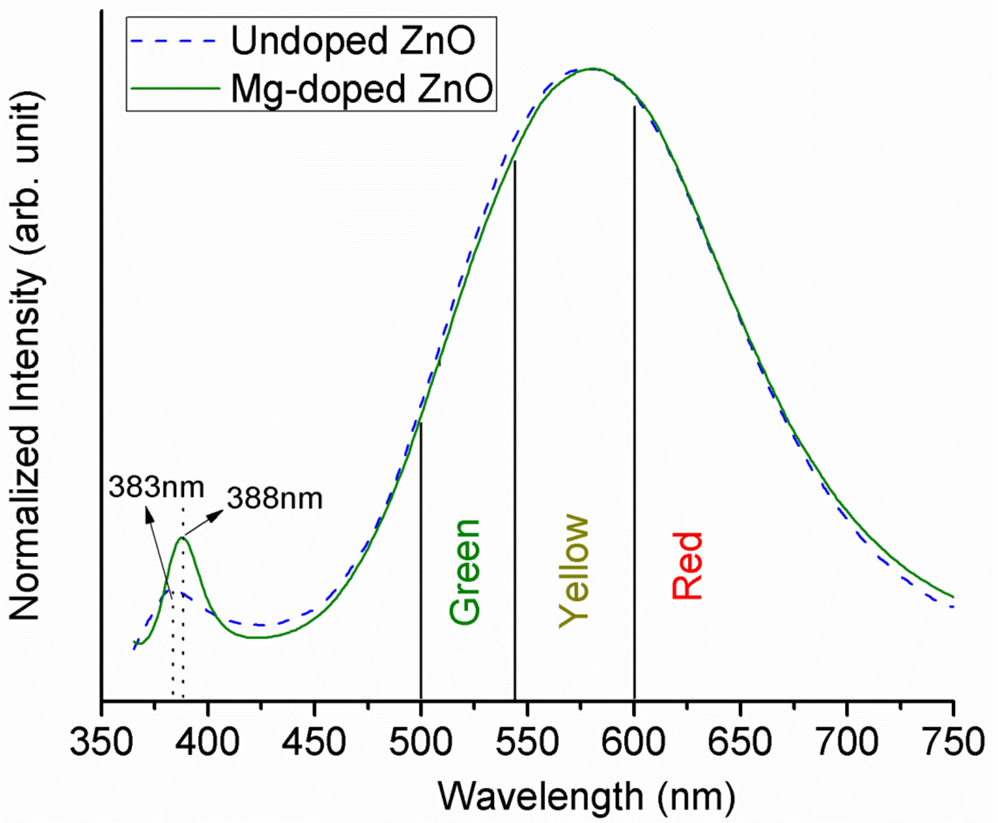

Figure 3.11 Room temperature PL spectra of undoped and Mg-doped ZnO nanorods grown at 60℃ on silicon substrate.

PL spectroscopy is a widely used technique to investigate impurities, dopant or crystal defects in semiconductor crystals. Room temperature PL spectra recorded for undoped ZnO and Mg-doped nanorods are shown in Figure 3.11. Narrow peaks in the UV region centered at 383 nm, and 388 nm were observed for undoped and Mg-doped nanorods, respectively. The UV narrow peaks known as near band edge (NBE) emission are mainly attributed to free exciton recombination in the ZnO lattice [118]. There are broad peaks at visible range centered at 578 nm, and 581 nm for undoped and Mg-doped nanorods, respectively that are known as defect emission. The PL emission data of undoped and Mg-doped ZnO nanorods are summarized in Table 3-6. Both UV and visible emissions are typical of ZnO wurtzite hexagonal crystal structure which has been reported many times before [119]. Therefore, PL spectra confirm the dominant wurtzite crystal for our undoped and Mg-doped samples in consistent with our XRD and Raman results.

The green, yellow and, red emission in ZnO PL spectra originate from different types of defects centers [147]. From Figure 3.11, it can be seen that the defect emission in the green region remained unchanged after Mg addition indicating to the no significant changes in the number of surface defects for both undoped and Mg-doped nanorods [122]. Higher yellow emission in the PL spectra of Mg-doped sample can be related to the larger number of oxygen vacancies consistently with our Raman and XPS analysis. Slightly higher red emission can be attributed to the formation of Mg^{2+} compounds in the host crystal lattice or a larger number of zinc interstitials as has been detected in our Raman spectra [122].

The intensity of the NBE of the Mg-doped sample has increased considerably as compared to that of the undoped ZnO. The effect of water desorption on UV emission enhancement in ZnO nanostructures has been reported before [148]. Therefore, stronger UV emission in Mg-doped sample can be related to the smaller amount of chemisorbed water which is consistent with the weaker O_H peak in its XPS spectra. On the other hand, higher NBE emission can be connected to the larger Mg-doped nanorods sizes than undoped ZnO nanorods. Larger nanorods exhibit more crystal symmetry which yields production of larger number of charge carriers with the similar energy levels. NBE enhancement of ZnO nanorods due to the size increment was reported by Zhao et al. [149]. Radiative recombination of those electrons and holes will be exhibited in NBE emission larger peak. Stronger exciton emission can be the evidence of higher ZnO crystal quality and lower number of nonradiative centers in Mg-doped ZnO [150].

The UV emission peak experienced a 5 nm red shift by Mg addition which implies a narrower band gap for Mg-doped nanorods. NBE might shift upon the doping of ZnO nanorods due to several reasons such as excitonic transition, appearance of dopant-induced structural disorder surface defects, and oxygen vacancies [151]. ZnO has an open structure that can accommodate native defects such as zinc interstitials and oxygen vacancies [120]. Gayen et al. [120] suggested that NBE shift is connected to Mg incorporation at those interstitial sites. Moreover, the NBE to defect emission area ratio in percent increased from 6.18 % for undoped nanorods to 8.3 % for Mg-doped samples. This is in accordance with our XRD and XPS results which predicts a higher crystal quality and less defective medium for our Mg-doped nanorods, respectively. XRD results also showed larger lattice constant for Mg-doped sample. Mg^{2+} doping of ZnO usually leads to the blue shift of the NBE peak. In other words Mg^{2+} doping of ZnO widen the band gap in many previous reports [152]. The anomalous red shift of NBE peak position of Mg-doped ZnO in our case might be due to its lattice distortion. Although, red shift of the NBE of ZnO due to Mg^{2+} doping has been reported before, too [153].

EDS results show a small amount of Mg^{2+} incorporated into our ZnO nanorods. While the small amount of doped Mg^{2+} cations made major changes such as PL red shift, better uniformity, bigger sizes and lattice constant to our ZnO nanorods. The large impact of Mg^{2+} dopant may be explained based on a process that happened at the early stages of the growth. The role of dopant in governing nano-crystal shapes can be explained by the formation of initial growth seeds with different crystallographic sizes at the primary growth stage [154]. In our experiment the seed layer was drop casted in the exact same manner for both undoped and Mg-doped samples. However, the largest number of Mg^{2+} ions were in the bottle at the beginning of the growth process, and the number of available Mg^{2+} was reduced as the growth proceeded. Thus, NBE red shift can be attributed to the larger lattice constant that had happened due to the formation of the larger nucleation sites or incorporation of Mg^{2+} at the early stage of the growth. Larger lattice constant can be attributed to the strain created across our nanorods by Mg^{2+} addition. This lattice deformation exhibits in the (002) peak shifts in the XRD patterns (Figure 3.6). Finally, we believe that the more intense NBE emission for Mg-doped ZnO nanorods is due to their higher crystal quality as well as their higher surface coverage (Figure 3.4).

3.2 Low temperature hydrothermal growth of arrays of Ni-doped ZnO nanorods

Ni-doped ZnO is one of the various candidate materials for obtaining room temperature ferromagnetism properties [155-157]. In fact, Ni^{2+} doping of ZnO can provide the spin sources for a spintronic based device [158]. The ion radius of Ni^{2+} (0.69 Å) is slightly smaller than the Zn^{2+} (0.74 Å) [159], so it can be easily incorporated into the ZnO lattice. Experimental results show that incorporating transition metals such as Ni^{2+} into ZnO nanorods could enhance their gas sensitivity [160]. Ni-doping of ZnO would be also in favor of photocatalytic activity of ZnO by moving its absorbance band towards the visible range [79, 161].

Experimental results showed that magnetization of transition metal-doped ZnO depends on their preparation process [158]. Large amounts of Ni^{2+} can be incorporated into ZnO via different deposition methods [7, 162-164]. These techniques usually require either harsh conditions, or a high-temperature post-annealing to crystallize the amorphous deposited material. Post-annealing can result in the formation of undesired multiple phases in the final material. The majority of the materials deposited by using these techniques are in the form of thin films or nanoparticles [164, 165]. However, 1-D magnetic/semiconductor heterostructures are of particular interest in nanoscale spintronics due to the possibility of magnetization tuning. Jung et al.[166] reported the fabrication of Ni-doped ZnO nanorods hetereostructures via metal organic vapour phase epitaxy. He et al.[7] implanted Ni^{2+} ions into ZnO nanorods through a physical method following by a high temperature annealing. Thermal diffusion of metal transient into already synthesized ZnO nanorods at a high temperature has also been reported before [167]. Ni-doped ZnO nanodisks have been synthesized via hydrothermal methods at a temperature as high as 150℃ [168]. Cui et al.[169] successfully doped ZnO nanorods with Ni^{2+} and Co^{2+} at 90℃ by extending the hydrothermal method to an electro chemical process. Finally, incorporation of Ni^{2+} in ZnO nanorods with different level via solution method at 80℃ has been successfully done [159]. In this section, different properties of Ni-doped ZnO nanorods synthesized by a hydrothermal method at ~60℃ will be given.

The speciation diagram of Ni(II) is shown in Figure 3.12. It can be seen that before the growth solution was heated, the only cationic species that could exist are Ni^{2+} and $Ni(NH_3)_5^{2+}$. However, the number of $Ni(NH_3)_5^{2+}$ ions decreases shortly after the start of the growth. Similar to Mg, the broad range of pH in which Ni(II) can exist in the form of Ni^{2+} implies that higher concentration of Ni^{2+} (> 5mM) can be introduced to the growth solution as the dopant.

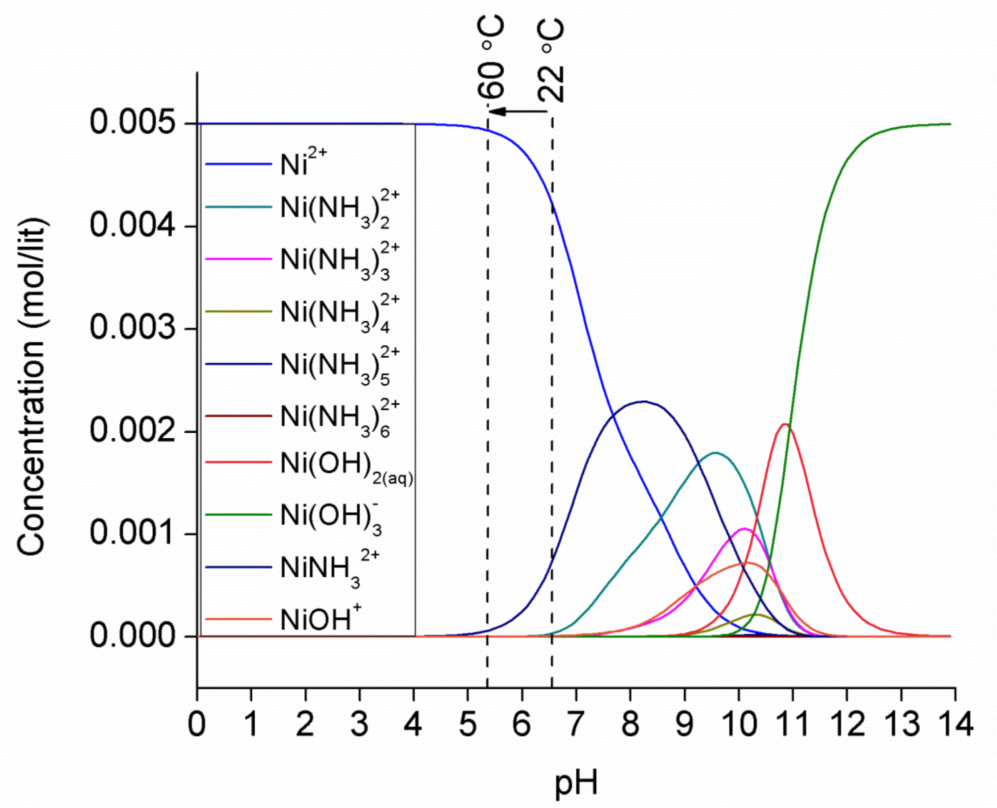

Figure 3.12 Speciation diagrams of Ni(II) species at 60℃ as a function of pH ranging from 0 to 14 as computed with Visual MINTEQ software.

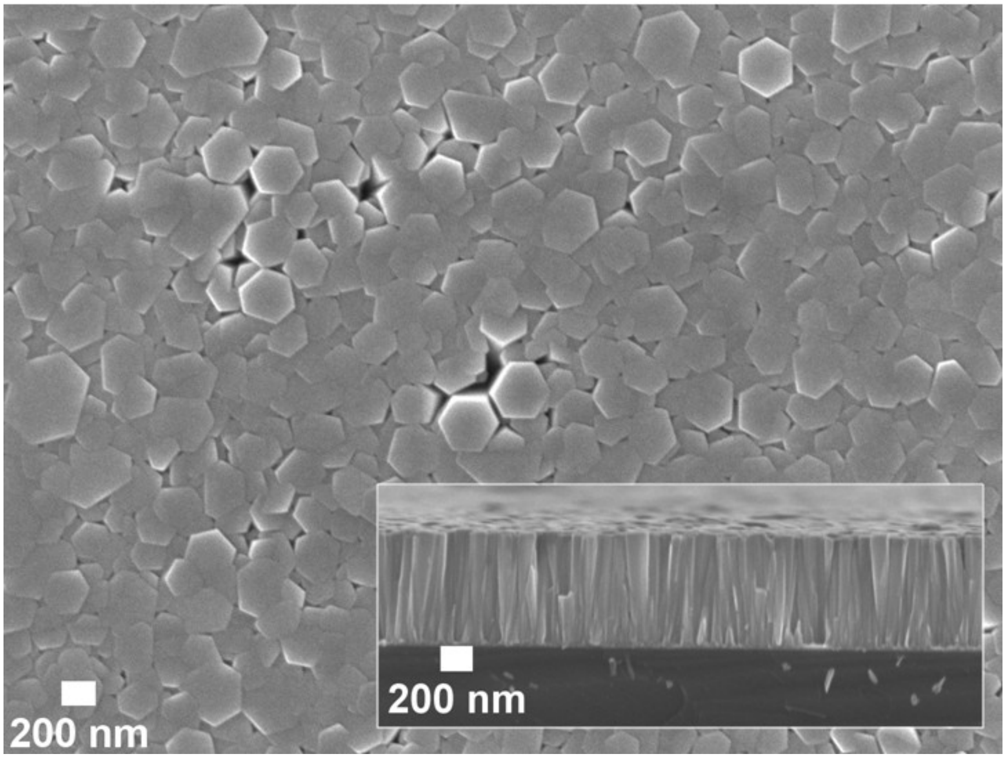

Figure 3.13 SEM images of the top and cross section of Ni-doped ZnO nanorods grown at 60℃ on silicon substrate.

The SEM images of Ni-doped ZnO nanorods are shown in Figure 3.13. It can be seen that the hexagonal shape of ZnO nanorods remained unchanged after Ni^{2+} addition. The nanorod coverage is enhanced across the substrate and more uniform nanorods are obtained by introducing Ni^{2+} ions inside the growth bottle. The average height and diameter increased to 1.2 μm and 243 nm, respectively as a result of Ni^{2+} doping. The size information of Ni-doped nanorods is summarized in Table 3-2. Our result is in agreement with previous reports where size of ZnO nanorods increased proportionally to the amount of Ni^{2+} precursor introduced to the growth bottle [159, 168]. But our nanorods have less size variation in terms of diameter and height compared to the previous reports. The addition of Ni^{2+} might also affect the surface energy of ZnO along its different crystal planes as compared to undoped ZnO growth. Ni^{2+} compounds can attach to the fastest growth plane (002) and hinder the growth along this plane. Thus, the crystal growth will continue more effectively along other crystal planes resulting in thicker nanorods with larger diameter. This is consistent with a reduction of the aspect ratio of nanorods from 6.5 to 4.9 by the addition of Ni^{2+}. However, the growth perturbation along the fastest growth plane (002) is temporary due to the small amount of Ni^{2+} precursor in the growth bottle.

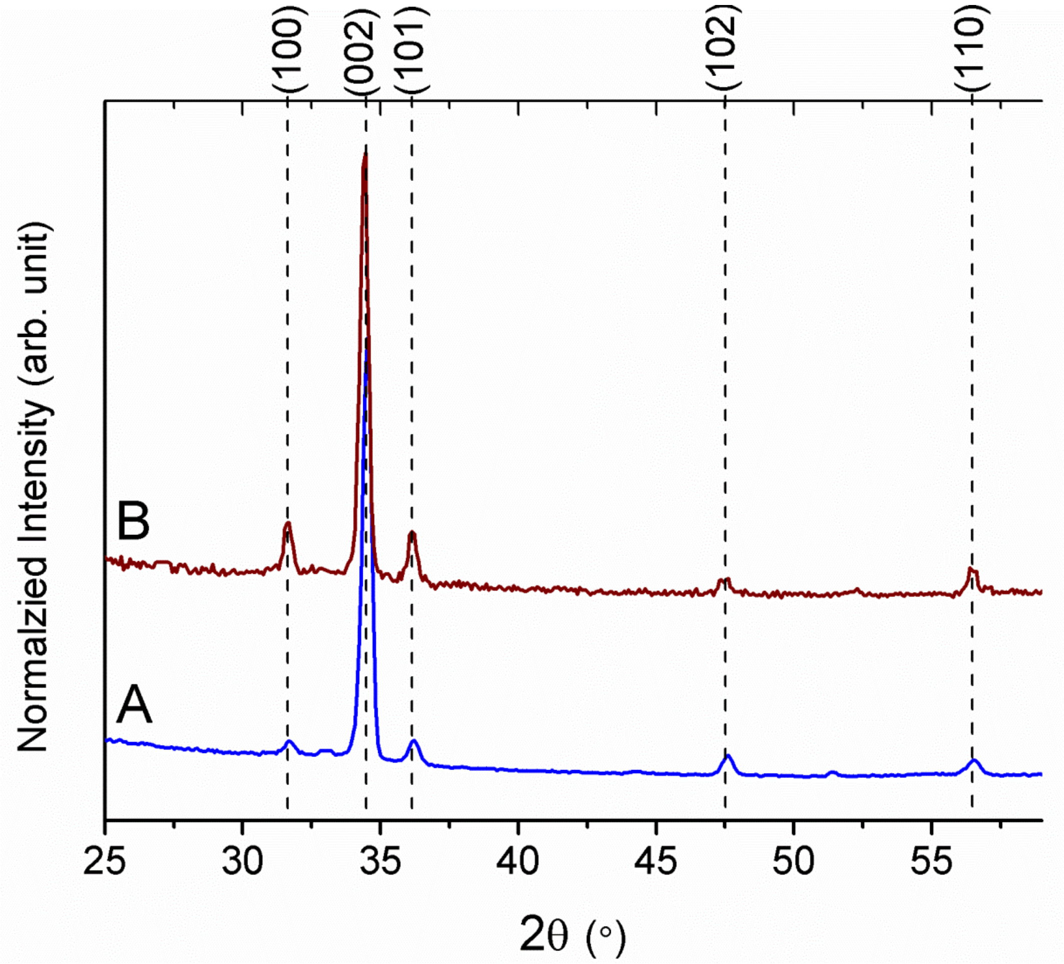

Figure 3.14 XRD patterns of A) undoped and B) Ni-doped ZnO nanorods grown at 60℃ on silicon substrate. (Traces were shifted vertically for visibility)

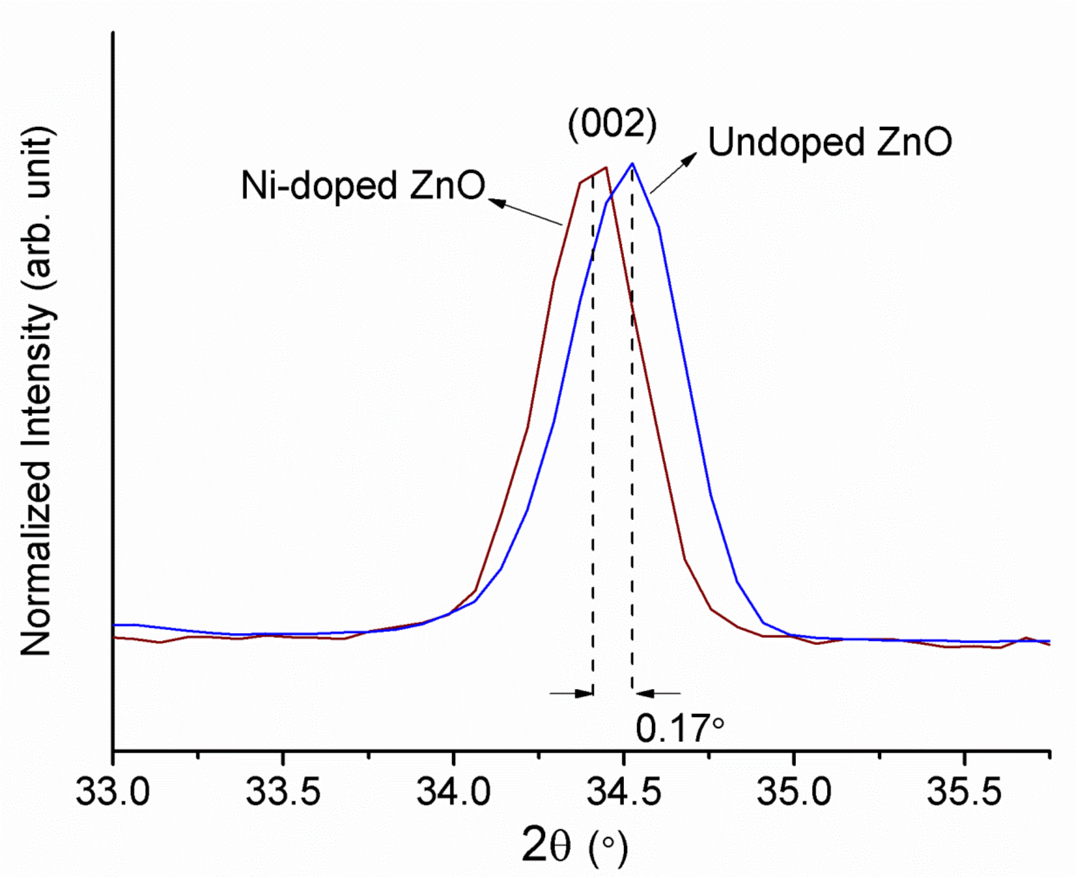

Figure 3.15 High resolution (002) peak position of undoped and Ni-doped ZnO grown at 60℃ on silicon substrate.

The crystal phase of Ni-doped and undoped ZnO nanorods were investigated by XRD and the patterns are shown in Figure 3.14. The peaks for both samples are indexed to hexagonal wurtzite ZnO crystal structure. No additional peaks of a secondary phase were detected in terms of Ni^{2+} in forms of metal or its oxide. Therefore, no agglomeration of Ni^{2+} was observed in our synthesis and all the incorporated Ni^{2+} has dissolved in the wurtzite crystal lattice. Crystallinity along most of the planes remained unchanged for Ni-doped nanorods in comparison with the undoped ZnO. However, the intensity has slightly increased along (100) and (101) crystal planes which could be due to the larger diameters of Ni-doped nanorods. Larger diameter in Ni-doped nanorods could be the result of faster growth along the (100) and (101) faces, consistently with the SEM results. It has been argued that the Ni^{2+} doped ZnO has higher surface energy on the (101) and (100) surfaces compared to the undoped ZnO [168]. Therefore, it is more convenient for Ni-doped nanorods to grow along these two faces than in the case of undoped ZnO. This fact is in agreement with our XRD data that shows stronger peaks for both (100) and (101) planes for Ni-doped nanorods.

The strong (002) peak indicates dominant arrays of ZnO nanorods perpendicular to the substrate. A small shift (0.17 °) of the (002) peak to a lower 2Θ angle value for Ni-doped nanorods can be seen in Figure 3.15. This shift is attributed to the lattice deformation due to the incorporation of Ni^{2+} in ZnO lattice. Subsequently, a higher lattice constant along the c-axis as well as larger crystal plane spacing along the (002) plane for Ni-doped sample were calculated based on XRD data, which is consistent with previous reports about the low concentration substitution of Zn by Ni^{2+} dopant at low temperature [159, 169, 170]. A summary of the crystallographic data of Ni-doped nanorods is given in Table 3-3. Incorporation of Ni^{2+} into ZnO crystal might cause a lattice distortion. Due to the comparable ionic radius of Ni^{2+} and Zn^{2+} the lattice parameter variations are small. By applying the crystallographic data of Figure 3.14 into equation 3-1 the degree of alignment of Ni-doped nanorods was calculated. Comparing the calculated results to those of undoped ZnO, the degree of texture was reduced from 82% to 74% .

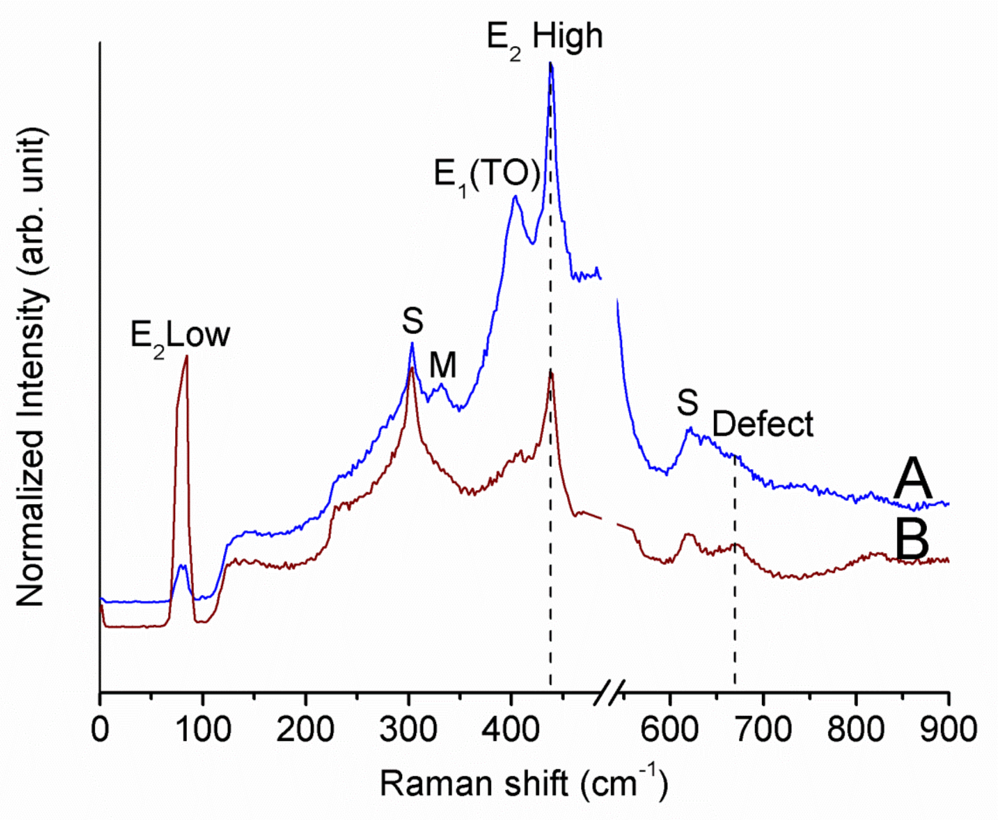

Figure 3.16 Room temperature micro-Raman scattering spectra of A) undoped and B) Ni-doped ZnO nanorods grown at 60℃ on silicon substrate. (Traces were shifted vertically for visibility)

Figure 3.16 shows the Raman spectra of undoped and Ni-doped ZnO nanorods. Our results correspond with the well-known features of ZnO, showing Raman active E_1 and E_2 peaks [111]. As for Mg the M mode at ~332 cm^{-1} attributed to difference modes $E_2(H)$-$E_2(L)$ as multiple-phonon scattering processes [113, 135]. We believe that the M peak disappearance is related to the flat top shape of Ni-doped nanorods as can be seen in Figure 3.13.

In Ni-doped ZnO micro-Raman spectra the peaks at 78.7 cm^{-1}, 403 cm^{-1} and ~437.7 cm^{-1} are assigned to the $E_2(L)$, $E_1(TO)$ and $E_2(H)$ modes, respectively. A summary of Raman active modes of Ni-doped nanorods are given in Table 3-4. The sharp $E_2(H)$ peak is evidence of strong wurtzite crystal orientation in both Ni-doped and undoped samples [112] demonstrating that the overall crystal structure of the ZnO nanorods is not affected by Ni addition, in accord with our XRD patterns. There is hardly any change of the $E_2(H)$ peak position after Ni-doping. The dominant $E_2(H)$ peak also implies that the majority of nanorods are perpendicular to the substrate. The intensity of $E_2(L)$ has increased drastically with doping of Ni^{2+}. On the other hand, the intensity of E_1(TO) is suppressed in the Ni-doped sample. This could happen because of better crystal orientation of the Ni-doped ZnO nanorods, where the E_2(L) and E_2(H) become the two dominant peaks as the representatives of ZnO wurtzite crystal structure. The broadening of E_2 (L and H) peaks could be due to the wurtzite lattice distortion in Ni-doped sample. There is also a small peak at 669 cm^{-1} in the Raman spectra of both undoped and Ni-doped crystals. An additional vibrational mode in the range of 635-670 cm^{-1} has been reported in doped ZnO before [136, 171-173]. Yang et al.[172] have attributed this mode to additional impurities in ZnO crystal. This mode has also been connected to defects in nanocrystals such as oxygen vacancies and zinc interstitials [136], or intrinsic host-lattice defects [171] in other reports. This peak became more distinct for our Ni-doped sample, suggesting larger number of those defects in our Ni-doped nanorods. This fact will be confirmed with PL spectroscopy.

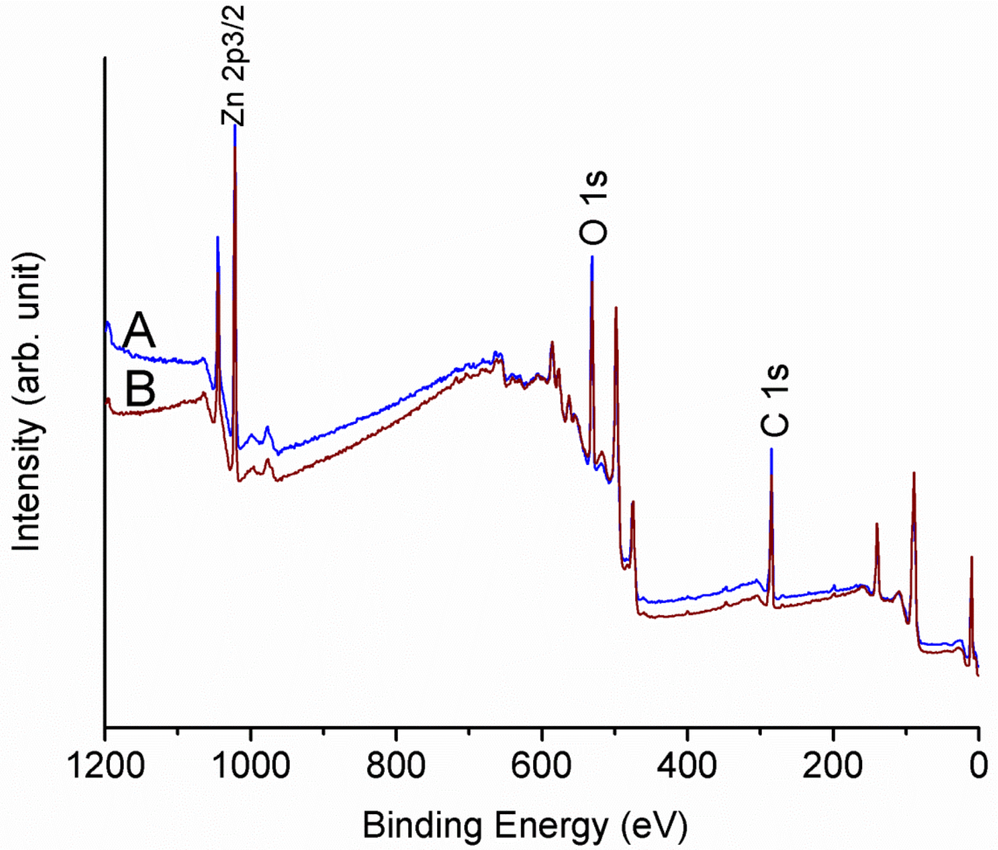

Figure 3.17 XPS spectra of A) undoped and B) Ni-doped ZnO nanorods grown at 60℃ on silicon substrate. (Traces were shifted vertically for visibility)

The XPS spectrum of the Ni-doped ZnO nanorods is shown in Figure 3.17 jointly with the one for undoped one. As can be seen, there is a good agreement in the XPS spectra of Ni-doped and undoped ZnO nanorods. An attempt to detect Ni^{2+} cations in the doped nanorods using XPS was not successful due to the low concentration of Ni^{2+}. The atomic number of Ni^{2+} was later detected in the EDS spectrum which is shown in Figure 3.18. The EDS results show that the Ni content of our sample is 0.4 atomic% on average.

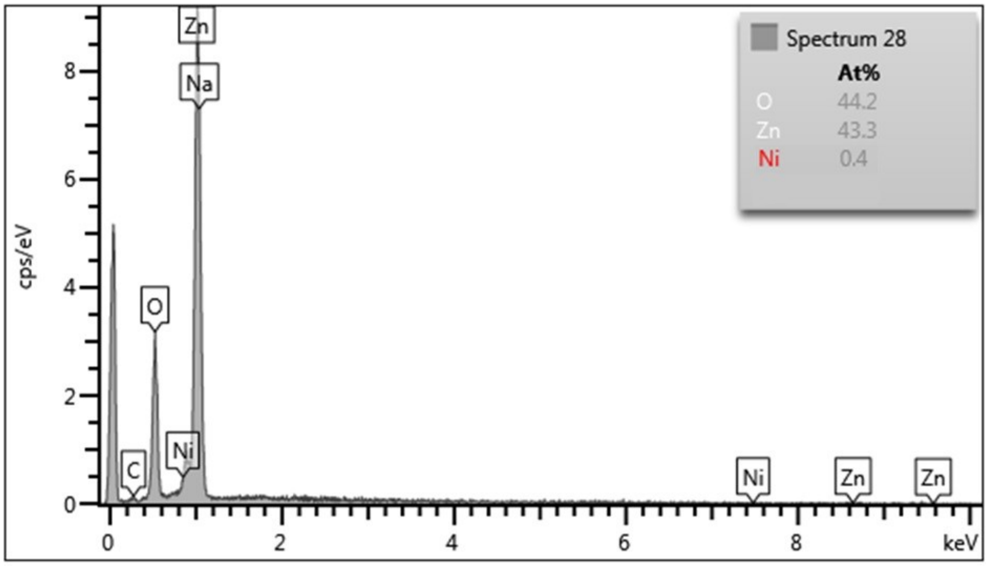

Figure 3.18 EDS elemental microanalysis of Ni-doped ZnO grown at 60℃ on silicon substrate.

No significant changes in the chemical shift and signal due to doping were found for the Zn 3d, Zn 3p, and Zn 3s peaks. More precise measurements show that the Zn 2p peaks shifted towards lower energies (-0.5 eV) due to Ni^{2+} doping. This energy shift can be due to the decrease in surface energy of Ni-doped nanorods. The FWHM of the Zn 2p peaks were also found to be smaller for the Ni-doped sample (1.79 eV) as compared to the undoped ZnO (1.85 eV). The narrowing suggests the presence of less Zn states defects within Ni-doped ZnO structure.

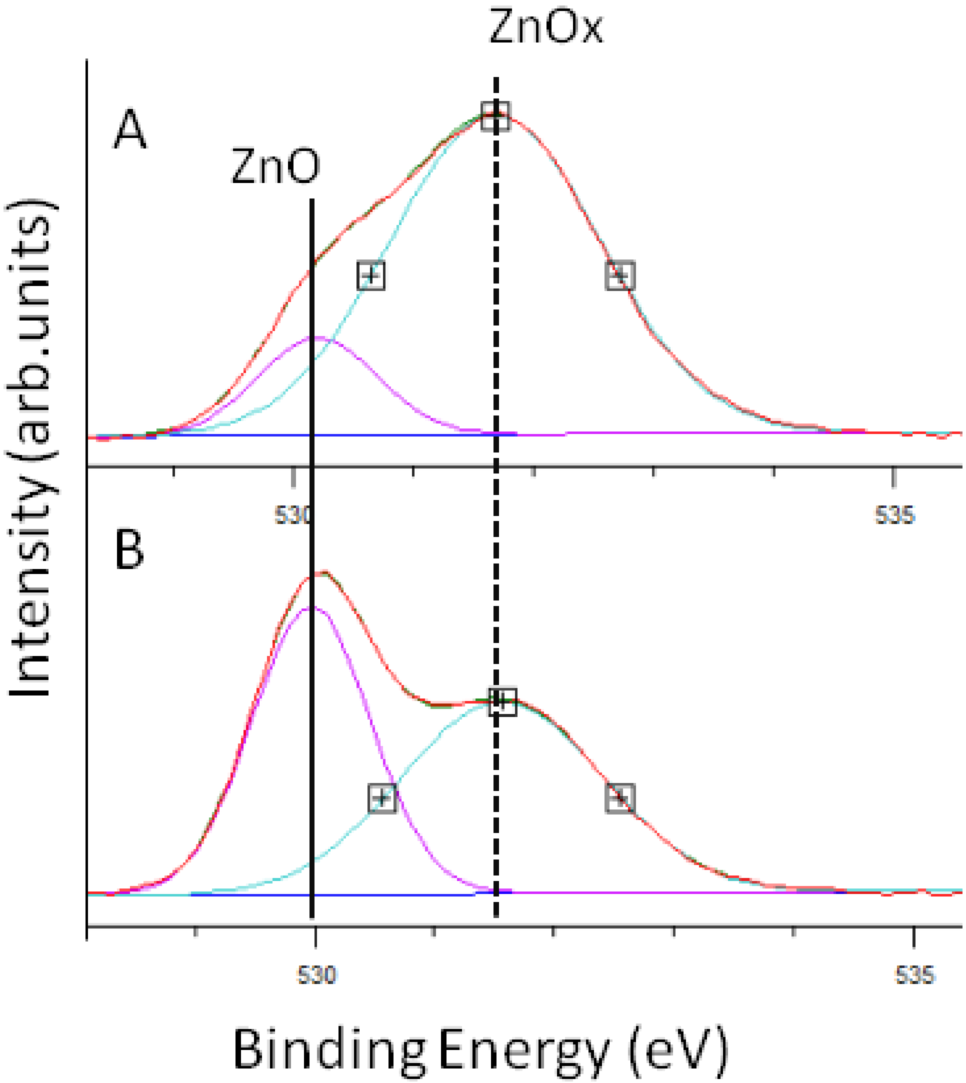

Figure 3.19 XPS spectra of O 1s core level of A) undoped and B) Ni-doped ZnO nanorods grown at 60℃ on silicon substrate.

The asymmetric O 1s peak (Figure 3.19) was fitted with two subspectral components at 530.2 eV and 531.6 eV. The lower energy peak is assigned to O^{-2} ions (O_L) in stoichiometric Zn-O-Zn regions. Whereas the higher binding energy peak is attributed to O^{-2} ions (O_H) in oxygen deficient ZnOx regions and/or to hydroxyl groups resulting from chemisorbed water [141, 143]. Based on the curved fitting results shown in Figure 3.19 the surface O_H percentage decreases 52% after Ni addition which is the evidence of better oxidized stoichiometric surroundings in doped nanorods and/or less hydroxyl groups attached to the surface. Similar components in O 1s have been observed before [143-145], and based on O 1s/Zn 2p XPS intensity the stoichiometry of ZnOx(OH)y was suggested [143, 146]. In our case this ratio is slightly reduced from 3.8 for undoped ZnO to 3.3 for Ni-doped nanorods. This speculation will be further investigated by PL spectroscopy. We believe that the smaller surface percentage of O_H peak in our case is related to the larger number of stoichiometric oxygen on the surface of the Ni-doped ZnO as compared to undoped ZnO nanorods. The surface chemistry information of Ni-doped ZnO nanorods are summarized in Table 3-5.

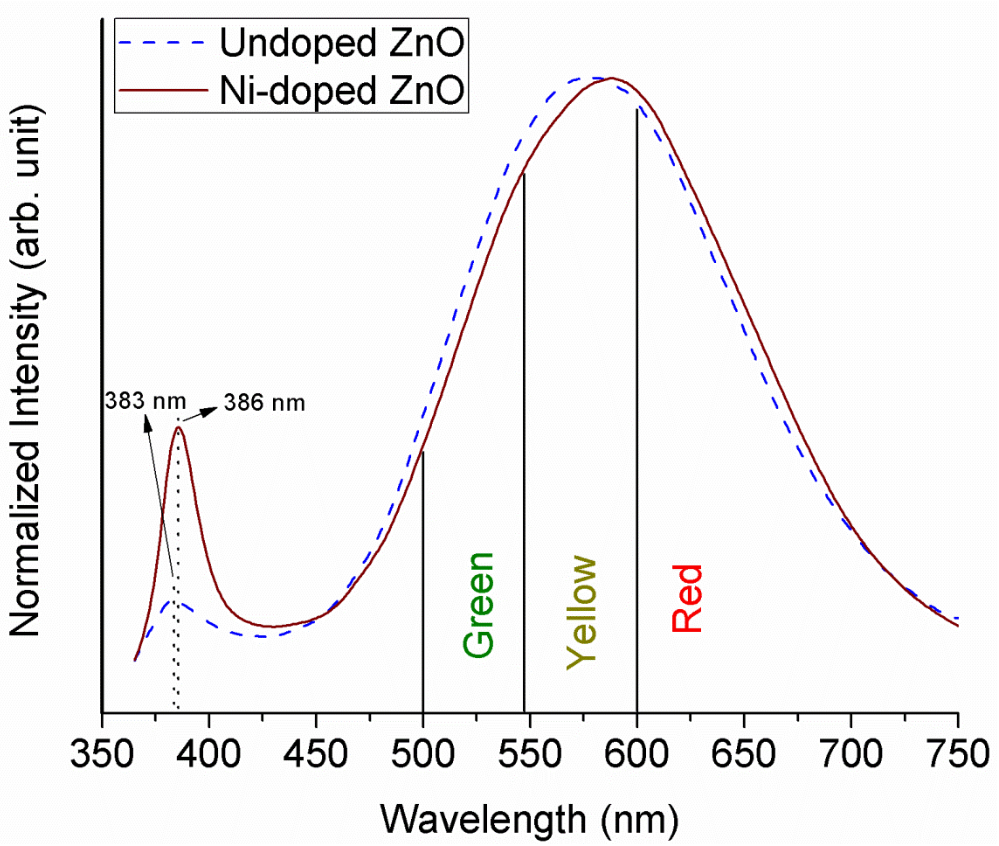

Figure 3.20 Room temperature PL spectra of undoped and Ni-doped ZnO nanorods grown at 60℃ on silicon substrate.

Room temperature PL spectra recorded for Ni-doped nanorods are shown in Figure 3.20. A narrow peak in UV region centered at 386 nm was detected for Ni-doped nanorods. The broad peak in the visible range centered at 585 nm was also detected for Ni-doped nanorods, which is known to be related to defect emission. The PL emission data of Ni-doped ZnO nanorods are summarized in Table 3-6. The PL measurement also confirms the dominant wurtzite crystal structure for our Ni-doped samples in accord with our previous results. The defect emission of our Ni-doped sample has increased compared to the undoped ZnO. The increase in the defect emission can be connected to the deformation of the band structure due to the lattice distortion which was detected in the XRD patterns [173]. A slight increase in green emission can be attributed to an increase in the number of intrinsic host-lattice defect such as zinc interstitials due to the incorporation of Ni^{2+} into ZnO crystal. This attribution is consistent with our micro-Raman spectra analysis. Higher yellow emission in the PL spectra of Ni-doped sample can be related to the larger number of oxygen vacancies in consistent with our Raman and XPS analysis. Slightly higher red emission can be attributed to the formation of Ni^{2+} compounds in the host crystal lattice or to a larger number of zinc interstitials as has been detected in our Raman spectra [122].

The intensity of the NBE has increased considerably as a result of Ni^{2+} doping. Stronger UV emission in Ni-doped sample can be related to the smaller amount of chemisorbed water, which is in accordance with the weaker O_H peak in its XPS spectra. On the other hand, higher NBE emission can be connected to the larger Ni-doped nanorods sizes than undoped ZnO nanorods as described before. The lower FWHM of (002) plane in XRD pattern of Ni-doped sample in comparison to undoped ZnO nanorods is evidence of lower lattice constant variation in our Ni-doped sample. This could be another reason for the sharp exciton emission peak of Ni-doped nanorods in Figure 3.20. Another reason for the NBE enhancement might be related to the decrease in the number of nonradiative centers in undoped ZnO by Ni^{2+} addition. Thus intense UV emission in Ni-doped samples could be due to the improved crystal parameters. From the SEM images it can be seen that the size and uniformity of the nanorods has improved due the existence of Ni^{2+} dopant in the growth solution. This idea is supported by the fact that NBE to defect emission ratio was increased from 6.18 % for undoped nanorods to 12 % for Ni-doped samples. Generally, this ratio is regarded as an indicator of ZnO crystal grade [168, 170].

There is a 3 nm red shift in the NBE emission of Ni-doped nanorods in comparison to undoped ZnO. In general, incorporation of Ni^{2+} in ZnO crystal lattice yields in a red shift of NBE peak [7, 159, 174], while there are still reports of blue shift in ZnO exciton emission after Ni-doping [168, 173]. The blue shift is mainly attributed to the Burstein-Moss effect [173]. This effect can be explained based on the occupation of conduction band edge of ZnO by excessive carriers provided by the impurities which are Ni^{2+} ions in our case, whereas, the red shift is connected to the change of the energy band structure [174]. According to the XRD data the lattice constant increased as a result of Ni^{2+} addition. Thus the NBE emission red shifted following the change of energy band levels of Ni-doped nanorods. This is in accordance with previous reports where red shift in NBE was detected due to lattice constant increase [159, 170].

Similar to Mg, EDS results show a small amount of Ni^{2+} incorporated into our ZnO nanorods. In fact, more energy is required to substitute Zn^{2+} ions with Ni^{2+} in ZnO lattice due to the stronger Ni-O bonding as compared to Zn-O. Therefore, we expect lower amounts of Ni^{2+} incorporated in ZnO nanorods with low temperature synthesis methods [159]. In practice, this is not an issue since investigating the effect of Ni^{2+} dopant concentration on NBE of ZnO thin film showed that lower concentrations of Ni^{2+} are more favorable for getting higher NBE emission [175]. Major changes such as PL red shift, better uniformity, bigger sizes and lattice constant observed for our ZnO nanorods by Ni addition. The big impact that small amount of Ni^{2+} made to the properties of our ZnO nanorods can be explained in a similar way to those in Mg-doped nanorods. Therefore, we believe that the more intense NBE emission for Ni-doped ZnO nanorods is due to their better coverage (Figure 3.13). And the NBE red shift is due to the larger lattice constant that happened due to the formation of the larger nucleation sites or incorporation of Ni^{2+} at the early stage of the growth. Larger lattice constant can be attributed to the strain created across our nanorods by Ni^{2+} addition. This lattice deformation appears in the (002) peak shifts in XRD patterns (Figure 3.15). The NBE red shift in the Ni-doped ZnO nanorods can be attributed to this larger lattice constant. The defect emission increased at the same time due to the higher number of oxygen vacancies and zinc interstitials.

3.3 Low temperature hydrothermal growth of arrays of Mn-doped ZnO nanorods

According to Mandal et al.[176] Mn^{2+} and Co^{2+} are the two most soluble cations in ZnO nanocrystals. Therefore, Mn^{2+} is a good candidate to be doped into ZnO nanorods via hydrothermal method, where low temperature is expected to hinder the incorporation of dopant ions into the host lattice. In practice, doping of ZnO by Mn^{2+} is one of the most significant approaches towards development of ferromagnetic diluted magnetic semiconductors (DMS) with a Curie temperature above room temperature [177]. On the other hand, Ahmed et al.[65] reported that undoped ZnO oxygen gas sensitivity can be improved by Mn^{2+} addition. Successful incorporation of Mn^{2+} into ZnO lattice through common chemical based methods such as chemical vapor deposition method [178], chemical bath deposition method [130], and solution growth method has already been reported. Compared to all these techniques low temperature hydrothermal method stands out due to its large scale, low price device fabrication potential. The incorporation of Mn^{2+} ions into the ZnO lattice at low temperature is challenging due to the strong Mn-O bonding. Therefore, the achievable doping percentage of Mn^{2+} in ZnO crystal using solution growth method is expected to be lower than that from nonequilibrium high temperature methods like CVD. To tackle this problem, a solution-based Mn^{2+} doping of ZnO nanorods has been done at relatively high temperature (~200) in the past. However, the doped nanorods grown with this approach were not uniform in size, and they were randomly aligned relative to the substrate. Later Singh et al.[130] synthesised Mn-doped ZnO nanorods at low temperature (65℃) on top of the seeded glass. The nanorods alignment improved in their report, while their uniformity was hindered, most probably due to the formation of inhomogeneous clusters which were combination of coated ZnO and MnO nano particles. Non-treated substrates can also be the main reason for the random alignment of nanorods which were synthesised at low temperature by Panigrahy et al. [179]. Similarly, Mn^{2+} doped ZnO nanorods prepared via hydrothermal method in other reports have shown a lack of uniformity due to the size dispersion of the seed nanoparticles [180, 181]. Therefore, the challenge of Mn-doping of ZnO under mild conditions without affecting the morphology and uniformity is still unsolved. In this section, the structural, surface chemical and optical properties of Mn-doped ZnO nanorods synthesized by a hydrothermal method at 60℃, will be discussed. The coverage, alignment and uniformity of Mn-doped ZnO nanorods are considerably improved as compared to undoped ZnO ones.

The speciation diagram of Mn(II) is shown in Figure 3.21. It can be seen that before the decomposition of HMTA, the only cationic species that could exist is Mn^{2+}. The broad range of pH in which Mn(II) can exist in the form of Mn^{2+} implies that higher concentration of Mn^{2+} (>5mM) can be introduced to the growth solution as the dopant.

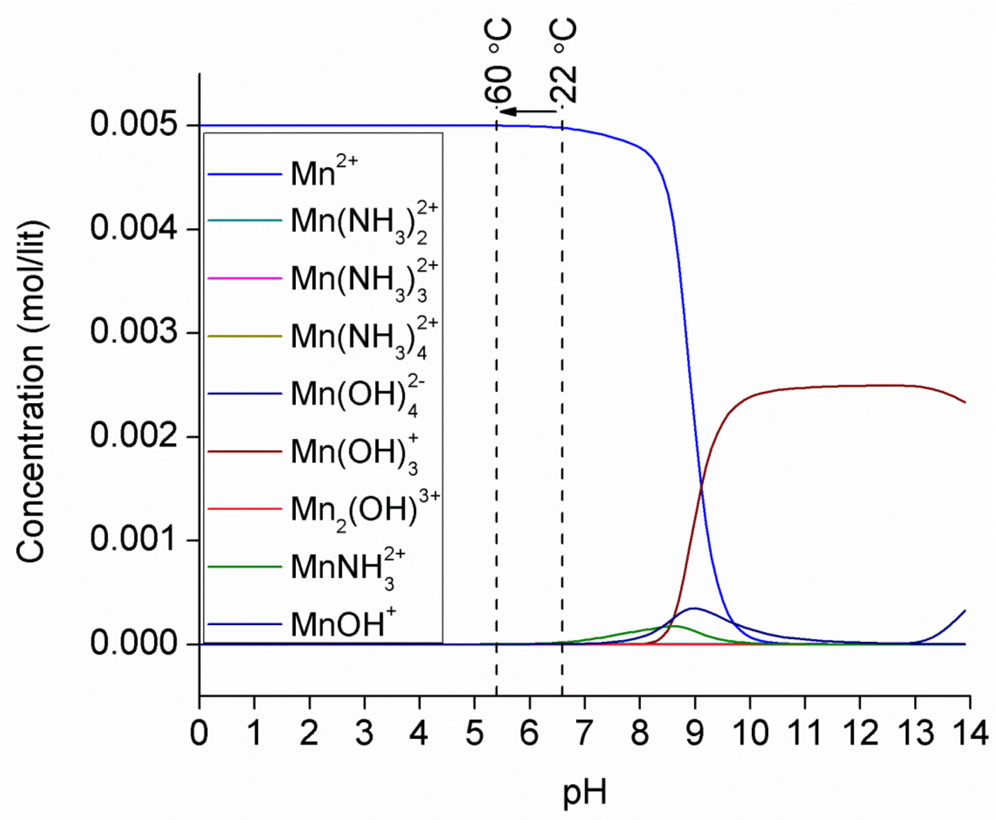

Figure 3.21 Speciation diagrams of Mn(II) species at 60 °C as a function of pH ranging from 0 to 14 as computed with Visual MINTEQ software.

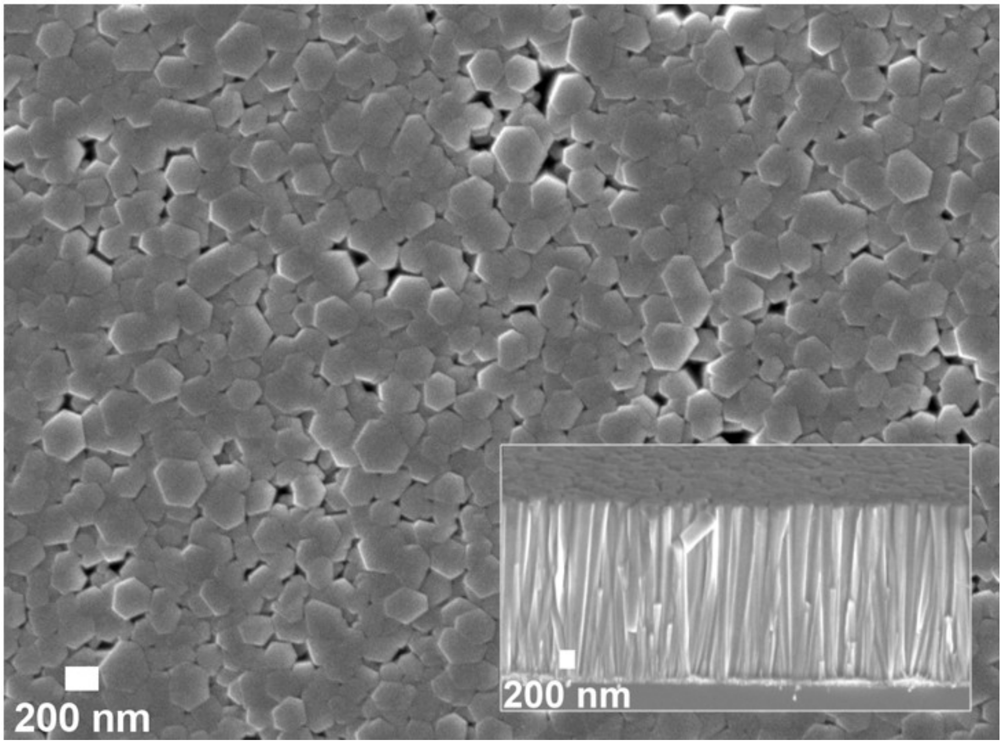

Figure 3.22 SEM images of the top and cross section of Mn-doped ZnO nanorods grown at 60℃ on silicon substrate.

SEM images from the top and cross section of Mn-doped ZnO nanorods are shown in Figure 3.22. It can be seen that the hexagonal shape of ZnO nanorods remained unchanged after Mn^{2+} addition. The nanorods coverage is enhanced across the substrate and considerably uniform nanorods are obtained by Mn^{2+} addition. The average height has increased to 2.1 μm and the diameter to 205 nm on average as a result of Mn^{2+} doping. The size information of Mn-doped nanorods is summarized in Table 3-2. Our result is in agreement with the previous reports where the nanorods sizes increased due to incorporation of Mn^{2+} into ZnO lattice [130, 180]. Our nanorods have less size variation in terms of both diameter and height in comparison to the previous reports as well as enlargement along both height and diameter.

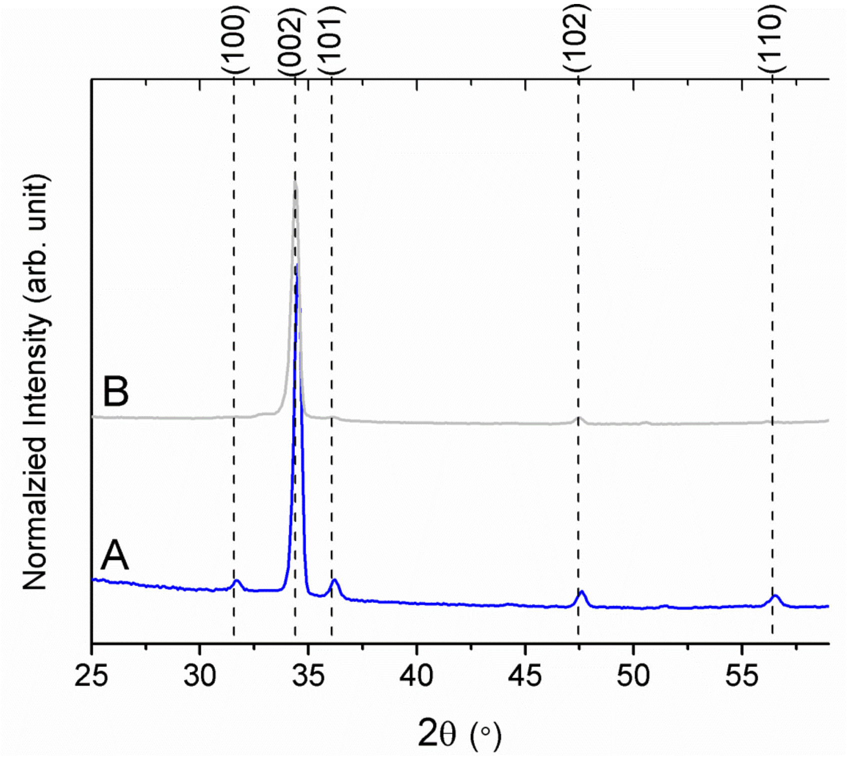

Figure 3.23 XRD patterns of A) undoped and B) Mn-doped ZnO nanorods grown at 60℃ on silicon substrate. (Traces were shifted vertically for visibility)

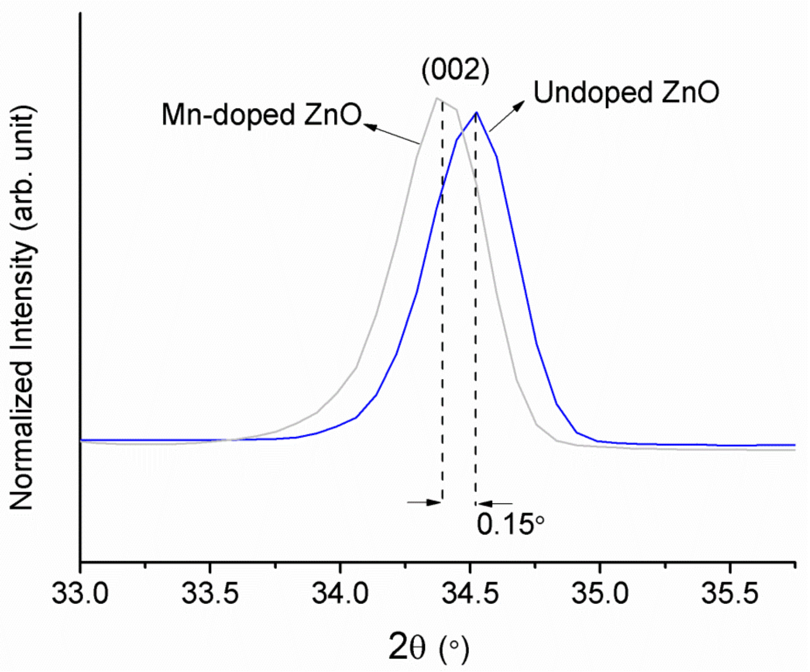

Figure 3.24 High resolution (002) peak position of undoped and Mn-doped ZnO grown at 60℃ on silicon substrate.

The crystal phase of Mn-doped ZnO nanorods were investigated by XRD and the patterns are shown in Figure 3.23. The peaks for Mn-doped ZnO are indexed to hexagonal wurtzite ZnO crystal structure. No additional peaks of a secondary phase were detected in terms of Mn^{2+} in forms of metal or its oxide. Therefore, no agglomeration of Mn^{2+} happened in our synthesis and all the incorporated Mn^{2+} has dissolved in the wurtzite crystal lattice. Crystallinity along most of the planes has not changed for Mn-doped nanorods in comparison with the undoped ZnO. A strong (002) peak indicates dominant arrays of ZnO nanorods perpendicular to the substrate. A small shift (0.15°) of (002) peak to lower 2Θ angle value for Mn-doped nanorods is detected. This shift is attributed to the lattice expansion due to Mn^{2+} addition. Subsequently, higher lattice constant along the c-axis as well as larger crystal plane spacing along the (002) plane for Mn-doped sample were calculated based on the XRD data, which is consistent with previous reports about the substitution of Zn^{2+} by Mn^{2+} dopants at low temperature [130, 181-184]. A summary of crystallographic data of Mn-doped ZnO nanorods is given in Table 3-3. Incorporation of Mn^{2+} into ZnO crystal might cause a lattice expansion. The lattice constant enlargement is due to the Mn^{2+} larger ionic radius (0.66 A) as compared to that of Zn (0.6 A) in tetrahedral coordination [130]. By applying the crystallographic data of Figure 3.23 into equation 3-1 the degree of alignment of Mn-doped nanorods was calculated. Comparing the calculated results to those of undoped ZnO show that the crystallographic orientation of the Mn-doped nanorods enhanced to 91%.

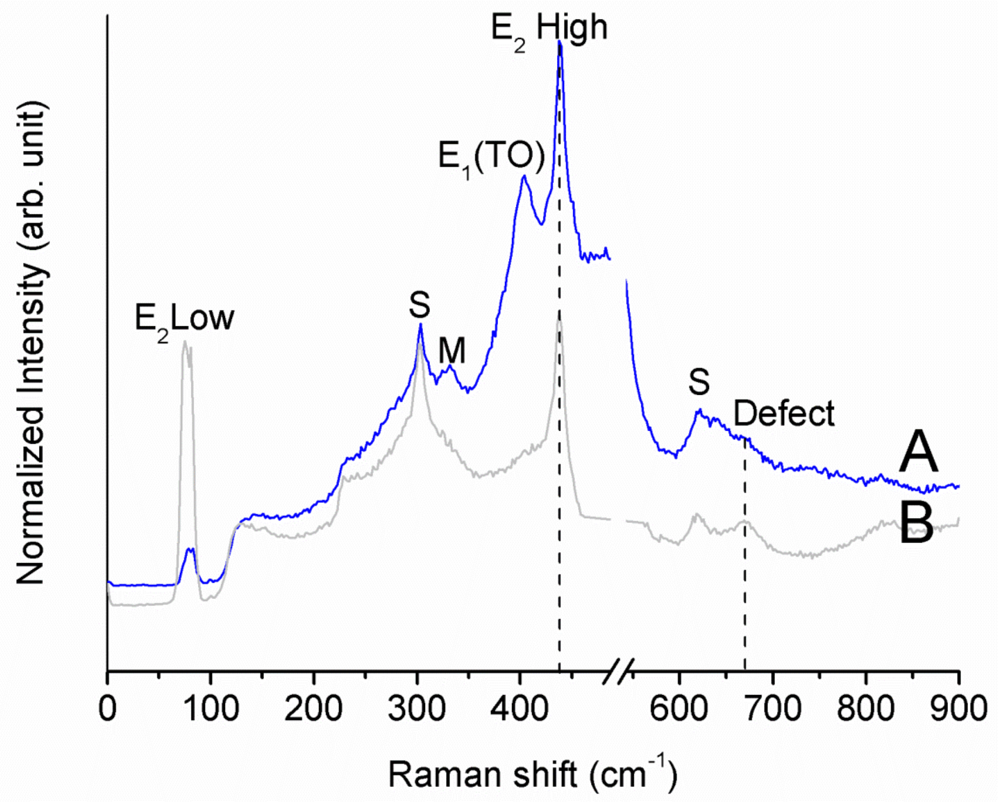

Figure 3.25 Room temperature micro-Raman scattering spectra of A) undoped and B) Mn-doped ZnO nanorods grown at 60℃ on silicon substrate. (Traces were shifted vertically for visibility)

Figure 3.25 shows the Raman spectra of undoped and Mn-doped ZnO nanorods. Our results correspond with the well-known features of ZnO, showing dominant Raman active E_1 and E_2 peaks [111]. Similar to the Mg and Ni-doped nanorods, we believe that the M peak disappearance is related to the flat top shape of Mn-doped nanorods. In Mn-doped ZnO micro-Raman spectra the peaks at 76.9 cm^{-1}, 404 cm^{-1} and ~437.8 cm^{-1} are assigned to the E_2(L), E_1(TO) and E_2(H) modes, respectively. A summary of Raman active modes of Mn-doped nanorods is given in Table 3-4. The E_2(H) peak is evidence of strong wurtzite crystal orientation in Mn-doped samples [112] demonstrating that the overall crystal structure of the ZnO nanorods is not affected by the doping process. However, based on the size of the dopant atom and its electronic structure, the behavior of E_2(H) peak might slightly change. The E_2(H) peak position for Mn-doped nanorods has slightly (+0.1 cm^{-1}) shifted to higher energies as compared to undoped ZnO. The broadening, shift, and asymmetry of E_2(H) and E2(L) peak can be explained based on a spatial correlation model [65, 185]. Based on this model, modification of the lattice vibrational modes can be one of the consequences of lattice distortion, which can be visualized via Raman spectra [85]. According to the measurements of isotopic mass substitution, the frequency shift of E_2(H) mode in ZnO films is mainly appears because of the vibration of oxygen atoms [186, 187]. It has been argued that the missing oxygen mass at oxygen vacancy sites can blue shift the frequency of the E_2(H) mode [85, 188]. Therefore, our Mn-doped ZnO crystal has an oxygen deficiency as compared to undoped ZnO.

The intensity of E_2(L) has increased drastically with doping of Mn^{2+}. This peak represents the vibration of the Zn sublattice in Raman spectra [130, 189]. Thus, the E_2(L) peak behaviour can be significantly affected by the substitution of Zn^{2+} ions by cation dopant [85]. This substitution breaks the lattice translational symmetry which eventually causes broadening in the allowed Raman peaks [185]. The asymmetric broadening of E_2(H) peak can be explained in a similar manner. Moreover, the magnetic behaviour of the doped sample can be altered due to the original lattice deformation. The intensity of E_1(TO) is suppressed in the Mn-doped sample. This could happen because of better crystal orientation of Mn-doped ZnO nanorods, where the E_2(L) and E_2(H) become the two dominant peaks as the representatives of ZnO wurtzite crystal structure.

There is also a peak appearing at 669 cm^{-1} in the Raman spectra of Mn-doped crystals. The nature of this peak is still under debate [190, 191]. Additional vibrational mode in the range of 635-670 cm^{-1} has been reported in doped ZnO crystals before [136, 171-173, 192]. Wang et al.[193] measured a Raman peak at 663 cm^{-1} which was increasing proportionally with Mn^{2+} concentration in their Mn-doped ZnO nanoparticles. In their report, this peak was assigned partly to two phonon processes [A_1(LO)+E_2(L)], and precipitation of Mn based compounds such as Zn_2MnO_4. Whereas, this mode has been connected to the appearance of defects in nanocrystals such as oxygen vacancies and zinc interstitials [136], or intrinsic host-lattice defect [171, 194] in other reports. This peak became more distinct for our Mn-doped sample, suggesting either a larger number of those defects, or substitution of Zn^{2+} by Mn^{2+} ions in Mn-doped nanorods. This fact will be confirmed with PL spectroscopy.

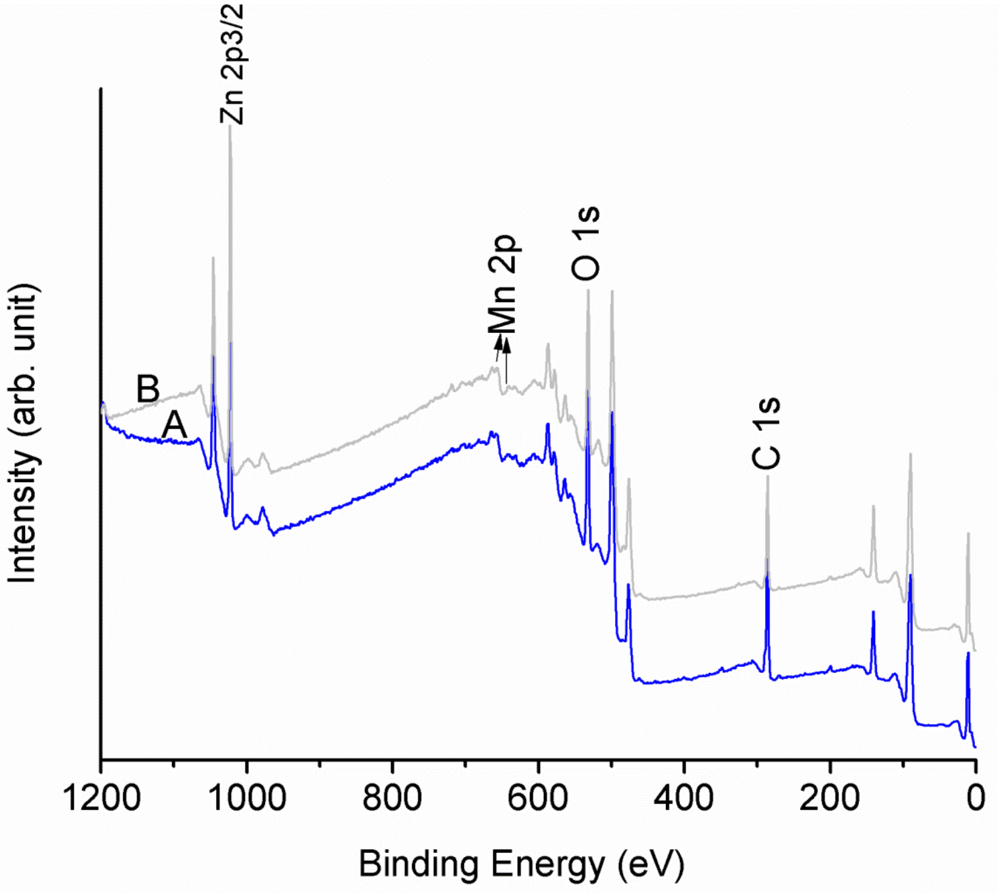

Figure 3.26 XPS spectra of A) undoped and B) Mn-doped ZnO nanorods grown at 60℃ on silicon substrate. (Traces were shifted vertically for visibility)

The XPS spectra of the undoped and Mn-doped ZnO nanorods are shown in Figure 3.26 for comparison. As can be seen there is a good agreement in the XPS spectra of Mn-doped and undoped ZnO nanorods. However, two additional low intensity peaks were detected for Mn-doped sample correspond to Mn 2p orbitals which implies a uniform distribution of Mn^{2+} ions in the ZnO lattice. The high resolution Mn 2p XPS binding energy region is shown in Figure 3.27. This graph was fitted with a Gaussian function showing two peaks at 640.5 eV and 656 eV corresponding to Mn 2p 3/2 and 2p 1/2, respectively which is indicating that the Mn is mainly exists in the form of Mn^{2+} ions on the surface of ZnO nanorods, in agreement with previous reports [179, 192]. The lower binding energy of Mn 2p 3/2 in comparison to the reported binding energy of commercial MnO (640.7 ev) can be related to the substitution of Mn^{2+} with Zn in the host crystal lattice [195]. The atomic composition percentage of Mn^{2+} in the ZnO was calculated to be 5 % according to the following equation [143]:

$$\frac{N_{E1}}{N_{E2}} = \frac{A_{E1}/S_{E1}}{A_{E2}/S_{E2}} \qquad (3\text{-}2)$$

where N is the atomic number, A_E the XPS peak area of a kind of element, and S the elemental sensitivity factor which are 2.6 and 4.8 for Mn and Zn, respectively. This value can be used as a measure of Mn^{2+} doping percentage in ZnO crystal.

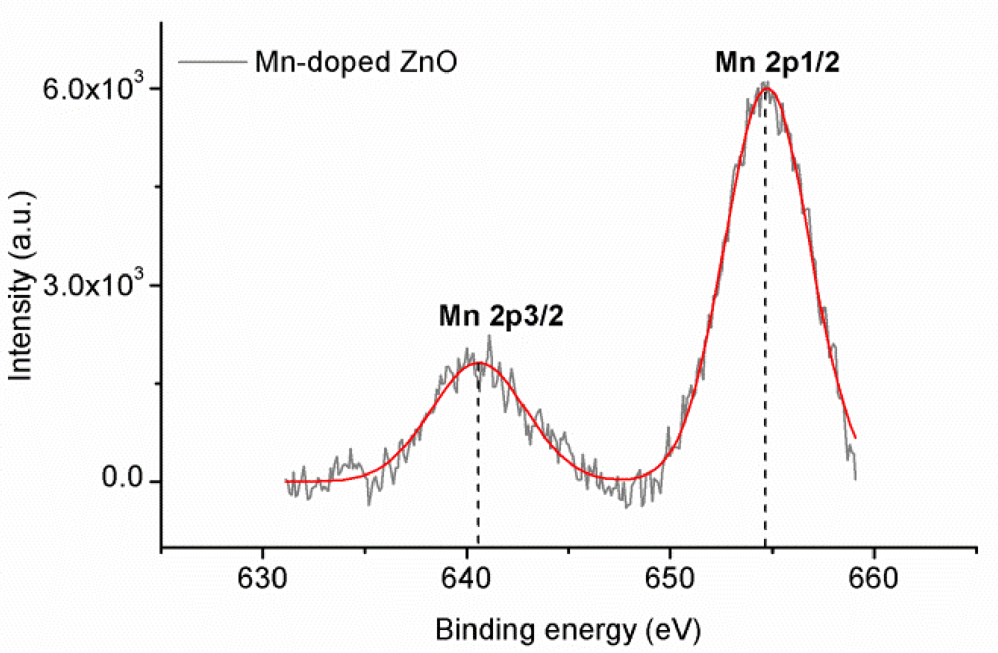

Figure 3.27 High resolution XPS spectra of Mn 2p orbital's peaks grown at 60℃ on silicon substrate.

More precise measurements show that Zn 2p peaks shifted to lower energies (-0.4 eV) due to Mn^{2+} addition. This energy shift is attributed to the formation of Zn-Mn bonds in the surface of the host crystal lattice [195]. Gue et al.[195] argued that the smaller electronegativity of Mn compared to O is the reason for binding energy reduction in Zn-Mn bonds as compared to Zn-O bonds. The energy reduction can be also due to the decrease in (001) surface energy of Mn-doped nanorods in comparison to the energy of the same plane in undoped ZnO case. The FWHM of the Zn 2p peaks were also found to be smaller for the Mn-doped sample (1.75 eV) as compared to the undoped ZnO (1.85 eV). This narrowing suggests the presence of less Zn states defects within Mn-doped ZnO structure.

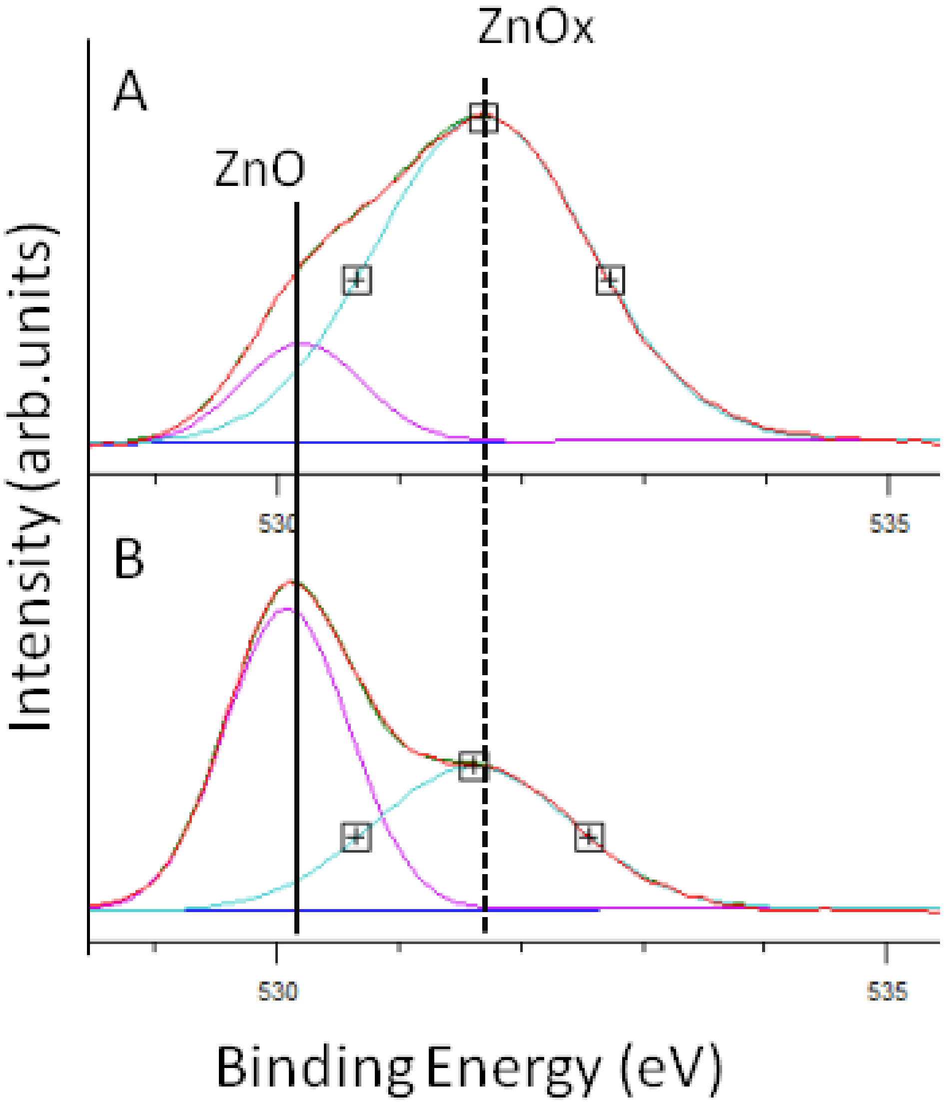

Figure 3.28 High resolution XPS spectra of O 1s core level of A) undoped and B) Mn-doped ZnO nanorods grown at 60℃ on silicon substrate.

The asymmetric O 1s peak of Mn-doped nanorods is shown in Figure 3.28. This peak was fitted by two subspectral components at 530.2 eV and 531.6 eV. The lower energy peak is assigned to O^{2-} ions (O_L) in stoichiometric Zn-O-Zn region. Whereas the higher binding energy peak is attributed to O^{2-} ions (O_H) in an oxygen deficient ZnOx region or to the hydroxyl groups resulting from chemisorbed water [141, 143, 195-197]. Based on the curved fitting results showed in Figure 3.28, the surface O_H percentage decreases to 42 % after Mn^{2+}addition which is the evidence of better oxidized stoichiometric surroundings in doped nanorods and/or less hydroxyl groups attached to the surface. Similar components in O 1s have been observed before [143-145], and based on O 1s/Zn 2p XPS intensity ratios the stoichiometry of ZnOx(OH)y was suggested [143, 146]. In our case this ratio decreased from 3.8 for undoped ZnO to 2.8 for Mn-doped nanorods implying that the overall number of oxygen atoms versus zinc was reduced by Mn^{2+} addition. Thus in our case the smaller O_H peak should be related to the lower number of hydroxyl groups on the surface of our Mn-doped ZnO as compared to undoped ZnO nanorods. The surface chemistry information of Mn-doped ZnO nanorods is summarized in Table 3-5. The oxygen-deficient character of Mn-doped nanorods will be evident in its PL spectra.

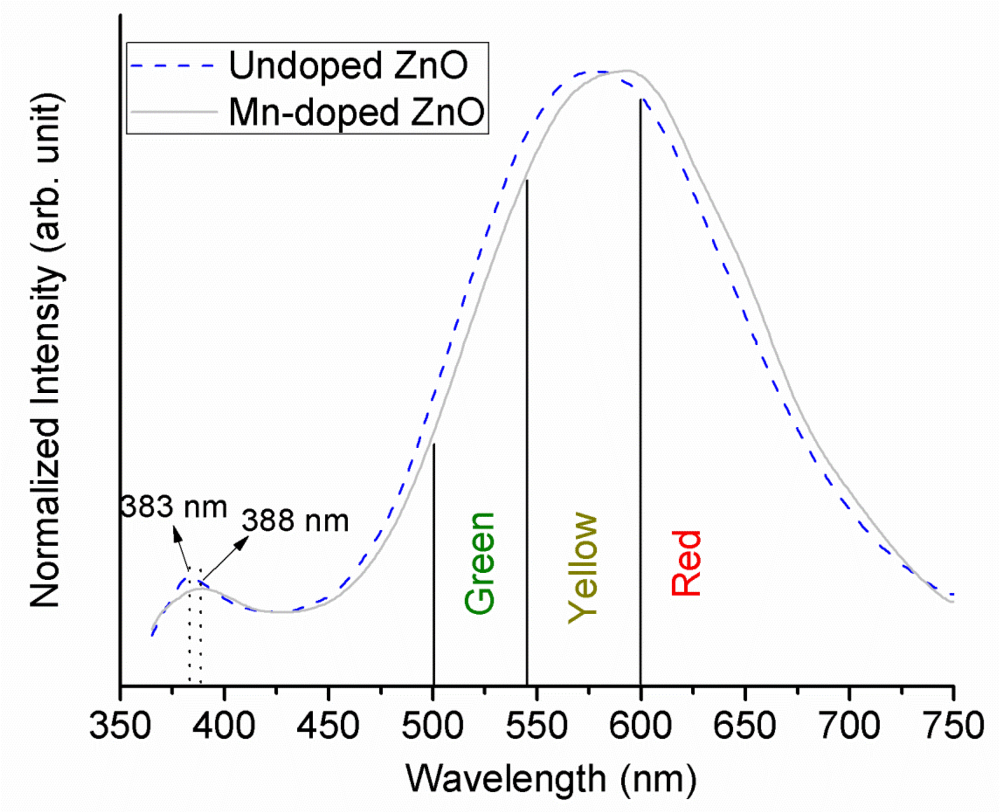

Figure 3.29 Room temperature PL spectra of undoped and Mn-doped ZnO nanorods grown at 60℃ on silicon substrate.

Room temperature PL spectrum of Mn-doped ZnO is shown in Figure 3.29. It reveals one peak in UV region centered at 388 nm. There is also a broad peak in the visible range approximately centered at 587 nm for Mn-doped nanorods. The PL emission data of Mn-doped ZnO nanorods are summarized in Table 3-6. The PL measurements also confirm the dominant wurtzite crystal for our Mn-doped samples are consistent with our previous analysis results. The defect emission of our Mn-doped sample is increased as compared to that of the undoped ZnO, similar to a report by Singh et al.[130]. The increase in defect emission can be connected to the deformation of the band structure due to the lattice expansion in Mn-doped nanorods which was detected in XRD patterns [173]. Defect emission broad band is deconvolved into green, yellow, and red emission corresponding to different types of intrinsic and extrinsic defects centers [121, 122, 147]. A slight change in green emission of our Mn-doped nanorods can be attributed to an increase in the number of singly-charged oxygen vacancies [130, 198, 199]. This attribution is consistent with our micro-Raman spectra analysis. The yellow emission, on the other hand, is attributed to the doubly-charged oxygen vacancies [198] or surface oxygen interstitials [200]. Therefore, the yellow defect emission raise in our Mn-doped nanorods can be related to an increase in number of the mentioned defects points in a way consistent with our XPS results.

The extrinsic source of defects in our Mn-doped nanorods can be related to the formation of Mn compounds such as Zn_2MnO_4 which was detected in our Raman spectrum. An orange band relates to the $^4T_1 \rightarrow {}^6A_1$ transition for Mn^{2+} ions in Mn-doped nanorods, that has been reported before [201]. A red shift of the defect emission broad peak as a function of Mn^{2+} doping was reported by Phan et al. [185]. They claimed that the intrinsic defect emission would be absorbed by extrinsic defects located at lower energy levels and the secondary emission from the extrinsic defects would lead to a red shift, eventually. Based on the discussion above we conclude that in our Mn-doped nanorods there is an enhancement of the visible emission accompanied by a partial red shift due to the larger number of zinc and oxygen surface interstitials/vacancies and/or formation of Mn compounds.

Although the intensity of the NBE peak for our ZnO nanorods has not changed noticeably with the addition of Mn^{2+}, a 5 nm red shift was detected for the NBE peak of the Mn-doped sample. Band gap reduction as a consequence of incorporation of Mn^{2+} into ZnO crystal lattice has been reported before [179, 195]. This shift was attributed to the strong exchange interaction between the “d” orbital electrons of Mn and “s” and “p” orbital electrons of the host band [179, 202]. The other reason might be related to a change in the energy band level of Mn-doped nanorods. According to the XRD data the lattice constant increased as a result of Mn^{2+} incorporation into ZnO lattice. A quench in NBE emission of Mn-doped ZnO nanorods as compared to undoped ZnO was reported before [179, 183, 184, 195] which was not observed in our case showing that our method is an efficient way of Mn^{2+} doping of ZnO. The NBE to defect emission ratio dropped to 5% for Mn-doped nanorods. Crystal quality degradation is attributed to the larger number of defect centers in case of the Mn-doped nanorods which is in consistent with previous reports [183, 184]. The positive role of the defect points in ferromagnetism properties of nanorods has been reported before [198]. Therefore, we predict an improvement in the magnetic properties of our Mn-doped nanorods which would need more analysis in future works.

3.4 Low temperature hydrothermal growth of arrays of Co-doped ZnO nanorods

Co^{2+} is another cation that is highly soluble in ZnO which has large magnetic momentum [176, 203]. A large concentration of Co^{2+} can be doped in ZnO without the formation of a secondary phase, allowing the tuning of its room temperature ferromagnetism behaviour [203, 204]. Thus, Co-doped ZnO is one of the most attractive diluted magnetic semiconductors for spin electronic based devices [205-207]. Furthermore, gas sensing performance and response time of ZnO nanorods were significantly improved by Co^{2+} addition [208-211]. Although the role of dopant in the sensitivity of ZnO is still under debate [210]; this behaviour is likely to be ralated to the release of large numbers of trapped electrons in Co-doped nanocrystal as compared to undoped ZnO. Significant impact of Co^{2+} addition on the visible light photocatalysis character of ZnO nanostructure was reported [80, 212, 213]. This effect was connected to a band gap red-shift and/or increase in oxygen vacancies as a result of Co^{2+} addition. It has been shown that the magnetic, optical and electronic properties of Co-doped ZnO depends on its preparation method and conditions [203, 214, 215]. Synthesis of Co-doped ZnO nanocrystal through various techniques has been reported before [203, 205, 206, 210, 216]. Recently, a microwave-assisted hydrothermal method was used to synthesize randomly oriented Co-doped ZnO nanorods in form of powder [214]. There are also reports of uncontrolled, randomly oriented Co-doped ZnO nanorods synthesized via chemical methods [80, 179, 212, 213, 217-228]. However, for a variety of applications such as solar cells, spintronic devices, or photocatalytic devices vertical standing arrays of ZnO nanorods are desirable [98]. Vertical arrays of Co-doped ZnO nanorods were grown using hydrothermal method before, without optimal device surface coverage and nanorods vertical orientation [209, 210, 229-231]. There are various reports of growth of arrays of Co-doped ZnO nanorods [208, 210, 232-235] similar to what we report here. But, we believe that the uniformity and surface coverage of our Co-doped nanorods is enhanced considering our simple seeding step as compared to previous reports. Moreover, the coverage, alignment and uniformity of Co-doped ZnO nanorods have considerably improved in comparison to the undoped ZnO growth.

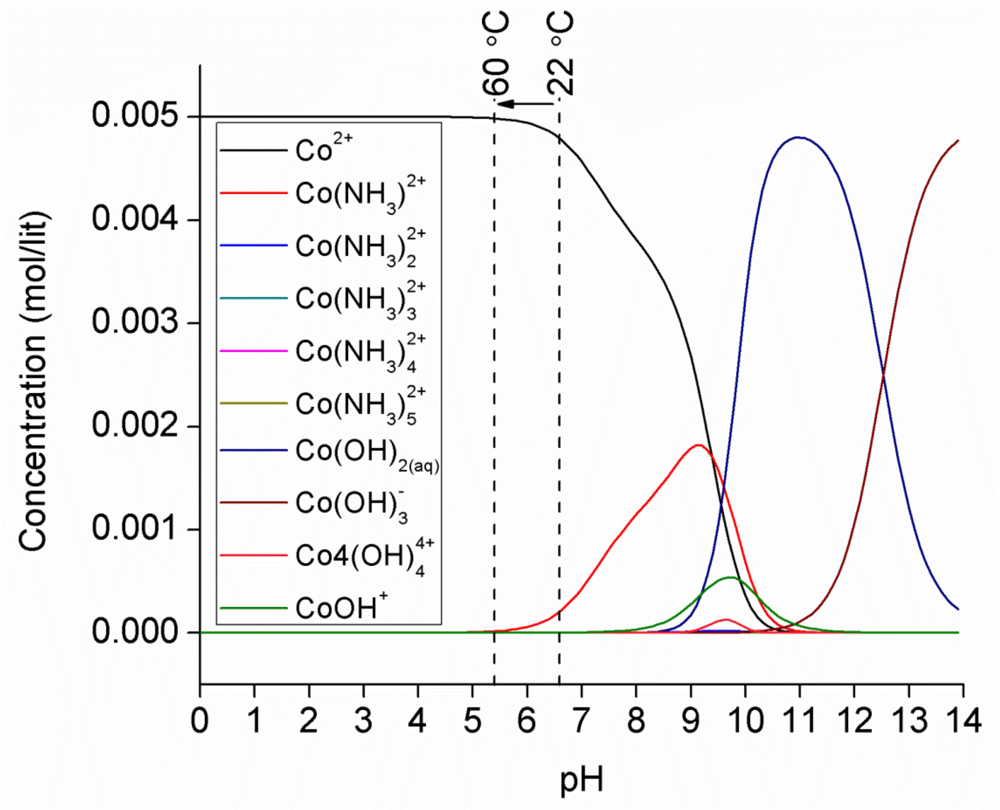

Figure 3.30 Speciation diagrams of Co(II) species at 60 °C as a function of pH ranging from 0 to 14 as computed with Visual MINTEQ software.

The speciation diagram of Co(II) is shown in Figure 3.30. It can be seen that before the growth solution was heated, Co^{2+} and $Co(NH_3)^{2+}$ are the only cationic species which are formed in my growth solution. However, the number of $Co(NH_3)^{2+}$ ions decreases abruptly shortly after the start of the growth. Similar to Mg, Mn and Ni, the broad range of pH in which Co(II) can exist in the form of Co^{2+} implies that even higher concentration of Co (>5mM) can be introduced to the growth solution as the dopant.

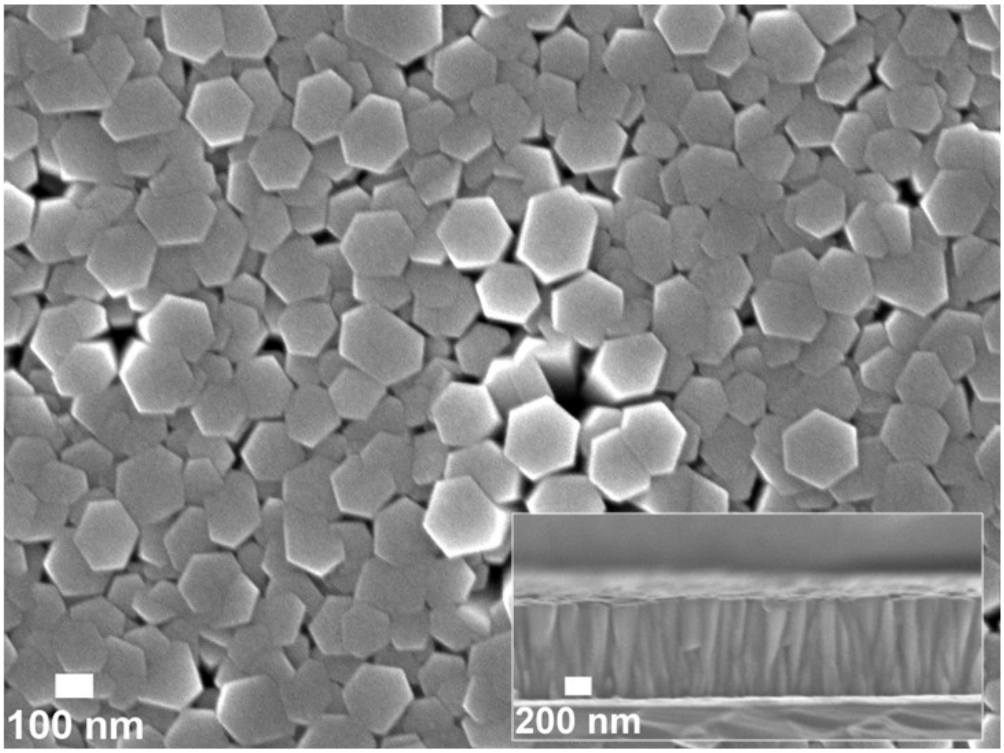

Figure 3.31 SEM images of the top and cross section of Co-doped ZnO nanorods grown at 60℃ on silicon substrate.

The SEM images of the top and cross section of the Co-doped ZnO nanorods are shown in Figure 3.31. It can be seen that the hexagonal shape of ZnO nanorods remained unchanged by Co^{2+} addition. The nanorod surface coverage was enhanced across the substrate and considerably uniform nanorods were obtained as a result of Co^{2+} addition. The average height and diameter increased to 731 nm and 168 nm as a result of Co^{2+} doping. The size information of Co-doped nanorods is summarized in Table 3-2. Our results are in agreement with previous reports where the nanorod diameter increased due to incorporation of Co^{2+} into the ZnO lattice [208, 232-234]. Beside that, the hexagonal shape of Co-doped ZnO becomes more prominent as compared to the undoped ZnO nanorods.

The crystal growth rate of ZnO along its different planes is as follows: [001]>[101]>[100]. The difference in growth rate along different ZnO crystal planes is the main reason of formation of a nanorod shape under appropriate hydrothermal growth conditions. It was suggested that the growth rate of ZnO crystal reduces along [001] plane while it increases along [101] and [100] planes by Co^{2+} addition [232, 233]. The lower growth rate along [001] was attributed to the attachment of Co compounds to this plane during the synthesis process [232]. Therefore, more effective growth along the [101] and [100] planes can be the main reason of larger diameter observed for our Co-doped nanorods as compared to undoped ZnO. The length of our Co-doped nanorods increased, but their aspect ratio reduced to 4.3 as compared to undoped ZnO nanorods aspect ratio (6.5) in consistent with previous reports [233]. One should keep in mind that the Co^{2+} concentration is much smaller than that of the Zn^{2+} cations in the growth solution. Thus, the growth perturbation along the fastest growth plane (002) is temporary and with a long enough growth time vertical growth ensures at normal speeds.

The XRD patterns of both undoped and Co-doped ZnO vertically normalized are shown in Figure 3.32. The XRD patterns indicate the formation of single wurtzite phase with c-axes preferred orientation. However, due to high concentration of Co^{2+} in the growth solution at the beginning, a weak peak (labeled by an asterisk *) at 38 ° was detected. This peak arises due to the formation of Co^{2+} compounds and it is attributed to the (101) crystal plane of $Co(OH)_2$ [227]. According to Fu et al.[228] the solid solubility of Co^{2+} cations in ZnO matrix could be higher for longer hydrothermal growth. This can be the main reason of formation of a Co secondary phase, considering the long (24 h) synthesis time in our case. From Figure 3.32 it can be seen that the intensity of the [100] and [101] planes was reduced and that (002) became the dominant peak in the XRD pattern of Co-doped nanorods. A strong (002) peak in the Co-doped ZnO XRD pattern indicates the dominant presence of perpendicular arrays of ZnO nanorods on the substrate. A small shift (0.11°) of the (002) peak to lower 2Θ angle value for Co-doped nanorods is also detected. This shift can be connected to the larger lattice spacing of Co-doped nanocrystal along the (002) plane as compared to undoped ZnO which is in consistent with some of the previous reports [169, 208, 210]. In contrast, there are many reports which claim a smaller unit cell for ZnO nanocrystal doped by Co^{2+} [211, 236]. Che et al.[219] argued that for small amounts of Co^{2+} (Less than 5 %) the ZnO lattice constant along the (002) plane increases proportionally to Co^{2+} concentration according to Vegard law. However, the lattice parameter did not obey this rule for higher concentration in our case (10%). It has been suggested that Co^{2+} ions could gain radius between 0.65 Å and 0.74 Å depending on their spins which are larger than Zn^{2+} ionic radii (0.60 Å) [237, 238].

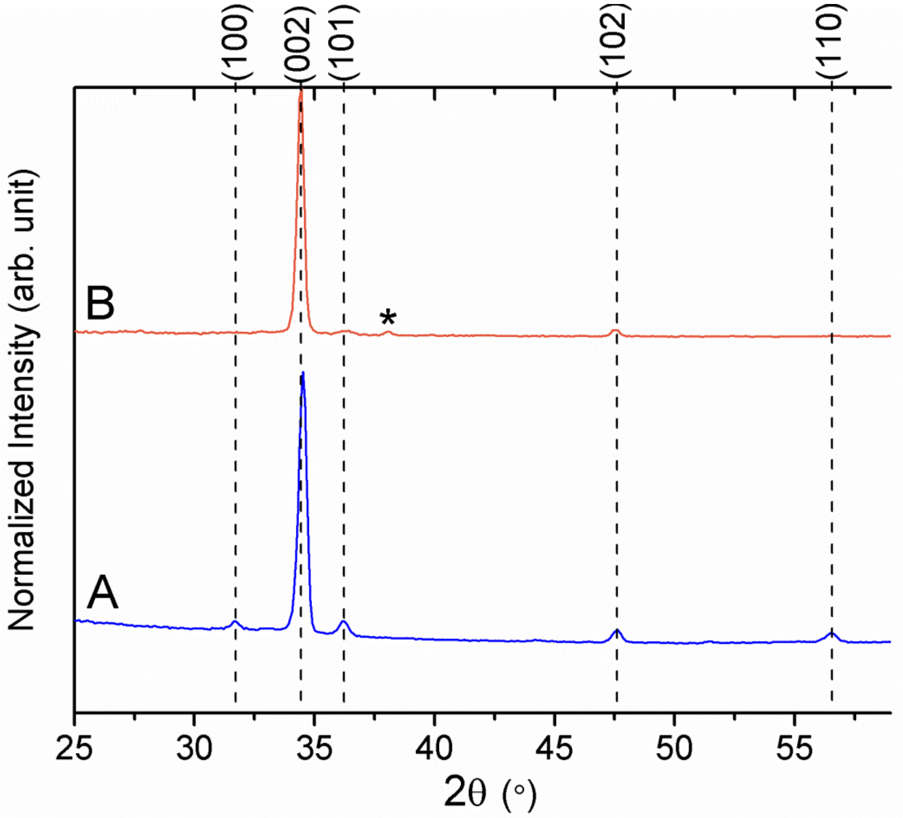

Figure 3.32 XRD patterns of A) undoped and B) Co-doped ZnO nanorods grown at 60℃ on silicon substrate. (Traces were shifted vertically for visibility)

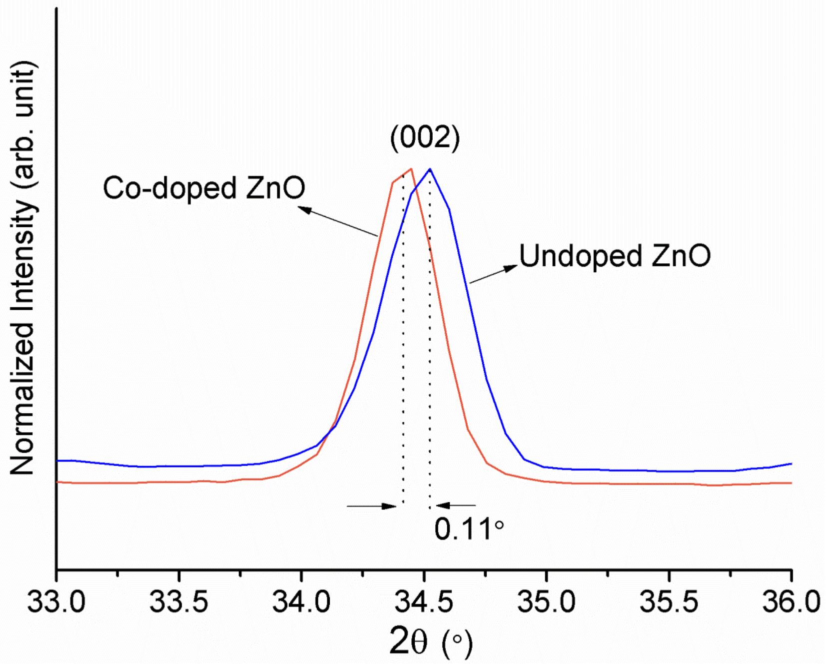

Figure 3.33 High resolution (002) peak position of undoped and Co-doped ZnO grown at 60℃ on silicon substrate.

Therefore, the increase in lattice parameter of our Co-doped nanorods might be due to the incorporation of Co^{2+} ions with octahedral coordination into the ZnO crystal lattice. Due to the comparable ionic radius of Co^{2+} and Zn^{2+} these changes are small. Furthermore, the FWHM of the (002) peak of the Co-doped sample was measured. The results showed a reduction in FWHM of (002) peak of the Co-doped sample as compared to undoped ZnO showing an improvement in crystallinity as a result of Co^{2+} addition. Similar results were reported before [211, 234, 239]. Song et al.[239] suggested that Co^{2+} doping has a stabilization effect on the phase of ZnO in its (002) preferred orientation form at significantly lower growth temperature. By applying the crystallographic data of Figure 3.32 into equation 3-1 the degree of alignment of Co-doped nanorods was calculated. Comparing the calculated results between the degree texture of undoped ZnO (82%) and Co-doped nanorods (94%) shows a significant incline in crystallographic orientation of the Co-doped nanorods. A summary of the crystallographic data of Co-doped nanorods is given in Table 3-3.

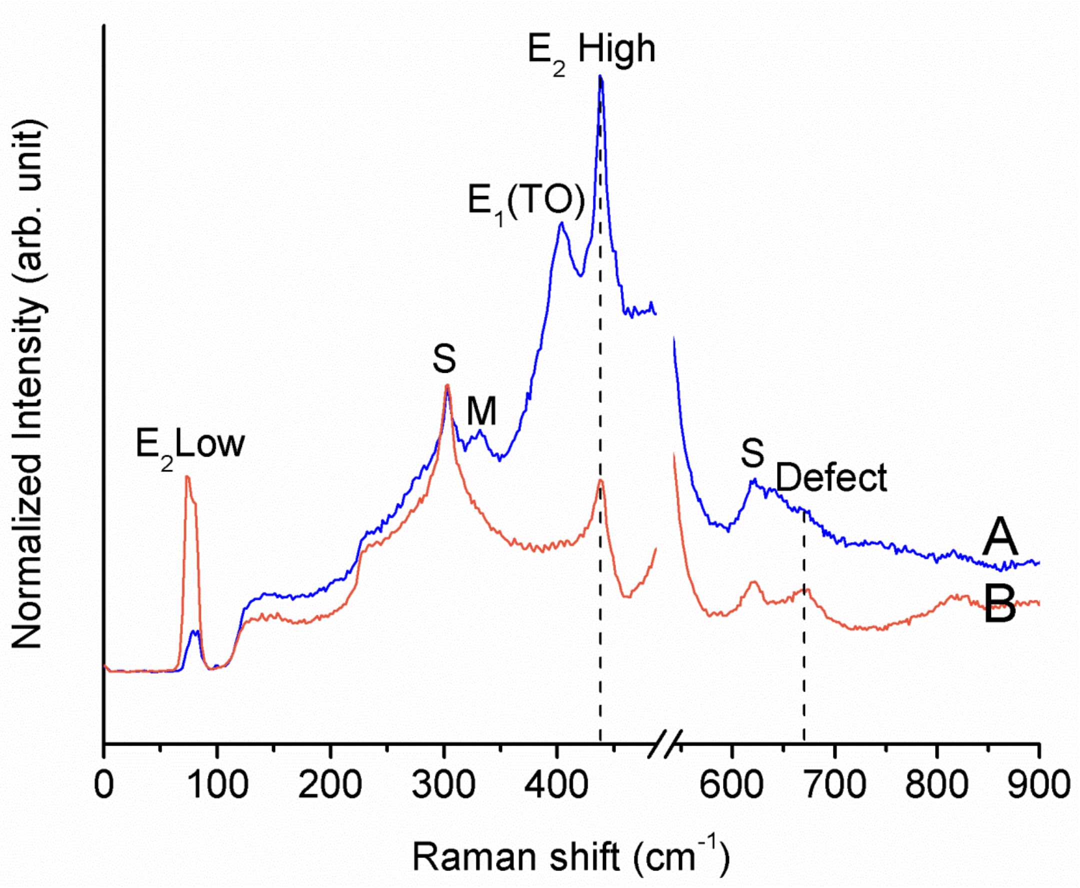

Figure 3.34 Room temperature micro-Raman scattering spectra of A) undoped and B) Co-doped ZnO nanorods grown at 60℃ on silicon substrate. (Traces were shifted vertically for visibility)

Room temperature micro-Raman spectra of undoped and Co-doped ZnO nanorods are shown in Figure 3.34 for better comparison. Apart from the silicon substrate peaks, the two dominant peaks in our Co-doped ZnO correspond to E_2(H) and E_2(L) vibrational modes suggesting an unchanged single wurtzite hexagonal crystal structure as the host lattice. Figure 3.34 shows that, by increasing the diameter of Co-doped nanorods, the M peak disappeared in Raman spectra. In Co-doped ZnO micro-Raman spectra the peaks at 77 cm^{-1} and ~437.9 cm^{-1} are assigned to the E_2(L), and E_2(H) modes, respectively. A summary of Raman active modes of Co-doped nanorods is given in Table 3-4. The E_2(H) peak is evidence of wurtzite crystal orientation in both Co-doped and undoped samples [112], demonstrating that the overall crystal structure of the ZnO nanorods is not affected by the Co^{2+} addition. However, The E_2(H) peak position for Co-doped nanorods has slightly (+0.2 cm^{-1}) shifted to higher energies as compared to undoped ZnO. The E_2(H) peak intensity has also decreased by Co^{2+} addition in comparison to undoped ZnO. Huang et al. [240] ascribed the increase in the E_2 phonon frequency to the compressive stress of the host lattice. Thus, the small shift of E_2(H) peak to higher energies in our case might be related to the induced local stress in the host lattice. The compressive form of the stress also confirms the fact that the radii of Co^{2+} ion dopant which is dissolved in ZnO lattice is larger than Zn^{2+}, consistent with our XRD results. Moreover, it has been argued that missing oxygen mass at oxygen vacancy sites can blue shift the frequency of the E_2(H) mode [85, 188]. We explain this fact by suggesting that oxygen atoms have smaller share, in Co-doped wurtzite crystal lattice than before due to the incorporation of Co^{2+} ions into the host crystal lattice. As previously shown, XRD patterns showed the formation of a secondary phase of Co compound. Wang et al. [223] suggested the existence of Zn-Co-O compounds in ZnO crystal as a result of Co^{2+} addition. The appearance of an extra peak at ~672 cm^{-1} in our Co-doped ZnO Raman spectra can be also related to the vibrational mode of this phase. Yang et al.[172] have attributed this peak to additional impurities (dopants) in ZnO crystal. This peak became more distinct for our Co-doped sample, suggesting substitution of Zn^{2+} by Co^{2+} ions in Co-doped nanorods. Strong exchange interaction between substituted Co^{2+} and oxygen can result in a solid bond between them across the lattice [230]. Considering the shorter Co-O bond length, we believe that oxygen will be physically more confined and its common arms with Zn^{2+} ions are more stretched in our Co-doped ZnO nanocrystal. Therefore, the oxygen atoms showed less vibration in the host lattice, whereas Zn^{2+} ions have more vibration freedom in our Co-doped ZnO crystal lattice than before. This can also be the main reason for the higher intensity of E_2(L) peak in our Co-doped nanorods as compared to undoped ZnO. As has been reported before, this peak represents the vibration of the Zn sublattice in Raman spectra [130, 189]. Thus, the E_2(L) peak behaviour can be significantly affected by substitution of Zn^{2+} ions with cation dopant [85]. This substitution breaks lattice translational symmetry which eventually causes broadening in the allowed Raman peaks [185]. The asymmetric broadening of E_2(H) peak can be explained in the similar manner. The intensity of E_1(TO) suppressed abruptly in Co-doped sample. This could occur in favour of single crystal orientation of Co-doped ZnO nanorods, where the E_2(L) and E_2(H) become the two dominant peaks as the representatives of ZnO wurtzite crystal structure. The crystal induced stress is consistent with our XRD results in a comparison between undoped and Co-doped ZnO.

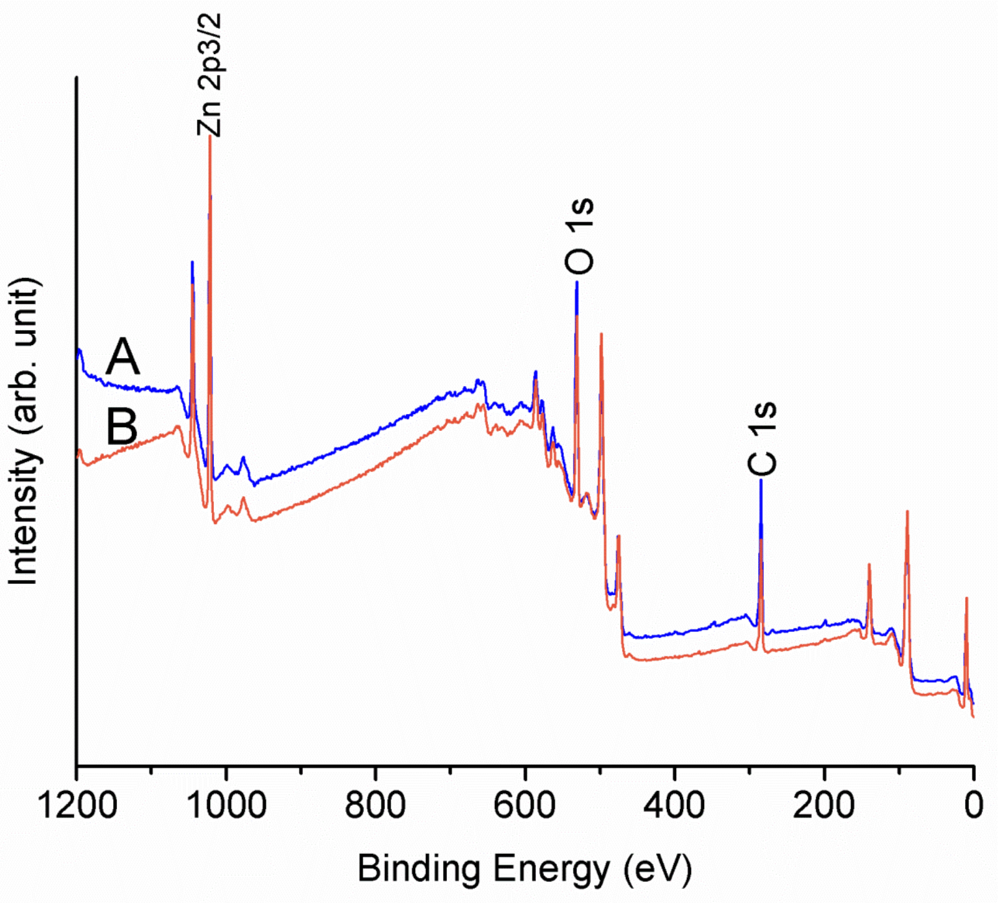

Figure 3.35 XPS spectra of A) undoped and B) Co-doped ZnO nanorods grown at 60℃ on silicon substrate. (Traces were shifted vertically for visibility)

The XPS spectrum of the Co-doped ZnO nanorods is shown in Figure 3.35 as well as the undoped ZnO for better comparison. There is a good agreement between XPS spectra of Co-doped and undoped ZnO nanorods. An attempt to detect Co^{2+} in the doped nanorods using XPS was not successful due to the low concentration or non-homogeneous incorporation of Co^{2+} cations in the ZnO crystal. A low concentration of Co^{2+} cations can be detected in the EDS spectrum shown in Figure 3.36. The EDS results show that the Co^{2+} content of our sample is 0.4 atomic% on average.

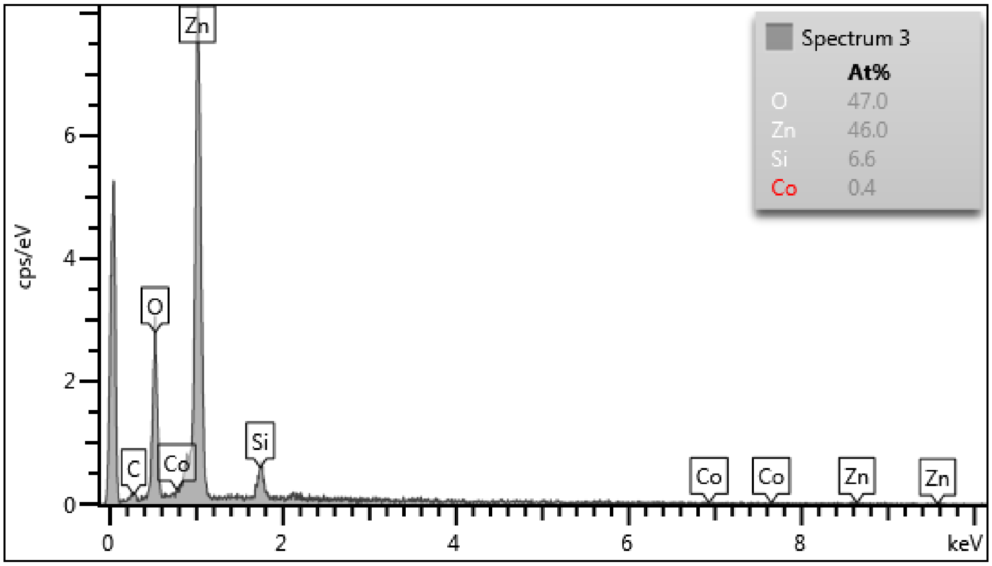

Figure 3.36 EDS elemental microanalysis of Co-doped ZnO grown at 60℃ on silicon substrate.

The chemical mechanism of Co-doped ZnO deposition during the hydrothermal growth has been reported many times before [232, 234]. Accordingly, $Zn(OH)_2$ and $Co(OH)_2$ are the main two compounds which are the building blocks of Co-doped ZnO nanostructures. It was suggested that the ZnO and $Zn(OH)_2$ are more readily formed than $Co(OH)_2$ under similar hydrothermal conditions. This can be the main reason for small amount of incorporated Co^{2+} into ZnO crystal, since most of the Co^{2+} cations will remain in the solution. The other reason of unsuccessful detection of Co^{2+} ions in XPS spectra might be related to the inhomogeneous distribution of Co^{2+} atoms in ZnO crystal lattice, in a way that no significant dopant atoms incorporated to the top of the nanorods. Since XPS only observes the top surface of the sample. This can also justify the detection of Co compounds with the XRD, based on its high penetration depth.

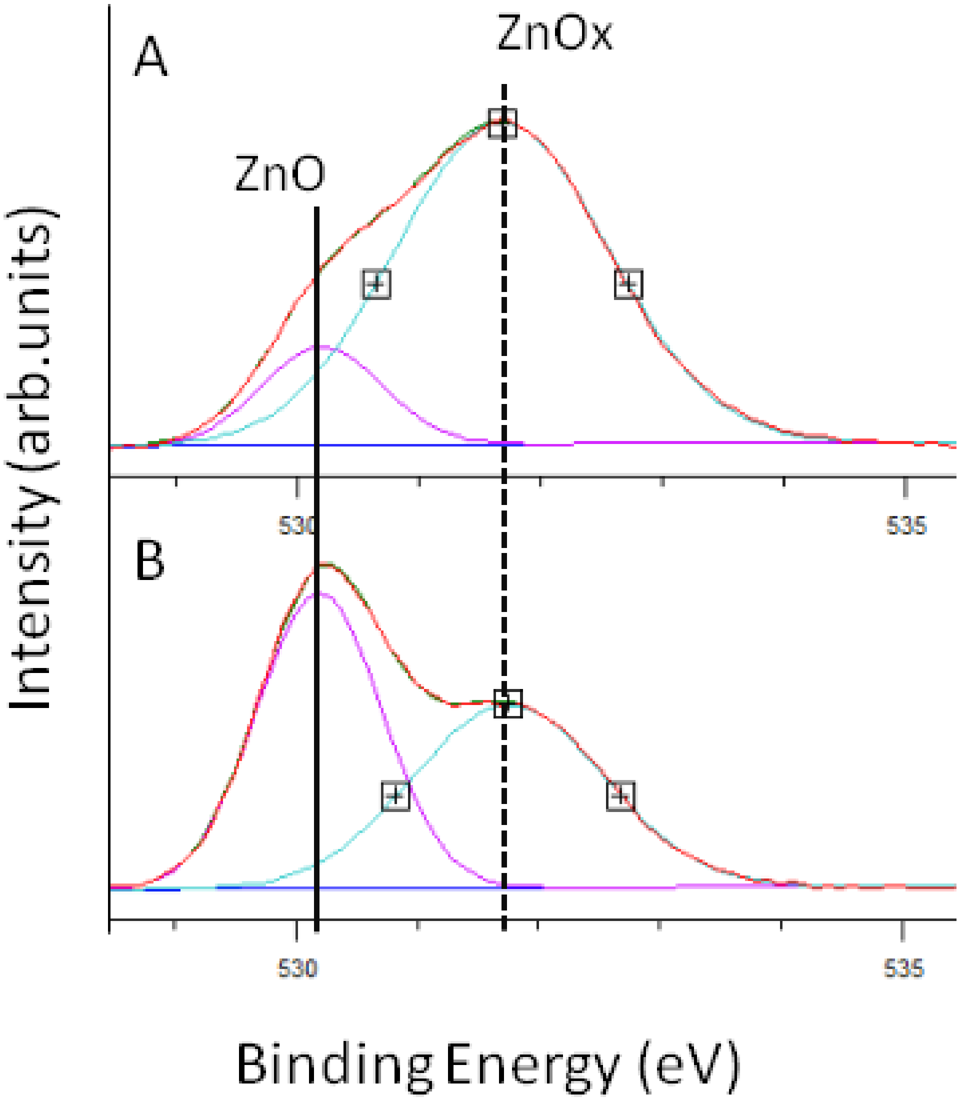

Figure 3.37 High resolution XPS spectra of O 1s core level of A) undoped and B) Co-doped ZnO nanorods grown at 60℃ on silicon substrate.

More precise measurements show an energy shift for the Zn 2p 3/2 peak as large as -0.3 eV as a result of Co^{2+} doping. The FWHM of the Zn 2p peak was also found to be smaller for the Co-doped sample (1.76 eV) as compared to the undoped ZnO (1.85 eV). This narrowing suggests the presence of less Zn states defects within Co-doped ZnO structure.

The asymmetric O 1s peak (Figure 3.37) of Co-doped ZnO was decomposed into two subspectral peaks. The first peak centered at ~530.2 eV can be assigned to O^{2-} ions (O_L) in stoichiometric Zn^{2+} and Co^{2+} ions with their full complement of nearest-neighbor O^{2-} ions [80]. The second peak centered at ~531.8 eV can be associated to O^{-2} ions (O_H) in an oxygen deficient ZnOx region and/or hydroxyl groups similar to what has been reported before [80, 141, 211]. Based on curved fitting results shown in Figure 3.37 the intensity of O_H decreases to 48% which is a sign of smaller concentration of hydroxyl groups resulting from the chemisorbed water [80, 143, 179]. The O 1s/Zn 2p ratio slightly decreased from 3.8 for undoped ZnO to 3.1 for Co-doped nanorods which shows a lower number of oxygen atoms in the Co-doped ZnO nanorods. The oxygen deficient structure of Co-doped ZnO sample will exhibit itself later as a wide visible emission peak in PL spectra. The surface chemistry information of Co-doped ZnO nanorods is summarized in Table 3-5.

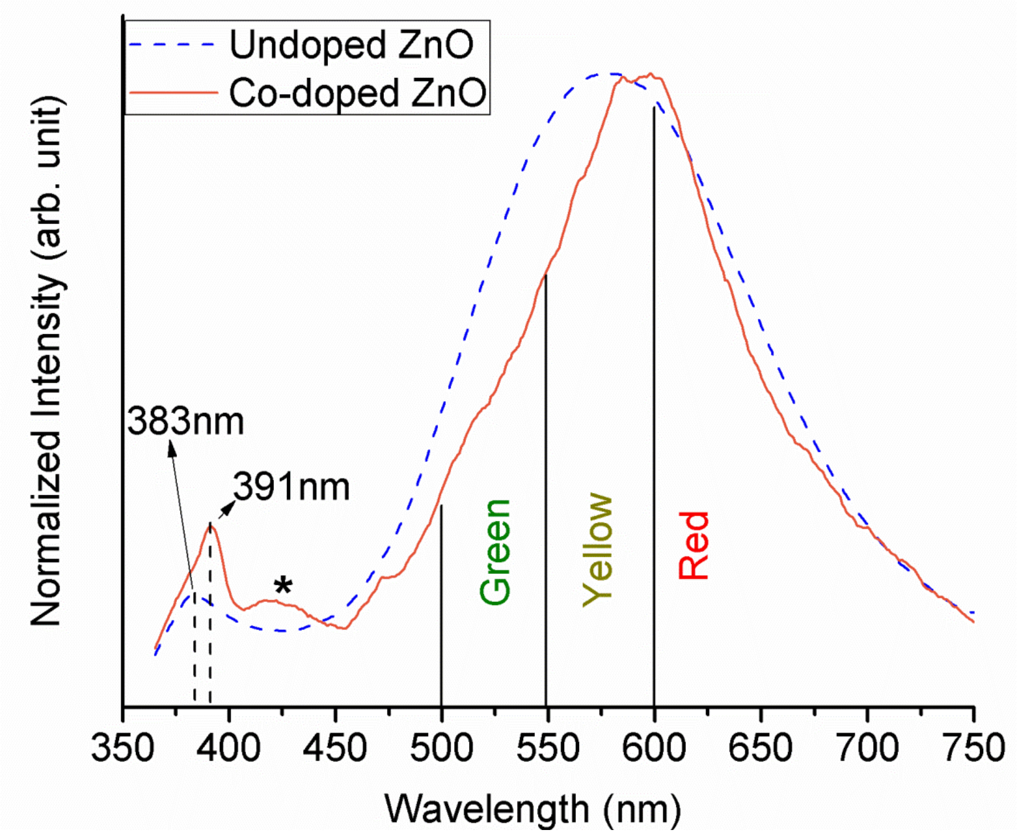

Figure 3.38 Room temperature PL spectra of undoped and Co-doped ZnO nanorods grown at 60℃ on silicon substrate.

Room temperature PL spectra recorded for Co-doped nanorods is shown in Figure 3.38. A narrow peak in UV region centered at 391 nm was measured for Co-doped nanorods. There is also a broad peak at visible range centered at 591 nm for Co-doped nanorods. The PL emission data of Co-doped ZnO nanorods is summarized in Table 3-6. The PL measurement also confirms the dominant wurtzite crystal structure for our Co-doped samples in accord with our previous analysis results. A small shoulder (labeled by an asterisk) detected in Co-doped PL spectra might be due to the transition of electrons from Zn interstitials to valence band [212, 225] implying larger number of these defects in our Co-doped nanorods. The defect emission of our Co-doped sample in the region of 550 to 750 nm has increased as compared to the undoped ZnO in consistent with previous study [208]. This increase can be connected to the deformation of the band structure due to the lattice distortion which was detected in our XRD patterns [173]. It has been also argued that increasing the rod diameter may lead to more defect emission [241]. This prediction is in consistent to our SEM images which show larger diameters for our Co-doped nanorods.

As it can be seen in Figure 3.38, the PL emission in the green region reduced after Co^{2+} addition which implies lower level of oxygen vacancies/interstitials in our Co^{2+} doped sample [212]. Therefore, we believe that the higher defect emission of our Co-doped nanorods is not connected to the formation of oxygen traps in the host crystal lattice, in contrast to some previous reports [208, 242], unless we attribute the oxygen defect emission to the yellow region based on the previous studies [208]. This is also in contrast to our XPS results indicating almost the same oxygen/zinc ratio and less OH groups for the Co-doped nanorods. The defect emission increased in the yellow-orange as well as in the red region. Red emission is attributed to the zinc vacancies [122] or Co^{2+} ions in ZnO crystal lattice [225]. Therefore, visible emission enhancement and its red shift in our Co-doped PL spectra can be related to the zinc vacancies/interstitials, and Co doping which is consistent with our micro-Raman and XPS results.

The intensity of the NBE emission has increased considerably as a result of Co^{2+} doping. Stronger UV emission in Co-doped samples can be related to the smaller amount of chemisorbed water, which is in accordance with the weaker O_H peak in its XPS spectra. Furthermore, our XPS results show that the surface oxygen vacancies are suppressed for the Co-doped sample, although the overall number of oxygens has been slightly reduced. A lower number of surface defects might be another reason for higher exciton emission, based on a report by Gao et al.[243]. The lower FWHM of the (002) plane in the XRD pattern of Co-doped sample as compared to undoped ZnO nanorods is evidence of better crystallinity of our Co-doped sample which can also result in a sharper UV emission peak.

The UV emission peak has shifted towards higher wavelength as much as 8 nm. The UV emission peak red shift as a result of Co^{2+} addition has been reported many times before [179, 234, 244]. This shift is attributed to the strong exchange interaction between the “d” orbital electrons of the dopant and “s” and “p” orbitals electron of the host band [179]. The NBE to defect emission ratio was decreased from 6.18 % for undoped nanorods to 4.6 % for Co-doped samples. The mentioned crystal degradation occured in our Co-doped nanorods due to the introduction of more defect centers [208].

3.5 Low temperature hydrothermal growth of arrays of Cu-doped ZnO nanorods

Large amounts of Cu^{2+} can be incorporated into ZnO crystal on the grounds of the high ionization energy and the low formation energy of group IB elements [245]. Moreover, similar to most group II-IV materials, bonding in ZnO is largely ionic which favors doping with Cu^{2+} [144]. Therefore, Cu^{2+} can be considered as a good p-type doping candidate for ZnO with many important applications. Cu^{2+} can also be used as an impurity for ZnO band gap tuning. Theoretical studies suggested that Cu^{2+} dopants could narrow the host lattice band gap by forming a single-acceptor state above the ZnO valence band [246]. Moreover, theoretical calculations show that group IB elements such as Cu^{2+} prefer to occupy substitutional sites rather than interstitials due to the lower formation energy [246]. Although these studies predict a reduced formation of natural donor defect under oxygen abundant conditions, experimental results conveyed an enhanced green emission for Cu-doped ZnO [94]. Shrinkage of the band gap and creation of additional defects in the ZnO crystal lattice due to Cu doping may increase its optical absorption and hence enhance its photocatalytic properties [247, 248]. Defect-controlled photosensitive Cu-doped ZnO nanorods applicable for UV photodetectors were reported by Sarkar and Basak [249]. The effect of doping concentration on optical, piezoelectric, ferroelectric-like and charge storage properties of Cu-doped ZnO has been reported previously [4, 250]. The other interesting characteristics of Cu-doped ZnO can be its room temperature ferromagnetisation [251, 252]. Huang et al.[253] suggested Cu^{2+} doping as an effective way of gaining a bright and stable structured green luminescence with high internal quantum efficiency from ZnO nanorods. Cu-doped ZnO nanowire-based LED structures with tunable electroluminescence emission at room temperature, grown with an electrochemical deposition technique have been reported before [245]. There are also reports of H_2 gas sensitivity enhancement in Cu-doped ZnO as compared to undoped ZnO [144]. The sensitivity improvement was attributed to a reduction of the conductivity as Cu acts as an acceptor level in the host lattice.

So far Cu-doped ZnO has been synthesised by various techniques; but solution-based low temperature methods are often more preferable [4]. The other advantage of aqueous growth can be related to the formation of hydrogen bonds to the surface of ZnO nanorods. Incorporation of hydrogen into ZnO lattice plays an important role in its ferromagnetism properties [254].

Hydrogen in fact can be more easily inserted in ZnO crystal in an aqueous ambient. Hydrothermal growth of arrays of Cu-doped ZnO nanorods has been reported before [94, 247-250, 252, 254-259]. In this section, various properties of Cu-doped ZnO nanorods are discussed. Although the nanorods coverage was hindered due to the Cu^{2+} doping, the PL emission has been considerably improved in terms of the UV emission in comparison to previous reports.

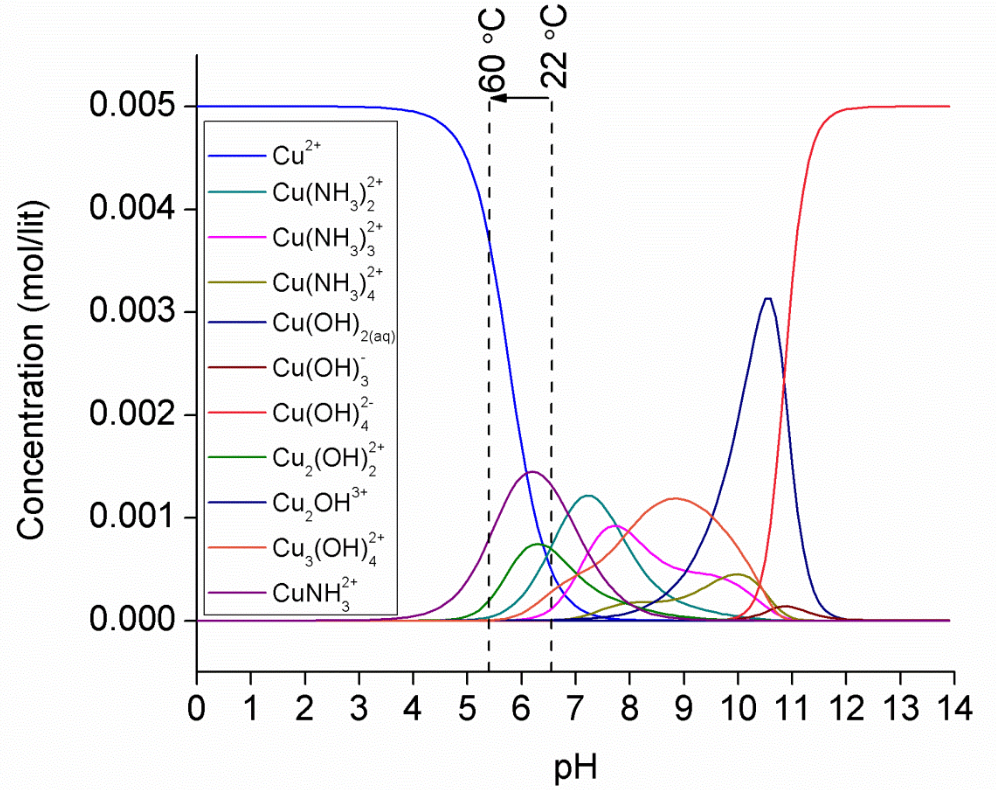

Figure 3.39 Speciation diagrams of Cu(II) species at 60 °C as a function of pH ranging from 0 to 14 as computed with Visual MINTEQ software.

The speciation diagram of Cu(II) is shown in Figure 3.39. It can be seen that before the start of the growth, the cationic species which are formed are Cu^{2+} and $Cu(NH_3)_2^{2+}$, $Cu(OH)_3^-$, $Cu_2(OH)_2^{2+}$, and $Cu_3(OH)_4^{2+}$. The number of $Cu(NH_3)_5^{2+}$, $Cu_2(OH)_2^{2+}$, $Cu_3(OH)_4^{2+}$ ions decreases at the early stage of the growth. Whereas, the number of Cu^{2+} , $Cu_2(OH)_2^{2+}$, and $Cu(NH_3)_2^{2+}$ increases as the pH reduced from 6.5 to 5.5. Therefore, in case of Cu doping, Cu^{2+} and Zn^{2+} are not the only cations in the growth solution. The speciation diagram shows the formation of considerable number of $Cu(NH_3)_2^{2+}$ and $Cu_2(OH)_2^{2+}$ ions in the pH range at the early stage of the growth. Thus the decomposition of HMTA is not the only decisive factor in controlling of the number of hydroxide compounds in the growth solution. We believe that the adsorption of Cu compounds to the polar surface of ZnO hexagonal hinders the nanorods c-axis growth. Therefore, nanorods grow more effectively along the side with presence of Cu^{2+} dopant, and as a result thicker nanorods can be obtained.

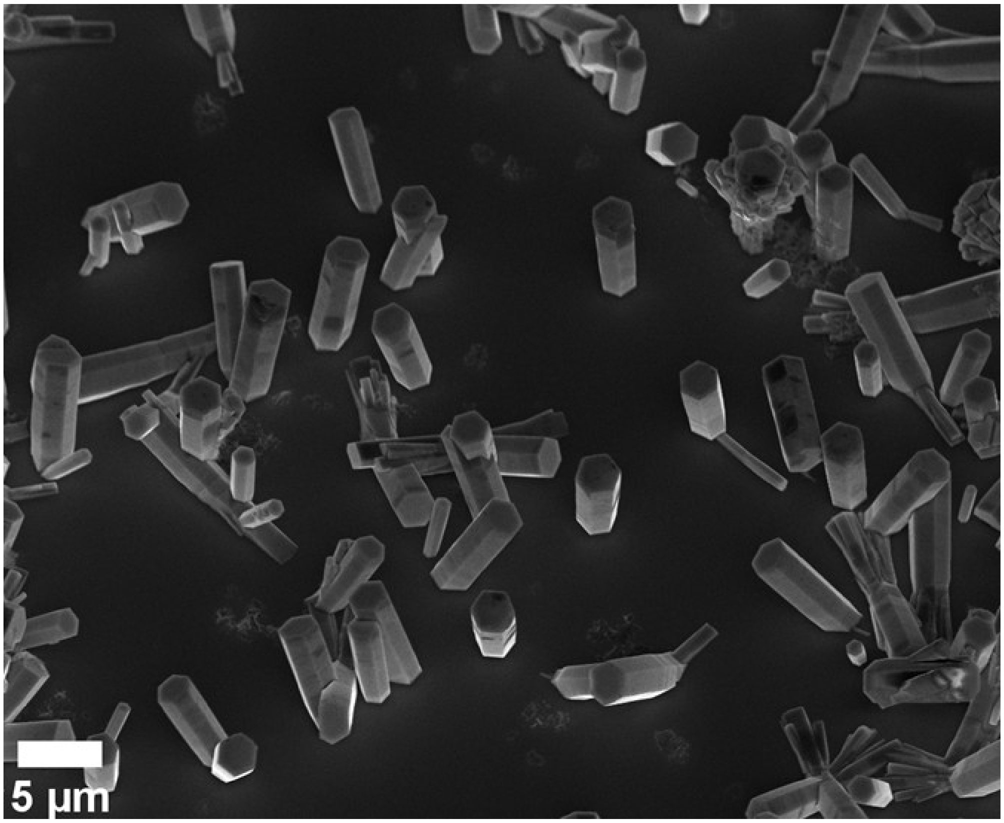

Figure 3.40 SEM images of the Cu-doped ZnO nanorods grown at 60℃ on silicon substrate.

A SEM image of Cu-doped ZnO nanorods is shown in Figure 3.40. It can be seen that the hexagonal shape of ZnO nanorods remained unchanged by Cu^{2+} addition, with their average height increased to 4.7 µm and their average diameter increased to 1.9 µm. The size information of Cu-doped nanorods is summarized in Table 3-2. Our result is in agreement with previous reports where the nanorods were enlarged due to the incorporation of Cu^{2+} into ZnO lattice [250, 259-261]. The size enhancement might be due to the lattice distortion which has been attributed to the unpaired hole in Cu atomic d-shell [260]. Experimental results showed that the ZnO nanorod growth rate increases by the addition of Cu^{2+} ions [250]. The aspect ratio of nanorods decreased from 6.5 to 2.7 for Cu-doped ZnO similar to previous report [252]. The aspect ratio reduction can be related to the face-selective electrostatic adsorption of Cu^{2+} ions [261]. The localization of Cu compounds at the surface of (001) plane can reduce the access of Zn^{2+} active ions to this plane and as a result hinder the nanorod growth along the c-axis direction. However, due to the small amount of dopant precursors the growth hindrance along the c-axis is temporary and long growth times result in tall nanorods.

According to the SEM image shown in Figure 3.40, the number density of Cu-doped nanorods across the substrate reduced in comparison to the undoped ZnO nanorod growth. Similar growth disruption in Cu-doped ZnO nanorods grown by hydrothermal methods has been reported before [249, 259, 260, 262]. A small amount of Cu^{2+} ions in the growth solution can strongly inhibit the nucleation of ZnO nanorods at the early stage of the growth. $Zn(OH)_2$ and $Cu(OH)_2$ are two of the reaction products in the hydrothermal growth of Cu-doped ZnO nanorods [256, 257]. The concentration of $Cu(OH)_2$ and its solvability are less than the Zn compound during the hydrothermal growth. Therefore, $Cu(OH)_2$ is much more stable than $Zn(OH)_2$ in similar hydrothermal conditions. This particular situation allows competition for nucleation between Zn and Cu compounds at the adsorption sites on the seed layer surface [256]. Since, Cu^{2+} compounds cannot act as a nucleation site for further ZnO nanorods growth due to the surface energy state [257], This hinders the adsorption of Zn^{2+} complexes at the seed layer and eventually reduces the number density of ZnO nanorods on the substrate.

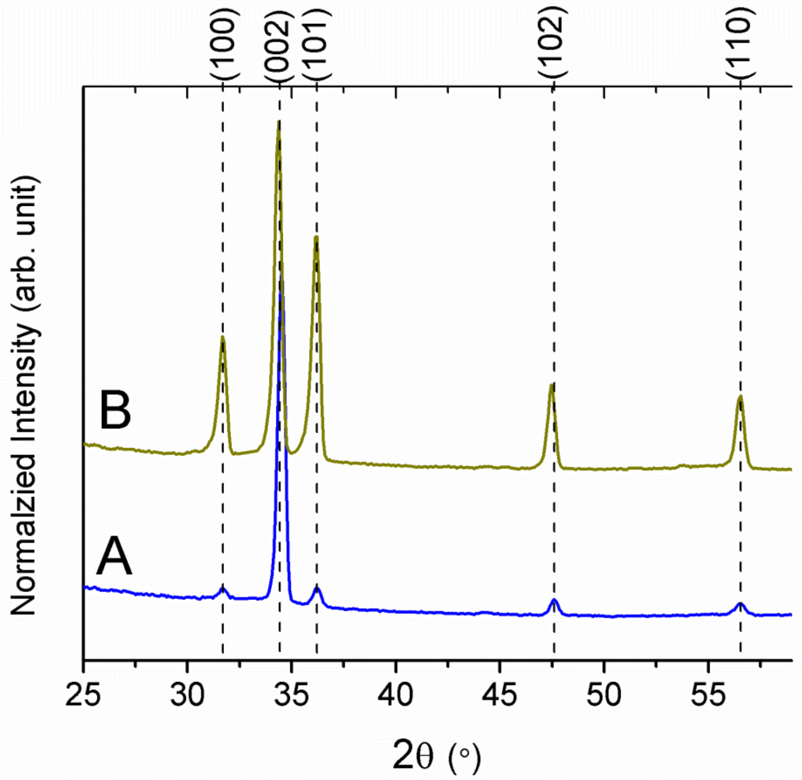

Figure 3.41 XRD patterns of A) undoped and B) Cu-doped ZnO nanorods grown at 60℃ on silicon substrate. (Traces were shifted vertically for visibility)

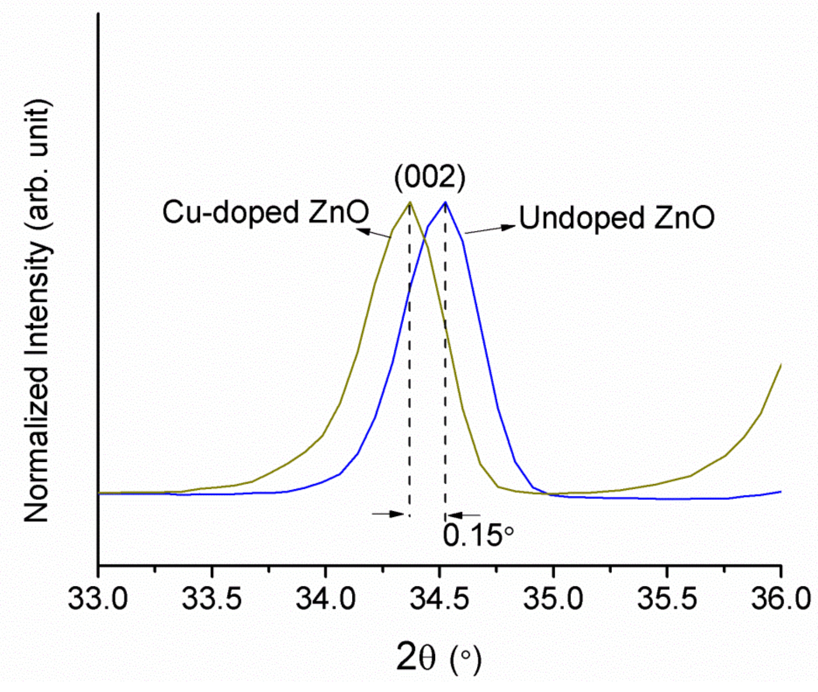

Figure 3.42 High resolution (002) peak position of undoped and Cu-doped ZnO grown at 60℃ on silicon substrate.

The Crystal phase of Cu-doped nanorods was investigated by XRD and the result is shown in Figure 3.42. The peaks for the Cu-doped samples are assigned to a hexagonal wurtzite ZnO crystal structure. No other peaks corresponding to Cu^{2+} and its related secondary phases were detected in the Cu-doped ZnO XRD pattern. Therefore, no agglomeration of Cu occurred in our synthesis, and all the incorporated Cu^{2+} was dissolved in the ZnO wurtzite crystal lattice. The most intense peak in the XRD pattern is indexed to the (002) plane suggesting that the Cu-doped nanorods grow mainly along the (001) plane which is consistent with our SEM images. The crystallinity along the (001) plane has remained almost the same for our Cu-doped nanorods in contrast to some of the reports where the (002) peak intensity was reduced by increasing the Cu^{2+} concentration [144, 259]. The FWHM of (002) peak of our Cu-doped ZnO has slightly increased suggesting a negligible extra crystal disorder as compared to undoped ZnO. As can be seen in Figure 3.42, the peak intensities corresponding to all other crystal planes increased for Cu-doped nanorods. This is in agreement with analysis of SEM images, suggesting that incorporating Cu^{2+} into the solution improves growth rates along crystal planes other than (001) which is naturally the fastest growth plane. As it has been mentioned before, Cu compounds may attach to the (001) plane and reduce access of the Zn^{2+} ions to it. Therefore, the growth can proceed more effectively along the (100) and (101) planes. This will result in thicker nanorods since the (100) plane is assigned to the ZnO nanorod’s sides.

A small shift (0.15 °) of the (002) peak to a lower 2Θ angle value for Cu-doped nanorods can be detected. This shift is attributed to the nonuniform substitution of Cu^{2+} ions into the Zn^{2+} sites [263]. Subsequently, larger lattice constant along the c-axis, as well as larger crystal plane spacing along the (002) plane calculated for Cu-doped sample was based on XRD data. This is consistent with previous reports about the substitution of Zn^{2+} by Cu^{2+} dopant at low temperature [78, 250, 259, 263]. A summary of the crystallographic data of Cu-doped nanorods is given in Table 3-3. The slight difference in lattice parameters of Cu-doped ZnO was attributed to the formation of complex defect compounds [144]. The lattice constant enlargement might be due to the Cu^{+} (0.96 A) larger ionic radii in comparison to Zn^{2+} (0.74 A) in tetrahedral coordination. On the other hand, substitution of Zn with smaller Cu^{2+} (ionic radii 0.57 A) makes the mentioned shift unusual. This unexpected shift is attributed to the lattice distortion caused by the stress during the preparation [263]. This assumption is in accordance with the broadening of the (001) plane as well as its shift for the Cu-doped nanorods which is a sign of minor strain in its crystal lattice. Due to the comparable ionic radius of Cu and Zn the lattice parameter changes are small. By applying the crystallographic data of Figure 3.42 into equation 3-1 the degree of alignment of Cu-doped nanorods was calculated. Comparing the calculated results to those of undoped ZnO (82%) shows that the degree of texture of the Cu-doped nanorods dropped to 48%.

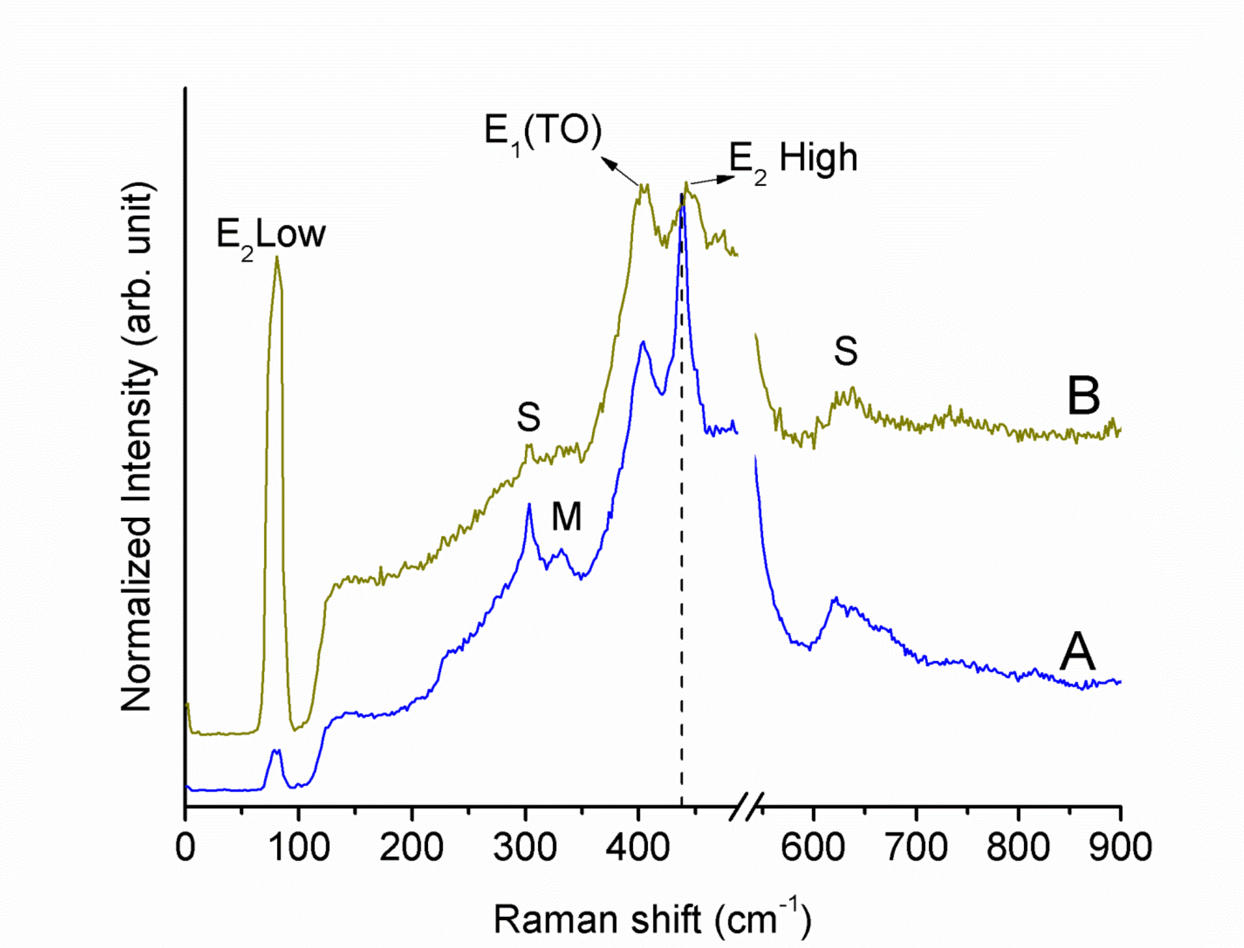

Figure 3.43 Room temperature micro-Raman scattering spectra of A) undoped and B) Cu-doped ZnO nanorods grown at 60℃ on silicon substrate. (Traces were shifted vertically for visibility)

Figure 3.43 shows the Raman spectra of undoped and Cu-doped ZnO nanorods. As it was discussed before, the lower E_2(H) peak intensity should be the main reason for the disappearance of the M peak in Cu-doped Raman spectra. The peaks at 78.8 cm^{-1}, 404 cm^{-1} and ~441.6 cm^{-1} are assigned to the E_2(L), E_1(TO) and E_2(H) modes, respectively. A summary of Raman active modes of Cu-doped nanorods is given in Table 3-4 for comparison.

Although the E_2(H) peak was detected in Cu-doped Raman spectra, its intensity was reduced demonstrating that the quality of wurtzite ZnO crystal is affected by the Cu-doping process. This reduction can be due to the high Cu^{2+} content in our ZnO nanorods which will be further determined by XPS analysis. The diminishing of the $E_2(H)$ peak due to the Cu^{2+} doping has been reported before [144, 253, 264] and it has been attributed to the weakening or perturbation of host wurtzite crystal structure [253, 265]. In addition, based on the size of the dopant atom and its electronic structure, the behavior of the $E_2(H)$ peak slightly changes. The $E_2(H)$ peak position for Cu-doped nanorods has shifted (+3.9 Cm^{-1}) to higher energies as compared to undoped ZnO. The broadening, shift, and asymmetry of the $E_2(H)$ and $E_2(L)$ peaks can be explained by a spatial correlation model [65, 185]. According to isotopic mass dependence of the frequency shift measurements, the $E_2(H)$ mode in ZnO films appears mainly because of the vibration of the oxygen atoms [186, 187]. Kumar et al.[266] attributed the red shift of $E_2(H)$ peak to the higher number of oxygen vacancies. Therefore, the blue shift of our $E_2(H)$ peak should be related to less oxygen-deficient lattice in comparison to undoped ZnO. The number ratio of O/Zn atoms was measured by XPS and the results are given in Table 3-5.

The intensity of $E_2(L)$ was increased by Cu^{2+} addition. This peak represents the vibration of the Zn sublattice in Raman spectra [130, 189]. Thus, the $E_2(L)$ peak behaviour can be significantly affected by substitution of the Zn^{2+} ions by cation dopant [85]. This substitution breaks the lattice translational symmetry which eventually causes broadening in the allowed Raman peaks [185]. The asymmetric broadening of $E_2(H)$ peak can be explained in a similar manner. Moreover, the magnetic behaviour of the doped sample can be altered due to the original lattice deformation. The intensity of $E_1(TO)$ is comparable to $E_2(H)$, suggesting that the crystal quality of nanorods has degraded by Cu^{2+} doping. This fact is consistent with our XRD results where the (002) peak is broadened in Cu-doped XRD pattern, implying the same degradation. There is no vibrational mode in the spectra belonging to any secondary phase in the Cu-doped sample, in accordance with our XRD results.

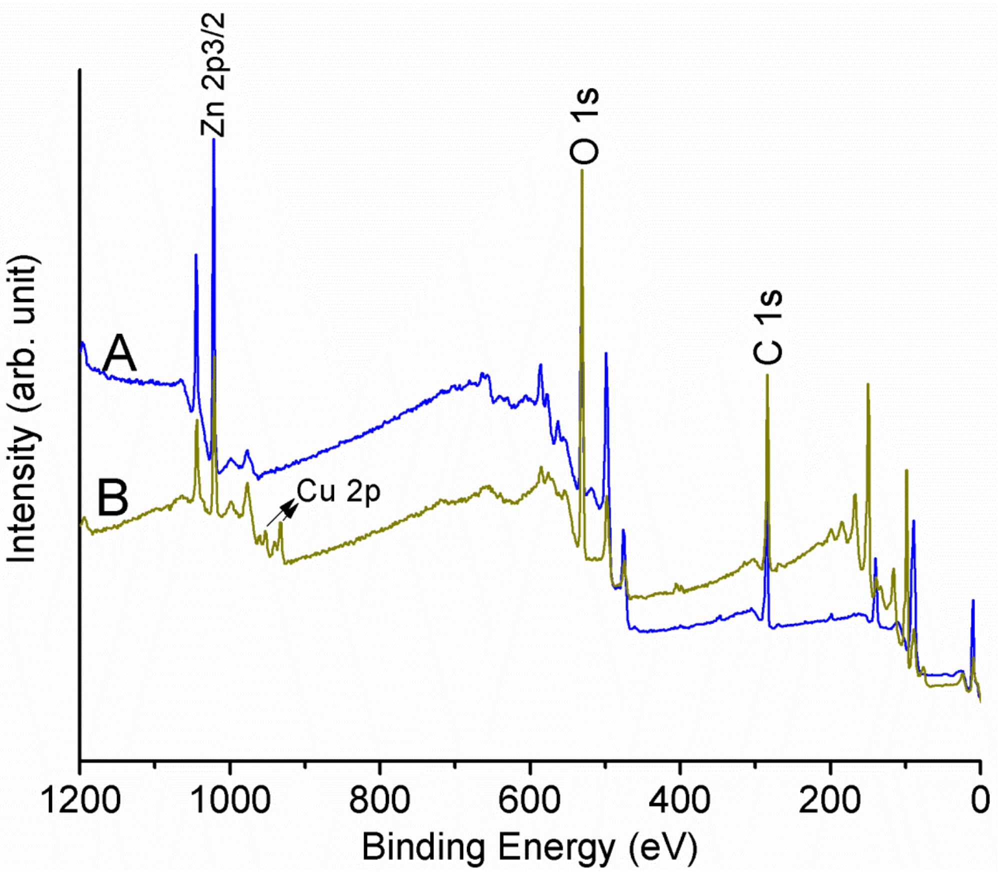

Figure 3.44 XPS spectra of A) undoped and B) Cu-doped ZnO nanorods grown at 60℃ on silicon substrate. (Traces were shifted vertically for visibility)

The XPS spectra of undoped and Cu-doped ZnO nanorods are shown in Figure 3.44. As it can be seen in the figure there is a good agreement between the XPS spectra of Cu-doped and undoped ZnO nanorods. However, two additional weak peaks were detected for the Cu-doped sample corresponding to Cu 2p orbitals, which implies a uniform distribution of Cu ions into the ZnO lattice. The high resolution Cu 2p XPS binding energy region is shown in Figure 3.45. Two extra peaks in Figure 3.45 located at ~937 eV and ~945 eV are due to satellite bands. The presence of these bands indicates that our Cu-doped samples might also contain CuO or Cu-O bonds with d^9 configuration in their ground state [267]. The Cu 2p peaks can be used to identify the amount of divalent or monovalent Cu at the surface of the sample [78, 249, 263]. In our case Cu 2p was fitted with Gaussian function, showing two peaks at 932.8 eV and 952.6 eV corresponding to Cu 2p 3/2 and 2p 1/2 respectively, suggesting that Cu^+ is the main doping component in agreement with our XRD analysis. The amount of Cu^{2+} in our doped samples should be small. The formation of Cu^+ instead of divalent Cu^{2+} compound can be due to the fully paired electrons in the $3d^{10}$ configuration of Cu^+ ion. Thus, Cu^+ ions are more stable [260]. It has been reported that Cu^+ ions do not exhibit a magnetic moment [247]. Therefore, we predict that our Cu-doped sample should not be a good candidate for room temperature ferromagnetism applications. The lower binding energy of Cu 2p 3/2 in comparison to the reported binding energy of commercial CuO (933 eV) can be related to the substitution of Cu^{2+} with Zn^{2+} in the host crystal lattice. The atomic composition percentage of Cu^{2+} in the ZnO was calculated to be 3 % by applying the fitted peak data showed in Figure 3.45 into equation 3-2 where *S,* the elemental sensitivity factor for Cu, is 6.3.

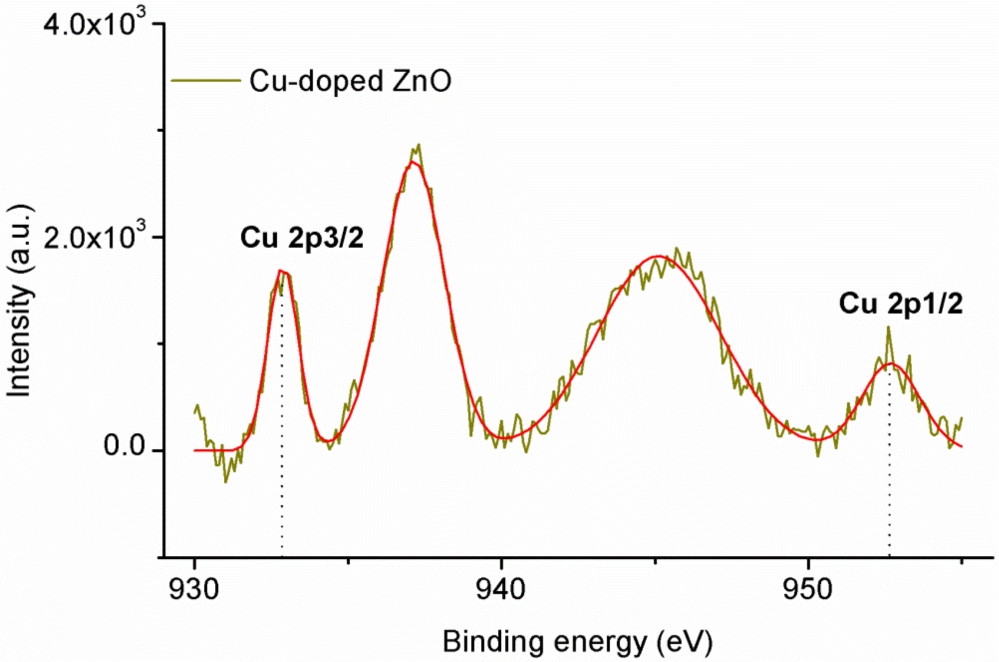

Figure 3.45 High resolution XPS spectra of Cu 2p orbital’s peaks grown at 60℃ on silicon substrate.

More precise measurements show that the Zn 2p3/2 peak is shifted to higher energies, as large as +0.9 eV, due to Cu^{2+} doping. A similar trend was reported before and a positive shift in Zn 2p energy has been observed due to different dopant materials such as Sb, Ag, Li, Al, Cu [141, 144, 268, 269]. This shift might be due to the reduction of the surface band bending, or incorporation of Cu^{2+} ions into ZnO crystal [269]. The FWHM of the Zn 2p peaks were also found to be larger for the Cu-doped sample (2.5 eV) as compared to the undoped ZnO (1.85 eV) in consistent to similar past report [144]. The widening indicates the possible formation of Cu-Zn-O bonds.

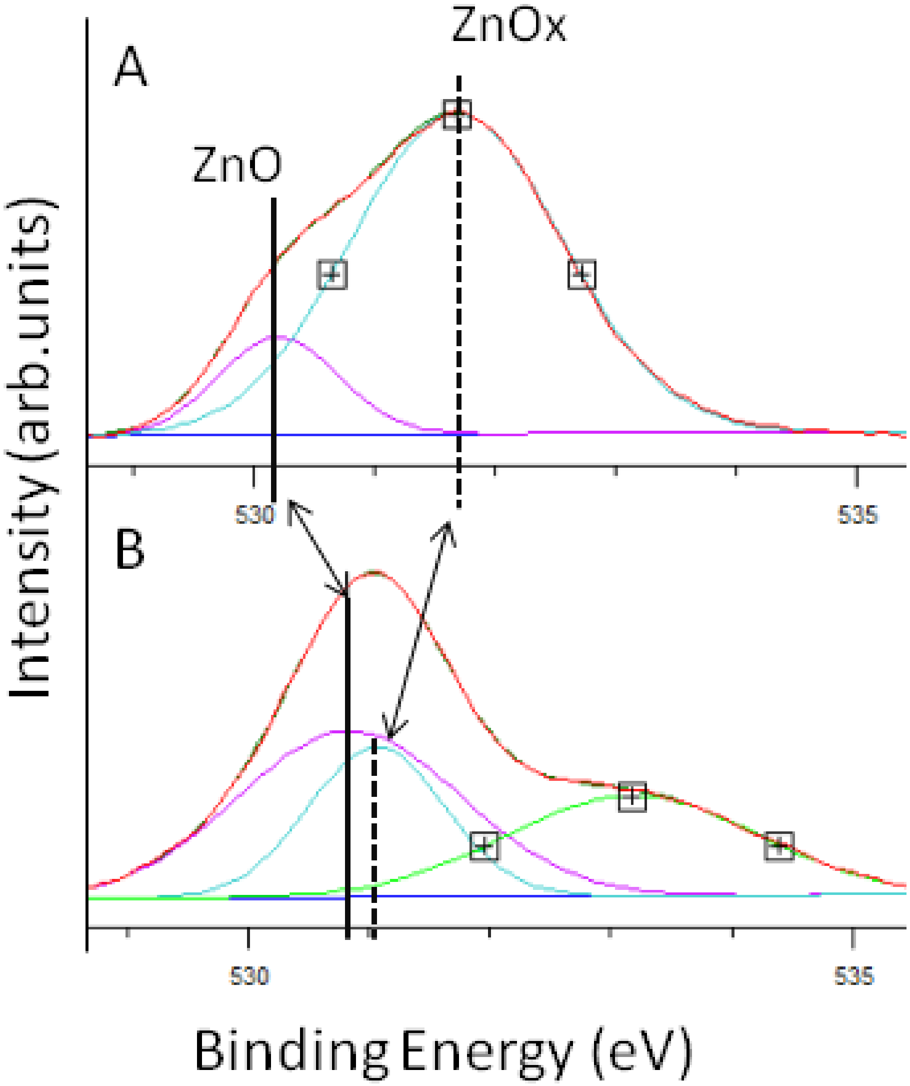

Figure 3.46 High resolution XPS spectra of O 1s core level of A) Undoped and B) Cu-doped ZnO nanorods grown at 60℃ on silicon substrate.

The asymmetric O 1s peak of Cu-doped nanorods (Figure 3.46) was deconvolved with three subspectral components at ~530.8 eV, ~531 eV, and ~533.2 eV which are assigned to O^{-2} ions (O_L) in stoichiometric Zn-O-Zn, O^{-2} ions (O_H) in an oxygen deficient ZnOx region, and Cu-Zn-O or adsorbed oxygen species, respectively following previous reports [141, 196]. Similar components in O 1s were observed in Cu-doped ZnO, before [143-145]. In our case the O 1s/Zn 2p ratio increased from 3.8 for undoped ZnO to 13.2 for Cu-doped nanorods indicating an oxygen abundant structure. This increase is partially because of susbtitution of Zn^{2+} with Cu^{2+} cations in crystal lattice [144, 270]. It can be seen in Figure 3.46 that a third subspectral peak appeared at ~533.2 eV suggesting that Cu compounds are now successfully involved in the ZnO crystal lattice. The possibility of formation of monovalent Cu in Cu-V_O bonds has been verified before where V_O represents oxygen vacancies [271]. CuO_4 is another possible compound with strong Cu-O covalent bonds inside the ZnO ionic lattice which was suggested by Ma et al.[272]. Based on curved fitting results shown in Figure 3.46 the surface O_L percentage increased to 44 % after Cu addition which is the evidence of more oxidized stoichiometric surroundings in Cu-doped nanorods. Noipa et al. [270] reported larger amounts of oxygen in Cu-doped ZnO nanorods as compared to undoped ZnO particularly at ~3% Cu^{2+} doped ZnO. In the same manner the smaller area of O_H is a sign of smaller concentration of oxygen vacancies on the surface of Cu-doped nanorods. The O_H peak was also attributed to the hydroxyl groups resulting from the chemisorbed water in some of the literature [143, 195, 197]. The surface chemistry information of Cu-doped ZnO nanorods is summarized in Table 3-5. These results suggesting lower defect emission in the PL spectrum of Cu-doped nanorod which will be further confirmed.

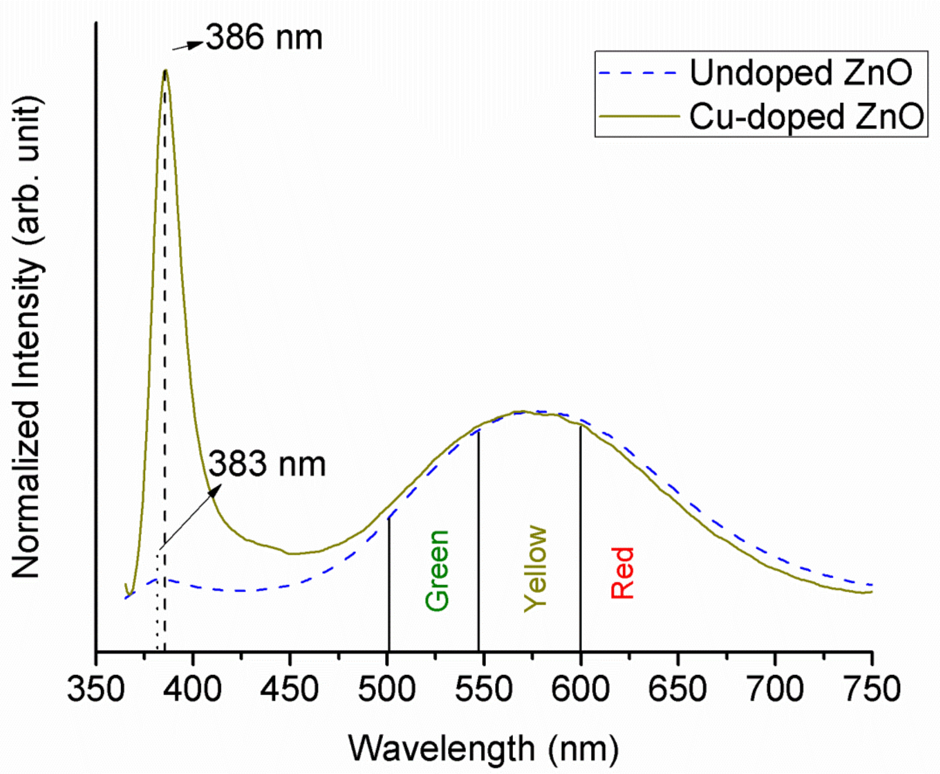

Figure 3.47 Room temperature PL spectra of undoped and Cu-doped ZnO nanorods grown at 60℃ on silicon substrate.

The influence of Cu^{2+} dopant on luminescence of Cu-doped ZnO nanorods was investigated by a PL setup at room temperature. The PL signal is a measure of the recombination rate of the photo generated carriers in a semiconductor material [273]. Thus, the higher PL intensity indicates a larger number of radiative electron-holes recombination. On the other hand, charged carriers may also undergo non-radiative recombination or photocatalytic reaction [78]. Therefore, PL measurements can be a good test to compare optical properties. Room temperature PL spectra shown in Figure 3.47 reveals a peak in the UV region centered at 387 nm for Cu-doped nanorods. There is also a broad peak in the visible range approximately centered at 576 nm for Cu-doped nanorods, assigned as defect emission. The PL emission data of Cu-doped ZnO nanorods is summarized in Table 3-6. PL measurements also confirm the dominant wurtzite crystal for our Cu-doped samples in accord with our previous analysis results.

The defect emission of our Cu-doped sample decreased significantly as compared to the undoped ZnO, similar to previous reports [78, 257, 274]. The doping of transition metal ions into undoped ZnO may minimize the defect emission by providing competitive pathways for recombination [179]. Similarly, the defect emission broad band can be deconvolved into green, yellow, and red emission corresponding to different types of intrinsic and extrinsic defects centers [121, 122, 147]. A detailed description of possible electronic transitions in ZnO forbidden area due to the existence of defect centers has been reported by Xu et al.[11]. The Green emission in PL spectra of Cu-doped nanorods are suggested to be related to Cu transitions [144, 248, 253], singly ionized oxygen [275], Zn vacancies, and Zn interstitials or surface defects [252, 257]. The yellow emission, on the other hand, is attributed to doubly charged oxygen vacancies [198], surface oxygen interstitials [200, 257] or hydroxyl groups on the surfaces [257]. The red emission reduction can also be related to lower Zn interstitials or oxygen vacancies in our Cu-doped nanorods general. Therefore, the defect emission reduction in our Cu-doped nanorods can be related to the decrease in number of the mentioned defects points in accordance with our XPS results where an oxygen abundant structure was predicted. In fact, highly stoichiometric oxygens were detected by XPS on the surface of our Cu-doped nanorods as compared to undoped ZnO. Lower number of surface defects such as hydroxyl groups and Zn states defects were detected on the surface of the Cu-doped nanorods via XPS technique. Moreover, Xu et al.[257] suggested that Cu^{2+} doping might increase the possibility of non-radiative recombination in the surface of ZnO nanorods. Thus our results are in accordance with the fact that incorporation of the cations into undoped ZnO reduces the nanorods surface defects emission [179].There is clearly a blue shift in the defect emission of our Cu-doped nanorods as compared to undoped ZnO. A similar shift as a function of Cu^{2+} doping was reported before [78, 257, 274, 275]. The shift was attributed to the recombination of photo-induced carriers on impurity levels induced by Cu^{2+} ions, based on the fact that Cu^{2+} centers are optically active in ZnO [270, 276, 277]. It has been argued that the recombination of donor-acceptor pairs involving shallow donors (i.e. Zn^{+}) and singly ionized acceptors (i.e. Cu^{+}) state yield an emission in blue-green visible range [278]. In addition, Cu^{2+}-Cu^{+} transitions could be responsible for the higher blue emission in PL spectra of our Cu-doped nanorods [278]. This is also in agreement with our XPS data which predicted a considerable amount of monovalent Cu^{+} in our doped nanorods. Therefore the majority of the defect emission in the PL emission of our doped nanorods are due to the existence of little amount of divalent or monovalent Cu^{+} ions in the host lattice. The intensity of the NBE peak increased significantly for our Cu-doped ZnO nanorods as compared to undoped ZnO. XRD results showed more pronounced crystallinity along all wurtzite crystal planes. On the other hand, larger nanorods exhibit more crystal symmetry which yields to the production of larger number of charge carriers with the similar energy levels. ZnO crystal quality enhancement with addition of Cu^{2+} has been reported before [257]. A 4 nm red shift was detected for the NBE peak of the Cu-doped sample as compared to undoped ZnO. Band gap reduction as a consequence of incorporation of Cu^{2+} into ZnO crystal lattice has been reported before [248, 259, 263, 279]. This shift might be related to a change in the energy band level of Cu-doped nanorods due to the ZnO band electrons and the localized Cu^{2+} ions impurity spin coupling [256, 259, 280]. The other reason can be connected to the host lattice deformation as a result of Cu^{2+} doping [250] which is consistent with our XRD results. Sahu et al.[275] and Hsu et al.[274] attributed this shift to the accumulation of Cu states near the valence and conduction bands. A quench in NBE emission of Cu-doped ZnO nanorods as compared to undoped ZnO was reported before [259, 263] which was not observed in our case showing that our method is an efficient way of Cu^{2+} doping of ZnO. The NBE to defect emission ratio increased to 70% for Cu-doped nanorods. The enhanced NBE emission of Cu-doped ZnO implies that the optical quality is improved as well as the crystal quality based on the lower defect states. Noting that the majority of the defect centers are located at the surface of our nanorods [248], the lower surface area to volume ratio of Cu-doped nanorods can be another reason of higher NBE/defect emission ratio in accordance with previous reports [149, 252, 281].

3.6 Low temperature hydrothermal growth of arrays of Cr-doped ZnO nanorods

Optical, electrical and magnetic properties of ZnO nanomaterials can be tuned by Cr^{3+} doping. Incorporation of Cr^{3+} into ZnO may affect the optical properties of the host material in favor of its photocatalytic activity by shifting its absorption edge to the visible region [93, 282]. Moreover, Cr^{3+} can be one of the most effective cation dopants for producing room temperature ferromagnetism properties in ZnO crystals [283, 284]. Although the origin of this effect is controversial [283], the smaller ion radius of Cr^{3+}(0.62 A) than Zn^{2+}(0.74 A) and their similar electronegativity is suggested to be responsible for this behaviour in Cr-doped ZnO [285]. The electronic properties of ZnO can be significantly affected by cation doping. Higher conductivity was measured in Cr-doped ZnO thin films in comparison to undoped ZnO due to its lower dielectric constant [286]. In addition, Cr^{3+} doping can significantly enhance the gas sensitivity properties of ZnO nanocrystal. Higher acetone gas sensitivity has been reported for the Cr-doped ZnO in comparison to undoped ZnO [287, 288]. It has been also shown that Cr^{3+} dopant can reduce the operating temperature of ZnO nanorod gas sensitivity down to 100℃ [289]. Recently, Cr-doped ZnO nanoparticles were used as an impurity remover in water dye contamination [290]. There is also a report of an improvement in antibacterial activity of ZnO nanoparticles by Cr^{3+} addition [291].

Cr-doping of ZnO through the various techniques has been reported before [283, 284, 289-293]. It has been argued that the synthesis of wurtzite ZnO and incorporation of substitutional defect at the same time is not trivial [294]. We were able to synthesize Cr-doped ZnO nanorods by using a hydrothermal method at the lowest temperature (60 ℃) ever reported to the best of our knowledge. We expect to get different results from the previous reports [282, 285], due to our different synthesis conditions. The morphology and properties of ZnO are greatly affected by the preparation conditions and chemical environment of the synthesis process [288, 294]. Although the nanorods coverage was hindered in our experiment, the PL emission has considerably improved in favor of UV emission by Cr^{3+} addition in contrast to the previous reports.

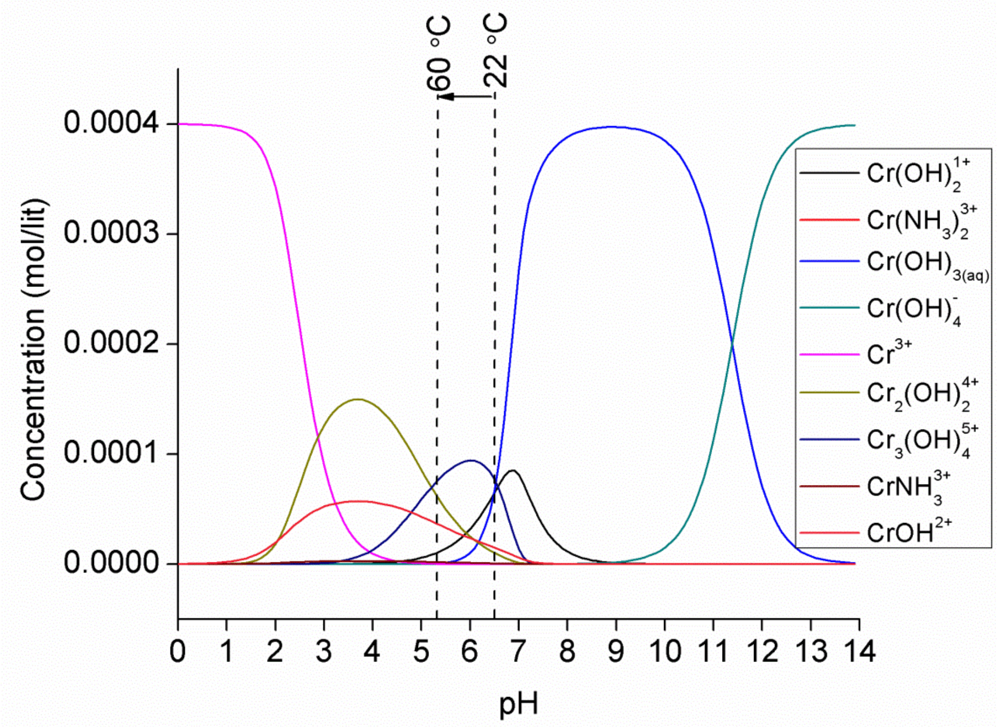

Figure 3.48 Speciation diagrams of Cr(III) species at 60 °C as a function of pH ranging from 0 to 14 as computed with Visual MINTEQ software.

The speciation diagram of Cr(III) is shown in Figure 3.48. It should be mentioned that the simulation could not be done based on the initial concentration of Cr^{3+} (5 mM) that was used in my experiment due to the strong Cr^{3+} ionic strength which is formed under the applied conditions. Therefore, I computed the speciation diagram for the maximum concentration of 0.4 mM at 60℃. It can be seen that in the pH range between 5.4 and 6.5, the cationic species which can be formed are $Cr_3(OH)_4^{5+}$, $Cr(OH)_2^{1+}$, $Cr_2(OH)_2^{4+}$, $CrOH^{2+}$, $Cr(NH_3)_2^{3+}$,and $Cr(OH)_{3(aq)}$. In contrast, to the other dopants the Cr^{3+} cannot be formed in the pH pH range between 5.4 and 6.5. This can be the main reason of inhibition of nanorods growth in the case of Cr^{3+} doping. We believe that the adsorption of these positive ions to the polar surface of ZnO hexagonal hinders the nanorods c-axis growth. Therefore, nanorods grow more effectively along the side with presence of Cr^{3+} dopant, and as a result thicker nanorods can be obtained. Moreover, at the early stage of the growth the possibility of adsorption of these positive Cr^{3+} compound to the negative polar surfaces of seed nanoparticles is very high due to the large number of these ions and their stabilities in the solution. Therefore, lower nanorods surface coverage is expected in case of Cr^{3+} doping in comparison to undoped ZnO nanorods growth.

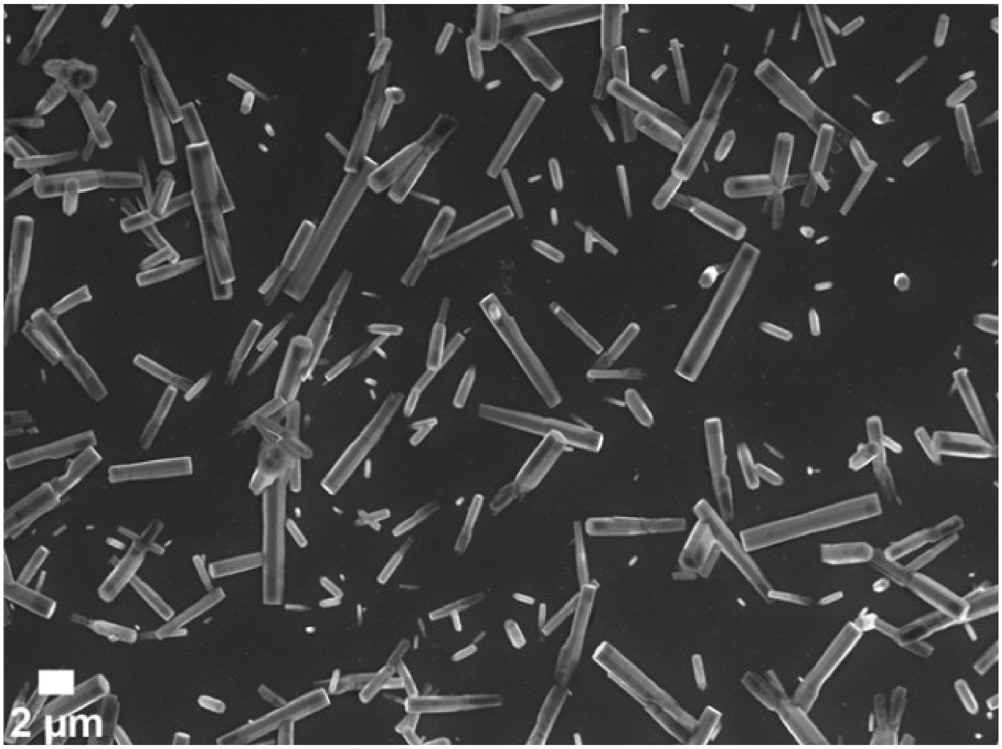

Figure 3.49 SEM images of the top of the Cr-doped ZnO nanorods grown at 60℃ on silicon substrate.

An SEM image of Cr-doped ZnO nanorods is shown in Figure 3.49. It can be seen that ZnO nanorods uniformity is significantly inhibited by Cr^{3+} addition, although larger nanorods were obtained. The number density of Cr-doped nanorods across the substrate reduced as compared to the undoped ZnO nanorod growth consistently with previous reports [287]. We believe that the Cr^{3+} compound adsorption at the surface of the seed layer hinders the usual adsorption of Zn^{2+} complex at the seed layer and eventually reduces the density of ZnO nanorods on the substrate. This is in accordance with Li et al. [235] where Cr-doped ZnO nanorods in hydrothermal synthesis were indifferent to the presence of ZnO seed layer on the surface of the substrate. The extra Zn^{2+} cations which remained in the growth solution subsequently participated in the growth of those nanorods which had a chance to nucleate. This resulted in larger size nanorods in comparison to undoped ZnO uniform growth. The average height increased to 3.9 μm and the diameter enhanced to 1 μm on average as a result of Cr^{3+} doping. The size information of Cr-doped nanorods is summarized in Table 3-2. Our results are in agreement with previous reports where larger ZnO nanorods were obtained by incorporation of Cr^{3+} into their crystal lattice [285, 287]. The aspect ratio of nanorods decreased from 6.5 to 3.9 for the undoped ZnO and Cr-doped

ZnO, respectively. As it was mentioned before the (001) plane is the fastest growth direction of ZnO crystal under the normal hydrothermal growth condition. Cr^{3+} addition can affect the growth rate of ZnO crystals along its c-axis in two ways. First, the localization of Cr^{3+} compounds at the (001) planes can reduce the access of Zn^{2+} active ions to this plane and as a result it hinders the nanorods growth along the c-axis direction. Secondly, Cr^{3+} addition can change the energy of some crystallographic planes in ZnO nanocrystal which will subsequently affect the growth rate of these planes in a hydrothermal process [291]. Therefore, the growth rate along different crystal planes of ZnO crystal can be affected by Cr^{3+} addition. These results are further confirmed by XRD analysis.

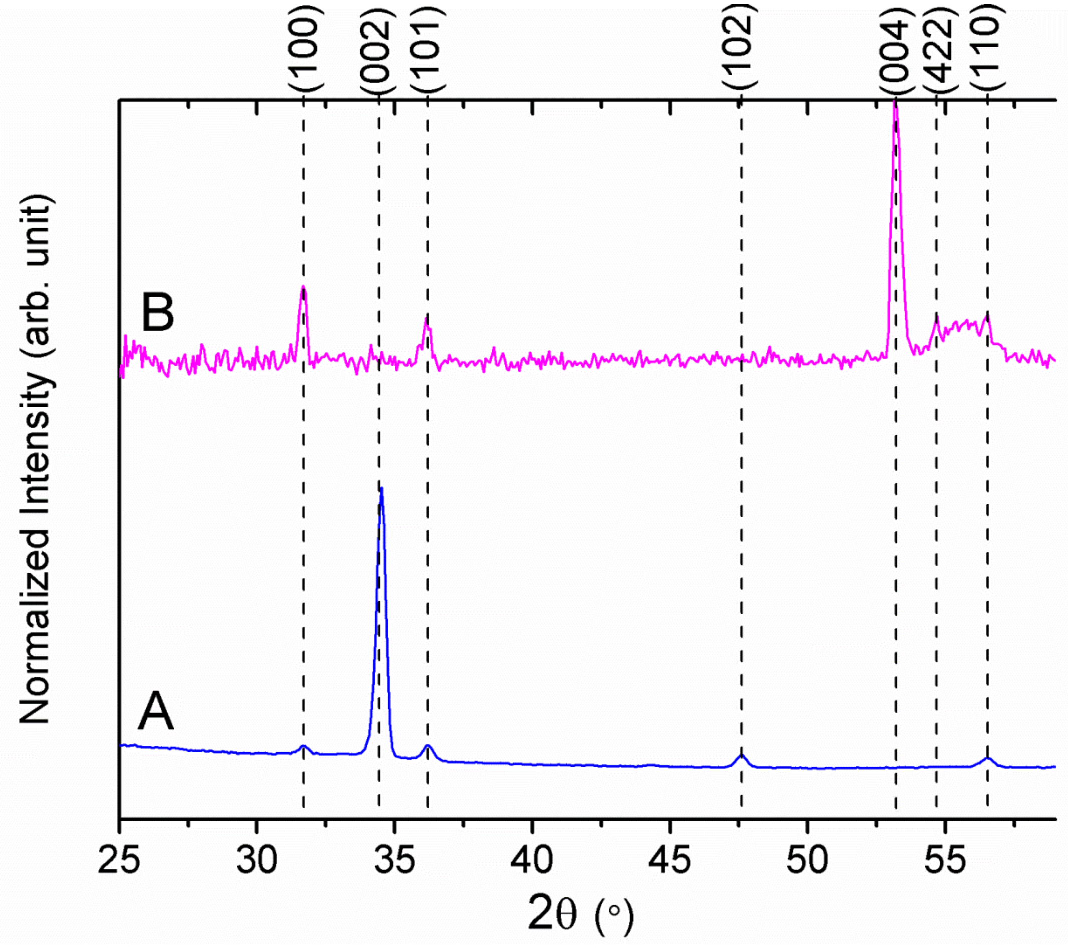

Figure 3.50 XRD patterns of A) undoped and B) Cr-doped ZnO nanorods grown at 60℃ on silicon substrate. (Traces were shifted vertically for visibility)

The Crystal phase of Cr-doped ZnO nanorods was investigated by XRD and the result is shown in

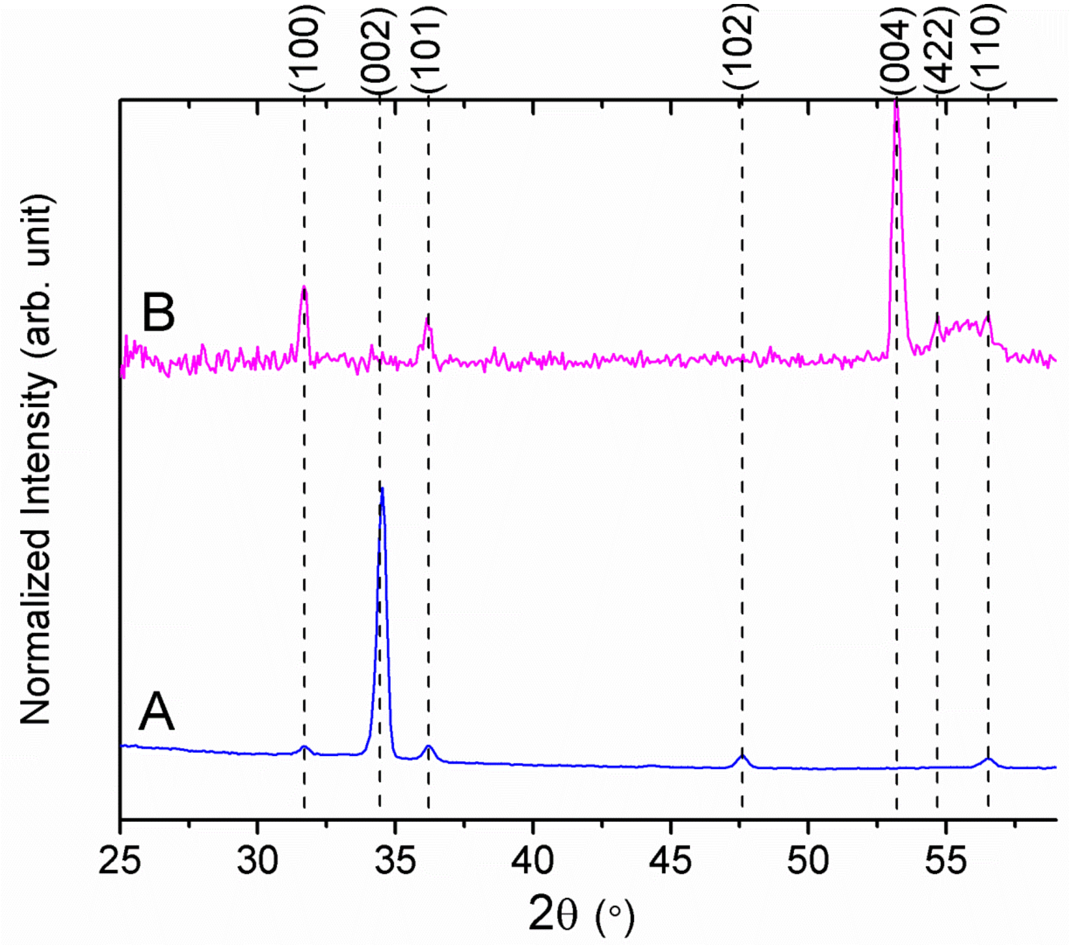

Figure 3.50. The majority of the peaks in Cr-doped nanorods can be assigned to the hexagonal wurtzite crystal structure. However, the typical wurtzite peak at ~34° is significantly suppressed in Cr-doped XRD pattern which implies that the crystallization along (002) plane in the Cr-doped sample is considerably lower than the undoped ZnO. On the contrary, crystallization is improved along (100), (101), (110), and (422) planes showing more effective side growth for Cr-doped nanorods which is consistent with our SEM images. The main difference between the XRD pattern of doped and undoped samples is related to the appearance of a peak at ~53 ° which has been indexed to a (004) plane correspond to diffraction and reflections from the carbon atoms [295]. Carbon might be attached to my sample as a contamination during the characterization process. The small shoulder labeled by as asterisk (*) can be assigned to the (311) plane of secondary phase $ZnCr_2O_4$ [296]. The solubility limit of Cr^{3+} into the ZnO host lattice is reported to be ~3% [288, 297]. However, formation of Cr^{3+} compounds at high concentration (more than 4%) has been reported before [294, 296]. The appearance of Cr^{3+}

secondary phase is attributed to the probable residence of some Cr^{3+} cations on the octahedral interstitial sites of the host lattice [297]. Therefore, the XRD pattern shows that crystallinity of ZnO nanorods doped by Cr^{3+} ions at low temperature has been significantly reduced. By applying the crystallographic data of

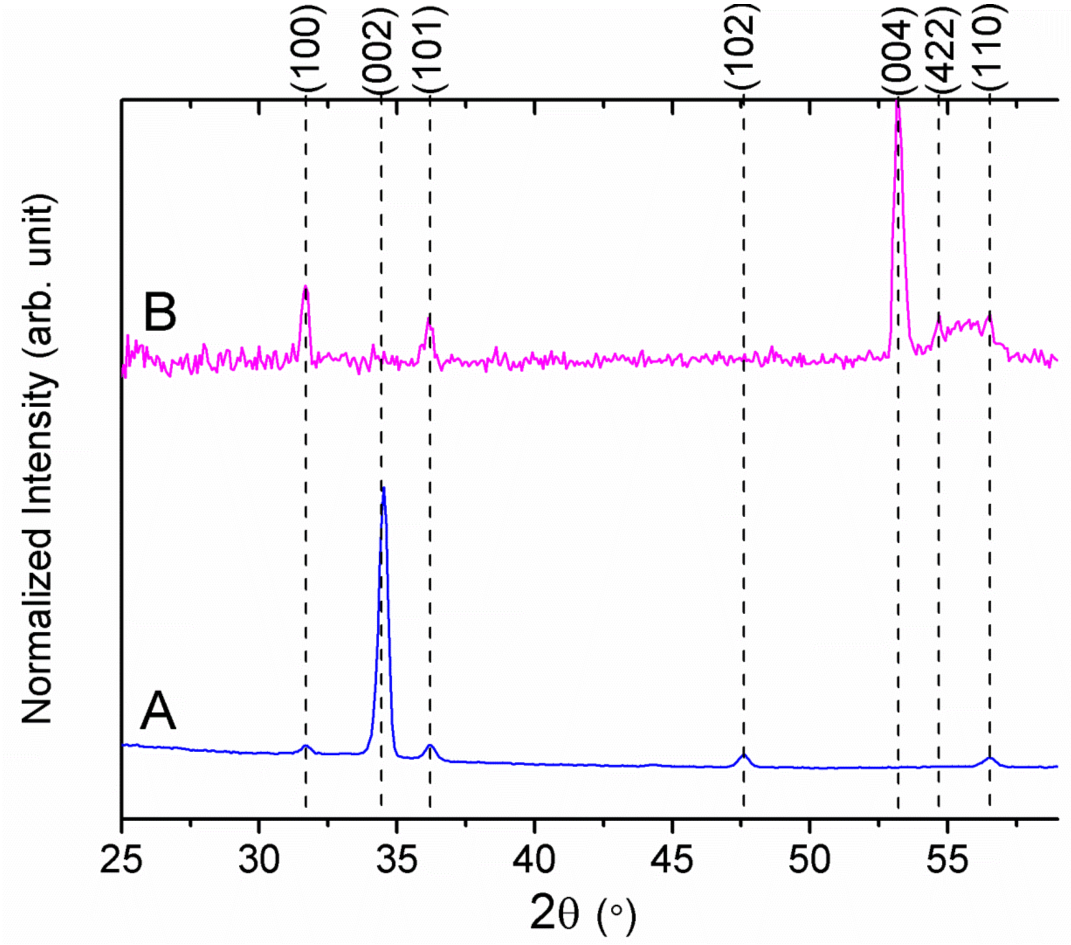

Figure 3.50 into equation 3-1 the degree of alignment of Cr-doped nanorods was calculated. Comparing the calculated results to those of undoped ZnO (82%) shows that the Cr-doped nanorods dropped to 22%. A summary of the crystallographic data of Cr-doped nanorods is given in Table 3-3.

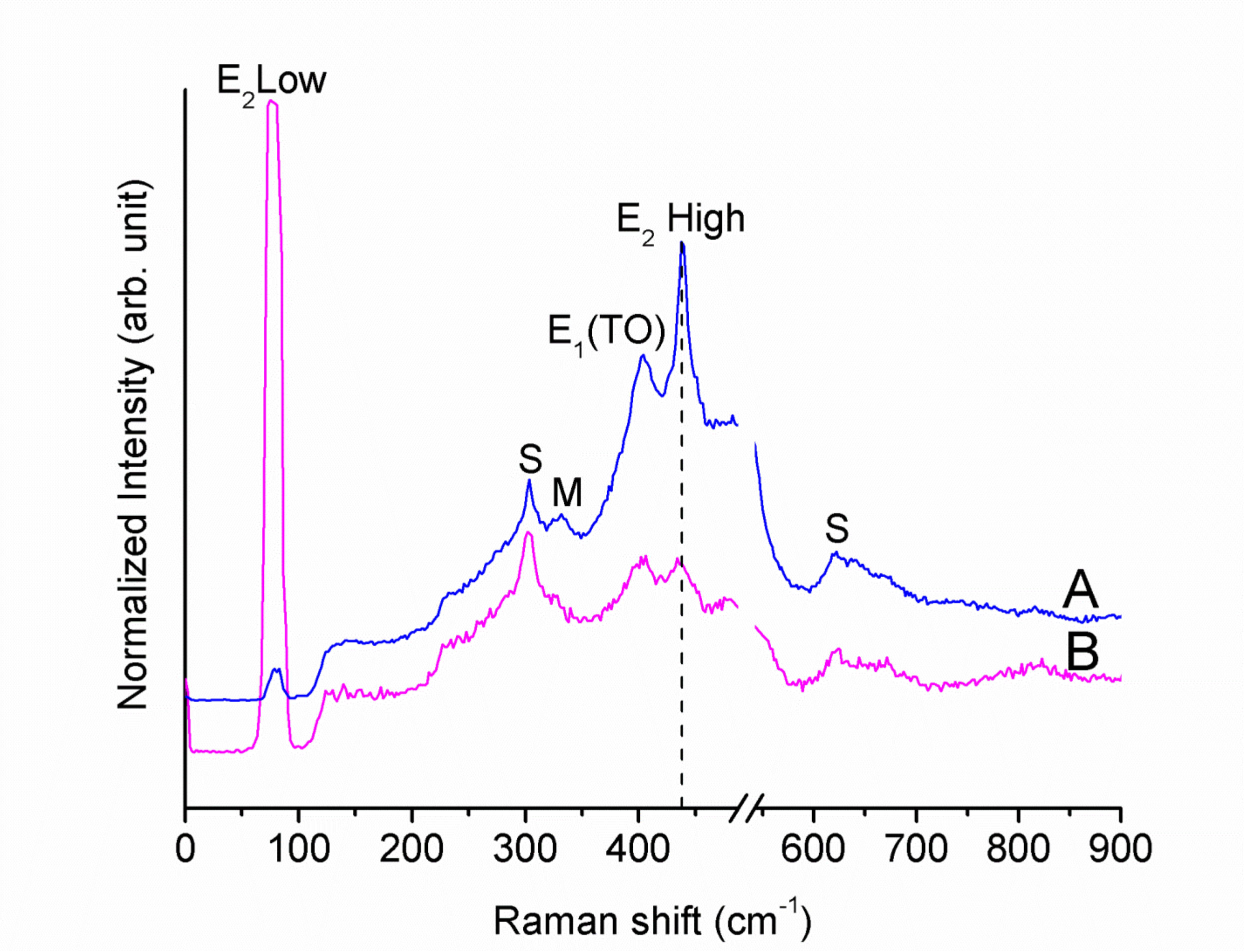

Figure 3.51 Room temperature micro-Raman scattering spectra of A) undoped and B) Cr-doped ZnO nanorods grown at 60℃ on silicon substrate. (Traces were shifted vertically for visibility)

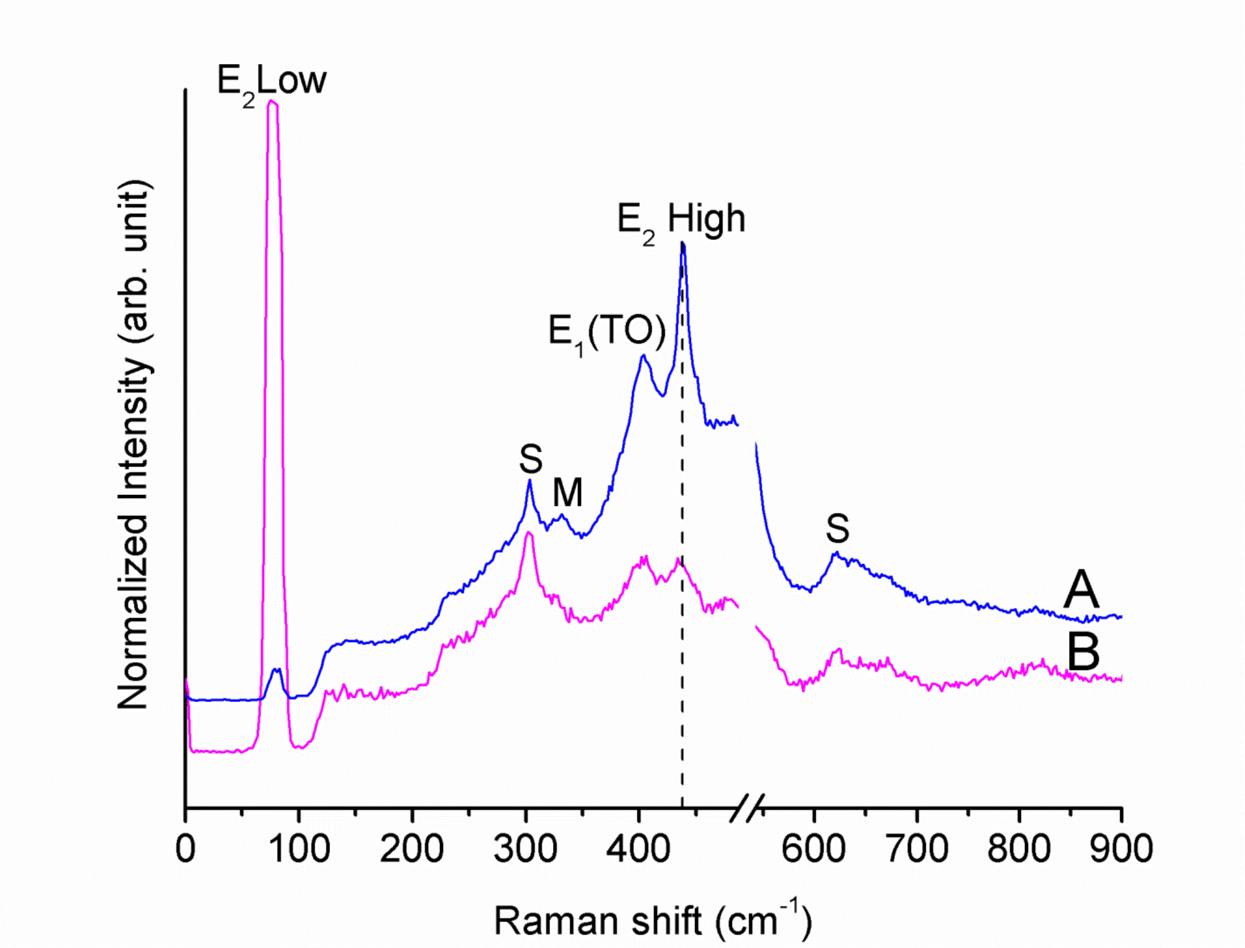

Figure 3.51 shows the micro-Raman spectra of undoped and Cr-doped ZnO nanorods. Our results correspond to the well-known features of ZnO, showing Raman active E_1 and E_2 peaks [111]. Similarly, lower E_2(H) peak intensity should be the main reason of disappearance of the M peak in the Cr-doped Raman spectra. The peaks at 78.9 cm^{-1}, 402.1 cm^{-1} and ~441.6 cm^{-1} are assigned to the E_2(L), E_1(TO) and E_2(H) modes, respectively. A summary of Raman active modes of Cr-doped nanorods is given in Table 3-4. Although the E_2(H) peak was detected in Cr-doped Raman spectra its intensity was reduced, demonstrating large internal stress or structural disorder in Cr-doped nanorods [284]. Large concentration of Cr^{3+} content in our ZnO nanorods will be later determined by XPS analysis. The diminishing of E_2(H) peak due to the Cr doping has been reported before and it has been attributed to the increment of the host lattice defects in ZnO matrix [266, 297]. Manoj et al. [298] ascribed the Cr-doped Raman peak variation to the local stress arising as a result of a change in the nanorod size with incorporation of Cr^{3+} ions into the Zn^{2+} lattice sites. Local stress was calculated by comparing the Cr-doped XRD peak position to undoped ZnO XRD pattern as the reference. A large (362 Gpa) tensile stress along the c-axis

of Cr-doped ZnO was calculated which is consistent with our XPS result. In addition, based on the size of the dopant atom and its electronic structure, the behavior of E_2(H) peak was slightly changed. The E_2(H) peak position for Cr-doped nanorods has shifted (-3.6 cm^{-1}) to lower energies as compared to undoped ZnO as has been reported before [266, 284]. The broadening, shift, and asymmetry of E_2(H) and E_2(L) peak can be similarly explained based on spatial correlation model [185]. According to isotopic mass dependence of the frequency shift measurements, E_2(H) mode in ZnO films mainly appears because of the vibration of oxygen atoms [186, 187]. It has been argued that the missing oxygen mass at the oxygen vacancy site can blue shift the frequency of E_2(H) mode [85, 188]. Therefore, the red shift of the E_2(H) in our Cr-doped sample can be related to its larger oxygen/zinc atomic ratio in comparison to undoped ZnO. The O/Zn ratio was measured by XPS and the results are given in Table 3-5.

The intensity of E_2(L) has increased by Cr^{3+} addition. This peak represents the vibration of the Zn sublattice in Raman spectra [130, 189]. Thus, the E_2(L) peak behaviour can be significantly affected by substitution of Zn^{2+} ions by cation dopant [85]. The Cr^{3+} substitution breaks lattice translational symmetry which eventually causes broadening in the allowed Raman peaks [185]. The asymmetric broadening of E_2(H) peak can be explained in the similar manner. The intensity of E_1(TO) is comparable to E_2(H) suggesting that the crystal quality of the nanorods is degraded by Cr^{3+} doping. This fact is in consistent with our XRD results where the (002) peak was broadened for the Cr-doped sample implying the same crystal degradation.

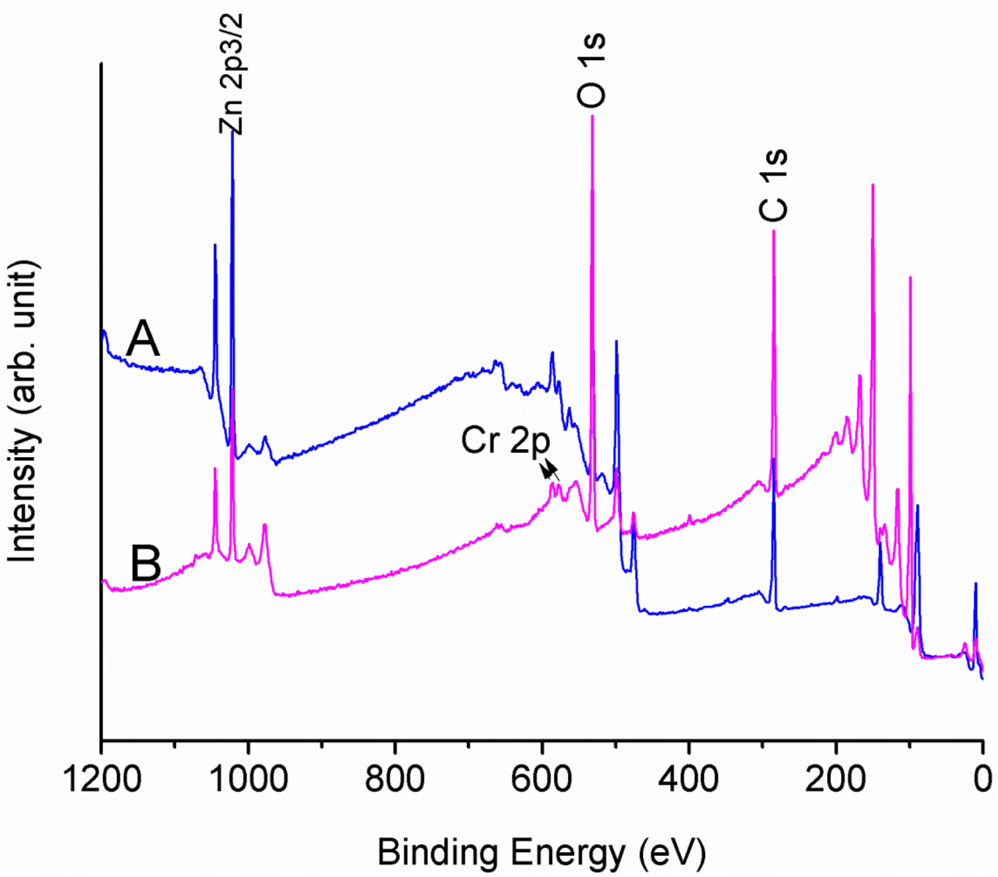

Figure 3.52 XPS spectra of A) undoped and B) Cr-doped ZnO nanorods grown at 60℃ on silicon substrate. (Traces were shifted vertically for visibility)

The XPS spectrum of the Cr-doped ZnO nanorods is shown in Figure 3.52. As it can be seen there is a good agreement between the XPS spectra of Cr-doped and undoped ZnO nanorods. However, two additional weak peaks were detected for Cr-doped sample corresponding to Cr 2p orbitals which implies the successful incorporation of Cr^{3+} ions into the ZnO lattice. A high-resolution Cr 2p XPS binding energy region is shown in Figure 3.53. In our case the Cr 2p peaks are fitted with a Gaussian functions centered at ~577.9 eV and ~587.5 eV, corresponding to Cr 2p 3/2 and 2p 1/2 respectively, and suggesting that Cr^{3+} and Cr^{6+} are the main doped components in agreement with our XRD and XPS results [283, 290]. It appears that the majority of Cr cations occupy vacant octahedral (Cr^{3+}) and tetrahedral (Cr^{6+}) sites sequentially in the ZnO host lattice. The high valance Cr^{6+} ions are precursors for secondary oxide phases, such as the antiferromagnetic Cr_2O_3 and paramagnetic CrO_3 phase [283]. However, only the formation of $ZnCr_2O_4$ phase was detected in the XRD pattern of our doped nanorods. Therefore, we predict that the majority of Cr compounds are in the form of Cr^{3+} ions located at interstitial centers of the host lattice. The atomic composition percentage of Cr^{3+} in the ZnO was calculated to be 19 % by applying the fit data showed in Figure 3.53 into the equation (3-2) where S, the elemental sensitivity factor, is 2.3 for Cr. The high Cr^{3+} percentage can be due to the signal from the surface of the substrate rather than the cations which are assumed to be doped in our nanorods. Our result is surprisingly close to the Cr:Zn ratio that is reported by Lin et al.[285].

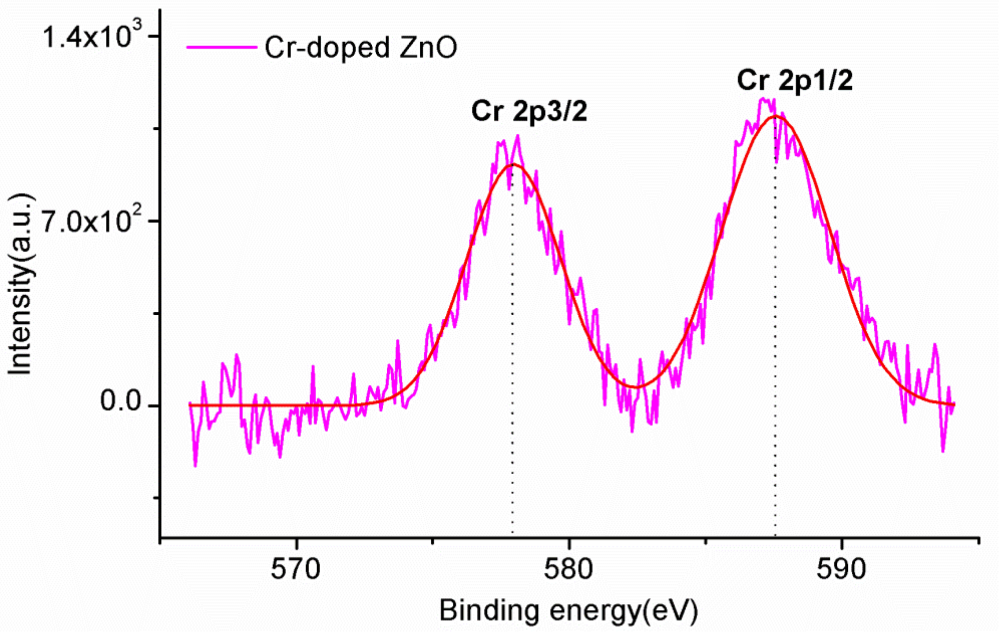

Figure 3.53 High resolution XPS spectra of Cr 2p orbital's peaks grown at 60℃ on silicon substrate.

More precise measurements shows that the Zn 2p 3/2 peak is shifted to higher energies (as much as +0.4 eV) due to Cr^{3+} doping. As discussed before, this shift might be due to the reduction of the surface band bending, or due to the incorporation of Cr^{3+} ions into ZnO crystal [269]. The FWHM of the Zn 2p peaks were also found to be larger for the Cr-doped sample (1.9 eV) as compared to the undoped ZnO (1.85 eV). The widening indicates the possible formation of Cr-Zn-O bonds.

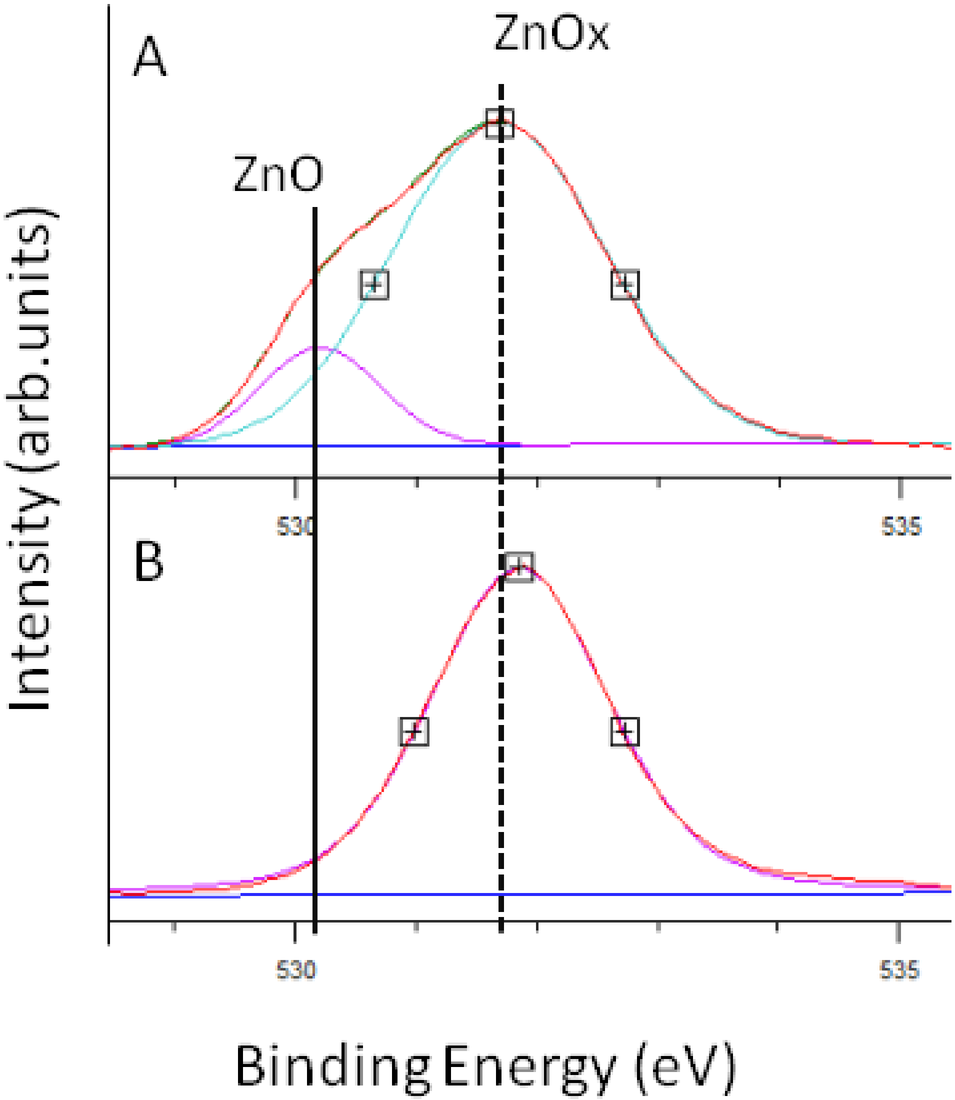

Figure 3.54 High resolution XPS spectra of O-1s core level of A) undoped and B) Cr-doped ZnO nanorods grown at 60℃ on silicon substrate.

The high resolution symmetric O 1s peak of Cr-doped ZnO nanorods is shown in Figure 3.54. The peak at 532 eV is mainly attributed to the O^{2-} ions in an oxygen deficient ZnOx region and/or Cr-Zn-O compounds [285]. This peak is also attributed to hydroxyl groups resulting from the chemisorbed water in many other literature [143, 195, 197]. The shift in O 1s should be mainly because of larger number of hydroxyl groups attached to the surface of nanorods. We predict that the Cr-doped nanorods will be more photocatalytic active due to the larger peak in oxygen deficient region with reference to Liqiang et al. [143] report. In our case O 1s/Zn 2p ratio increased from 3.8 for undoped ZnO to 15.5 for Cr-doped nanorods. Thus, Cr-doped nanorods have an oxygen abundant lattice which will later exhibit its effect in lower visible emission in PL spectra. The surface chemistry information of Cr-doped ZnO nanorods is summarized in Table 3-5.

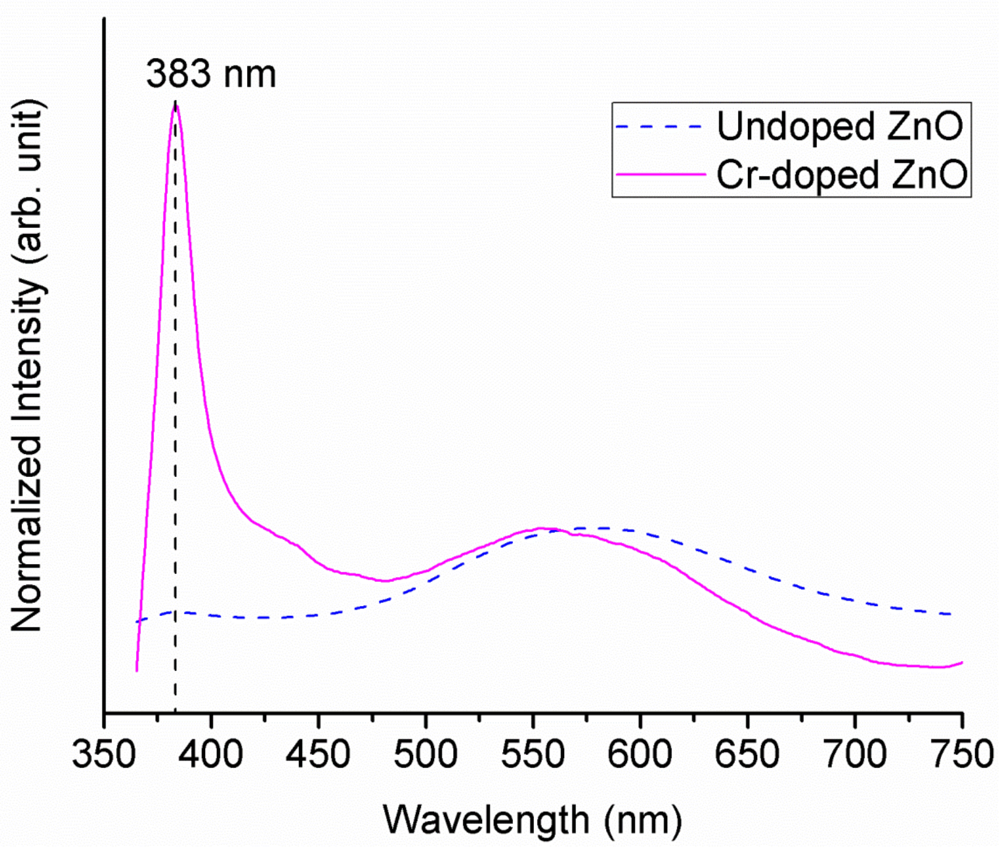

Figure 3.55 Room temperature PL spectra of undoped and Cr-doped ZnO nanorods grown at 60℃ on silicon substrate.

The influence of Cr^{3+} on luminescence of Cr-doped ZnO nanorods was investigated by a PL setup at room temperature. The higher PL intensity indicates the larger number of radiative electron-holes recombination. On the other hand, charged carriers may also involve with non-radiative recombination or photocatalytic reaction [78]. Therefore, PL measurement can be a good test to compare optical properties. Room temperature PL spectrum of Cr-doped ZnO is shown in Figure 3.55. The peaks at 383 nm and 565 nm of Cr-doped PL spectra are attributed to NBE and defect attributed emission, respectively. The PL emission data of Cr-doped ZnO nanorods is summarized in Table 3-6. Although the UV peak position remained unchanged, there is clearly a blue shift for the visible emission of Cr-doped sample as compared to undoped ZnO. A similar result was observed by Manoj et al. [298], with the difference that the intensity of the NBE peak has increased in our case compared to the undoped sample. The PL measurement also confirms the strong wurtzite phase for our undoped and Cr-doped samples in agreement with our previous analysis results. The defect emission of our Cr-doped sample decreased significantly as compared to the undoped ZnO. XPS results show an increased concentration of oxygen. Therefore, the defect emission reduction can be related to the lower number of oxygen vacancies centers in the Cr-doped nanorods crystal lattice. The defect emission reduction has also been attributed to the formation of new recombination pathways by Cr^{3+} addition [179]. The slight increase in the blue region (425 nm) of PL spectra can be related to the formation of Cr^{3+} compounds in the host crystal lattice in accord with our XPS and XRD results. In fact, this peak arises from recombination of a bound exciton between a shallow Cr^{3+} donor level and valence band hole [294]. The intensity of the NBE peak has increased significantly for our Cr-doped ZnO nanorods as compared to undoped ZnO. This can be due to the larger Cr-doped nanorods sizes than undoped ZnO nanorods. Radiative recombination of those electron and holes will be exploit in NBE emission larger peak. Another reason for the NBE enhancement might be related to the decrease in the number of nonradiative centers or defect centers in undoped ZnO by Cr^{3+} addition. Therefore, the optical properties of ZnO can be slightly tuned by Cr^{3+} addition.

3.7 Effect of different concentration of Na doping on optical and structural properties of ZnO nanorods

As synthesized ZnO is naturally a n-type material due to the donor nature of its intrinsic defect points. Finding a reliable way to fabricate a p-type ZnO is crucial for future optoelectronic devices. Na is one of the suitable candidates in the group I elements as a dopant to achieve stable p-type ZnO. Na has a shallow acceptor level between 164 and 170 meV and provides a high hole concentration up to 3×10^{18} cm^{-3} [299]. Theoretically, Na^+ can enter the ZnO lattice interstitially in combination with neighbouring oxygen vacancies [300]. In addition, the photovoltaic properties of ZnO nanorods can be improved by Na^+ addition [301]. This enhancement was attributed to the smaller number of intrinsic defects in Na-doped nanorods as compared to undoped ZnO. In the same direction, Lee et al. [302] reported an improved photoelectrochemical water splitting photocurrent for ZnO doped with Na^+. Besides, it has been shown that the photo-induced hydrophilicity of ZnO thin film can be modified by Na^+ addition [303]. Thus, Na-doped ZnO thin films can be potentially used in the production of self-cleaning coatings, antifogging materials or microfluidic devices. Na^+ doping can also increase the photocatalytic performance of ZnO for organic pollutants in water [304].

Na-doped ZnO has been prepared by various methods [299, 302, 305-309]. Hydrothermal growth of Na-doped ZnO nanorods has been recently reported by Yue et al.[310]. They used NaCl as the dopant precursor, where Na^+ addition significantly affected the aspect ratio of nanorods. In this report, for the first time we report the Na-doped synthesis of free standing arrays of ZnO nanorods by using different concentrations of $NaNO_3$ via hydrothermal method at temperatures as low as 60℃. The effect of different concentrations of Na^+ cations on the morphology, crystal structure, surface chemicals, and photoluminescence of the ZnO nanorods are discussed.

The growth was done by dissolving different concentrations (0.1 M, 0.25 M, 0.5 M, and 1 M) of $NaNO_3$ in DI water. The Na^+ solution was then added to the growth solution containing zinc nitrate and HMTA with 1:1 ratios with concentration of 25 mM. The substrate cleaning and seed layer preparation are discussed in chapter 2. We identify each sample by its dopant concentration through this report. ZnO nanorods doped with different concentration of Na^+ showed different morphological, structural and optical properties.

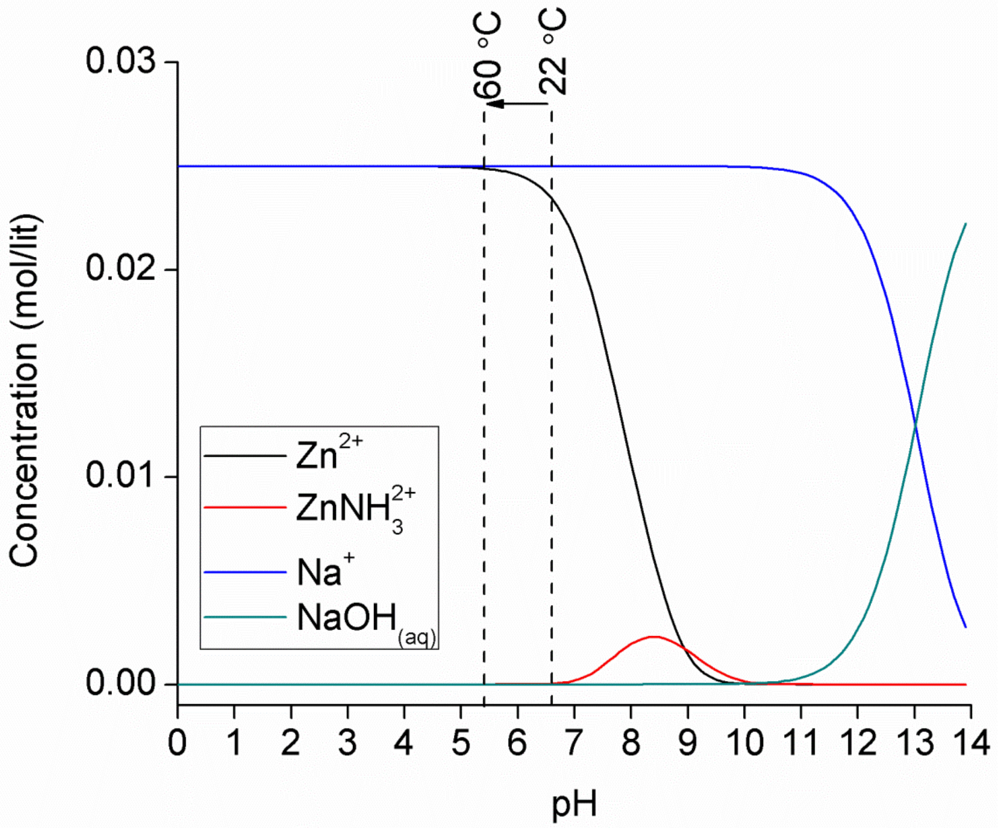

Figure 3.56 Speciation diagrams of Na species at 60 °C with concentration of 25 mM as a function of pH ranging from 0 to 14 as computed with Visual MINTEQ software.

The speciation diagram of Na$^+$ with the concentration of 50 mM is shown in Figure 3.56. It can be seen that at the early stage of the growth, the only cationic species which forms are Na$^+$, and Zn^{2+}. Similarly, the broad range of pH in which Na can exist in the form of Na$^+$ implies that higher concentration of Na$^+$ (> 50 mM) can be introduced to the growth solution as the dopant.

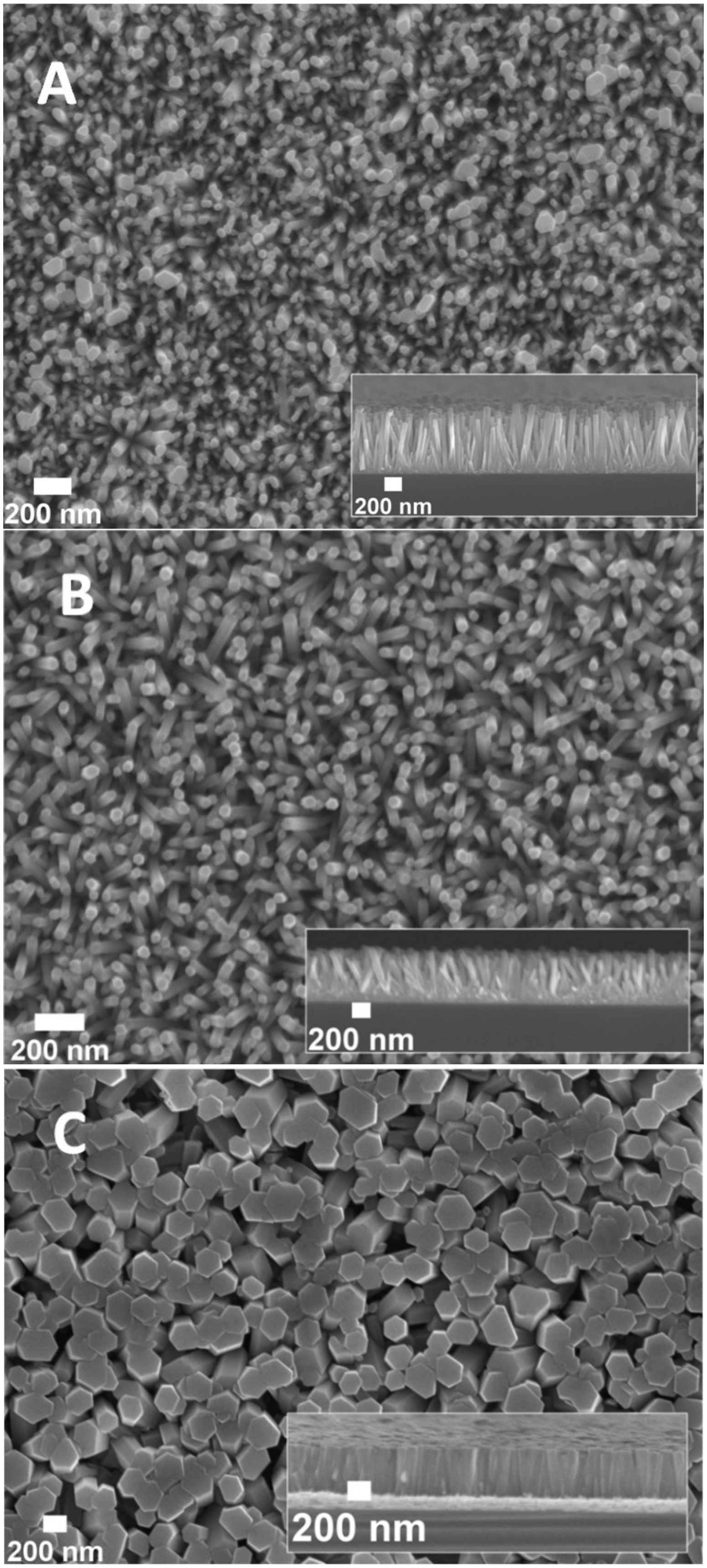
A
200 nm
200 nm
B
200 nm
200 nm
C
200 nm
200 nm

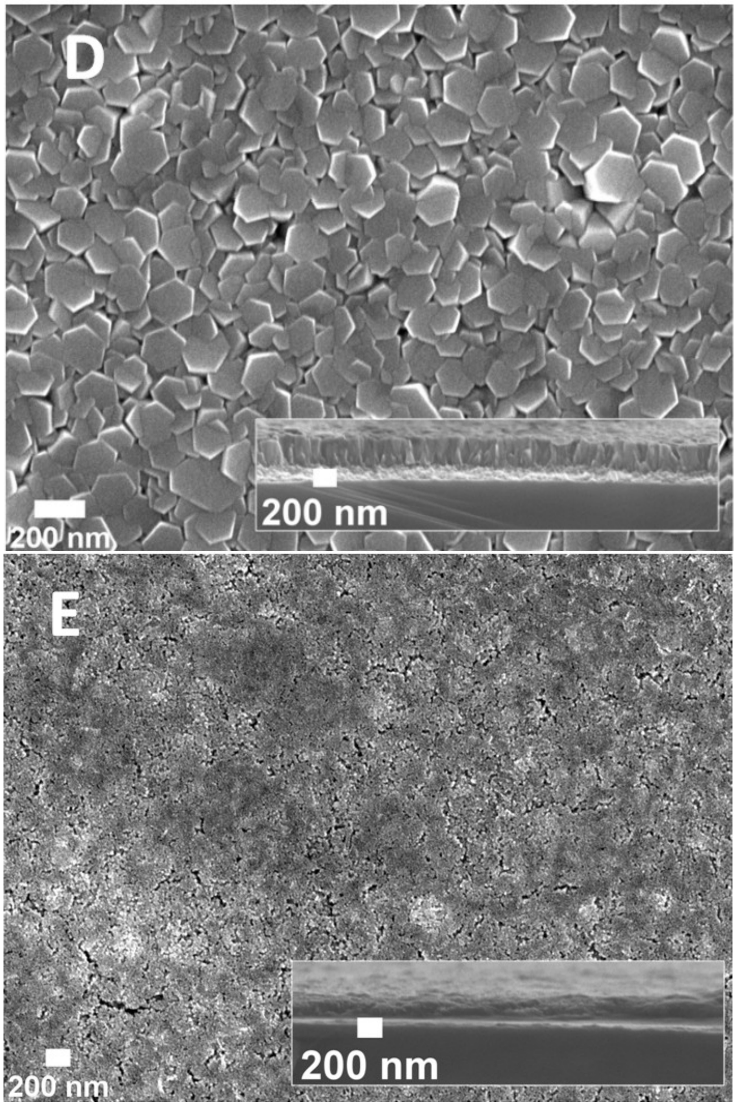

Figure 3.57 SEM images of the top and cross section of A) undoped ZnO B) 0.1 M C) 0.25 M D) 0.50 M E) 1 M Na-doped ZnO nanorods grown at 60℃ on silicon substrates.

The SEM images of the undoped ZnO nanorods and Na-doped ZnO nanorods with different concentrations are shown in Figure 3.57. The evolution of height and diameter of ZnO nanorods as a function of $NaNO_3$ concentration is shown in Figure 3.58. It can be seen that the nanorods diameter gradually increased proportional to the Na^+ concentration in the growth solution. From Figure 3.58, it appears that the trend of diameter growing slows down for high Na^+ concentrations. In the case of 1 M Na^+ doping concentration nanorods disappeared and a thin film of Na-doped ZnO was formed instead. We believe that by increasing the dopant concentration the possibility of coalescence of nanorods rises due to the larger diameters. This process continues until the nanorods loose their shape and a thin film of Na-doped ZnO is formed as shown in Figure 3.58(E).

The nanorods' height decreased gradually by Na^+ addition. The increase of diameter and decrease of height as a function of NaCl doping concentration was reported before [301, 310]. An average diameter reduction of ZnO nanorods by $NaNO_3$ addition was also reported before by Ko et al. [309]. Lee et al.[302] have also observed a similar trend and they have explained this effect based on the mass conservation rule. According to this rule the longer the nanorods grow, the smaller diameter will become and vice versa. The proposed model matches to our results, where longer nanorods gained smaller diameters.

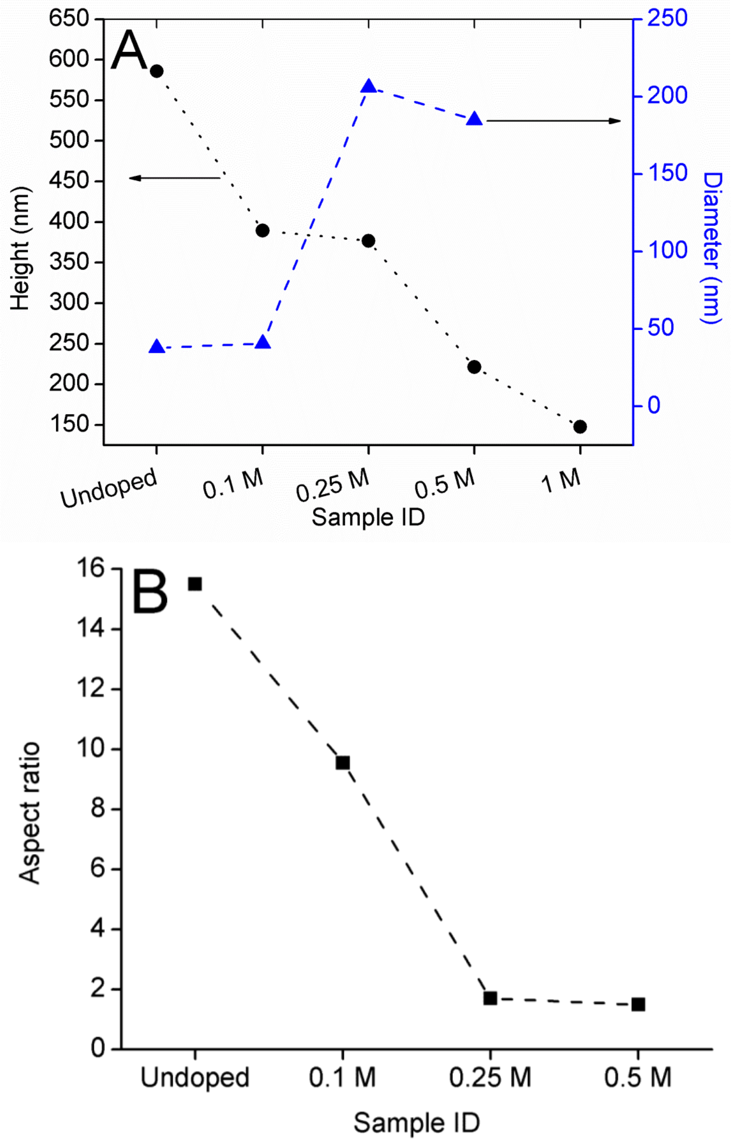

Figure 3.58 A) Height and Diameter distribution and B) Aspect ratio of undoped and Na-doped ZnO nanorods.

The aspect ratio variation of Na-doped ZnO nanorods was calculated based on their SEM images, and the results are shown in Figure 3.58(B). The data shows a decline in the aspect ratio of the Na-doped nanorods as a function of the dopant concentration. In fact, Na^+ ions which are released in the growth solution can be effectively attracted onto the (002) planes, inhibiting the nanorod growth along the [001] direction [302]. Therefore, the aspect ratio of the nanorods declined as relatively large amount of $NaNO_3$ was introduced to the growth solution. Based on our SEM images showed in Figure 3.57 it can be concluded that low level of incorporation of Na into ZnO host lattice has almost no effect on the hexagonal rod shape; whereas at higher concentration the morphology of the nanorods is under strong affect by Na^+ cations.

The crystal phase of undoped and Na-doped ZnO nanorods was investigated by XRD and the patterns are shown in Figure 3.60. The majority of the peaks are assigned to hexagonal wurtzite ZnO crystal structure. An extra peak (assigned with an asterisk) was detected at ~ 52°. This peak is related to ZnO_2 cubic phase according to the PDF card 13-0311. The conversion of ZnO nanorods into thin film at higher dopant concentration can be explained by the new phase formation which is detected in the XRD patterns. We believe that the * peak disappeared for the 0.25 M sample due to the major incorporation of Na^+ cations into the interstitial centers across the ZnO host lattice. Comparing the intensity of XRD patterns shows that the crystallinity changed along different crystal planes as Na^+ incorporated into ZnO crystal lattice. This change could be due to different atomic environment in ZnO crystal as a result of the presence of an impurity [127]. Our XRD results suggest that nanorods grow more effectively along their A and B axis`s by Na^+ addition in agreement with our SEM images shown in Figure 3.57, where thicker nanorods were obtained by Na^+ addition. By applying the crystallographic data of Figure 3.59 into equation 3-1 the degree of alignment of Na-doped nanorods was calculated. The calculation results are summarized in Table 3-1. It can be seen that the degree of crystal orientation of nanorods has been reduced by Na^+ addition.

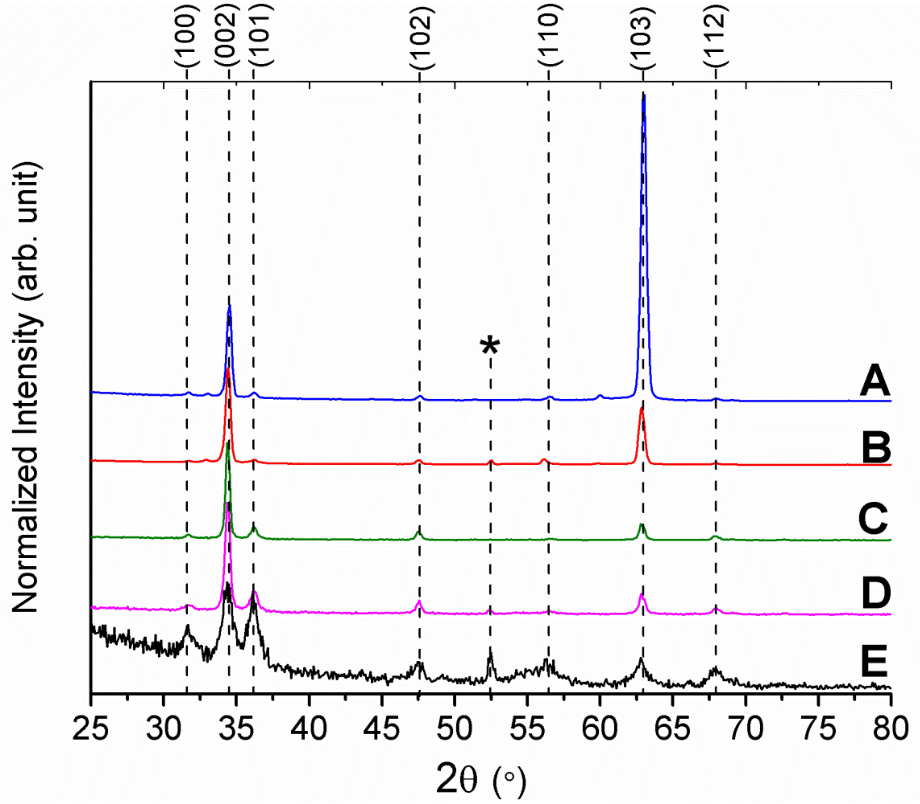

Figure 3.59 XRD patterns of A) undoped ZnO nanorods B) 0.1 M $NaNO_3$ C) 0.25 M $NaNO_3$ D) 0.50 M $NaNO_3$ E) 1 M $NaNO_3$ samples. (Traces were shifted vertically for visibility)

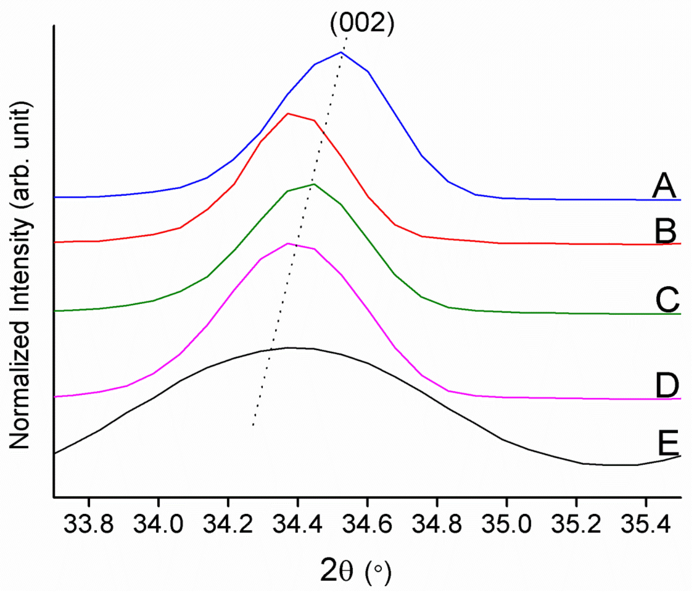

Figure 3.60 High resolution (002) peak position of A) undoped ZnO nanorods B) 0.1 M $NaNO_3$ C) 0.25 M $NaNO_3$ D) 0.50 M $NaNO_3$ E) 1 M $NaNO_3$ samples. (Traces were shifted vertically for visibility)

High resolution peak position of (002) plane of undoped and Na-doped nanorods are shown in Figure 3.60. The (002) plane of Na-doped sample has gradually shifted towards the lower 2Θ angle due to a lattice deformation. The small shift implies slightly higher lattice constant along the c-axis as well as larger crystal plane spacing for the Na-doped samples in comparison to the undoped ZnO. The lattice parameters data are illustrated in Figure 3.61(A). The results show that the lattice constants are increased by incorporation of Na^+ into the ZnO host lattice. Similar results were reported before and the lattice parameter enhancement was attributed to the substitution of smaller Zn^{2+} (0.74 $\overset{\circ}{A}$) ions with larger Na^+ (0.95 $\overset{\circ}{A}$) ions [299, 305, 311]. The drop in the lattice constant of the 0.25 M sample can be related to the stress release of nanorods as a result of occupancy of interstitial centers by Na^+ cations at higher doping concentration [305, 312]. A summary of crystal lattice information of undoped and Na-doped samples is given in Table 3-1. It can be seen that the FWHM of the (002) peaks is gradually increased by Na^+ addition.

Table 3-1 Experimental results of crystal characterization of undoped and Na-doped ZnO nanorods

Sample ID	(002) Peak Position *2Θ* (˚)	Plane Spacing (Å)	Lattice Constant (Å)	FWHM (˚)	Degree of Texture
Undoped ZnO	34.52	2.594	5.189	0.3957	82%
0.10 M $NaNO_3$	34.39	2.604	5.208	0.3469	83%
0.25 M $NaNO_3$	34.43	2.601	5.203	0.4021	90%
0.50 M $NaNO_3$	34.37	2.606	5.212	0.4247	76%
1 M $NaNO_3$	34.34	2.608	5.216	0.8338	39%

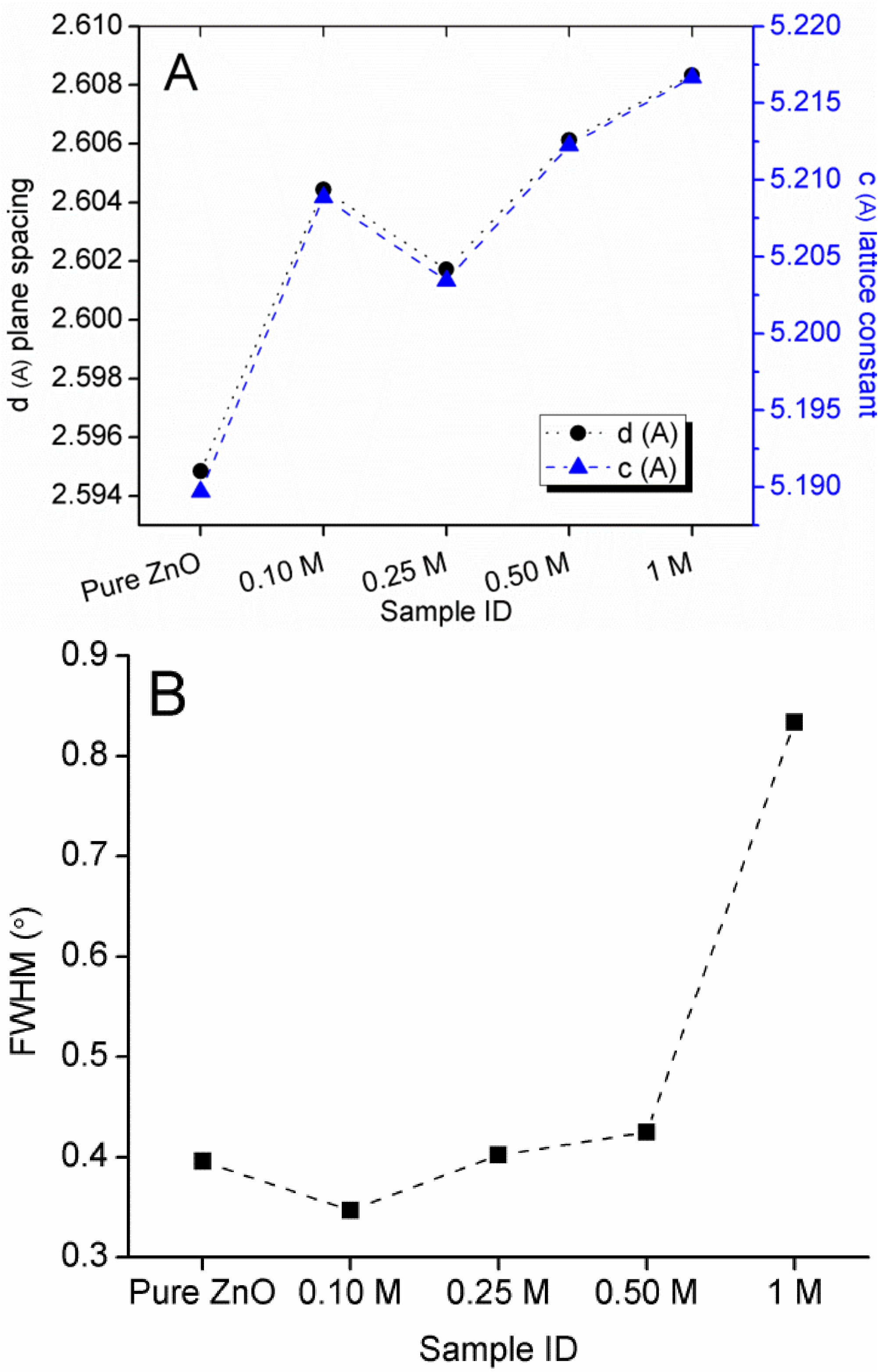

Figure 3.61 A) Plane spacing and c-lattice constant, B) FWHM of (002) peaks of undoped and Na-doped ZnO nanorods.

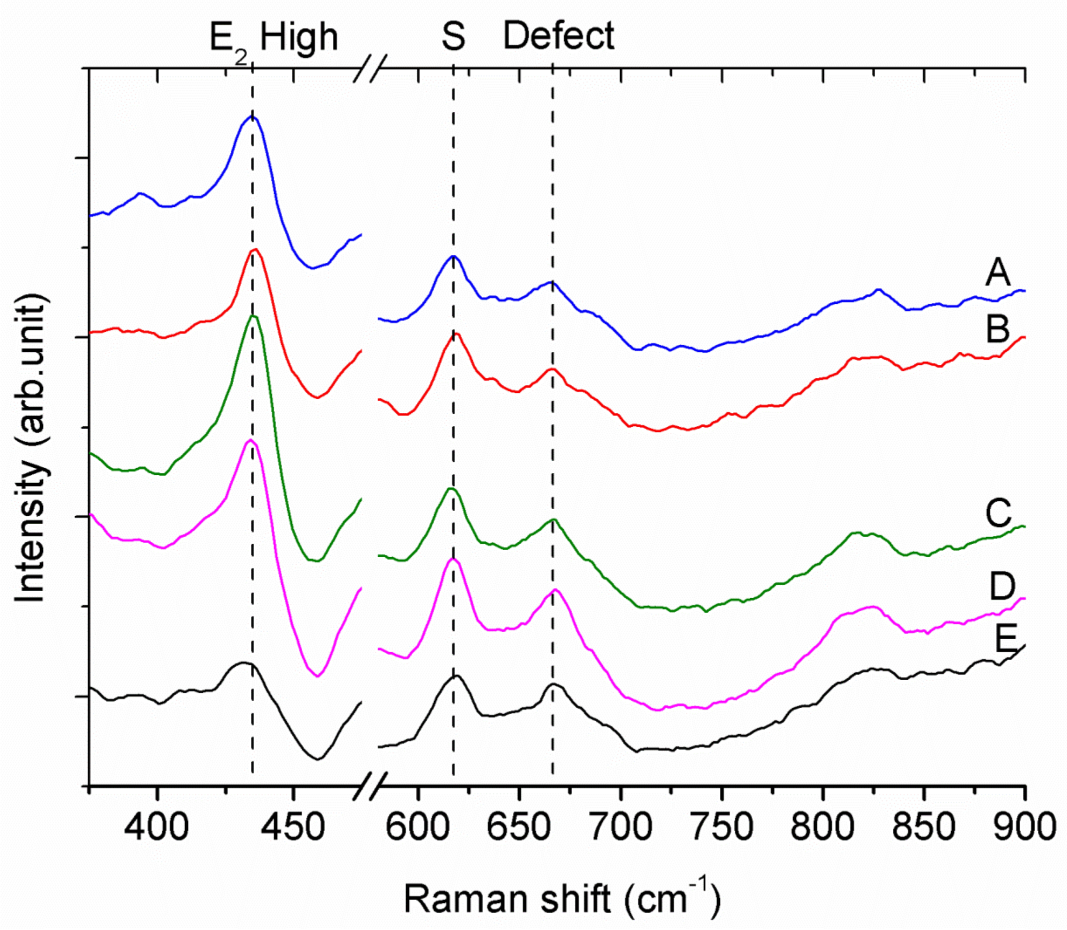

Figure 3.62 Micro-Raman spectra of A) undoped ZnO B) 0.1 M $NaNO_3$ C) 0.25 M $NaNO_3$ D) 0.50 M $NaNO_3$ E) 1 M $NaNO_3$ sample. (Traces were shifted vertically for visibility)

Figure 3.62 shows the Raman spectra of undoped and Na-doped ZnO nanorods doped with different concentration. The E_2(H) peak is evidence of strong wurtzite crystal orientation in Na-doped and undoped ZnO nanorods [112] demonstrating that the overall crystal structure of the ZnO nanorods is not affected by the doping process in accordance with our XRD results. The dominant E_2(H) peak also implies that the majority of nanorods are perpendicular to the substrate. On the other hand, E_2(H) peak of the 1 M Na-doped sample has broadened and slightly shifted to lower frequencies. A similar behaviour for the E_2(H) peak was reported before for ZnO doped with high Na^+ doping concentration [313, 314], and it was attributed to the formation of doping induced tensile stress along the ZnO crystal c-axis [314]. The asymmetric shape of this peak could be explained in terms of resonant anharmonic interaction of this mode with the band of combined transverse and longitudinal acoustic modes [135]. The S peak approximately centered at 616 cm^{-1} is due to the silicon substrate as has been reported before [134]. The similar shape and intensity of the small peak at 665 cm^{-1} implies that the number of the oxygen vacancies or zinc interstitials defect were not changed by Na^+ addition [136].

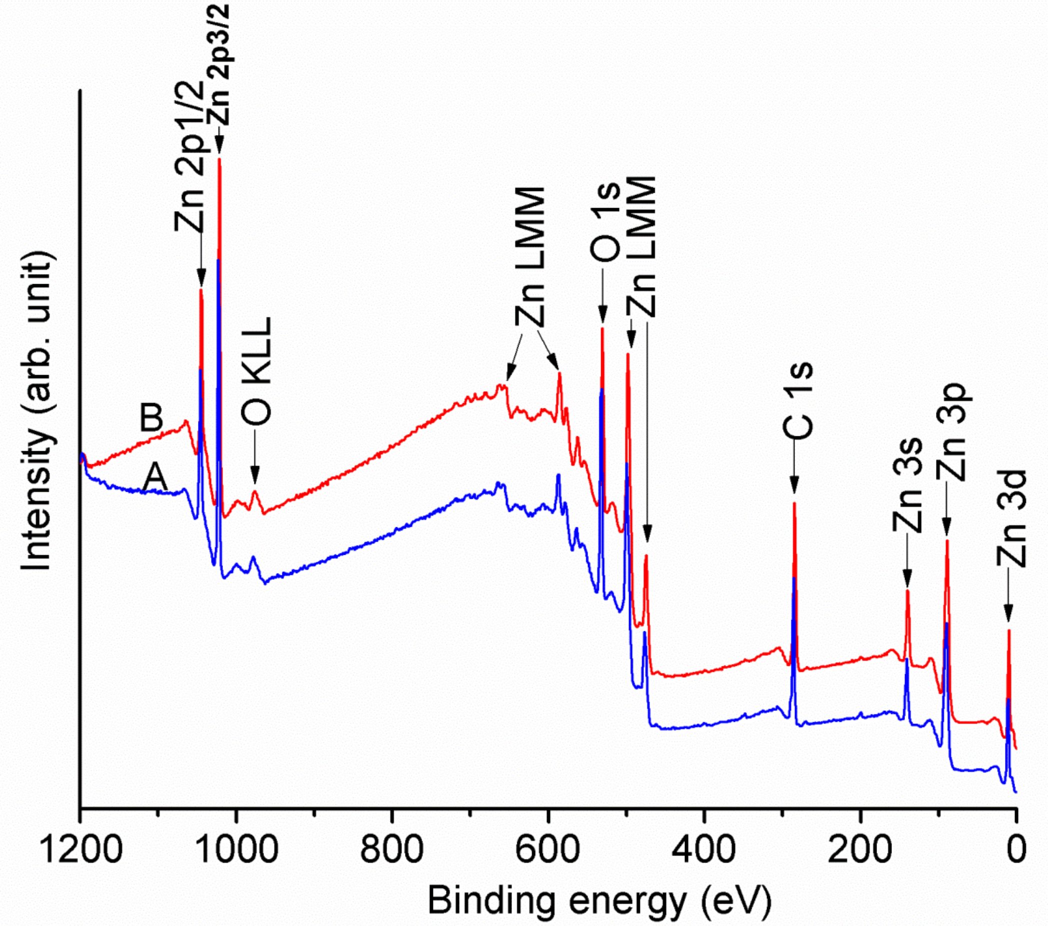

Figure 3.63 XPS spectra of A) undoped ZnO nanorods and B) 0.25 M sample. (Traces were shifted vertically for visibility)

The XPS spectra of undoped and 0.25 M Na-doped ZnO nanorods are shown in Figure 3.63. As can be seen there is a good agreement in XPS spectra of Na-doped and undoped ZnO nanorods. More precise measurements show that the Zn 2p peaks are shifted to lower energies (-0.4 eV) due to Na^+ addition. The peaks detected at 1021.3 eV and 1044.4 eV correspond to the Zn 2p3/2 and Zn 2p1/2 core levels, respectively in Na-doped sample XPS spectrum. Similarly, the binding energy shift can be related to the lower surface energy of Na-doped nanorods as compared to undoped ZnO nanorods. The FWHM of the Zn 2p peaks were also found to be smaller for the Na-doped sample (1.80 eV) as compared to the undoped nanorods (1.85 eV). This narrowing suggests the presence of less Zn states defects within Na-doped ZnO structure.

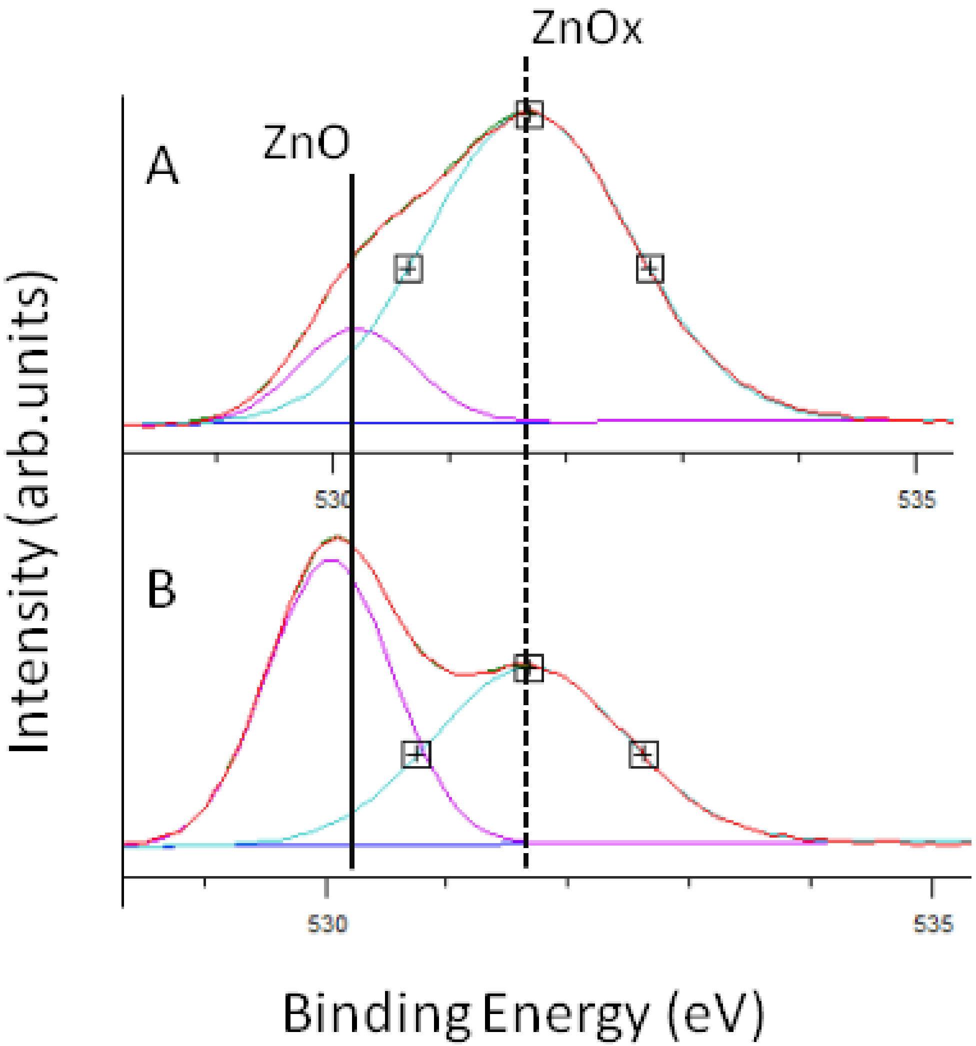

Figure 3.64 XPS O 1s peak of undoped and 0.25 M Na-doped ZnO nanorods.

The asymmetric shape of the O 1s peaks of undoped and Na-doped ZnO are shown in Figure 3.64. These peaks are deconvolved by two subspectral components at 530.2 eV and 531.6 eV. Based on the curve fitting results shown in Figure 3.64, the surface O_H percentage decreased to 48% after Na^+ addition which can be an evidence of better surroundings oxidized stoichiometric of Na-doped nanorods and/or less hydroxyl groups attached to their surface in comparison to undoped ZnO. In case of Na^+ doping the O 1s/Zn 2p ratio remained almost the same implying that the overall number of oxygen atoms versus zinc did not change by Na^+ addition. This speculation will be further investigated by PL measurements. Finally, the smaller surface percentage of the O_H peak should be related to the lower number of hydroxyl groups on the surface of our Na-doped ZnO as compared to undoped ZnO nanorods. The detection of Na^+

cations was not successful due to the XPS detection limit (~1 at% for light atoms), but their presence can be confirmed by EDS spectroscopy [308]. Typical EDS spectrum of 0.5 M sample is shown in Figure 3.65. The results show that Na^+ content of the 0.5 M sample is 6.2 weight% on average.

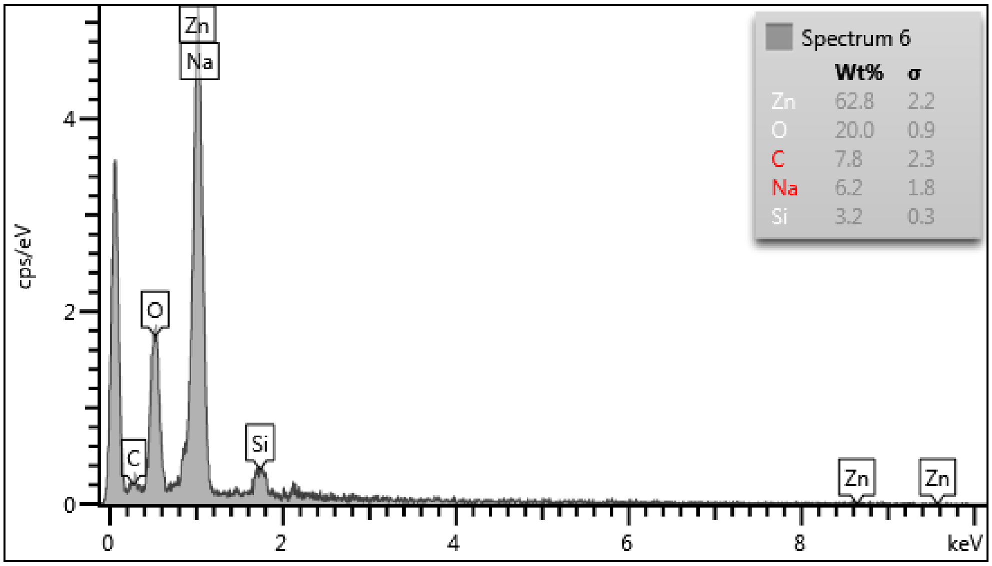

Figure 3.65 EDS elemental microanalysis of 0.5 M Na-doped ZnO nanorods.

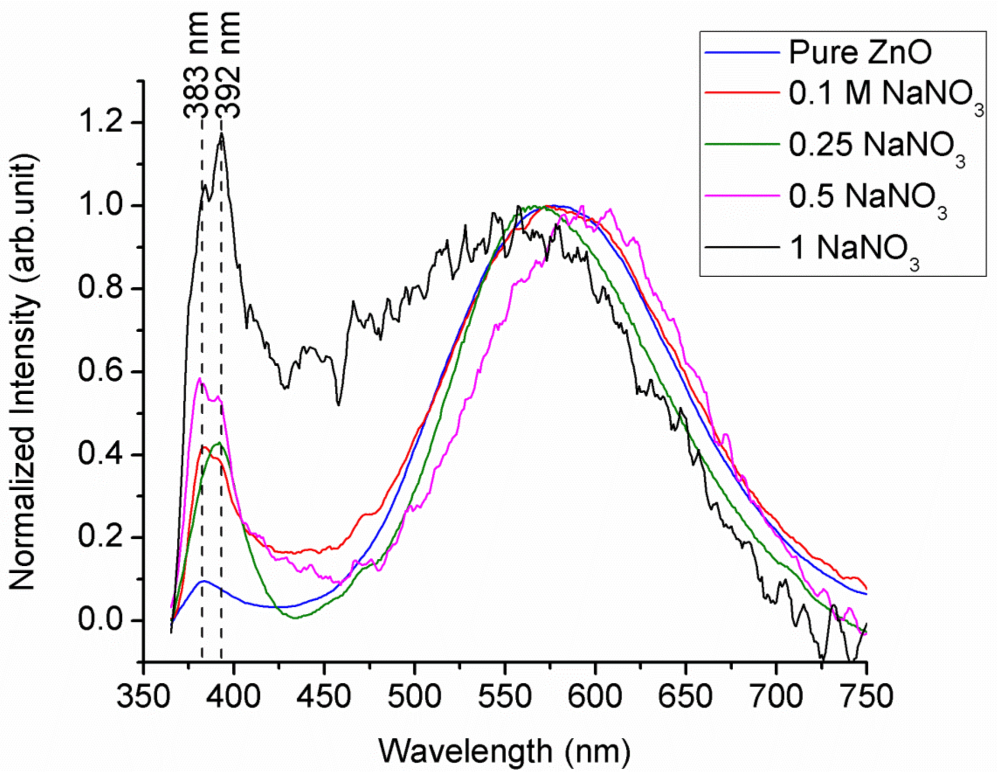

Figure 3.66 Room temperature PL spectra of undoped and Na-doped ZnO nanorods at different concentrations grown at 60℃ on silicon substrate.

Room temperature PL spectra were recorded for undoped and Na-doped ZnO nanorods with different concentrations, and the results are shown in Figure 3.66. Two peaks centered at 383 nm, and 392 nm were measured for undoped and Na-doped ZnO nanorods, respectively. The broad peaks detected at visible range centered roughly at 582 nm. PL measurements confirm the dominant wurtzite crystal for our undoped and Na-doped samples in consistent with our XRD and Raman results [119]. The NBE peak intensity of Na-doped samples increased as a function of Na^+ concentration. Similar results were reported before for low levels of Na^+ doping [301, 311]. Therefore, the stronger UV emission in the PL spectra of Na-doped samples can be related to the smaller amount of chemisorbed water, which is in consistent to their weaker O_H peak shown in Figure 3.64 [148]. Another reason for the NBE enhancement might be related to a decrease in the number of nonradiative centers in undoped ZnO by Na^+ addition [315].

As it can be seen in Figure 3.66 the UV peak started to split into two subspectral peaks by Na^+ addition. The first one, centered at ~383 nm, is representative of the undoped ZnO nanorods NBE, whereas the second peak (~392 nm) indicates to the band gap shrinkage of ZnO nanorods due to the Na^+ doping. The only exception is 0.25 M sample which shows only one narrow peak at 392 nm. The anomalous behavior of NBE peak of samples doped with different Na^+ dopant concentration is related to the different doping paths that Na atoms take during the growth.

As it has been mentioned before, ZnO has an open structure that can accommodate native defects such as zinc interstitials and oxygen vacancies [120]. The NBE shift of the doped samples is due to the Na^+ incorporation at those interstitial sites. It was suggested that at lower Na^+ doping concentration the majority of the dopants tend to substitute the zinc atoms rather than occupying the interstitials [305, 312].

The appearance of the peak at 392 nm in 0.1 M sample PL spectrum indicates to the start of the interstitials process. By further increase of the concentration to 0.25 M the interstitials occupancy process is enhanced which leads to the release of stress along the doped nanorods c-axis. The single peak at 392 nm for 0.25 M sample indicates that all the nanorods are uniformly doped with Na^+ at the concentration where Na to Zn ratio in the solution is 10:1. Moreover, the absence of a secondary phase peak in the XRD patterns as well as the smaller lattice constant of the 0.25 M sample in comparison to the other samples is the evidence of a dominant interstitials occupancy process. At higher concentration the NBE peak was split again. However, the peak at 392 nm for the 1 M doped sample is stronger than the peak at 383 nm in comparison to the samples which were doped with lower Na^+ concentration.

The higher intensity detected for the Na-doped samples in the region between 400 nm to 480 can be related to the formation of Na-O-Zn compounds which were detected in our XRD patterns. This peak is attributed to zinc vacancy defect points in previous reports [301, 311]. This peak has also been attributed to the formation of larger number of grain boundaries in the Na-doped ZnO crystal [316]. Therefore, the extra peak at ~450 nm can be due to the formation of Na^+ compounds, zinc vacancies or a larger number of grain boundaries in our high concentration Na-doped samples. The intensity of the defect related peaks remained unchanged suggesting that the Na^+ doping of ZnO by using our method does not affect the number of oxygen vacancies. This is also in accordance with our XPS results where the O/Zn ratio remained almost unchanged after Na^+ addition.

In summary, undoped and Na-doped ZnO nanorods with different dopant concentration were synthesized by using a hydrothermal method at temperatures as low as 60 ° C. According to the

SEM images at high doping morality (1 M) the nanorods convert into a thin film. Based on the morphology analysis, the aspect ratio of ZnO nanorods were decreased as a function of Na^+ doping concentration. XRD patterns proved the unchanged hexagonal crystal structure of ZnO nanorods doped with Na^+. Moreover, a gradual increase for the lattice constant of Na-doped sample along their c-axis was calculated. Room temperature micro-Raman spectrum confirmed the XRD results by depicting a strong $E_2(H)$ peak for all Na-doped samples, although it was broadened and slightly shifted to lower frequencies for higher Na^+ doping concentration (1 M). The weight% of Na-doped nanorods was measured to be 6.2% by EDS for 0.5 M sample. The XPS results indicate that the O/Zn atomic ratio was not significantly changed by the Na-doping process implying that the concentration of oxygen vacancies remained the same after doping it with Na^+. The PL measurement showed an extra UV peak for Na-doped samples at 392 nm. We attributed this peak to the NBE of Na-doped sample. Based on our PL spectrum analysis to achieve single phase Na-doped ZnO nanorods the molarity ratio of zinc to sodium in the growth solution must be 1:10. Then, all nanorods were uniformly doped with Na^+, and they only exhibit one single peak at 392 nm as their NBE. The broad visible emission which is attributed to the defect points remained almost the same for undoped and Na-doped samples indicating that the Na^+ doping does not affect the common defect centers in ZnO nanorods.

Results' summary of cation doping of ZnO nanorods

Table 3-2 Summary of geometry information of undoped and cation-doped ZnO nanorods

Sample	Diameter (nm)	Height (nm)	Aspect Ratio
Undoped ZnO	54	352	6.5
Mg-ZnO	104	677	6.5
Ni-ZnO	243	1200	4.9
Mn-ZnO	205	2100	10.2
Co-ZnO	168	731	4.3
Cu-ZnO	1900	4700	2.5
Cr-ZnO	1000	3900	3.9

Undoped ZnO nanorods were synthesized by using a hydrothermal method at temperatures as low as 60℃. Similarly, highly textured doped nanorods were synthesized by adding the dopant precursor to the growth solution. The morphology of the undoped and doped nanorods were imaged from the top and cross section by the SEM and their data are summarized in Table 3-2. Geometry information of the samples confirms that doping can significantly change the height and diameter of ZnO nanorods. The size enhancement in doped nanorods was attributed to the different cationic compounds that can be formed in the growth solution. Accordingly, Cu^{2+} addition yielded the lowest aspect ratio nanorods as compared to other used metal dopants in this project. This difference is connected to the face-selective electrostatic adsorption properties of Cu^{2+} cations. The highest aspect ratio, on the other hand, was achieved by Mn^{2+} addition. Mn-doped ZnO nanorods gained an aspect ratio as large as 10.2 in comparison to the 6.2 aspect ratio of undoped ZnO nanorods. The crystal structure of the undoped and doped nanorods was thoroughly investigated by XRD and the results are summarized in Table 3-3. Crystallographic results show that the low temperature doping has a small influence on the ZnO crystal plane spacing and lattice constant along the (002) direction. Moreover, XRD data shows that crystal quality has slightly degraded in general by dopant addition, mainly due to dopant-induced stress in the host crystal lattice.

Table 3-3 Experimental results of crystal characterization of undoped and cation-doped ZnO nanorods

Sample	(002) Peak Position 2Θ (˚)	Plane Spacing d (Å)	Lattice Constant c (Å)	FWHM (˚)	Degree of Texture
Undoped ZnO	34.52	2.59	5.18	0.3957	82%
Mg-ZnO	34.44	2.60	5.20	0.3921	69%
Ni-ZnO	34.35	2.60	5.21	0.4043	74%
Mn-ZnO	34.37	2.60	5.21	0.4043	91%
Co-ZnO	34.44	2.60	5.20	0.4021	94%
Cu-ZnO	34.37	2.60	5.21	0.4048	48%
Cr-ZnO	34.13	2.62	5.24	N/A	22%

Furthermore, results showed that the degree of texture is greatly under affect of dopant element. Comparing the results in Table 3-3 shows that the highest crystal alignment can be achieved by Co^{2+} and Mn^{2+} addition. In contrast, the minimum degree of texture was measured for Cr-doped ZnO nanorods, illustrating crystal degradation in that sample in comparison to the others.

Supplementary crystal information was obtained by room temperature micro-Raman analysis of the undoped and c-doped ZnO nanorods. The frequency's values of Raman active modes of undoped and c-doped samples are shown in Table 3-4. No significant shift was detected for the $E_2(H)$ peak as a typical ZnO wurtzite hexagonal crystal structure for the Mg and Ni-doped ZnO nanorods. This mode is shifted to higher frequencies as much as +3.9 cm^{-1} by Cu^{2+} addition which can be due to its large lattice distortion or its less oxygen deficient structure. In contrast, the $E_2(H)$ mode was shifted to lower frequency as large as -3.6 cm^{-1} by Cr^{3+} addition. We believe this shift is connected to its large dopant-induced tensile stress. The peak position for the other active modes remained essentially unaffected.

Table 3-4 Experimental measurement results of the active modes of undoped and cation-doped ZnO nanorods

Sample	E_2 Low (cm^{-1})	E_2 High (cm^{-1})	E_1(TO) (cm^{-1})
Undoped ZnO	78.8	437.7	403.9
Mg-ZnO	76.7	437.7	405.7
Ni-ZnO	78.7	437.7	403.8
Mn-ZnO	76.9	437.8	404.0
Co-ZnO	77.0	437.9	N/A
Cu- ZnO	78.8	441.6	403.9
Cr-ZnO	78.9	434.1	402.1

The chemical compositions of undoped and doped samples were investigated by XPS and EDS and the results are summarized in Table 3-5. The Zn 2p peak remained mainly unchanged except for Cu and Cr-doped samples. This peak was shifted +0.9 eV and +0.4 eV for Cu and Cr-doped nanorods, respectively. This shift is attributed to the surface band bending as a result of incorporation of cations into the ZnO crystal. Based on the data given in Table 3-5, the oxygen to zinc atomic number ratio was mostly reduced by cation doping, except for Cu^{2+} and Cr^{3+} dopants. This implies a reduction in the number of oxygen vacancy defect centers in those doped samples, as compared to undoped ZnO. The O 1s peak analysis also shows less hydroxyl groups attached to the surface of the doped nanorods except for the Cr-doped nanorods. Thus, the Cr-doped nanorods should be our most promising candidate for application in a photocatalytic active device. In our report, the amounts of Mn^{2+}, Cu^{2+}, and Cr^{3+} cations were directly measured by XPS, while the direct detection of Mg^{2+}, Ni^{2+}, and Co^{2+} cations were only possible by EDS due to their small incorporated amount. The maximum dopant content in our doped ZnO nanorods was for the Cr-doped sample and the minimum incorporation was in Ni and Co-doped samples. The variation of different doping elements amount can be related to their different solubility into ZnO host lattice.

Table 3-5 Experimental XPS and EDS measurement results of undoped and cation-doped ZnO nanorods

Sample	Zn-2P 3/2 (eV)	Zn-2P 1/2 (eV)	Spin-orbit interaction split	FWHM (Zn-2p 3/2) (eV)	Atomic Number ratio of O/Zn	O_L,O_H Approximate surface percentage	XPS doped Element Peak Position (eV)	Average Atomic %
Undoped ZnO	1021.7	1044.8	23.1	1.85	3.8	14%, 85%	N/A	N/A
Mg-ZnO	1021.5	1044.6	23.1	1.75	2.6	55%, 44%	No peak	0.5%
Ni-ZnO	1021.2	1044.4	23.2	1.79	3.3	47%, 52%	No peak	0.4%
Mn-ZnO	1021.3	1044.4	23.1	1.75	2.8	57%, 42%	640.5, 656	5.0%
Co-ZnO	1021.4	1044.5	23.1	1.76	3.1	51%, 48%	No peak	0.4%
Cu-ZnO	1022.6	1045.6	23	2.50	13.2	44%, 24%	932.8, 952.6	3.0%
Cr-ZnO	1022.1	1045.2	23.1	1.90	15.5	0%, 100%	578, 587.5	19.0%

In order to investigate the effect of cation doping on the optical properties of ZnO nanorods, room temperature PL measurements were done and the results are shown in Table 3-6. Two main peaks were detected at UV and visible regions for all the samples which are typical of ZnO hexagonal nanorods synthesized by a hydrothermal method. The relatively narrow NBE peak was detected with slightly different intensities and wavelengths. The highest NBE peak area was related to the Cu-doped ZnO nanorods which can be due to their large sizes. The cation doping provoked a red shift in NBE peak position of ZnO nanorods in comparison to the undoped ZnO nanorods except for the Cr-doped sample. The biggest shift was obtained for Co-doped nanorods showing the biggest impact of doping on its host lattice band gap. The defect-attributed peaks were mainly detected at the same region for all the samples, yet with different peak areas, which indicate the difference in the number and type of defect centers for different doped nanorods. The lowest defect emission peak area was obtained for Cr-doped ZnO which also yielded the highest NBE/defect emission ratio as compared to the other doped samples. The Cu-doped sample shows the second highest NBE/defect ratio (70%). This can be due to the larger sizes of the nanorods and their lower number of oxygen vacancy sites. Experimental results of some of the recent reports are also included in Table 3-6 for comparison purposes. Finally, this report can be used as a comprehensive reference for engineering of the morphological, structural and optical properties of ZnO nanorods which are prepared using a low temperature doping synthesis as an economical mass production approach.

Table 3-6 Room temperature PL measurement results obtained for undoped and cation-doped ZnO nanorods

Sample	NBE Peak (nm)	Photon energy difference (meV)	NBE Peak Area	Defect Emission Peak (nm)	Defect Emission Area	NBE/Defect Ratio	Bandgap Shift, our results (nm)	Bandgap Shift (nm)
Undoped ZnO	383	N/A	6.8×10^6	578	1.1×10^8	6.18 %	N/A	N/A
Mg-ZnO	388	42	2.0×10^7	581	4.2×10^8	8.3 %	-5	-5 [153]
Ni-ZnO	386	25	1.6×10^7	585	1.3×10^8	12.0 %	-3	-5 [7]
Mn-ZnO	388	42	7.4×10^6	586	1.5×10^8	5.0 %	-5	-3 [179]
Co-ZnO	391	67	1.2×10^6	593	2.6×10^7	4.6 %	-8	-2 [234]
Cu-ZnO	387	34	3.6×10^7	576	5.1×10^7	70 %	-4	-6 [259]
Cr-ZnO	383	0	2.9×10^7	578	9.1×10^6	310 %	0	0 [298]

Chapter 4 Conclusion and future approach

We have grown well-separated single ZnO nanorods in an arbitrary pattern on different substrates including glass and silicon, using a thin texture film of ZnO nanoparticles known as seed layer to compensate for crystal mismatch. Based on XRD results, in order to achieve the best crystal orientation the seed layer must be annealed at temperatures over 300℃. Raman scattering spectra confirm that as-grown and patterned nanorods have the same wurtzite crystal structure and orientation, although we see a slight tilt of the c-axis in the patterned ZnO nanorods. Micro-PL of both patterned and as-grown ZnO nanorods show a sharp narrow peak at NBE confirming their high quality crystal structure. In addition, we found negligible visible emission in the PL spectrum of the seed layer, implying that the majority of the defect emission is arising from bulk defects such as zinc and oxygen vacancies or lattice imperfections. The proposed method is a practical technique for synthesizing positioned controlled single ZnO nanorods on any type of substrates for applications where low aspect ratios are desirable, such as optoelectronic structures supporting a single transversal optical mode.

Undoped and C-doped (C: Mg^{2+}, Ni^{2+}, Mn^{2+}, Co^{2+}, Cu^{2+}, Cr^{3+}) ZnO nanorods were synthesized by a hydrothermal method at temperatures as low as 60 ℃. The effect of doping on

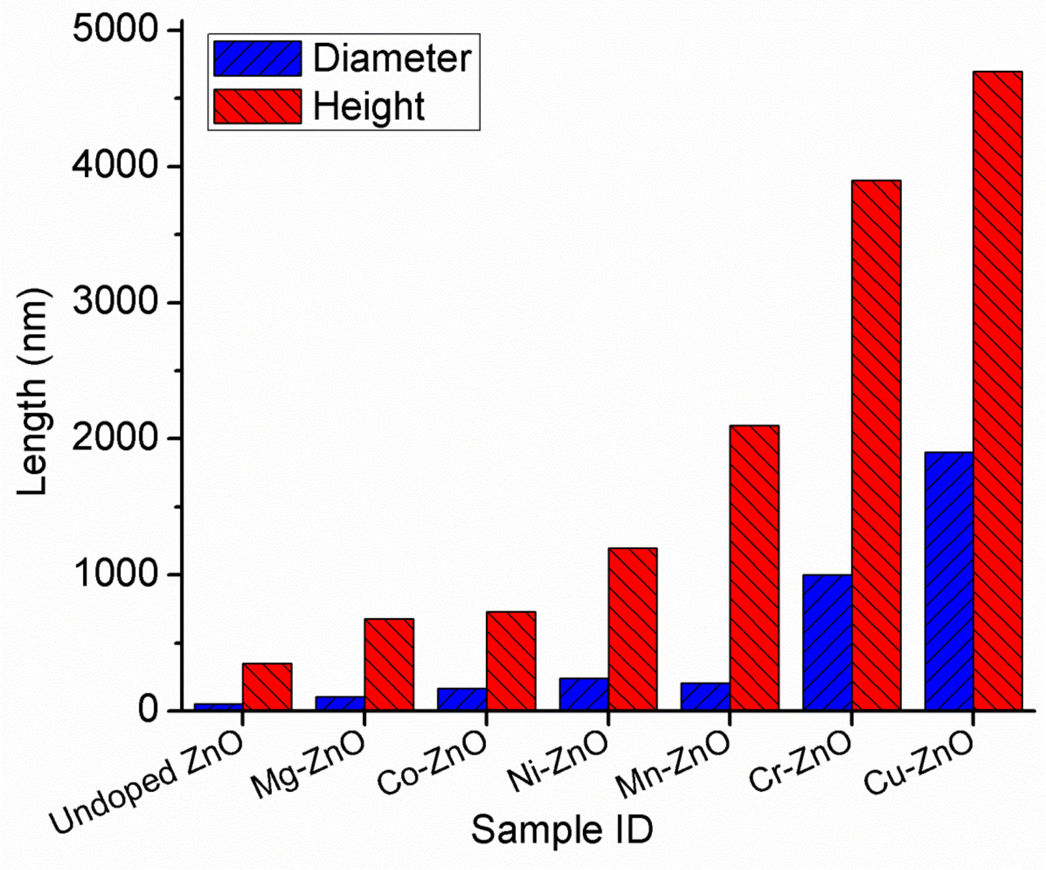

Figure 4.1 Summary of the height and diameter of the undoped and cation-doped ZnO nanorods, grown at 60℃ by a hydrothermal method.

morphology of the ZnO nanorods was visualized by taking their cross section and top SEM images. Geometry information of the samples confirms that cation doping can significantly change the height and diameter of ZnO nanorods. The effect of each cation dopants on the geometry of ZnO nanorods is summarized in Figure 4.1. The Cu^{2+} addition yielded the highest increase in height of the nanorods, yet lowest aspect ratio nanorods as compared to other cation dopants. The Mg^{2+} addition, on the other hand, had the smallest effect on the geometry of the doepd ZnO nanorods. The highest aspect ratio, was achieved by Mn^{2+} addition. Mn-doped ZnO nanorods gain an aspect ratio as large as 10.2 in comparisons to the 6.2 aspect ratio of undoped ZnO nanorods. Therefore, in terms of the morphology Mn^{2+} is the best choice for fabrication of single ZnO nanorods photonic based devices. Since, it provides the largest aspect ratio adjustment range, which is the main factor in terms of geometry in an optoelectronic device.

The crystallinity change of the ZnO nanorods due to each doping element was thoroughly investigated according to their X-ray Diffraction (XRD) patterns. Crystallographic results show that the low temperature doping has a small influence on ZnO crystal plane spacing and lattice constant along the (002) plane direction. However, data show that in general crystal quality was slightly degraded by dopant addition, mainly due to dopant induced stress in the host crystal lattice. Furthermore, the degree of texture is greatly affected by the cation doping. The highest crystal alignment can be achieved by Co^{2+} and Mn^{2+} addition as it is shown in Figure 4.2. In contrast, the minimum degree of texture was measured for Cr-doped ZnO nanorods, as a sign of its significant crystal degradation in comparison to the undoped ZnO.

The optical Raman active modes of undoped and doped nanorods were measured with a micro-Raman set up at room temperature. Micro-Raman analysis shows that the E_2(H) peak position, which is typical of hexagonal ZnO wurtzite, is not significantly shifted by cation addition except for Cu^{2+} and Cr^{2+}. This mode was shifted to higher frequency (+3.9 cm^{-1}) by Cu^{2+} addition which could be due to the large induced-lattice distortion or its less oxygen deficient structure. In contrast, the E_2(H) mode has shifted to lower frequency (-3.6 cm^{-1}) with the addition of Cr^{2+}. We believe this shift is connected to the large lattice tensile stress induced by the dopant. The peak position for the other active modes remained free of significant changes.

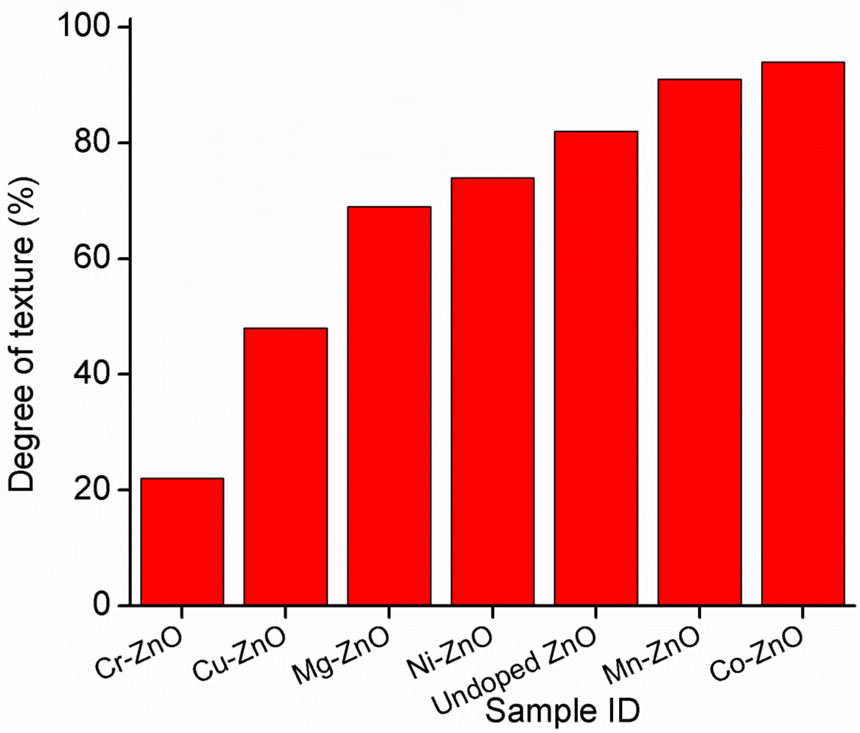

Figure 4.2 Effect of different cation dopants on degree of texture of ZnO nanorods grown at 60℃ on silicon substrate.

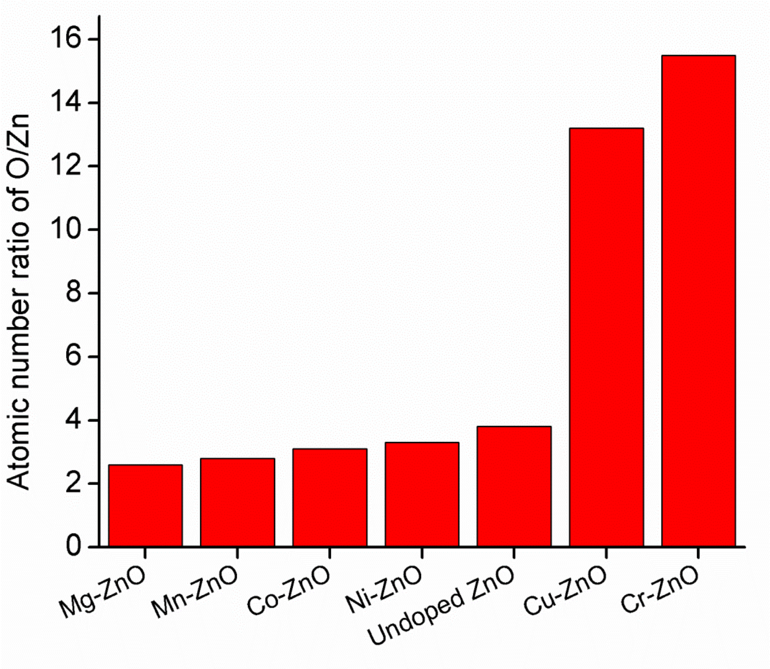

Figure 4.3 Atomic number ratio of O/Zn of undoped and cation-doped ZnO nanorods grown at 60℃ by a hydrothermal method.

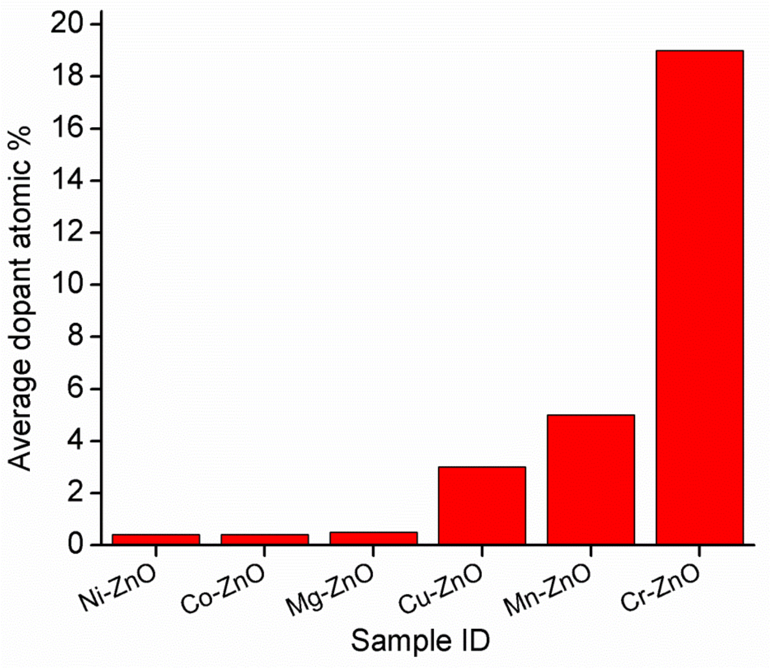

Figure 4.4 Average dopant atomic % of cation-doped ZnO nanorods grown at 60℃ by a hydrothermal method.

The surface chemistry of undoped and doped ZnO nanorods were investigated by XPS and EDS. The Zn 2p peak remained mainly unchanged except for the Cu^{2+} and Cr-doped samples.

This peak was shifted by +09 eV and +0.4 eV for Cu^{2+} and Cr-doped nanorods, respectively. This shift is attributed to the surface band bending decline, or incorporation of dopant ions into ZnO crystal. The oxygen to zinc atomic number ratio was measured and the trend is shown in Figure 4.3. It can be seen that this factor is mainly reduced by cation doping, except for Cu^{2+} and Cr^{2+} dopants which implies less oxygen vacancy defect centers as compared to undoped ZnO. The O 1s peak analysis also shows less hydroxyl groups attached to the surface of the doped nanorods except for the Cr-doped nanorods. In our report, the amount of Mn^{2+}, Cu^{2+}, and Cr^{3+} doped cations were directly measured by XPS, while the direct detection of Mg^{2+}, Ni^{2+}, and Co^{2+} dopant was only possible by EDS due to their small amount of incorporation. The cations incorporation trend is summarized in Figure 4.4. The maximum detected dopant content in our doped ZnO nanorods was Cr^{3+} and the minimum incorporation was with Ni^{2+} and Co^{2+} cations. The large percentage of detected Cr^{3+} can be related to signal from the surface of the substrate rather than the Cr^{3+} doped cations. The variation in the amount of incorporated doping elements can be related to their different solubility in the ZnO host lattice.

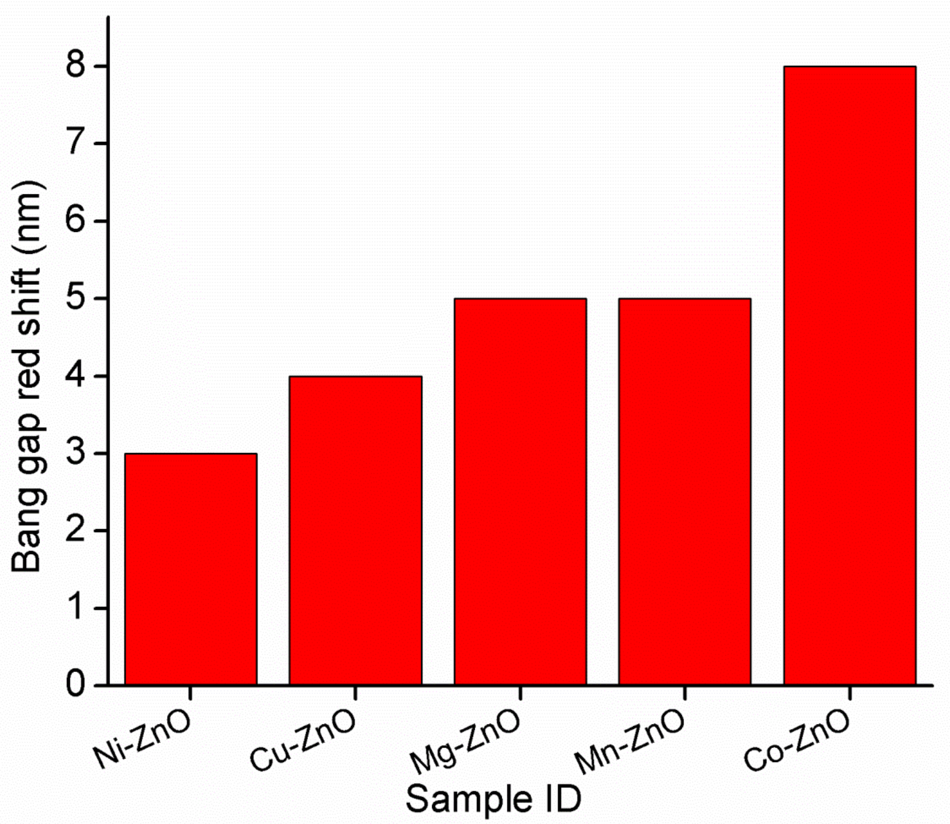

Figure 4.5 Band gap shift of ZnO nanorods, doped with different cations at 60℃ by using a hydrothermal method.

The band gap and defect emission of undoped and doped nanorods were measured by a PL setup at room temperature and the results are shown in Figure 4.5. Two main peaks were detected for all samples which are typical of ZnO hexagonal nanorods synthesized by hydrothermal methods. The relatively narrow peak (NBE) was detected in the UV region for all the samples with slightly different intensities and wavelengths. The highest NBE peak area was obtained for Cu-doped ZnO nanorods which can be related to their largest size as compared to the undoped and other doped nanorods. Our results show that doping caused a red shift in NBE peak position of ZnO nanorods in comparison to our undoped ZnO nanorods except for Cr-doped sample. The largest shift (8 nm) was obtained for Co-doped nanorods. The NBE red shift is mainly attributed to the strong interaction between the dopant and the lattice electronic orbitals. The wide peak detected at visible region is commonly attributed to defect centers in the ZnO crystal lattice. These peaks were mostly detected in the same region for all the samples, yet with different peak areas indicating a difference in the number and the type of defect centers in doped nanorods. The lowest defect emission peak area was obtained for Cr-doped ZnO yielding the highest NBE/defect ratio. The Cu-doped sample shows the second highest NBE/defect ratio (70%). This can be due to the larger size of the nanorods and their lower oxygen vacancy sites.

In the final step, ZnO nanorods were doped with different concentration of Na^+ by using a hydrothermal method at temperatures as low as 60 °C. Results show that at high doping molarity (1 M), the nanorods converted into a thin film. The aspect ratio of ZnO nanorods were gradually decreased as a function of the Na^+ concentration. XRD patterns proved the unchanged hexagonal crystal structure of ZnO nanorods doped with Na^+. Moreover, a gradual increase for the lattice constant of Na-doped sample along their c-axis was calculated. Room temperature micro-Raman spectrum confirmed the XRD results by depicting an strong $E_2(H)$ peaks for all Na-doped samples, although the peak was broadened and slightly shifted to lower frequencies for higher Na^+ doping concentration (1 M). The weight% of Na-doped nanorods was measured to be 6.2% by EDS for 0.5 M sample. The XPS results indicate that the O/Zn atomic ratio was not significantly changed by Na^+ doping implying that the concentration of oxygen vacancies remained constant after doping it with Na^+. The PL measurement showed an extra UV peak for Na-doped samples at 392 nm. We attributed this peak to the NBE of Na-doped sample. Based on our PL spectrum analysis to achieve single phase Na-doped ZnO nanorods the molarity ratio of zinc to sodium in the growth solution must be 1:10. For this ratio, all nanorods were uniformly doped with Na^+, and they only exhibit one single peak at 392 nm as their NBE. No significant change was detected in the broad visible emission attributed to the defect points in Na-doped samples. The PL spectra indicating that the common defect centers in ZnO nanorods were not affected by Na^+ doping.

Table 4-1 Summary of properties of the cation doped ZnO nanorods in comparison to the undoped sample

	Undoped	Mg^{2+}	Ni^{2+}	Mn^{2+}	Co^{2+}	Cu^{2+}	Cr^{3+}
Aspect ratio	6.5	6.5	4.9	10.2	4.3	2.5	3.9
Degree of texture (%)	82	69	74	91	94	48	22
O/Zn atomic number ratio	3.8	2.6	3.3	2.8	3.1	13.2	15.5
Photon energy difference (meV)	N/A	42	25	42	67	34	0

A general summary for comparison of the most significant properties of cation doped ZnO nanorods is shown in Table 4-1. Our results can be used as a comprehensive reference regarding the engineering of the morphological, structural and optical properties of doped ZnO nanorods by using a low temperature doping synthesis as an economical mass production approach. As a next step one needs to find the optimum concentration of each cation dopant for a purpose-built device. By combining the patterning technique (chapter 2) with the cation doping synthesis of ZnO nanorods, one can grow well separated cation doped ZnO nanorods. Moreover, by repeating the growth on the same sample with and without doping precursor, one can fabricate an epitaxial hetero-structure of ZnO nanocrystal in a single nanorod. This could be a fascinating approach towards the observation of strong light-material interactions. However, It should be noted that the MQW in a single nanorod which is made with our technique will not perform very efficient at room temperature due to the small band gap contrast between the cation doped and undoped ZnO.

One of the examiner was suggested to use XPS depth-profile or Rutherford backscattering spectroscopy (RBS) to determine the location and the concentration of the dopants. He also suggested to use elemental mapping from EDS or HRTEM for better understanding of the location of the cation dopants. Besides, rock-curve XRD was proposed as an effective method with good accuracy to assess the orthogonality of the nanorod orientation onto the substrate. The electrical properties of cation doped ZnO nanorods was suggested to be analyzed by an in-situ electrical characterization setup and X-ray absorption spectroscopy (XAS), X-ray emission spectroscopy (XES), and Resonance inelastic X-ray scattering (RIXS).

References

[1] L. Vayssieres, K. Keis, S.-E. Lindquist, and A. Hagfeldt, "Purpose-built anisotropic metal oxide material: 3D highly oriented microrod array of ZnO," *The Journal of Physical Chemistry B,* vol. 105, pp. 3350-3352, 2001.

[2] Ü. Özgür, Y. I. Alivov, C. Liu, A. Teke, M. Reshchikov, S. Doğan, V. Avrutin, S.-J. Cho, and H. Morkoc, "A comprehensive review of ZnO materials and devices," *Journal of Applied Physics,* vol. 98, p. 041301, 2005.

[3] (web of science). *WEB OF SCIENCE*. Available: http://apps.webofknowledge.com/WOS_GeneralSearch_input.do?product=WOS&search_mode=GeneralSearch&SID=2FFBfx8uRFUOCI3JHNx&preferencesSaved=

[4] S. K. Shrama, N. Saurakhiya, S. Barthwal, R. Kumar, and A. Sharma, "Tuning of structural, optical, and magnetic properties of ultrathin and thin ZnO nanowire arrays for nano device applications," *Nanoscale Research Letters,* vol. 9, pp. 1-17, 2014.

[5] Y. Zhang, H. Jia, R. Wang, C. Chen, X. Luo, D. Yu, and C. Lee, "Low-temperature growth and Raman scattering study of vertically aligned ZnO nanowires on Si substrate," *Applied Physics Letters,* vol. 83, pp. 4631-4633, 2003.

[6] S. Fujihara, Y. Ogawa, and A. Kasai, "Tunable Visible Photoluminescence from ZnO Thin Films through Mg-Doping and Annealing," *Chemistry of Materials,* vol. 16, pp. 2965-2968, 2004/07/01 2004.

[7] J. H. He, C. S. Lao, L. J. Chen, D. Davidovic, and Z. L. Wang, "Large-Scale Ni-Doped ZnO Nanowire Arrays and Electrical and Optical Properties," *Journal of the American Chemical Society,* vol. 127, pp. 16376-16377, 2005/11/01 2005.

[8] A. Kaushik, B. Dalela, R. Rathore, V. S. Vats, B. L. Choudhary, P. A. Alvi, S. Kumar, and S. Dalela, "Influence of Co doping on the structural, optical and magnetic properties of ZnO nanocrystals," *Journal of Alloys and Compounds,* vol. 578, pp. 328-335, 2013.

[9] M. Wang, K. E. Lee, S. H. Hahn, E. J. Kim, S. Kim, J. S. Chung, E. W. Shin, and C. Park, "Optical and photoluminescent properties of sol-gel Al-doped ZnO thin films," *Materials Letters,* vol. 61, pp. 1118-1121, 2007.

[10] Y. S. Wang, P. J. Thomas, and P. O'Brien, "Optical Properties of ZnO Nanocrystals Doped with Cd, Mg, Mn, and Fe Ions," *The Journal of Physical Chemistry B,* vol. 110, pp. 21412-21415, 2006/11/01 2006.

[11] C. Xu, X. Sun, X. Zhang, L. Ke, and S. Chua, "Photoluminescent properties of copper-doped zinc oxide nanowires," *Nanotechnology,* vol. 15, p. 856, 2004.

[12] A. N. Andriotis and M. Menon, "Band gap engineering via doping: A predictive approach," *Journal of Applied Physics,* vol. 117, p. 125708, 2015.

[13] P. Kelkar, V. Kozlov, H. Jeon, A. V. Nurmikko, C. C. Chu, D. C. Grillo, J. Han, C. G. Hua, and R. L. Gunshor, "Excitons in a II-VI semiconductor microcavity in the strong-coupling regime," *Physical Review B,* vol. 52, pp. R5491-R5494, 1995.

[14] S. Halm, S. Kalusniak, S. Sadofev, H.-J. Wünsche, and F. Henneberger, "Strong exciton-photon coupling in a monolithic ZnO/(Zn, Mg) O multiple quantum well microcavity," *Applied Physics Letters,* vol. 99, p. 181121, 2011.

[15] S. Christopoulos, G. B. H. von Högersthal, A. J. D. Grundy, P. G. Lagoudakis, A. V. Kavokin, J. J. Baumberg, G. Christmann, R. Butté, E. Feltin, J. F. Carlin, and N. Grandjean, "Room-Temperature Polariton Lasing in Semiconductor Microcavities," *Physical Review Letters,* vol. 98, p. 126405, 2007.

[16] C. Weisbuch, M. Nishioka, A. Ishikawa, and Y. Arakawa, "Observation of the coupled exciton-photon mode splitting in a semiconductor quantum microcavity," *Physical Review Letters,* vol. 69, p. 3314, 1992.

[17] P. Sun-Hong, K. Seon-Hyo, and H. Sang-Wook, "Growth of homoepitaxial ZnO film on ZnO nanorods and light emitting diode applications," *Nanotechnology,* vol. 18, p. 055608, 2007.

[18] F. Hideki, S. Takemasa, N. Ryo, and S. Keiji, "ZnO nanorod array random lasers fabricated by a laser-induced hydrothermal synthesis," *New Journal of Physics,* vol. 18, p. 103046, 2016.

[19] Z. L. Wang and J. Song, "Piezoelectric Nanogenerators Based on Zinc Oxide Nanowire Arrays," *Science,* vol. 312, pp. 242-246, 2006-04-14 00:00:00 2006.

[20] S. Xu and Z. L. Wang, "One-dimensional ZnO nanostructures: solution growth and functional properties," *Nano Research,* vol. 4, pp. 1013-1098, 2011.

[21] X. Wang, J. Zhou, C. Lao, J. Song, N. Xu, and Z. L. Wang, "In situ field emission of density-controlled ZnO nanowire arrays," *ADVANCED MATERIALS-DEERFIELD BEACH THEN WEINHEIM-,* vol. 19, p. 1627, 2007.

[22] M. J. S. Spencer, I. Yarovsky, W. Wlodarski, and K. Kalantar-zadeh, "Interaction of hydrogen with zinc oxide nanorods: why the spacing is important," *Nanotechnology,* vol. 22, p. 135704, 2011.

[23] Y. D. Suh, S. Hong, G. Kim, K.-I. Hwang, J.-H. Choi, W.-H. Hong, J. Yeo, and S. H. Ko, "Selective electro—thermal growth of zinc oxide nanowire on photolithographically patterned electrode for microsensor applications," *International Journal of Precision Engineering and Manufacturing-Green Technology,* vol. 3, pp. 173-177, 2016.

[24] H. J. Fan, P. Werner, and M. Zacharias, "Semiconductor nanowires: from self-organization to patterned growth," *Small,* vol. 2, 2006// 2006.

[25] Y. Wei, W. Wu, R. Guo, D. Yuan, S. Das, and Z. L. Wang, "Wafer-scale high-throughput ordered growth of vertically aligned ZnO nanowire arrays," *Nano Letters,* vol. 10, pp. 3414-3419, 2010.

[26] D. Yuan, R. Guo, Y. Wei, W. Wu, Y. Ding, Z. L. Wang, and S. Das, "Heteroepitaxial patterned growth of vertically aligned and periodically distributed ZnO nanowires on GaN using laser interference ablation," *Advanced Functional Materials,* vol. 20, pp. 3484-3489, 2010.

[27] M.-H. Jung and H. Lee, "Selective patterning of ZnO nanorods on silicon substrates using nanoimprint lithography," *Nanoscale Research Letters,* vol. 6, p. 1, 2011.

[28] J. H. Kim, D. Andeen, and F. F. Lange, "Hydrothermal Growth of Periodic, Single-Crystal ZnO Microrods and Microtunnels," *Advanced Materials,* vol. 18, pp. 2453-2457, 2006.

[29] C. Li, G. Hong, P. Wang, D. Yu, and L. Qi, "Wet chemical approaches to patterned arrays of well-aligned ZnO nanopillars assisted by monolayer colloidal crystals," *Chemistry of Materials,* vol. 21, pp. 891-897, 2009.

[30] J. W. Hsu, Z. R. Tian, N. C. Simmons, C. M. Matzke, J. A. Voigt, and J. Liu, "Directed spatial organization of zinc oxide nanorods," *Nano Letters,* vol. 5, pp. 83-86, 2005.

[31] S.-H. Yi, S.-K. Choi, J.-M. Jang, J.-A. Kim, and W.-G. Jung, "Patterned growth of a vertically aligned zinc oxide rod array on a gallium nitride epitaxial layer by using a hydrothermal process," *Journal of the Korean Physical Society,* vol. 53, pp. 227-231, 2008.

[32] S. H. Jung, E. Oh, K. H. Lee, W. Park, and S. H. Jeong, "A sonochemical method for fabricating aligned ZnO nanorods," *Advanced Materials,* vol. 19, pp. 749-753, 2007.

[33] B. Kang, S. Pearton, and F. Ren, "Low temperature (< 100 C) patterned growth of ZnO nanorod arrays on Si," *Applied physics letters,* vol. 90, p. 083104, 2007.

[34] Y.-J. Kim, C.-H. Lee, Y. J. Hong, G.-C. Yi, S. S. Kim, and H. Cheong, "Controlled selective growth of ZnO nanorod and microrod arrays on Si substrates by a wet chemical method," *Applied physics letters,* vol. 89, p. 163128, 2006.

[35] Y. Tak and K. Yong, "Controlled growth of well-aligned ZnO nanorod array using a novel solution method," *The Journal of Physical Chemistry B,* vol. 109, pp. 19263-19269, 2005.

[36] S.-H. Yi, S.-K. Choi, J.-M. Jang, S.-H. Ko, J.-A. Kim, and W.-G. Jung, "Patterned growth of ZnO nanorod by solution chemical method," in *Integrated Optoelectronic Devices 2007*, 2007, pp. 64741L-64741L-8.

[37] H. W. Kang, J. Yeo, J. O. Hwang, S. Hong, P. Lee, S. Y. Han, J. H. Lee, Y. S. Rho, S. O. Kim, and S. H. Ko, "Simple ZnO nanowires patterned growth by microcontact printing for high performance field emission device," *The Journal of Physical Chemistry C,* vol. 115, pp. 11435-11441, 2011.

[38] X. Chen, X. Yan, Z. Bai, P. Lin, Y. Shen, X. Zheng, Y. Feng, and Y. Zhang, "Facile fabrication of large-scale patterned ZnO nanorod arrays with tunable arrangement, period and morphology," *CrystEngComm,* vol. 15, pp. 8022-8028, 2013.

[39] Z. Szabó, R. Erdélyi, J. Makai, J. Balázs, and J. Volk, "Highly ordered three-dimensional ZnO nanorods for novel photonic devices," *physica status solidi (c),* vol. 8, pp. 2895-2898, 2011.

[40] G.-C. Yi, Y.-j. Kim, and C.-h. Lee, "Zinc Oxide Microstructures and a Method of Preparing the Same," ed: Google Patents, 2007.

[41] M. H. Huang, S. Mao, H. Feick, H. Yan, Y. Wu, H. Kind, E. Weber, R. Russo, and P. Yang, "Room-temperature ultraviolet nanowire nanolasers," *Science,* vol. 292, pp. 1897-1899, 2001.

[42] S. Nozaki, S. N. Sarangi, S. N. Sahu, and K. Uchida, "Selective growth of ZnO nanorods by the hydrothermal techniqueInvited talk at the 6th International Workshop on Advanced Materials Science and Nanotechnology IWAMSN2012, 30 October 2 November 2012, Ha Long, Vietnam," *Advances in Natural Sciences: Nanoscience and Nanotechnology,* vol. 4, p. 015008, 2013.

[43] S. Xu, Y. Wei, M. Kirkham, J. Liu, W. Mai, D. Davidovic, R. L. Snyder, and Z. L. Wang, "Patterned growth of vertically aligned ZnO nanowire arrays on inorganic substrates at low temperature without catalyst," *Journal of the American Chemical Society,* vol. 130, pp. 14958-14959, 2008.

[44] S. Xu, Y. Ding, Y. Wei, H. Fang, Y. Shen, A. K. Sood, D. L. Polla, and Z. L. Wang, "Patterned growth of horizontal ZnO nanowire arrays," *Journal of the American Chemical Society,* vol. 131, pp. 6670-6671, 2009.

[45] S. Oh, T. Nagata, J. Volk, and Y. Wakayama, "Nanoimprint for fabrication of highly ordered epitaxial ZnO nanorods on transparent conductive oxide films," *Applied Physics Express,* vol. 5, p. 095003, 2012.

[46] H.-H. Park, X. Zhang, K. W. Lee, K. H. Kim, S. H. Jung, D. S. Park, Y. S. Choi, H.-B. Shin, H. K. Sung, and K. H. Park, "Position-controlled hydrothermal growth of ZnO nanorods on arbitrary substrates with a patterned seed layer via ultraviolet-assisted nanoimprint lithography," *CrystEngComm,* vol. 15, pp. 3463-3469, 2013.

[47] S. Li and A. Waag, "GaN based nanorods for solid state lighting," *Journal of Applied Physics,* vol. 111, p. 071101, 2012.

[48] A. C. Scofield, S.-H. Kim, J. N. Shapiro, A. Lin, B. Liang, A. Scherer, and D. L. Huffaker, "Bottom-up photonic crystal lasers," *Nano letters,* vol. 11, pp. 5387-5390, 2011.

[49] C. L. Yu, H. Kim, N. de Leon, I. W. Frank, J. T. Robinson, M. McCutcheon, M. Liu, M. D. Lukin, M. Loncar, and H. Park, "Stretchable photonic crystal cavity with wide frequency tunability," *Nano letters,* vol. 13, pp. 248-252, 2012.

[50] J. Kwon, S. Hong, H. Lee, J. Yeo, S. S. Lee, and S. H. Ko, "Direct selective growth of ZnO nanowire arrays from inkjet-printed zinc acetate precursor on a heated substrate," *Nanoscale Research Letters,* vol. 8, pp. 1-6, 2013.

[51] S. H. Ko, D. Lee, N. Hotz, J. Yeo, S. Hong, K. H. Nam, and C. P. Grigoropoulos, "Digital selective growth of ZnO nanowire arrays from inkjet-printed nanoparticle seeds on a flexible substrate," *Langmuir,* vol. 28, pp. 4787-4792, 2011.

[52] J. Yeo, S. Hong, G. Kim, H. Lee, Y. D. Suh, I. Park, C. P. Grigoropoulos, and S. H. Ko, "Laser-induced hydrothermal growth of heterogeneous metal-oxide nanowire on flexible substrate by laser absorption layer design," *ACS Nano,* vol. 9, pp. 6059-6068, 2015.

[53] J. Yeo, S. Hong, M. Wanit, H. W. Kang, D. Lee, C. P. Grigoropoulos, H. J. Sung, and S. H. Ko, "Rapid, one-step, digital selective growth of ZnO nanowires on 3D structures using laser induced hydrothermal growth," *Advanced Functional Materials,* vol. 23, pp. 3316-3323, 2013.

[54] J. B. In, H. J. Kwon, D. Lee, S. H. Ko, and C. P. Grigoropoulos, "In Situ Monitoring of Laser-Assisted Hydrothermal Growth of ZnO Nanowires: Thermally Deactivating Growth Kinetics," *Small,* vol. 10, pp. 741-749, 2014.

[55] K. Kwon, J. Shim, J. O. Lee, K. Choi, and K. Yu, "Localized Laser-Based Photohydrothermal Synthesis of Functionalized Metal-Oxides," *Advanced Functional Materials,* vol. 25, pp. 2222-2229, 2015.

[56] S. Hong, J. Yeo, W. Manorotkul, H. W. Kang, J. Lee, S. Han, Y. Rho, Y. D. Suh, H. J. Sung, and S. H. Ko, "Digital selective growth of a ZnO nanowire array by large scale laser decomposition of zinc acetate," *Nanoscale,* vol. 5, pp. 3698-3703, 2013.

[57] S. Hong, H. Lee, J. Yeo, and S. H. Ko, "Digital selective laser methods for nanomaterials: From synthesis to processing," *Nano Today,* 2016.

[58] J. Yeo, G. Kim, S. Hong, J. Lee, J. Kwon, H. Lee, H. Park, W. Manoroktul, M. T. Lee, and B. J. Lee, "Single Nanowire Resistive Nano-heater for Highly Localized Thermo-Chemical Reactions: Localized Hierarchical Heterojunction Nanowire Growth," *Small,* vol. 10, pp. 5015-5022, 2014.

[59] K. Gautam, I. Singh, P. Bhatnagar, and K. R. Peta, "Role of Cl doping on the growth and relaxation dynamics of ZnO nanorods synthesized by hydrothermal method," *Chemical Physics Letters,* vol. 662, pp. 196-200, 2016.

[60] T. Plakhova, M. Shestakov, and A. Baranov, "Effect of textured seeds on the morphology and optical properties of solution-and vapor-grown ZnO nanorod arrays," *Inorganic Materials,* vol. 48, pp. 469-475, 2012.

[61] V. Consonni, E. Sarigiannidou, E. Appert, A. Bocheux, S. Guillemin, F. Donatini, I.-C. Robin, J. Kioseoglou, and F. Robaut, "Selective area growth of well-ordered ZnO nanowire arrays with controllable polarity," *ACS Nano,* vol. 8, pp. 4761-4770, 2014.

[62] D. F. Liu, Y. J. Xiang, X. C. Wu, Z. X. Zhang, L. F. Liu, L. Song, X. W. Zhao, S. D. Luo, W. J. Ma, J. Shen, W. Y. Zhou, G. Wang, C. Y. Wang, and S. S. Xie, "Periodic ZnO Nanorod Arrays Defined by Polystyrene Microsphere Self-Assembled Monolayers," *Nano Letters,* vol. 6, pp. 2375-2378, 2006/10/01 2006.

[63] A. Hassanpour, N. Bogdan, J. A. Capobianco, and P. Bianucci, "Hydrothermal selective growth of low aspect ratio isolated ZnO nanorods," *Materials & Design,* vol. 119, pp. 464-469, 2017.

[64] R. Garcia, A. W. Knoll, and E. Riedo, "Advanced scanning probe lithography," *Nature nanotechnology,* vol. 9, pp. 577-587, 2014.

[65] F. Ahmed, N. Arshi, M. Anwar, R. Danish, and B. H. Koo, "Mn-doped ZnO nanorod gas sensor for oxygen detection," *Current Applied Physics,* vol. 13, pp. S64-S68, 2013.

[66] J. Mathew, T. Hitoshi, and K. Tomoji, "p-Type Electrical Conduction in ZnO Thin Films by Ga and N Codoping," *Japanese Journal of Applied Physics,* vol. 38, p. L1205, 1999.

[67] S. B. Zhang, S. H. Wei, and A. Zunger, "Intrinsic \textit{n} -type versus \textit{p} -type doping asymmetry and the defect physics of ZnO," *Physical Review B,* vol. 63, p. 075205, 2001.

[68] G. C. Park, S. M. Hwang, S. M. Lee, J. H. Choi, K. M. Song, H. Y. Kim, H.-S. Kim, S.-J. Eum, S.-B. Jung, and J. H. Lim, "Hydrothermally grown in-doped ZnO nanorods on p-GaN films for color-tunable heterojunction light-emitting-diodes," *Scientific reports,* vol. 5, 2015.

[69] G. D. Yuan, W. J. Zhang, J. S. Jie, X. Fan, J. X. Tang, I. Shafiq, Z. Z. Ye, C. S. Lee, and S. T. Lee, "Tunable n-Type Conductivity and Transport Properties of Ga-doped ZnO Nanowire Arrays," *Advanced Materials,* vol. 20, pp. 168-173, 2008.

[70] D. C. Look, B. Claflin, Y. I. Alivov, and S.-J. Park, "The future of ZnO light emitters," *physica status solidi (a),* vol. 201, pp. 2203-2212, 2004.

[71] C. Park, S. Zhang, and S.-H. Wei, "Origin of p-type doping difficulty in ZnO: The impurity perspective," *Physical Review B,* vol. 66, p. 073202, 2002.

[72] K.-K. Kim, H.-S. Kim, D.-K. Hwang, J.-H. Lim, and S.-J. Park, "Realization of p-type ZnO thin films via phosphorus doping and thermal activation of the dopant," *Applied Physics Letters,* vol. 83, pp. 63-65, 2003.

[73] Y. Ryu, T. Lee, and H. White, "Properties of arsenic-doped p-type ZnO grown by hybrid beam deposition," *Applied Physics Letters,* vol. 83, p. 87, 2003.

[74] J. Lu, Y. Zhang, Z. Ye, Y. Zeng, H. He, L. Zhu, J. Huang, L. Wang, J. Yuan, and B. Zhao, "Control of p-and n-type conductivities in Li-doped ZnO thin films," *Applied Physics Letters,* vol. 89, pp. 112113-112113, 2006.

[75] F. Xiu, Z. Yang, L. Mandalapu, D. Zhao, J. Liu, and W. Beyermann, "High-mobility Sb-doped p-type ZnO by molecular-beam epitaxy," *Applied Physics Letters,* vol. 87, pp. 152101-152101, 2005.

[76] H. S. Kang, B. D. Ahn, J. H. Kim, G. H. Kim, S. H. Lim, H. W. Chang, and S. Y. Lee, "Structural, electrical, and optical properties of p-type ZnO thin films with Ag dopant," *Applied Physics Letters,* vol. 88, p. 2108, 2006.

[77] Ü. Özgür, Y. I. Alivov, C. Liu, A. Teke, M. A. Reshchikov, S. Doğan, V. Avrutin, S.-J. Cho, and H. Morkoç, "A comprehensive review of ZnO materials and devices," *Journal of Applied Physics,* vol. 98, p. 041301, 2005.

[78] M. Wang, F. Ren, G. Cai, Y. Liu, S. Shen, and L. Guo, "Activating ZnO nanorod photoanodes in visible light by Cu ion implantation," *Nano Research,* vol. 7, pp. 353-364, 2014// 2014.

[79] J. Zhao, L. Wang, X. Yan, Y. Yang, Y. Lei, J. Zhou, Y. Huang, Y. Gu, and Y. Zhang, "Structure and photocatalytic activity of Ni-doped ZnO nanorods," *Materials Research Bulletin,* vol. 46, pp. 1207-1210, 2011.

[80] Y. Lu, Y. Lin, D. Wang, L. Wang, T. Xie, and T. Jiang, "A high performance cobalt-doped ZnO visible light photocatalyst and its photogenerated charge transfer properties," *Nano Research,* vol. 4, pp. 1144-1152, 2011// 2011.

[81] R. Ullah and J. Dutta, "Photocatalytic degradation of organic dyes with manganese-doped ZnO nanoparticles," *Journal of Hazardous Materials,* vol. 156, pp. 194-200, 2008.

[82] X. Qiu, L. Li, J. Zheng, J. Liu, X. Sun, and G. Li, "Origin of the enhanced photocatalytic activities of semiconductors: a case study of ZnO doped with Mg2+," *The Journal of Physical Chemistry C,* vol. 112, pp. 12242-12248, 2008.

[83] S. Kato, Y. Hirano, M. Iwata, T. Sano, K. Takeuchi, and S. Matsuzawa, "Photocatalytic degradation of gaseous sulfur compounds by silver-deposited titanium dioxide," *Applied Catalysis B: Environmental,* vol. 57, pp. 109-115, 2005.

[84] K. M. Lee, C. W. Lai, K. S. Ngai, and J. C. Juan, "Recent developments of zinc oxide based photocatalyst in water treatment technology: a review," *Water research,* vol. 88, pp. 428-448, 2016.

[85] J. Thakur, G. Auner, V. Naik, C. Sudakar, P. Kharel, G. Lawes, R. Suryanarayanan, and R. Naik, "Raman scattering studies of magnetic Co-doped ZnO thin films," *Journal of Applied Physics,* vol. 102, p. 093904, 2007.

[86] V. Vaithianathan, B.-T. Lee, and S. S. Kim, "Preparation of As-doped p-type ZnO films using a Zn3As2/ZnO target with pulsed laser deposition," *Applied Physics Letters,* vol. 86, p. 2101, 2005.

[87] H. Ko, Y. Chen, S. Hong, H. Wenisch, T. Yao, and D. C. Look, "Ga-doped ZnO films grown on GaN templates by plasma-assisted molecular-beam epitaxy," *Applied Physics Letters,* vol. 77, pp. 3761-3763, 2000.

[88] T. Minami, H. Sato, H. Nanto, and S. Takata, "Group III impurity doped zinc oxide thin films prepared by RF magnetron sputtering," *Japanese Journal of Applied Physics,* vol. 24, p. L781, 1985.

[89] T. Fukumura, Z. Jin, A. Ohtomo, H. Koinuma, and M. Kawasaki, "An oxide-diluted magnetic semiconductor: Mn-doped ZnO," *Applied Physics Letters,* vol. 75, pp. 3366-3368, 1999.

[90] C. L. Hsu and S. J. Chang, "Doped ZnO 1D nanostructures: synthesis, properties, and photodetector application," *Small,* vol. 10, pp. 4562-4585, 2014.

[91] Y. Liu, S.-J. Young, L. Ji, T. Meen, C. Hsiao, C. Huang, and S.-J. Chang, "UV enhanced field emission performance of Mg-doped ZnO nanorods," *IEEE Transactions on Electron Devices,* vol. 61, pp. 1541-1545, 2014.

[92] R. Vinod, M. J. Bushiri, P. Sajan, S. R. Achary, and V. Muñoz-Sanjosé, "Mn2+-induced room-temperature ferromagnetism and spin-glass behavior in hydrothermally grown Mn-doped ZnO nanorods," *physica status solidi (a),* vol. 211, pp. 1155-1161, 2014.

[93] C. Wu, L. Shen, Y.-C. Zhang, and Q. Huang, "Solvothermal synthesis of Cr-doped ZnO nanowires with visible light-driven photocatalytic activity," *Materials Letters,* vol. 65, pp. 1794-1796, 2011.

[94] O. Lupan, T. Pauporté, B. Viana, V. Ursaki, I. Tiginyanu, V. Sontea, and L. Chow, "UV-blue and green electroluminescence from Cu-doped ZnO nanorod emitters hydrothermally synthesized on p-GaN," *Journal of Nanoelectronics and Optoelectronics,* vol. 7, pp. 712-718, 2012.

[95] L. Vayssieres, "Growth of arrayed nanorods and nanowires of ZnO from aqueous solutions," *Advanced Materials,* vol. 15, pp. 464-466, 2003.

[96] S. Wang, C. Song, K. Cheng, S. Dai, Y. Zhang, and Z. Du, "Controllable growth of ZnO nanorod arrays with different densities and their photoelectric properties," *Nanoscale Research Letters,* vol. 7, p. 246, 2012.

[97] G. P. Li, L. Jiang, S. J. Wang, X. W. Sun, X. Chen, and T. Wu, "Buffer-Layer-Assisted Epitaxial Growth of Perfectly Aligned Oxide Nanorod Arrays in Solution," *Crystal Growth & Design,* vol. 11, pp. 4885-4891, 2011/11/02 2011.

[98] L. E. Greene, M. Law, D. H. Tan, M. Montano, J. Goldberger, G. Somorjai, and P. Yang, "General route to vertical ZnO nanowire arrays using textured ZnO seeds," *Nano letters,* vol. 5, pp. 1231-1236, 2005.

[99] S. Yamabi and H. Imai, "Growth conditions for wurtzite zinc oxide films in aqueous solutions," *Journal of Materials Chemistry,* vol. 12, pp. 3773-3778, 2002.

[100] L. E. Greene, B. D. Yuhas, M. Law, D. Zitoun, and P. Yang, "Solution-grown zinc oxide nanowires," *Inorganic chemistry,* vol. 45, pp. 7535-7543, 2006.

[101] S. Baruah and J. Dutta, "pH-dependent growth of zinc oxide nanorods," *Journal of crystal growth,* vol. 311, pp. 2549-2554, 2009.

[102] R. Parize, J. Garnier, O. Chaix-Pluchery, C. Verrier, E. Appert, and V. Consonni, "Effects of hexamethylenetetramine on the nucleation and radial growth of ZnO nanowires by chemical bath deposition," *The Journal of Physical Chemistry C,* vol. 120, pp. 5242-5250, 2016.

[103] M. C. Akgun, A. Afal, and H. E. Unalan, "Hydrothermal zinc oxide nanowire growth with different zinc salts," *Journal of Materials Research,* vol. 27, pp. 2401-2407, 2012.

[104] L. Spanhel, "Colloidal ZnO nanostructures and functional coatings: a survey," *Journal of sol-gel science and technology,* vol. 39, pp. 7-24, 2006.

[105] S. Guillemin, E. Appert, H. Roussel, B. a. Doisneau, R. Parize, T. Boudou, G. Bremond, and V. Consonni, "Controlling the structural properties of single step, dip coated ZnO seed layers for growing perfectly aligned nanowire arrays," *The Journal of Physical Chemistry C,* vol. 119, pp. 21694-21703, 2015.

[106] J. S. S. Michelle, Y. Irene, W. Wojtek, and K.-z. Kourosh, "Interaction of hydrogen with zinc oxide nanorods: why the spacing is important," *Nanotechnology,* vol. 22, p. 135704, 2011.

[107] T. Shinagawa, K. Shibata, O. Shimomura, M. Chigane, R. Nomura, and M. Izaki, "Solution-processed high-haze ZnO pyramidal textures directly grown on a TCO substrate and the light-trapping effect in Cu 2 O solar cells," *Journal of Materials Chemistry C,* vol. 2, pp. 2908-2917, 2014.

[108] A. Bananej and A. Hassanpour, "Modification of laser induced damage threshold of ZrO2 thin films by using time–temperature gradient annealing," *Applied Surface Science,* vol. 258, pp. 2397-2403, 2012.

[109] J. Yu, Y. Lai, Y. Wang, S. Cheng, and Y. Chen, "Polarized Raman scattering of single ZnO nanorod," *Journal of Applied Physics,* vol. 115, p. 033505, 2014.

[110] H. Morkoç and Ü. Özgür, *Zinc oxide: fundamentals, materials and device technology*: John Wiley & Sons, 2008.

[111] C.-T. Chien, M.-C. Wu, C.-W. Chen, H.-H. Yang, J.-J. Wu, W.-F. Su, C.-S. Lin, and Y.-F. Chen, "Polarization-dependent confocal Raman microscopy of an individual ZnO nanorod," *Applied physics letters,* vol. 92, pp. 223102-223102, 2008.

[112] J. Yang, J. Zheng, H. Zhai, and L. Yang, "Low temperature hydrothermal growth and optical properties of ZnO nanorods," *Crystal Research and Technology,* vol. 44, pp. 87-91, 2009.

[113] V. Ursaki, I. Tiginyanu, V. Zalamai, E. Rusu, G. Emelchenko, V. Masalov, and E. Samarov, "Multiphonon resonant Raman scattering in ZnO crystals and nanostructured layers," *Physical Review B,* vol. 70, p. 155204, 2004.

[114] R. Cuscó, E. Alarcón-Lladó, J. Ibáñez, L. Artús, J. Jiménez, B. Wang, and M. J. Callahan, "Temperature dependence of Raman scattering in ZnO," *Physical Review B,* vol. 75, p. 165202, 2007.

[115] A. Umar, S. Kim, Y.-S. Lee, K. Nahm, and Y. Hahn, "Catalyst-free large-quantity synthesis of ZnO nanorods by a vapor–solid growth mechanism: structural and optical properties," *Journal of Crystal Growth,* vol. 282, pp. 131-136, 2005.

[116] W. I. Park, D. Kim, S.-W. Jung, and G.-C. Yi, "Metalorganic vapor-phase epitaxial growth of vertically well-aligned ZnO nanorods," *Applied physics letters,* vol. 80, pp. 4232-4234, 2002.

[117] F. Khan, S. Ameen, M. Song, and H. S. Shin, "Influence of excitation wavelength on photoluminescence spectra of Al doped ZnO films," *Journal of Luminescence,* vol. 134, pp. 160-164, 2013.

[118] Y. Kong, D. Yu, B. Zhang, W. Fang, and S. Feng, "Ultraviolet-emitting ZnO nanowires synthesized by a physical vapor deposition approach," *Applied Physics Letters,* vol. 78, pp. 407-409, 2001.

[119] R. Zhang, P.-G. Yin, N. Wang, and L. Guo, "Photoluminescence and Raman scattering of ZnO nanorods," *Solid State Sciences,* vol. 11, pp. 865-869, 2009.

[120] R. Gayen, S. Das, S. Dalui, R. Bhar, and A. Pal, "Zinc magnesium oxide nanofibers on glass substrate by solution growth technique," *Journal of crystal growth,* vol. 310, pp. 4073-4080, 2008.

[121] A. Djurišić, Y. Leung, K. Tam, L. Ding, W. Ge, H. Chen, and S. Gwo, "Green, yellow, and orange defect emission from ZnO nanostructures: Influence of excitation wavelength," *Applied Physics Letters,* vol. 88, p. 103107, 2006.

[122] K. Tam, C. Cheung, Y. Leung, A. Djurišic, C. Ling, C. Beling, S. Fung, W. Kwok, W. Chan, and D. Phillips, "Defects in ZnO nanorods prepared by a hydrothermal method," *The Journal of Physical Chemistry B,* vol. 110, pp. 20865-20871, 2006.

[123] D. Zhao, Y. Liu, D. Shen, Y. Lu, J. Zhang, and X. Fan, "Photoluminescence properties of MgxZn1-xO alloy thin films fabricated by the sol-gel deposition method," *Journal of Applied Physics,* vol. 90, pp. 5561-5563, 2001.

[124] T. Minemoto, T. Negami, S. Nishiwaki, H. Takakura, and Y. Hamakawa, "Preparation of Zn 1− x Mg x O films by radio frequency magnetron sputtering," *Thin Solid Films,* vol. 372, pp. 173-176, 2000.

[125] H. Pan, J. Luo, H. Sun, Y. Feng, C. Poh, and J. Lin, "Hydrogen storage of ZnO and Mg doped ZnO nanowires," *Nanotechnology,* vol. 17, p. 2963, 2006.

[126] P. Shimpi, P.-X. Gao, D. G. Goberman, and Y. Ding, "Low temperature synthesis and characterization of MgO/ZnO composite nanowire arrays," *Nanotechnology,* vol. 20, p. 125608, 2009.

[127] B. Houng and C.-J. Huang, "Structure and properties of Ag embedded aluminum doped ZnO nanocomposite thin films prepared through a sol–gel process," *Surface and Coatings Technology,* vol. 201, pp. 3188-3192, 2006.

[128] S. Park, G. Gu, and C. Park, "Effects of Mg doping to optimize properties ZnO: Al for the transparent conductive oxide (TCO)," *physica status solidi (a),* vol. 208, pp. 2688-2691, 2011.

[129] J. Chen, D. Chen, J. He, S. Zhang, and Z. Chen, "The microstructure, optical, and electrical properties of sol–gel-derived Sc-doped and Al–Sc co-doped ZnO thin films," *Applied Surface Science,* vol. 255, pp. 9413-9419, 2009.

[130] A. K. Singh, G. S. Thool, P. R. Bangal, S. S. Madhavendra, and S. P. Singh, "Low temperature Mn doped ZnO nanorod array: Synthesis and its photoluminescence behavior," *Industrial & Engineering Chemistry Research,* vol. 53, pp. 9383-9390, 2014.

[131] J. Calleja and M. Cardona, "Resonant Raman scattering in ZnO," *Physical Review B,* vol. 16, p. 3753, 1977.

[132] P. Giri, S. Bhattacharyya, D. K. Singh, R. Kesavamoorthy, B. Panigrahi, and K. Nair, "Correlation between microstructure and optical properties of ZnO nanoparticles synthesized by ball milling," *Journal of Applied Physics,* vol. 102, p. 093515, 2007.

[133] X. Xu, C. Xu, Y. Lin, J. Li, and J. Hu, "Comparison on Photoluminescence and Magnetism between Two Kinds of Undoped ZnO Nanorods," *The Journal of Physical Chemistry C,* vol. 117, pp. 24549-24553, 2013.

[134] A. Hammouda, A. Canizarès, P. Simon, A. Boughalout, and M. Kechouane, "Improving the sensitivity of Raman signal of ZnO thin films deposited on silicon substrate," *Vibrational Spectroscopy,* vol. 62, pp. 217-221, 2012.

[135] R. Cuscó, E. Alarcón-Lladó, J. Ibáñez, L. Artús, J. Jiménez, B. Wang, and M. J. Callahan, "Temperature dependence of Raman scattering in ZnO," *Physical Review B,* vol. 75, p. 165202, 2007.

[136] H.-W. Zhang, Z.-R. Wei, Z.-Q. Li, and G.-Y. Dong, "Room-temperature ferromagnetism in Fe-doped, Fe-and Cu-codoped ZnO diluted magnetic semiconductor," *Materials Letters,* vol. 61, pp. 3605-3607, 2007.

[137] A. M. Venezia, "X-ray photoelectron spectroscopy (XPS) for catalysts characterization," *Catalysis Today,* vol. 77, pp. 359-370, 2003.

[138] Y. Boqian, F. Peterxian, K. Ashok, R. S. Katiyar, and A. Marc, "Structural and optical properties of N-doped ZnO nanorod arrays," *Journal of Physics D: Applied Physics,* vol. 42, p. 195402, 2009.

[139] X.-J. Yang, X.-Y. Miao, X.-L. Xu, C.-M. Xu, J. Xu, and H.-T. Liu, "Structure, X-ray photoelectron spectroscopy and photoluminescence properties of highly ordered ZnO microrods," *Optical Materials,* vol. 27, pp. 1602-1605, 2005.

[140] P. Y. Yu and M. Cardona, "Fundamentals of semiconductors: physics and materials properties. 3rd rev. & enl. ed," *Advanced texts in physics,* 2001.

[141] O. Lupan, L. Chow, L. K. Ono, B. R. Cuenya, G. Chai, H. Khallaf, S. Park, and A. Schulte, "Synthesis and characterization of Ag-or Sb-doped ZnO nanorods by a facile hydrothermal route," *The Journal of Physical Chemistry C,* vol. 114, pp. 12401-12408, 2010.

[142] J. Chu, X. Peng, K. Dasari, R. Palai, and P. Feng, "The shift of optical band gap in W-doped ZnO with oxygen pressure and doping level," *Materials Research Bulletin,* vol. 54, pp. 73-77, 2014.

[143] J. Liqiang, W. Dejun, W. Baiqi, L. Shudan, X. Baifu, F. Honggang, and S. Jiazhong, "Effects of noble metal modification on surface oxygen composition, charge separation and photocatalytic activity of ZnO nanoparticles," *Journal of Molecular Catalysis A: Chemical,* vol. 244, pp. 193-200, 2006.

[144] L. Chow, O. Lupan, G. Chai, H. Khallaf, L. Ono, B. R. Cuenya, I. Tiginyanu, V. Ursaki, V. Sontea, and A. Schulte, "Synthesis and characterization of Cu-doped ZnO one-dimensional structures for miniaturized sensor applications with faster response," *Sensors and Actuators A: Physical,* vol. 189, pp. 399-408, 2013.

[145] Y. Tak, D. Park, and K. Yong, "Characterization of ZnO nanorod arrays fabricated on Si wafers using a low-temperature synthesis method," *Journal of Vacuum Science & Technology B,* vol. 24, pp. 2047-2052, 2006.

[146] L. Armelao, M. Fabrizio, S. Gialanella, and F. Zordan, "Sol–gel synthesis and characterisation of ZnO-based nanosystems," *Thin Solid Films,* vol. 394, pp. 89-95, 2001.

[147] H. Ong and G. Du, "The evolution of defect emissions in oxygen-deficient and-surplus ZnO thin films: the implication of different growth modes," *Journal of crystal growth,* vol. 265, pp. 471-475, 2004.

[148] R. Xie, T. Sekiguchi, T. Ishigaki, N. Ohashi, D. Li, D. Yang, B. Liu, and Y. Bando, "Enhancement and patterning of ultraviolet emission in ZnO with an electron beam," *Applied Physics Letters,* vol. 88, p. 134103, 2006.

[149] Y. Zhao, Y. Li, Y. Jin, X. Zhang, W. Hu, I. Ahmad, G. McCartney, and Y. Zhu, "Growth and characterization of Cu-catalyzed ZnO nanowires," in *Journal of Physics: Conference Series*, 2007, p. 703.

[150] Q. Ahsanulhaq, A. Umar, and Y. B. Hahn, "Growth of aligned ZnO nanorods and nanopencils on ZnO/Si in aqueous solution: growth mechanism and structural and optical properties," *Nanotechnology,* vol. 18, p. 115603, 2007.

[151] J. Chiou, H. Tsai, C. Pao, F. Chien, W.-F. Pong, C. Chen, M.-H. Tsai, J.-J. Wu, C. Ko, and H. Chiang, "Mg-induced increase of band gap in Zn1− xMgxO nanorods revealed by

x-ray absorption and emission spectroscopy," *Journal of Applied Physics,* vol. 104, p. 013709, 2008.

[152] P. Shimpi, Y. Ding, E. Suarez, J. Ayers, and P.-X. Gao, "Annealing induced nanostructure and photoluminescence property evolution in solution-processed Mg-alloyed ZnO nanowires," *Applied Physics Letters,* vol. 97, p. 103104, 2010.

[153] J. Li, H. Zhuang, J. Wang, and P. Xu, "Fabrication and characterization of Mg-doped pencil-shaped ZnO microprisms," *Applied Surface Science,* vol. 257, pp. 2337-2340, 2011.

[154] Y. Yang, Y. Jin, H. He, Q. Wang, Y. Tu, H. Lu, and Z. Ye, "Dopant-induced shape evolution of colloidal nanocrystals: the case of zinc oxide," *Journal of the American Chemical Society,* vol. 132, pp. 13381-13394, 2010.

[155] Z. ShaoMin, Y. HongLei, L. LiSheng, C. XiLiang, L. ShiYun, H. YaoMing, Y. RuiJian, and L. Ning, "Magnetic properties of Ni-doped ZnO nanocombs by CVD approach," *Nanoscale Research Letters,* vol. 5, p. 1284, 2010.

[156] X. Liu, F. Lin, L. Sun, W. Cheng, X. Ma, and W. Shi, "Doping concentration dependence of room-temperature ferromagnetism for Ni-doped ZnO thin films prepared by pulsed-laser deposition," *Applied Physics Letters,* vol. 88, p. 2508, 2006.

[157] G. J. Huang, J. B. Wang, X. L. Zhong, G. C. Zhou, and H. L. Yan, "Synthesis, structure, and room-temperature ferromagnetism of Ni-doped ZnO nanoparticles," *Journal of Materials Science,* vol. 42, pp. 6464-6468, 2007.

[158] F. Pan, C. Song, X. Liu, Y. Yang, and F. Zeng, "Ferromagnetism and possible application in spintronics of transition-metal-doped ZnO films," *Materials Science and Engineering: R: Reports,* vol. 62, pp. 1-35, 2008.

[159] D. Wu, M. Yang, Z. Huang, G. Yin, X. Liao, Y. Kang, X. Chen, and H. Wang, "Preparation and properties of Ni-doped ZnO rod arrays from aqueous solution," *Journal of colloid and interface science,* vol. 330, pp. 380-385, 2009.

[160] P. Hu, N. Han, D. Zhang, J. C. Ho, and Y. Chen, "Highly formaldehyde-sensitive, transition-metal doped ZnO nanorods prepared by plasma-enhanced chemical vapor deposition," *Sensors and Actuators B: Chemical,* vol. 169, pp. 74-80, 2012.

[161] S. Kant and A. Kumar, "A comparative analysis of structural, optical and photocatalytic properties of ZnO and Ni doped ZnO nanospheres prepared by sol gel method," *Adv Mat Let,* vol. 3, pp. 350-354, 2012.

[162] Z. Yin, N. Chen, F. Yang, S. Song, C. Chai, J. Zhong, H. Qian, and K. Ibrahim, "Structural, magnetic properties and photoemission study of Ni-doped ZnO," *Solid state communications,* vol. 135, pp. 430-433, 2005.

[163] K. Ueda, H. Tabata, and T. Kawai, "Magnetic and electric properties of transition-metal-doped ZnO films," *Applied Physics Letters,* vol. 79, pp. 988-990, 2001.

[164] A. Farag, M. Cavaş, F. Yakuphanoglu, and F. Amanullah, "Photoluminescence and optical properties of nanostructure Ni doped ZnO thin films prepared by sol–gel spin coating technique," *Journal of Alloys and Compounds,* vol. 509, pp. 7900-7908, 2011.

[165] D. A. Schwartz, N. S. Norberg, Q. P. Nguyen, J. M. Parker, and D. R. Gamelin, "Magnetic quantum dots: synthesis, spectroscopy, and magnetism of Co2+-and Ni2+-doped ZnO nanocrystals," *Journal of the American Chemical Society,* vol. 125, pp. 13205-13218, 2003.

[166] S. W. Jung, W. I. Park, G. C. Yi, and M. Y. Kim, "Fabrication and Controlled Magnetic Properties of Ni/ZnO Nanorod Heterostructures," *Advanced Materials,* vol. 15, pp. 1358-1361, 2003.

[167] R. Vincent, D. Cherns, N. X. Nghia, and V. Ursaki, "Raman scattering in Me-doped ZnO nanorods (Me= Mn, Co, Cu and Ni) prepared by thermal diffusion," *Nanotechnology,* vol. 19, p. 475702, 2008.

[168] T. Al-Harbi, "Hydrothermal synthesis and optical properties of Ni doped ZnO hexagonal nanodiscs," *Journal of Alloys and Compounds,* vol. 509, pp. 387-390, 2011.

[169] J. B. Cui and U. J. Gibson, "Electrodeposition and room temperature ferromagnetic anisotropy of Co and Ni-doped ZnO nanowire arrays," *Applied Physics Letters,* vol. 87, p. 133108, 2005.

[170] K. Raja, P. Ramesh, and D. Geetha, "Synthesis, structural and optical properties of ZnO and Ni-doped ZnO hexagonal nanorods by Co-precipitation method," *Spectrochimica Acta Part A: Molecular and Biomolecular Spectroscopy,* vol. 120, pp. 19-24, 2014.

[171] H. Wang, Y. Chen, H. Wang, C. Zhang, F. Yang, J. Duan, C. Yang, Y. Xu, M. Zhou, and Q. Li, "High resolution transmission electron microscopy and Raman scattering studies of

room temperature ferromagnetic Ni-doped ZnO nanocrystals," *Applied Physics Letters,* vol. 90, p. 052505, 2007.

[172] L. Yang, X. Wu, G. Huang, T. Qiu, and Y. Yang, "In situ synthesis of Mn-doped ZnO multileg nanostructures and Mn-related Raman vibration," *Journal of Applied Physics,* vol. 97, p. 014308, 2005.

[173] B. Zhang, X.-T. Zhang, H.-C. Gong, Z.-S. Wu, S.-M. Zhou, and Z.-L. Du, "Ni-doped zinc oxide nanocombs and phonon spectra properties," *Physics Letters A,* vol. 372, pp. 2300-2303, 2008.

[174] R. Elilarassi and G. Chandrasekaran, "Synthesis and optical properties of Ni-doped zinc oxide nanoparticles for optoelectronic applications," *Optoelectronics Letters,* vol. 6, pp. 6-10, 2010.

[175] E. Liu, P. Xiao, J. Chen, B. Lim, and L. Li, "Ni doped ZnO thin films for diluted magnetic semiconductor materials," *Current Applied Physics,* vol. 8, pp. 408-411, 2008.

[176] S. Mandal, A. Das, T. Nath, and D. Karmakar, "Temperature dependence of solubility limits of transition metals (Co, Mn, Fe, and Ni) in ZnO nanoparticles," *Applied Physics Letters,* vol. 89, pp. 144105-144105, 2006.

[177] I. Djerdj, G. Garnweitner, D. Arčon, M. Pregelj, Z. Jagličić, and M. Niederberger, "Diluted magnetic semiconductors: Mn/Co-doped ZnO nanorods as case study," *Journal of Materials Chemistry,* vol. 18, pp. 5208-5217, 2008.

[178] J. Liu, M. Yu, and W. Zhou, "Well-aligned Mn-doped ZnO nanowires synthesized by a chemical vapor deposition method," *Applied Physics Letters,* vol. 87, 2005.

[179] B. Panigrahy, M. Aslam, and D. Bahadur, "Aqueous synthesis of Mn-and Co-doped ZnO nanorods," *The Journal of Physical Chemistry C,* vol. 114, pp. 11758-11763, 2010.

[180] M. Yang, Z. Guo, K. Qiu, J. Long, G. Yin, D. Guan, S. Liu, and S. Zhou, "Synthesis and characterization of Mn-doped ZnO column arrays," *Applied Surface Science,* vol. 256, pp. 4201-4205, 2010.

[181] M. Yuan, W. Fu, H. Yang, Q. Yu, S. Liu, Q. Zhao, Y. Sui, D. Ma, P. Sun, and Y. Zhang, "Structural and magnetic properties of Mn-doped ZnO nanorod arrays grown via a simple hydrothermal reaction," *Materials Letters,* vol. 63, pp. 1574-1576, 2009.

[182] D. Wu, Z. Huang, G. Yin, Y. Yao, X. Liao, D. Han, X. Huang, and J. Gu, "Preparation, structure and properties of Mn-doped ZnO rod arrays," *CrystEngComm,* vol. 12, pp. 192-198, 2010.

[183] J. Lang, Q. Han, C. Li, J. Yang, X. Li, L. Yang, D. Wang, H. Zhai, M. Gao, and Y. Zhang, "Effect of Mn doping on the microstructures and photoluminescence properties of CBD derived ZnO nanorods," *Applied Surface Science,* vol. 256, pp. 3365-3368, 2010.

[184] J. M. Baik and J. L. Lee, "Fabrication of Vertically Well-Aligned (Zn, Mn) O Nanorods with Room Temperature Ferromagnetism," *Advanced Materials,* vol. 17, pp. 2745-2748, 2005.

[185] S. Yu, R. Vincent, H. Bui, T. Thanh, V. Lam, and Y. Lee, "Influence of Mn doping on structural, optical, and magnetic properties of Zn1− xMnxO nanorods," *Journal of Applied Physics,* vol. 108, p. 044910, 2010.

[186] K. Samanta, P. Bhattacharya, R. Katiyar, W. Iwamoto, P. Pagliuso, and C. Rettori, "Raman scattering studies in dilute magnetic semiconductor Zn 1− x Co x O," *Physical Review B,* vol. 73, p. 245213, 2006.

[187] J. Serrano, F. Manjon, A. Romero, F. Widulle, R. Lauck, and M. Cardona, "Dispersive phonon linewidths: the E 2 phonons of ZnO," *Physical Review Letters,* vol. 90, p. 055510, 2003.

[188] H. Fukushima, T. Kozu, H. Shima, H. Funakubo, H. Uchida, T. Katoda, and K. Nishida, "Evaluation of oxygen vacancy in ZnO using Raman spectroscopy," in *2015 Joint IEEE International Symposium on the Applications of Ferroelectric (ISAF), International Symposium on Integrated Functionalities (ISIF), and Piezoelectric Force Microscopy Workshop (PFM)*, 2015, pp. 28-31.

[189] T. C. Damen, S. Porto, and B. Tell, "Raman effect in zinc oxide," *Physical Review,* vol. 142, p. 570, 1966.

[190] J. Duan, H. Wang, H. Wang, J. Zhang, S. Wu, and Y. Wang, "Mn-doped ZnO nanotubes: from facile solution synthesis to room temperature ferromagnetism," *CrystEngComm,* vol. 14, pp. 1330-1336, 2012.

[191] M. Sharma, R. Gayen, A. Pal, D. Kanjilal, and R. Chatterjee, "Room temperature ferromagnetism in Mn-doped zinc oxide nanorods prepared by hybrid wet chemical route," *Journal of Alloys and Compounds,* vol. 509, pp. 7259-7266, 2011.

[192] H. Wang, H. Wang, C. Zhang, F. Yang, C. Yang, H. Gu, M. Zhou, Q. Li, and Y. Jiang, "Effect of annealing on the magnetic properties of solution synthesized Zn 1− x Mn x O nanorods," *Materials Chemistry and Physics,* vol. 113, pp. 884-888, 2009.

[193] J. Wang, H. Zhong, Z. Li, and W. Lu, "Raman study for E2 phonon of ZnO in Zn1-xMnxO nanoparticles," *Journal of Applied Physics,* vol. 97, pp. 86105-86105, 2005.

[194] C. Bundesmann, N. Ashkenov, M. Schubert, D. Spemann, T. Butz, E. Kaidashev, M. Lorenz, and M. Grundmann, "Raman scattering in ZnO thin films doped with Fe, Sb, Al, Ga, and Li," *Applied Physics Letters,* vol. 83, 2003.

[195] Y. Guo, X. Cao, X. Lan, C. Zhao, X. Xue, and Y. Song, "Solution-based doping of manganese into colloidal ZnO nanorods," *The Journal of Physical Chemistry C,* vol. 112, pp. 8832-8838, 2008.

[196] T. Szörényi, L. Laude, I. Bertoti, Z. Kantor, and Z. Geretovszky, "Excimer laser processing of indium-tin-oxide films: An optical investigation," *Journal of Applied Physics,* vol. 78, pp. 6211-6219, 1995.

[197] S. Major, S. Kumar, M. Bhatnagar, and K. Chopra, "Effect of hydrogen plasma treatment on transparent conducting oxides," *Applied Physics Letters,* vol. 49, pp. 394-396, 1986.

[198] B. Panigrahy, M. Aslam, D. S. Misra, M. Ghosh, and D. Bahadur, "Defect-related emissions and magnetization properties of ZnO nanorods," *Advanced Functional Materials,* vol. 20, pp. 1161-1165, 2010.

[199] K. Vanheusden, W. Warren, C. Seager, D. Tallant, J. Voigt, and B. Gnade, "Mechanisms behind green photoluminescence in ZnO phosphor powders," *Journal of Applied Physics,* vol. 79, pp. 7983-7990, 1996.

[200] X. Xu, C. Xu, Y. Lin, T. Ding, S. Fang, Z. Shi, W. Xia, and J. Hu, "Surface photoluminescence and magnetism in hydrothermally grown undoped ZnO nanorod arrays," *Applied Physics Letters,* vol. 100, p. 172401, 2012.

[201] J. Li, H. Fan, X. Chen, and Z. Cao, "Structural and photoluminescence of Mn-doped ZnO single-crystalline nanorods grown via solvothermal method," *Colloids and Surfaces A: Physicochemical and Engineering Aspects,* vol. 349, pp. 202-206, 2009.

[202] H.-W. Zhang, E.-W. Shi, Z.-Z. Chen, X.-C. Liu, B. Xiao, and L.-X. Song, "Optical and magnetic resonance investigations of Zn 1− xMnxO magnetic semiconductors," *Journal of magnetism and magnetic materials,* vol. 305, pp. 377-380, 2006.

[203] N. Srinatha, K. Nair, and B. Angadi, "Microstructure, electronic structure and optical properties of combustion synthesized Co doped ZnO nanoparticles," *Physica B: Condensed Matter,* vol. 474, pp. 97-104, 2015.

[204] M. Bouloudenine, N. Viart, S. Colis, J. Kortus, and A. Dinia, "Antiferromagnetism in bulk Zn1-xCoxO magnetic semiconductors prepared by the coprecipitation technique," *Applied Physics Letters,* vol. 87, pp. 52501-52900, 2005.

[205] H. Yongde, Z. Legui, L. Jun, and H. Zuoqi, "Structural, morphological and magnetic properties of Zn1− x Co x O prepared by sol—gel and hydrothermal method combined," *Journal of Semiconductors,* vol. 37, p. 113002, 2016.

[206] A. Farha, S. A. Mansour, and M. Kotkata, "Structural, optical, and magnetic study of dilute magnetic semiconducting Co-doped ZnO nanocrystals synthesized using polymer-pyrolysis route," *Journal of Materials Science,* vol. 51, pp. 9855-9864, 2016.

[207] I. Djerdj, Z. Jagličić, D. Arčon, and M. Niederberger, "Co-doped ZnO nanoparticles: minireview," *Nanoscale,* vol. 2, pp. 1096-1104, 2010.

[208] D. Sett and D. Basak, "Highly enhanced H 2 gas sensing characteristics of Co: ZnO nanorods and its mechanism," *Sensors and Actuators B: Chemical,* 2016.

[209] Y.-J. Li, K.-M. Li, C.-Y. Wang, C.-I. Kuo, and L.-J. Chen, "Low-temperature electrodeposited Co-doped ZnO nanorods with enhanced ethanol and CO sensing properties," *Sensors and Actuators B: Chemical,* vol. 161, pp. 734-739, 2012.

[210] C. Zou, F. Liang, and S. Xue, "Synthesis and oxygen vacancy related NO 2 gas sensing properties of ZnO: Co nanorods arrays gown by a hydrothermal method," *Applied Surface Science,* vol. 353, pp. 1061-1069, 2015.

[211] M. Yin and S. Liu, "One-pot synthesis of Co-doped ZnO hierarchical aggregate and its high gas sensor performance," *Materials Chemistry and Physics,* vol. 149, pp. 344-349, 2015.

[212] S. Kuriakose, B. Satpati, and S. Mohapatra, "Enhanced photocatalytic activity of Co doped ZnO nanodisks and nanorods prepared by a facile wet chemical method," *Physical Chemistry Chemical Physics,* vol. 16, pp. 12741-12749, 2014.

[213] B. M. Rajbongshi and S. Samdarshi, "ZnO and Co-ZnO nanorods—Complementary role of oxygen vacancy in photocatalytic activity of under UV and visible radiation flux," *Materials Science and Engineering: B,* vol. 182, pp. 21-28, 2014.

[214] M. Fang and Z. Liu, "Structure and properties variations in Zn 1− x Co x O nanorods prepared by microwave-assisted hydrothermal method," *Materials Science in Semiconductor Processing,* vol. 57, pp. 233-238, 2017.

[215] J. El Ghoul, M. Kraini, and L. El Mir, "Synthesis of Co-doped ZnO nanoparticles by sol–gel method and its characterization," *Journal of Materials Science: Materials in Electronics,* vol. 26, pp. 2555-2562, 2015.

[216] J. Cui and U. Gibson, "Electrodeposition and room temperature ferromagnetic anisotropy of Co and Ni-doped ZnO nanowire arrays," *Applied Physics Letters,* vol. 87, p. 133108, 2005.

[217] Z.-P. Sun, L. Liu, L. Zhang, and D.-Z. Jia, "Rapid synthesis of ZnO nano-rods by one-step, room-temperature, solid-state reaction and their gas-sensing properties," *Nanotechnology,* vol. 17, p. 2266, 2006.

[218] P. M. Aneesh, C. T. Cherian, M. K. Jayaraj, and T. Endo, "Co2+ doped ZnO nanoflowers grown by hydrothermal method," *Journal of the Ceramic Society of Japan,* vol. 118, pp. 333-336, 2010.

[219] P. Che, W. Liu, L. Guo, L. He, and C. Chen, "High-temperature ferromagnetism in cobalt-doped ZnO single-crystalline nanorods," *Journal of magnetism and magnetic materials,* vol. 320, pp. 2563-2566, 2008.

[220] X. Zhou, S. Ge, D. Yao, and Y. Xiao, "Preparation, magnetic and optical properties of ZnO and ZnO: Co rods prepared by wet chemical method," *Journal of Alloys and Compounds,* vol. 463, pp. L9-L11, 2008.

[221] J. Zhao, X. Yan, Y. Lei, Y. Zhao, Y. Huang, and Y. Zhang, "Size control of Co-doped ZnO rods by changing the solvent," *Advances in Materials Research,* vol. 1, pp. 75-81, 2012.

[222] P. Li, S. Wang, J. Li, and Y. Wei, "Structural and optical properties of Co-doped ZnO nanocrystallites prepared by a one-step solution route," *Journal of Luminescence,* vol. 132, pp. 220-225, 2012.

[223] X. Wang, R. Zheng, Z. Liu, H.-p. Ho, J. Xu, and S. P. Ringer, "Structural, optical and magnetic properties of Co-doped ZnO nanorods with hidden secondary phases," *Nanotechnology,* vol. 19, p. 455702, 2008.

[224] S. Shi, Y. Yang, J. Xu, L. Li, X. Zhang, G.-H. Hu, and Z.-M. Dang, "Structural, optical and magnetic properties of Co-doped ZnO nanorods prepared by hydrothermal method," *Journal of Alloys and Compounds,* vol. 576, pp. 59-65, 2013.

[225] H. Hao, M. Qin, and P. Li, "Structural, optical, and magnetic properties of Co-doped ZnO nanorods fabricated by a facile solution route," *Journal of Alloys and Compounds,* vol. 515, pp. 143-148, 2012.

[226] N. Tahir, A. Karim, K. A. Persson, S. T. Hussain, A. G. Cruz, M. Usman, M. Naeem, R. Qiao, W. Yang, and Y.-D. Chuang, "Surface defects: possible source of room temperature ferromagnetism in Co-doped ZnO nanorods," *The Journal of Physical Chemistry C,* vol. 117, pp. 8968-8973, 2013.

[227] L. Yang, X. Wu, T. Qiu, G. Siu, and P. K. Chu, "Synthesis and magnetic properties of Zn Co x O nanorods," *Journal of Applied Physics,* vol. 99, p. 074303, 2006.

[228] J. Fu, X. Ren, S. Yan, Y. Gong, Y. Tan, K. Liang, R. Du, X. Xing, G. Mo, and Z. Chen, "Synthesis and structural characterization of ZnO doped with Co," *Journal of Alloys and Compounds,* vol. 558, pp. 212-221, 2013.

[229] F. Xian, X. Wang, L. Xu, X. Li, and W. Bai, "Color tunable electroluminescence from Co-doped ZnO nanorods/p-Si heterojunction," *Journal of Luminescence,* vol. 144, pp. 154-157, 2013.

[230] L. Yanmei, F. Qingqing, W. Mingzai, L. Yan, L. Qingrong, Z. Jun, and W. Baoming, "Structure and photoluminescence of arrayed Zn1− xCoxO nanorods grown via hydrothermal method," *Journal of Physics D: Applied Physics,* vol. 40, p. 4592, 2007.

[231] M. Patra, K. Manzoor, M. Manoth, S. Vadera, and N. Kumar, "Studies on structural and magnetic properties of Co-doped pyramidal ZnO nanorods synthesized by solution growth technique," *Journal of Physics and chemistry of solids,* vol. 70, pp. 659-664, 2009.

[232] X. He, H. Yang, Z. Chen, and S. S. Liao, "Effect of Co-doping content on hydrothermal derived ZnO array films," *Physica B: Condensed Matter,* vol. 407, pp. 2895-2899, 2012.

[233] F. C. Kartawidjaja, Z. Y. Lim, S. L. G. Ng, Y. Zhang, and J. Wang, "Morphology, Optical, and Magnetic Properties of Zn1− xCoxO Nanorods Grown via a Wet Chemical Route," *Journal of the American Ceramic Society,* vol. 93, pp. 3798-3802, 2010.

[234] C.-W. Liu, S.-J. Chang, C.-H. Hsiao, K.-Y. Lo, T.-H. Kao, B.-C. Wang, S.-J. Young, K.-S. Tsai, and S.-L. Wu, "Noise properties of low-temperature-grown Co-doped ZnO nanorods as ultraviolet photodetectors," *IEEE Journal of Selected Topics in Quantum Electronics,* vol. 20, pp. 89-95, 2014.

[235] D. Li, Z. T. Liu, Y. H. Leung, A. B. Djurišić, M. H. Xie, and W. K. Chan, "Transition metal-doped ZnO nanorods synthesized by chemical methods," *Journal of Physics and chemistry of solids,* vol. 69, pp. 616-619, 2008.

[236] T. T. Loan and N. N. Long, "Photoluminescence properties of Co-doped ZnO nanorods synthesized by hydrothermal method," *Journal of Physics D: Applied Physics,* vol. 42, p. 065412, 2009.

[237] M. G. Nair, M. Nirmala, K. Rekha, and A. Anukaliani, "Structural, optical, photo catalytic and antibacterial activity of ZnO and Co doped ZnO nanoparticles," *Materials Letters,* vol. 65, pp. 1797-1800, 2011.

[238] A. Mesaros, C. D. Ghitulica, M. Popa, R. Mereu, A. Popa, T. Petrisor, M. Gabor, A. I. Cadis, and B. S. Vasile, "Synthesis, structural and morphological characteristics, magnetic and optical properties of Co doped ZnO nanoparticles," *Ceramics International,* vol. 40, pp. 2835-2846, 2014.

[239] C. Song, K. Geng, F. Zeng, X. Wang, Y. Shen, F. Pan, Y. Xie, T. Liu, H. Zhou, and Z. Fan, "Giant magnetic moment in an anomalous ferromagnetic insulator: Co-doped ZnO," *Physical Review B,* vol. 73, p. 024405, 2006.

[240] Y. Huang, M. Liu, Z. Li, Y. Zeng, and S. Liu, "Raman spectroscopy study of ZnO-based ceramic films fabricated by novel sol–gel process," *Materials Science and Engineering: B,* vol. 97, pp. 111-116, 2003.

[241] Z. Liu, C. Ong, T. Yu, and Z. Shen, "Catalyst-free pulsed-laser-deposited ZnO nanorods and their room-temperature photoluminescence properties," *Applied Physics Letters,* vol. 88, p. 053110, 2006.

[242] T. Guo, Y. Zhang, Y. Luo, C.-W. Nan, and Y.-H. Lin, "Ferromagnetic and optical properties of Co doped ZnO hexagonal bipods," *Journal of Applied Physics,* vol. 112, p. 083916, 2012.

[243] M. Gao, J. Yang, L. Yang, Y. Zhang, H. Liu, H. Fan, J. Lang, Y. Sui, B. Feng, and Y. Sun, "Synthesis and characterization of aligned ZnO/MgO core–shell nanorod arrays on ITO substrate," *Applied Physics B,* vol. 112, pp. 539-545, 2013.

[244] B. Wang, C. Xia, J. Iqbal, N. Tang, Z. Sun, Y. Lv, and L. Wu, "Influences of Co doping on the structural, optical and magnetic properties of ZnO nanorods synthesized by hydrothermal route," *Solid State Sciences,* vol. 11, pp. 1419-1422, 2009.

[245] O. Lupan, T. Pauporté, T. Le Bahers, B. Viana, and I. Ciofini, "Wavelength-emission tuning of ZnO nanowire-based light-emitting diodes by Cu doping: experimental and computational insights," *Advanced Functional Materials,* vol. 21, pp. 3564-3572, 2011.

[246] Y. Yan, M. M. Al-Jassim, and S.-H. Wei, "Doping of ZnO by group-IB elements," *Applied Physics Letters,* vol. 89, p. 181912, 2006.

[247] R. C. Pawar, D.-H. Choi, J.-S. Lee, and C. S. Lee, "Formation of polar surfaces in microstructured ZnO by doping with Cu and applications in photocatalysis using visible light," *Materials Chemistry and Physics,* vol. 151, pp. 167-180, 2015.

[248] G. Liang, L. Hu, W. Feng, G. Li, and A. Jing, "Enhanced photocatalytic performance of ferromagnetic ZnO: Cu hierarchical microstructures," *Applied Surface Science,* vol. 296, pp. 158-162, 2014.

[249] S. Sarkar and D. Basak, "Defect controlled ultra high ultraviolet photocurrent gain in Cu-doped ZnO nanorod arrays: De-trapping yield," *Applied Physics Letters,* vol. 103, p. 041112, 2013.

[250] C. Lin, S. Young, C. Kung, H. Chen, M. Kao, L. Horng, and Y. Shih, "Structural dependence of photoluminescence and room-temperature ferromagnetism in lightly Cu-doped ZnO nanorods," *IEEE Transactions on Magnetics,* vol. 47, pp. 3366-3368, 2011.

[251] D. Buchholz, R. P. Chang, J. Song, and J. Ketterson, "Room-temperature ferromagnetism in Cu-doped ZnO thin films," *Applied Physics Letters,* vol. 87, 2005.

[252] A. Aravind, M. Jayaraj, M. Kumar, and R. Chandra, "Optical and magnetic properties of copper doped ZnO nanorods prepared by hydrothermal method," *Journal of Materials Science: Materials in Electronics,* vol. 24, pp. 106-112, 2013.

[253] X. Huang, C. Zhang, C. Tay, T. Venkatesan, and S. Chua, "Green luminescence from Cu-doped ZnO nanorods: role of Zn vacancies and negative thermal quenching," *Applied Physics Letters,* vol. 102, p. 111106, 2013.

[254] T. Li, H. Fan, J. Yi, T. S. Herng, Y. Ma, X. Huang, J. Xue, and J. Ding, "Structural and magnetic studies of Cu-doped ZnO films synthesized via a hydrothermal route," *Journal of Materials Chemistry,* vol. 20, pp. 5756-5762, 2010.

[255] S.-L. Young, H.-Z. Chen, M.-C. Kao, C.-Y. Kung, C.-C. Lin, T.-T. Lin, L. Horng, Y.-T. Shih, C.-J. Ou, and C.-H. Lin, "Magnetic properties of La-doped and Cu-doped ZnO nanowires fabricated by hydrothermal method," *International Journal of Modern Physics B,* vol. 27, p. 1362006, 2013.

[256] M. Raja, N. Muthukumarasamy, D. Velauthapillai, and R. Balasundaraprabhu, "Influence of copper on the morphology and properties of one dimensional ZnO nanorod structures," *Superlattices and Microstructures,* vol. 72, pp. 102-110, 2014.

[257] J. Xu, P. Liu, S. Shi, X. Zhang, L. Wang, Z. Ren, L. Ge, and L. Li, "Effect of Cu ions on the morphology, structure and luminescence properties of ZnO nanorod arrays prepared by hydrothermal method," *Applied Surface Science,* vol. 258, pp. 7118-7125, 2012.

[258] C. Liu, Z. Liu, J. Li, Y. Li, J. Han, Y. Wang, Z. Liu, and J. Ya, "Cu-doping ZnO/ZnS nanorods serve as the photoanode to enhance photocurrent and conversion efficiency," *Microelectronic Engineering,* vol. 103, pp. 12-16, 2013.

[259] M. Babikier, D. Wang, J. Wang, Q. Li, J. Sun, Y. Yan, Q. Yu, and S. Jiao, "Cu-doped ZnO nanorod arrays: the effects of copper precursor and concentration," *Nanoscale Research Letters,* vol. 9, p. 1, 2014.

[260] P. Rai, S. K. Tripathy, N.-H. Park, I.-H. Lee, and Y.-T. Yu, "CTAB-assisted hydrothermal synthesis of single-crystalline copper-doped ZnO nanorods and investigation of their photoluminescence properties," *Journal of Materials Science: Materials in Electronics,* vol. 21, pp. 1036-1041, 2010.

[261] W. Dai, X. Pan, C. Chen, S. Chen, W. Chen, H. Zhang, and Z. Ye, "Enhanced UV detection performance using a Cu-doped ZnO nanorod array film," *RSC Advances,* vol. 4, pp. 31969-31972, 2014.

[262] K. H. Kim, Z. Jin, Y. Abe, and M. Kawamura, "Structural and optical properties of Cu-, Ag, and Al-doped zinc oxide nanorods," *Superlattices and Microstructures,* vol. 75, pp. 455-460, 2014.

[263] D. Xu and W. Shen, "Cu-doped ZnO hemispherical shell structures: synthesis and room-temperature ferromagnetism properties," *The Journal of Physical Chemistry C,* vol. 116, pp. 13368-13373, 2012.

[264] J. Iqbal, N. Safdar, T. Jan, M. Ismail, S. Hussain, A. Mahmood, S. Shahzad, and Q. Mansoor, "Facile Synthesis as well as Structural, Raman, Dielectric and Antibacterial Characteristics of Cu Doped ZnO Nanoparticles," *Journal of Materials Science & Technology,* vol. 31, pp. 300-304, 2015.

[265] P. K. Sharma, R. K. Dutta, and A. C. Pandey, "Doping dependent room-temperature ferromagnetism and structural properties of dilute magnetic semiconductor ZnO: Cu 2+ nanorods," *Journal of magnetism and magnetic materials,* vol. 321, pp. 4001-4005, 2009.

[266] G. M. Kumar, P. Ilanchezhiyan, J. Kawakita, M. Subramanian, and R. Jayavel, "Magnetic and optical property studies on controlled low-temperature fabricated one-dimensional Cr doped ZnO nanorods," *CrystEngComm,* vol. 12, pp. 1887-1892, 2010.

[267] M. Shuai, L. Liao, H. Lu, L. Zhang, J. Li, and D. Fu, "Room-temperature ferromagnetism in Cu+ implanted ZnO nanowires," *Journal of Physics D: Applied Physics,* vol. 41, p. 135010, 2008.

[268] M. H. Shin, M. S. Park, S. H. Jung, J. H. Boo, and N. E. Lee, "Effect of doping elements on ZnO etching characteristics with CH4/H2/Ar plasma," *Thin Solid Films,* vol. 515, pp. 4950-4954, 2007.

[269] H. Ma, L. Yue, C. Yu, X. Dong, X. Zhang, M. Xue, X. Zhang, and Y. Fu, "Synthesis, characterization and photocatalytic activity of Cu-doped Zn/ZnO photocatalyst with carbon modification," *Journal of Materials Chemistry,* vol. 22, pp. 23780-23788, 2012.

[270] K. Noipa, S. Rujirawat, R. Yimnirun, V. Promarak, and S. Maensiri, "Synthesis, structural, optical and magnetic properties of Cu-doped ZnO nanorods prepared by a simple direct thermal decomposition route," *Applied Physics A,* vol. 117, pp. 927-935, 2014.

[271] W. Jansen, J. Beckers, J. vd Heuvel, A. D. vd Gon, A. Bliek, and H. Brongersma, "Dynamic behavior of the surface structure of Cu/ZnO/SiO 2 catalysts," *Journal of Catalysis,* vol. 210, pp. 229-236, 2002.

[272] Q. Ma, D. B. Buchholz, and R. P. Chang, "Local structures of copper-doped ZnO films," *Physical Review B,* vol. 78, p. 214429, 2008.

[273] J. Liqiang, Q. Yichun, W. Baiqi, L. Shudan, J. Baojiang, Y. Libin, F. Wei, F. Honggang, and S. Jiazhong, "Review of photoluminescence performance of nano-sized semiconductor materials and its relationships with photocatalytic activity," *Solar Energy Materials and Solar Cells,* vol. 90, pp. 1773-1787, 2006.

[274] C.-L. Hsu, Y.-D. Gao, Y.-S. Chen, and T.-J. Hsueh, "Vertical p-type Cu-doped ZnO/n-type ZnO homojunction nanowire-based ultraviolet photodetector by the furnace system with hotwire assistance," *ACS applied materials & interfaces,* vol. 6, pp. 4277-4285, 2014.

[275] D. Sahu, N. Panda, B. Acharya, and A. Panda, "Microstructural and optical investigations on sonochemically synthesized Cu doped ZnO nanobricks," *Ceramics International,* vol. 40, pp. 11041-11049, 2014.

[276] N. Kouklin, "Cu-Doped ZnO Nanowires for Efficient and Multispectral Photodetection Applications," *Advanced Materials,* vol. 20, pp. 2190-2194, 2008.

[277] A. Gupta, S. Kumar, and H. Bhatti, "Microwave assisted synthesis of ZnO: Cu nano-phosphors and their photoluminescence behaviour," *Journal of Materials Science: Materials in Electronics,* vol. 21, pp. 765-771, 2010.

[278] N. Garces, L. Wang, L. Bai, N. Giles, L. Halliburton, and G. Cantwell, "Role of copper in the green luminescence from ZnO crystals," *Applied Physics Letters,* vol. 81, pp. 622-624, 2002.

[279] Z. Zhang, J. B. Yi, J. Ding, L. M. Wong, H. L. Seng, S. J. Wang, J. G. Tao, G. P. Li, G. Z. Xing, and T. C. Sum, "Cu-doped ZnO nanoneedles and nanonails: morphological evolution and physical properties," *The Journal of Physical Chemistry C,* vol. 112, pp. 9579-9585, 2008.

[280] P. Dhamodharan, R. Gobi, N. Shanmugam, N. Kannadasan, R. Poonguzhali, and S. Ramya, "Synthesis and characterization of surfactants assisted Cu 2+ doped ZnO nanocrystals," *Spectrochimica Acta Part A: Molecular and Biomolecular Spectroscopy,* vol. 131, pp. 125-131, 2014.

[281] J. Iqbal, T. Jan, M. Shafiq, A. Arshad, N. Ahmad, S. Badshah, and R. Yu, "Synthesis as well as Raman and optical properties of Cu-doped ZnO nanorods prepared at low temperature," *Ceramics International,* vol. 40, pp. 2091-2095, 2014.

[282] C.-J. Chang, T.-L. Yang, and Y.-C. Weng, "Synthesis and characterization of Cr-doped ZnO nanorod-array photocatalysts with improved activity," *Journal of Solid State Chemistry,* vol. 214, pp. 101-107, 2014.

[283] Y. Hu, S. Li, and C. Chia, "Correlation between saturation magnetization and surface morphological features in Zn1-xCrxO thin films," *Applied Physics Letters,* vol. 98, p. 2503, 2011.

[284] S. Wang, W. Bo, M. Zhong, C. Liu, Y. Li, M. Zhu, Y. Hu, and H. Jin, "Effect of Cr content on the properties of magnetic field processed Cr-doped ZnO-diluted magnetic semiconductors," *Journal of Nanomaterials,* vol. 2012, p. 2, 2012.

[285] B.-Z. Lin, L. Zhou, S. U. Yuldashev, D.-J. Fu, and T.-W. Kang, "Optical and ferromagnetic properties of Cr doped ZnO nanorods," *Applied Surface Science,* vol. 315, pp. 124-130, 2014.

[286] O. Gürbüz and M. Okutan, "Structural, electrical, and dielectric properties of Cr doped ZnO thin films: Role of Cr concentration," *Applied Surface Science,* vol. 387, pp. 1211-1218, 2016.

[287] G. Zhang, X. Deng, P. Wang, X. Wang, Y. Chen, H. Ma, and D. Gengzang, "Morphology controlled syntheses of Cr doped ZnO single-crystal nanorods for acetone gas sensor," *Materials Letters,* vol. 165, pp. 83-86, 2016.

[288] N. Al-Hardan, M. Abdullah, and A. A. Aziz, "Performance of Cr-doped ZnO for acetone sensing," *Applied Surface Science,* vol. 270, pp. 480-485, 2013.

[289] C.-J. Chang, J.-K. Chen, and T.-L. Yang, "Cr-doped ZnO based NO 2 sensors with high sensitivity at low operating temperature," *Journal of the Taiwan Institute of Chemical Engineers,* vol. 45, pp. 1876-1882, 2014.

[290] A. Meng, J. Xing, Z. Li, and Q. Li, "Cr-Doped ZnO Nanoparticles: Synthesis, Characterization, Adsorption Property, and Recyclability," *ACS applied materials & interfaces,* vol. 7, pp. 27449-27457, 2015.

[291] K. Vijayalakshmi and D. Sivaraj, "Enhanced antibacterial activity of Cr doped ZnO nanorods synthesized using microwave processing," *RSC Advances,* vol. 5, pp. 68461-68469, 2015.

[292] W. Jin, I.-K. Lee, A. Kompch, U. Dörfler, and M. Winterer, "Chemical vapor synthesis and characterization of chromium doped zinc oxide nanoparticles," *Journal of the European Ceramic Society,* vol. 27, pp. 4333-4337, 2007.

[293] M. Zhu, Y. Hu, Y. Li, Y. Li, and H. Jin, "Magnetic properties of Cr-doped ZnO nanorods fabricated by hydrothermal method in a high pulsed magnetic field," *physica status solidi (a),* vol. 208, pp. 2384-2387, 2011.

[294] K. Jayanthi, S. Chawla, A. G. Joshi, Z. H. Khan, and R. Kotnala, "Fabrication of Luminescent, Magnetic Hollow Core Nanospheres and Nanotubes of Cr-Doped ZnO by Inclusive Coprecipitation Method 1," *The Journal of Physical Chemistry C,* vol. 114, pp. 18429-18434, 2010.

[295] M. Jamshidi, M. Ghaedi, K. Dashtian, S. Hajati, and A. Bazrafshan, "Sonochemical assisted hydrothermal synthesis of ZnO: Cr nanoparticles loaded activated carbon for simultaneous ultrasound-assisted adsorption of ternary toxic organic dye: derivative spectrophotometric, optimization, kinetic and isotherm study," *Ultrasonics sonochemistry,* vol. 32, pp. 119-131, 2016.

[296] R. Yathisha, Y. A. Nayaka, and C. Vidyasagar, "Microwave combustion synthesis of hexagonal prism shaped ZnO nanoparticles and effect of Cr on structural, optical and electrical properties of ZnO nanoparticles," *Materials Chemistry and Physics,* vol. 181, pp. 167-175, 2016.

[297] L. Duan, X. Zhao, J. Liu, T. Wang, and G. Rao, "Room-temperature ferromagnetism in lightly Cr-doped ZnO nanoparticles," *Applied Physics A,* vol. 99, pp. 679-683, 2010.

[298] M. K. Gupta, N. Sinha, and B. Kumar, "Dielectric studies and band gap tuning of ferroelectric Cr-doped ZnO nanorods," *Journal of Applied Physics,* vol. 112, p. 014303, 2012.

[299] M. Shaban and A. El Sayed, "Effects of lanthanum and sodium on the structural, optical and hydrophilic properties of sol–gel derived ZnO films: A comparative study," *Materials Science in Semiconductor Processing,* vol. 41, pp. 323-334, 2016.

[300] E.-C. Lee and K. Chang, "Possible p-type doping with group-I elements in ZnO," *Physical Review B,* vol. 70, p. 115210, 2004.

[301] İ. Polat, "Effects of Na-doping on the efficiency of ZnO nanorods-based dye sensitized solar cells," *Journal of Materials Science: Materials in Electronics,* vol. 25, pp. 3721-3726, 2014.

[302] W. C. Lee, G. E. Canciani, B. O. Alwhshe, and Q. Chen, "Enhanced photoelectrochemical water oxidation by Zn x M y O (M= Ni, Co, K, Na) nanorod arrays," *International Journal of Hydrogen Energy,* vol. 41, pp. 123-131, 2016.

[303] J. Lü, K. Huang, X. Chen, J. Zhu, F. Meng, X. Song, and Z. Sun, "Enhanced photo-induced hydrophilicity of the sol–gel-derived ZnO thin films by Na-doping," *Applied Surface Science,* vol. 257, pp. 2086-2090, 2011.

[304] C. Wu and Q. Huang, "Synthesis of Na-doped ZnO nanowires and their photocatalytic properties," *Journal of Luminescence,* vol. 130, pp. 2136-2141, 2010.

[305] Z. Ye, T. Wang, S. Wu, X. Ji, and Q. Zhang, "Na-doped ZnO nanorods fabricated by chemical vapor deposition and their optoelectrical properties," *Journal of Alloys and Compounds,* vol. 690, pp. 189-194, 2017.

[306] S. Ilican, "Effect of Na doping on the microstructures and optical properties of ZnO nanorods," *Journal of Alloys and Compounds,* vol. 553, pp. 225-232, 2013.

[307] Z. Qiu, X. Yang, J. Han, P. Zhang, B. Cao, Z. Dai, G. Duan, and W. Cai, "Sodium-Doped ZnO Nanowires Grown by High-pressure PLD and their Acceptor-Related Optical Properties," *Journal of the American Ceramic Society,* vol. 97, pp. 2177-2184, 2014.

[308] M. Lei, H. He, Q. Yu, C. Chen, Y. Lu, and Z. Ye, "Optical properties of Na-doped ZnO nanorods grown by metalorganic chemical vapor deposition," *Materials Letters,* vol. 160, pp. 547-549, 2015.

[309] W. Ko, S. Lee, G. Baek, and J. P. Hong, "Na mole concentration dependence on optical p-type behaviors of Na-doped ZnO nanowires," *Current Applied Physics,* vol. 14, pp. S103-S106, 2014.

[310] L. Yue, Z. Zhang, Y. Ma, and W. Zhang, "Effect of Na Doping on the Nanostructures and Electrical Properties of ZnO Nanorod Arrays," *Journal of Nanomaterials,* vol. 2016, 2016.

[311] L. Wang, F. Wu, D. Tian, W. Li, L. Fang, C. Kong, and M. Zhou, "Effects of Na content on structural and optical properties of Na-doped ZnO thin films prepared by sol–gel method," *Journal of Alloys and Compounds,* vol. 623, pp. 367-373, 2015.

[312] Y. Wang, X. Luo, L.-T. Tseng, Z. Ao, T. Li, G. Xing, N. Bao, K. Suzukiis, J. Ding, and S. Li, "Ferromagnetism and crossover of positive magnetoresistance to negative magnetoresistance in Na-Doped ZnO," *Chemistry of Materials,* vol. 27, pp. 1285-1291, 2015.

[313] A. Tabib, W. Bouslama, B. Sieber, A. Addad, H. Elhouichet, M. Férid, and R. Boukherroub, "Structural and optical properties of Na doped ZnO nanocrystals: Application to solar photocatalysis," *Applied Surface Science,* vol. 396, pp. 1528-1538, 2017.

[314] S. Kumar and R. Thangavel, "Structural and optical properties of Na doped ZnO nanocrystalline thin films synthesized using sol–gel spin coating technique," *Journal of sol-gel science and technology,* vol. 67, pp. 50-55, 2013.

[315] R. Krithiga, S. Sankar, and G. Subhashree, "Na to tailor the band gap and morphology of ZnO nanograins," *Journal of Materials Science: Materials in Electronics,* vol. 25, pp. 103-110, 2014.

[316] B. J. Jin, S. Im, and S. Y. Lee, "Violet and UV luminescence emitted from ZnO thin films grown on sapphire by pulsed laser deposition," *Thin Solid Films,* vol. 366, pp. 107-110, 2000.